

1 Central exclusive production of χ_c mesons in
2 $\sqrt{s} = 13 \text{ TeV}$ proton-proton collisions

3 Barak Raimond Gruberg Cazón
4 Linacre College, University of Oxford



5

6 Thesis submitted in partial fulfilment of the requirements for the degree of Doctor of
7 Philosophy at the University of Oxford

8

Trinity Term 2021

9 **Central exclusive production of χ_c mesons in**
10 **$\sqrt{s} = 13$ TeV proton-proton collisions**

11 Barak Raimond Gruberg Cazón
12 Linacre College, University of Oxford

13 Thesis submitted in partial fulfilment of the requirements for the degree of
14 Doctor of Philosophy at the University of Oxford

15 Trinity Term, 2021

16 **Abstract**

A measurement is made of the central exclusive production of χ_{c1} and χ_{c2} mesons in proton-proton collisions at a centre-of-mass energy of $\sqrt{s} = 13$ TeV, using data collected by the LHCb experiment corresponding to a total single-interaction integrated luminosity of 711 pb^{-1} . The χ_c candidates are reconstructed through their radiative decay into $J/\psi\gamma$, where we use photons that have converted into an electron pair, $\gamma \rightarrow e^+e^-$, and reconstruct the J/ψ through its dimuon final state. The new High Rapidity Shower Counter sub-detector HERSCHEL is used to reduce inelastic background. The product of the cross section and the branching fractions, where the J/ψ muons are measured to be within the pseudorapidity region $2 < \eta < 4.5$, are measured to be,

$$\sigma_{\chi_{c1} \rightarrow J/\psi [\mu^+\mu^-]\gamma}^{(2 < \eta_{\mu^+\mu^-} < 4.5)} = 19.5 \pm 15.0 \pm 15.2 \text{ pb}$$
$$\sigma_{\chi_{c2} \rightarrow J/\psi [\mu^+\mu^-]\gamma}^{(2 < \eta_{\mu^+\mu^-} < 4.5)} = 99.6 \pm 12.7 \pm 24.5 \text{ pb},$$

17 where the first uncertainty is statistical and the second is systematic. These results are found to
18 be in agreement with theoretical predictions.

*“No man is an island entire of itself; every man
is a piece of the continent, a part of the main;
if a clod be washed away by the sea, Europe
is the less, as well as if a promontory were, as
well as any manner of thy friends or of thine
own were; any man’s death diminishes me,
because I am involved in mankind.
And therefore never send to know for whom
the bell tolls; it tolls for thee.”*

— John Donne, *Devotions upon Emergent Occasions*

Acknowledgements

21 Very few things we accomplish, we accomplish on our own. This thesis would not have
22 been possible without the help of extraordinary people. I would like to recognise them for their
23 guidance, support, and company that have made my DPhil an enjoyable and fruitful experience.

24 First and foremost, I would like to thank my supervisor, Guy Wilkinson, for welcoming me
25 into the LHCb group and entrusting me early on with a number of projects that allowed me to
26 experience multiple facets of the field. His excellent supervision and feedback has helped me to
27 learn and grow enormously as a researcher. I would like thank him for his patience, honesty,
28 and for championing me and my work.

29 I would like to extend my gratitude to the people with whom I worked closely, including
30 Paolo Gandini who showed me the ropes during my early days in the Oxford group and guided
31 me through my first projects and the early stages of the analysis presented in this thesis, as
32 well as Nathan Jurik who provided crucial guidance during my stay at CERN and later stages
33 of said analysis. I would also like to acknowledge members of the HERSCHEL group, especially
34 Raphael Dumps, Daniel Johnson, and Heinrich Schindler, with whom I worked with in the
35 replacement and commissioning of the HERSCHEL modules. Of course, the members of the
36 CEP group who have provided fundamental insights and resources that made this analysis
37 possible cannot go unmentioned, in particular Ronan McNulty. I am very fortunate to have
38 worked with my fellow graduate students who created an engaging environment in the physics
39 department and made for excellent company during our daily coffee breaks.

40 A special debt of gratitude goes to Sue Geddes and Kim Proudfoot, the true heart of the
41 Oxford particle physics department, who have gone beyond their call of duty to help me navigate
42 this experience in the most seamless fashion possible during these uncertain times.

43 I am forever indebted to Linacre College for building a welcoming and diverse environment,
44 which provided an escape from work and ensured the delight of meeting extraordinary people
45 and forming long-lasting friendships. I would like to highlight Conor who I met during my first
46 year at Oxford, quickly became my best friend, and provided invaluable support and comic relief
47 ever since. Ashley is one of the most thoughtful people I have had the pleasure to meet and her
48 friendship, especially during these last few months, has made writing up a delightful experience.
49 I would also like to thank Erich for his life-long friendship, brotherly guidance and support.

50 Most importantly, I wish to thank Daniella for all her love and patience as my work and I
51 became a permanent feature of the living room. Her unwavering support and encouragement
52 have gotten me through the most challenging parts of this thesis. I would also like to extend
53 my gratitude to her family for welcoming me into their home with open arms.

54 I also do not wish to forget those who have helped prepare me for this path. I am thankful
55 for my pre-doctoral experience at Creighton University, where my supervisors Janet Seger and
56 Michael Cherney first introduced me to the world of particle physics, gave me the encouragement
57 and opportunity to form part of the STAR and ALICE collaboration, and ultimately ignited
58 my interest and love for the field.

59 Finally, I would like to thank my parents, sister, and nephew for their life-long love and
60 support. You have always been a driving force in my life in spite of the long distance and I am
61 eternally grateful for all the sacrifices you have made to help me get to where I am today.

62 Contents

63	1 Introduction	1
64	2 Theoretical overview	3
65	2.1 Quantum Chromodynamics	3
66	2.1.1 QCD Lagrangian	3
67	2.1.2 Colour confinement	5
68	2.1.3 Asymptotic freedom	6
69	2.1.4 Pomeron	9
70	2.2 Central exclusive production	9
71	2.3 CEP production mechanisms	10
72	2.3.1 Double-photon exchange	11
73	2.3.2 Photo-production	12
74	2.3.3 Double-pomeron exchange	12
75	2.4 CEP kinematics and dynamics	13
76	2.4.1 Bjorken- x in deep inelastic scattering	13
77	2.4.2 Bjorken- x in double-pomeron exchange	14
78	2.4.3 Characteristically low $p_T^2(X)$ in CEP	15
79	2.5 The Durham model	17
80	2.5.1 Hard process	18
81	2.5.2 Soft-process corrections	20
82	2.5.3 Spin selection rules - spin filter	21
83	2.6 Rapidity-gap-breaking background	24
84	2.7 χ_c meson	27
85	2.7.1 Quantum numbers	27
86	2.7.2 χ_c states as a CEP standard candle	28
87	2.7.3 χ_c radiative decays	28
88	2.8 Previous measurements	29
89	2.8.1 CDF II at Tevatron	29
90	2.8.2 LHCb at CERN	30
91	3 LHCb detector	32
92	3.1 LHCb Experiment	32
93	3.2 Vertex Locator (VELO)	36

94	3.3	Dipole magnet	37
95	3.4	Tracking system	38
96	3.4.1	Tracker Turicensis	39
97	3.4.2	Tracking stations	40
98	3.5	Particle identification	40
99	3.6	Calorimetry	43
100	3.6.1	Scintillating Pad and Pre-Shower Detector	43
101	3.6.2	Electromagnetic Calorimeter (ECAL)	43
102	3.6.3	Hadronic Calorimeter (HCAL)	44
103	3.7	Muon system	44
104	3.8	HERSCHEL	46
105	3.9	Trigger system	48
106	3.9.1	Level-0 trigger	48
107	3.9.2	High Level Trigger (HLT)	49
108	3.10	Reconstruction	49
109	3.10.1	Track reconstruction	49
110	3.10.2	Particle identification	52
111	3.10.3	Stripping and Turbo	53
112	3.11	Simulation	54
113	4	Event selection	55
114	4.1	CEP χ_c study: data sets, selection criteria, and simulation	55
115	4.1.1	CEP χ_c data sets	55
116	4.1.2	CEP χ_c online-selection criteria	56
117	4.1.3	CEP χ_c offline-selection criteria	57
118	4.1.4	Simulation samples for the CEP χ_c analysis	62
119	4.2	Converted-photon study: data sets, selection criteria, and simulation	66
120	4.2.1	D^{*0} and D^0 data set	66
121	4.2.2	D^{*0} and D^0 online-selection criteria	67
122	4.2.3	D^{*0} and D^0 offline-selection criteria	71
123	4.2.4	Simulation samples for converted-photon study	73
124	5	Efficiency determination	74
125	5.1	Determination of the photon-conversion efficiency	74
126	5.1.1	Strategy for the determination of the photon-conversion efficiency	74
127	5.1.2	Study of the photon acceptance in the calibration and signal samples	77
128	5.1.3	Determination of D^0 yields	78
129	5.1.4	Determination of D^{*0} yields	79
130	5.1.5	Efficiency denominator	84
131	5.1.6	Dependence of efficiency on detector occupancy	89
132	5.1.7	Summary of photon-conversion efficiency studies	96

133	5.2	Muon-reconstruction efficiencies	96
134	5.3	J/ψ mass-window efficiency	101
135	5.4	χ_c invariant-mass-difference window-selection efficiency	103
136	5.5	SPD efficiency	104
137	5.6	HERSCHEL efficiency	109
138	5.6.1	Dimuon-data selection	109
139	5.6.2	Dimuon transverse-momentum fit model	112
140	5.6.3	HERSCHEL efficiency calculation	112
141	6	Background and fit model	120
142	6.1	Combinatorial background	120
143	6.1.1	Continuum-combinatorial background	120
144	6.1.2	J/ψ -combinatorial background	122
145	6.2	$\psi(2S)$ feed-down background modelling	125
146	6.2.1	$\psi(2S)$ feed-down reconstruction	126
147	6.2.2	Photon-conversion efficiency and production-mechanism weights	129
148	6.2.3	$\psi(2S)$ feed-down fit and number of expected events	129
149	6.2.4	$\psi(2S)$ feed-down background with HERSCHEL	132
150	6.3	Inelastic χ_c background	133
151	6.3.1	Inelastic data set and selection	133
152	6.3.2	Combinatorial background in inelastic χ_c sample	134
153	6.3.3	$\psi(2S)$ feed-down background in inelastic χ_c sample	139
154	6.3.4	Inelastic χ_c background fit	139
155	6.4	Background summary	144
156	6.5	CEP χ_c fit model	145
157	6.5.1	Invariant-mass-difference parameterisation	145
158	6.5.2	$p_T^2(\chi_c)$ parameterisation	147
159	7	Results and assignment of systematic uncertainties	150
160	7.1	CEP χ_c fit results	150
161	7.2	CEP χ_c fit-validation study	154
162	7.3	Applying the photon-conversion-efficiency correction to the fit results	157
163	7.4	HERSCHEL stability check	157
164	7.5	Luminosity determination	162
165	7.6	Cross-section calculation	162
166	7.7	Assignment of systematic uncertainties	165
167	8	Summary and outlook	168
168		Bibliography	172

CHAPTER 1

Introduction

170 It is undeniable that human beings have an inherent desire to make sense of life and the world we
171 live in. Pushing the frontiers of knowledge has always been a continuous and collective endeavour.
172 The field of particle physics is no exception. Today, standing on the shoulders of giants, thousands
173 of members of the particle physics community continue to make an international effort to develop,
174 maintain, and run what is one of the most impressive and ambitious experimental instruments
175 built by humanity, the Large Hadron Collider (LHC). In this thesis, I present my efforts to
176 contribute to our collective goal of advancing the field of particle physics.

180 The majority of the proton-proton collisions studied at the LHC are inelastic. That is, the
181 incoming protons do not survive the collision and fragment into a large number of particles.
182 The complexity of these events can present an added challenge for event reconstruction, particle
183 identification, and background reduction. However, there is a production mechanism, known as
184 central exclusive production (CEP), where the two incoming protons can interact through the
185 exchange of intermediate particles, produce a single or few low-momentum particles, and remain
186 intact while scattering at small angles. This means that CEP has a distinctive experimental
187 signature where the signal consists of the final-state particles of the produced system in an
188 otherwise empty detector, thus providing a clean environment in which to study resonances and
189 other phenomena.

190 CEP can be mediated by one of three processes, one of which is purely electromagnetic,
191 another is mediated solely by the strong force, and one mediated by both the electromagnetic
192 and strong force, which give us access to the nature of these forces. Furthermore, the dynamics of
193 CEP, which are approximately independent of the produced system, give rise to unique quantum-
194 number-selection rules that effectively allow us to use this mechanism as a spin quantum-number
195 filter, which in principle enables us to measure and confirm the quantum-number nature of
196 newly discovered objects.

197 Although the Large Hadron Collider beauty experiment (LHCb) was designed to study
198 CP violation and suppressed decays in the beauty system, it is well equipped for the study
199 of CEP particularly because of its sensitivity to low momentum and transverse momentum
200 particles. Furthermore, the HERSCHEL sub-detector, which is a system of scintillating planes

201 at high rapidity, has the capability of vetoing inelastic background events. This makes CEP an
202 excellent laboratory for the study of Standard Model states and a discovery tool in the search
203 for unobserved states at LHCb.

204 The main focus of this thesis is the study of the CEP of χ_c mesons at the LHCb experiment.
205 Although significant advancements have been made on the theoretical front of CEP with the
206 development of the so-called Durham model, additional studies are necessary to validate and
207 further constrain theoretical models. The χ_c states are regarded as the *standard candle* for the
208 CEP processes mediated by the strong force. This study is a crucial benchmark that opens
209 LHCb up to a new frontier of future CEP studies, such as the CEP of the Higgs boson.

210 We study the production of χ_c mesons through their radiative decay into $J/\psi[\mu^+\mu^-]\gamma$.
211 Previous measurements of this decay mode have been limited on account of the resolution of
212 the mass peaks of χ_{c1} and χ_{c2} , which sit within 50 MeV/ c^2 of one another. To overcome this
213 problem, we reconstruct the photon using two electrons, known as converted photons, and utilise
214 the momentum resolution of the tracking of the LHCb experiment to improve the χ_c candidates'
215 mass resolution. To this end, we develop a novel method to measure the reconstruction efficiency
216 of converted photons using $D^*(2007)^0 \rightarrow D^0\gamma$ decays.

217 In Chapter 2 we introduce the theoretical background starting with an overview of quantum
218 chromodynamics, the theoretical model of strong interactions responsible for mediating the
219 CEP of χ_c mesons. We then introduce CEP, where we highlight some of the kinematic and
220 dynamic qualities crucial to this analysis before outlining the Durham model. We end with an
221 overview of previous studies and theoretical predictions of the CEP of χ_c mesons. A detailed
222 description of the LHC and the LHCb experiment are presented in Chapter 3 together with an
223 overview of the data acquisition, simulation, and reconstruction framework.

224 We then present the CEP χ_c analysis starting in Chapter 4 with an outline of the data
225 and simulation samples used for the CEP χ_c analysis as well as for the calibration data set
226 necessary for the study of converted photons. We then outline the selection process and criteria
227 applied to each of these samples. In Chapter 5 we present a series of efficiency studies including
228 the efficiency determination of the aforementioned photon-conversions, as well as for the muon
229 reconstruction, detector occupancy, the HERSCHEL veto procedure, and other studies associated
230 with selection cuts. Chapter 6 presents a series of background studies and covers the construction
231 of the fit model used to extract the CEP χ_c signal, the fit results of which are presented in
232 Chapter 7 together with a validation study of the model. Chapter 7 also presents the efficiency
233 corrected results, a HERSCHEL stability check, the luminosity determination, the calculation
234 of the cross-section, and a summary of systematic studies. We conclude with final remarks and
235 outlook in Chapter 8.

CHAPTER 2

236

237

238

Theoretical overview

2.1 Quantum Chromodynamics

Quantum chromodynamics (QCD) [1,2] is a well established and successful quantum field theory (QFT) which describes the strong interaction between six spin- $\frac{1}{2}$ fermions, known as quarks, and eight massless, force-carrying spin-1 bosons known as gluons. Unlike quantum electrodynamics, where only the fermions carry the electric charge, in QCD both quarks and gluons carry colour charge (for a total of $N_C = 3$ colour charges), which leads to interesting phenomena unique to the strong force. The quarks are separated into two categories: the first is up-type quarks with electromagnetic charge $+\frac{2}{3}$ (up u , charm c , and top t), with the second being down-type quarks with electromagnetic charge $-\frac{1}{3}$ (down d , strange s , and bottom or beauty b). More specifically, QCD is a non-Abelian gauge theory [3] generated by the special-unitary group of degree three, $SU(3)_C$, where the C highlights the fact that the theory only applies to colour-charge-carrying particles.

In QFT, each elementary particle has a field associated with it that permeates all space-time and these particles are localised, excited states of their underlying quantum fields. These fundamental fields cannot be measured directly, however there are observables related to these fields, such as charge, that are measurable. Different configurations of these fields, or gauges, can result in identical measurements of the observable. If this is the case, the field is said to be gauge invariant under that gauge transformation. These transformations can be global or local, that is, they can have a dependence on space-time. The dynamics of the theory are specified by the Lagrangian density, \mathcal{L} , which is required to be invariant under a continuous group of these local transformations.

2.1.1 QCD Lagrangian

The quark fields ψ_i and anti-quark fields $\bar{\psi}_i$ take the form of a triplet

$$\psi_i = \begin{pmatrix} \psi_1 \\ \psi_2 \\ \psi_3 \end{pmatrix} \quad \text{and} \quad \bar{\psi}_i = \begin{pmatrix} \bar{\psi}_1^* \\ \bar{\psi}_2^* \\ \bar{\psi}_3^* \end{pmatrix}, \quad (2.1)$$

262 respectively, where the indices $i = \{0, 1, 2\}$ correspond to the three colour charges. The
 263 local-phase transformation of the fermion wave-functions transform as

$$\psi(x) \rightarrow \psi'(x) = e^{ig_s \theta^a(x) \cdot T^a} \psi(x) \quad (2.2)$$

264 where g_s is the bare-strong-coupling constant, $i = \sqrt{-1}$, $\theta^a(x)$ are eight ($a = \{1, \dots, N_C^2 - 1 = 8\}$
 265 for each of the eight gluons) phase factors dependent on space-time coordinates, and T_a are known
 266 as colour-charge matrices and are the generators of the gauge group. The group generators take
 267 the form of 3×3 linearly independent hermitian ($T_a = T_a^\dagger$) matrices related to the Gell-Mann
 268 matrices λ_a , such that

$$T^a = \frac{1}{2} \lambda^a. \quad (2.3)$$

269 The term non-Abelian refers to the fact that the group generators do not commute, such that
 270 their commutation relation is given by

$$[T^a, T^b] = i f^{abc} T^c, \quad (2.4)$$

271 where f^{abc} are the $SU(3)_C$ colour-structure constants with indices a , b , and c , which cycle over
 272 the eight colour degrees-of-freedom. This phase transformation described by Eq. 2.2 corresponds
 273 to a rotation in colour-space such that the axis of rotation depends on the space-time coordinates.

274 Maintaining gauge invariance also requires that we satisfy the Dirac equation,

$$i\gamma^\mu \partial_\mu \psi = m\psi, \quad (2.5)$$

275 where γ_μ are gamma matrices, and $\partial^\mu = (\partial_t, -\vec{\nabla})$ is the four-gradient. This requires the
 276 introduction of new gauge fields. These correspond to the gluon fields, which have a time-like
 277 and three space-like components, and take the form of an octet A_a^μ . Therefore, we modify the
 278 four-gradient such that

$$\partial_\mu \rightarrow D_\mu = \partial_\mu + ig_s A_\mu^a T^a, \quad (2.6)$$

279 giving us the covariant derivative D_μ resulting in the quark-quark-gluon interaction vertex,
 280 shown in Fig. 2.1 (left).

281 The gluon field strength tensor $F_a^{\mu\nu}$, which characterises the interaction between quarks and
 282 gluons, is given by

$$F_a^{\mu\nu} = \partial^\mu A_a^\nu - \partial^\nu A_a^\mu + g_s f^{abc} A_b^\mu A_c^\nu. \quad (2.7)$$

283 The third term, $g_s f^{abc} A_b^\mu A_c^\nu$, represents the gluon self-interaction which arises from the fact
 284 that the gluons also carry colour charge and the generators of the group do not commute. This
 285 gives rise to triple and quartic gluon vertices, shown in Fig. 2.1 middle and right, respectively.

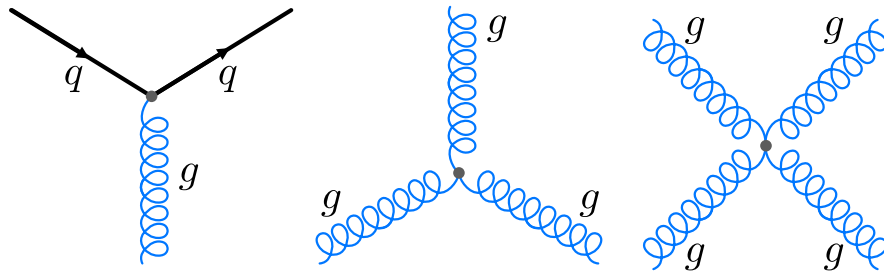


Figure 2.1. Feynman diagram of quark-quark-gluon (left), triple-gluon (middle), and quartic-gluon (right) vertex.

286 The dynamics of the quark and gluon are given by the QCD Lagrangian density

$$\mathcal{L}_{QCD} = \sum_f \bar{\psi}_f^i (i\gamma_\mu D^\mu - m_f)_{ij} \psi_f^j - \frac{1}{4} F_a^{\mu\nu} F_{\mu\nu}^a, \quad (2.8)$$

287 where m_f are fermion mass parameters. Note that there are no gluon mass terms of the form
 288 $m^2 A^\mu A_\mu$ present in the Lagrangian as these terms violate gauge invariance, explaining the
 289 massless nature of the gluon.

290 2.1.2 Colour confinement

291 The gluon-gluon self interaction gives rise to a phenomenon known as colour *confinement* that
 292 explains why we have not observed freely propagating quarks [1,2]. The strong interaction results
 293 in an attractive force between two quarks, and is mediated through the exchange of virtual
 294 gluons. Additional gluon-gluon interactions can occur between the virtual gluons, concentrating
 295 the colour fields as shown in Fig. 2.2. As a result, a large amount of energy can be stored in the
 296 colour fields, or string of colour force, which increases with the distance between the quarks, of
 297 about 1 GeV/fm.

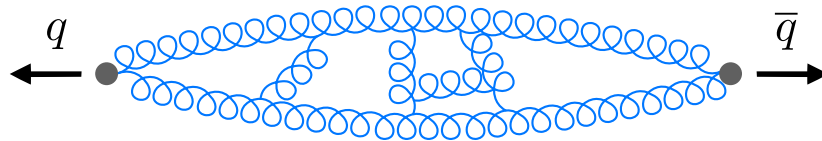


Figure 2.2. Schematic representation of two quarks moving in opposite directions and the concentration of colour fields as a result of additional gluon-gluon interactions between virtual gluons. Adapted from [2].

298 Naively, it would seem that it would be possible to force a quark from a hadron by applying
 299 a sufficiently large force. However, as the distance increases between the nucleon and the quark,
 300 the attractive force stored in these colour fields also increases. Given a large enough distance,
 301 the stored energy can be sufficiently large to create a quark anti-quark pair before the quark
 302 is ever free. This quark anti-quark production process occurs recursively until the energy of

303 the quark pairs is low enough to be bound in a colourless hadronic system of their own. This
 304 process is known as hadronisation and results in a collimated burst of particles known as a jet.
 305 A schematic representation of the hadronisation process is shown in Fig. 2.3.

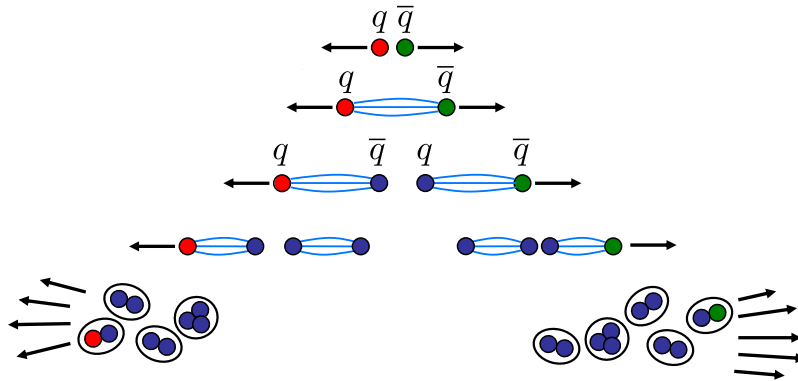


Figure 2.3. Schematic representation of the hadronisation process as two quarks move away from each other at high velocities. The energy stored in gluon tubes results in the recursive production of quark pairs until all quarks are confined in colourless hadrons. Adapted from [2].

306 As a result of this behaviour, quarks are only found in colour-singlet systems. The parton
 307 model [4] classifies hadrons into mesons composed of a quark anti-quark pair ($q\bar{q}$), and baryons
 308 composed of three quarks (qqq), or three anti-quarks ($\bar{q}\bar{q}\bar{q}$). In recent years more exotic hadrons
 309 have been discovered, which can be explained by tetraquark ($qq\bar{q}\bar{q}$) [5–7] or pentaquark states
 310 ($qqqq\bar{q}$) [8–11].

311 2.1.3 Asymptotic freedom

312 The strength of the interaction between gluons and quarks is given by the strong-coupling
 313 constant. However the value used in Feynman diagram calculations, often referred to as the *bare*-
 314 coupling constant, is not the same as the effective-coupling constant measured experimentally.

315 In QCD, quantum fluctuations in the fermion and boson fields can bring virtual quark and
 316 gluons in and out of existence, creating a cloud of electric and colour charge around a quark,
 317 as depicted in Fig. 2.4. Due to the electric attraction between the virtual-quark pairs and the
 318 probe quark, the anti-quarks in the $q\bar{q}$ pair tend to be closer to the probe quark. This effect is
 319 known as vacuum polarisation. This has a *screening* effect which reduces the effective value
 320 of g_s at larger distances from the probe quark. The gluon pairs have the opposite effect: they
 321 enhance the effective value of g_s at larger distances in what is known as an *anti-screening* effect.
 322 It transpires that the anti-screening effect of the gluon pairs dominates, and as a result the
 323 strong coupling decreases at shorter distances. Experimentally, small distances translate to large
 324 four-momentum transfers $Q^2 = -q^2$ as higher energies are needed to resolve smaller distances.
 325 As it turns out, the strong-coupling constant is not constant at all and has a strong dependence
 326 on Q^2 and is better described as a *running-coupling* constant.

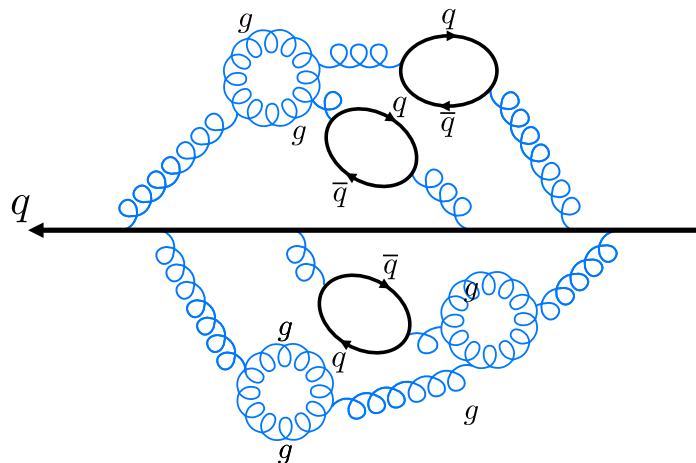


Figure 2.4. Schematic representation of QCD vacuum polarisation.

327 This behaviour has two interesting phenomenological effects. The first is the concept of
 328 confinement which we have already described in Sec. 2.1.2. Essentially, at large distances the
 329 coupling becomes so strong that the energy is sufficient for quark pair creation, making the
 330 isolation of a quark impossible and forcing quarks to be tightly bound within hadrons. The
 331 second is known as asymptotic freedom: at shorter and shorter distances, the strong coupling is
 332 smaller and smaller. Experimentally, this means that when probing quarks within a hadron at
 333 sufficiently high energy, that is interactions involving high four-momentum transfer entailing
 334 large- Q^2 values, the quarks begin to behave more like free particles.

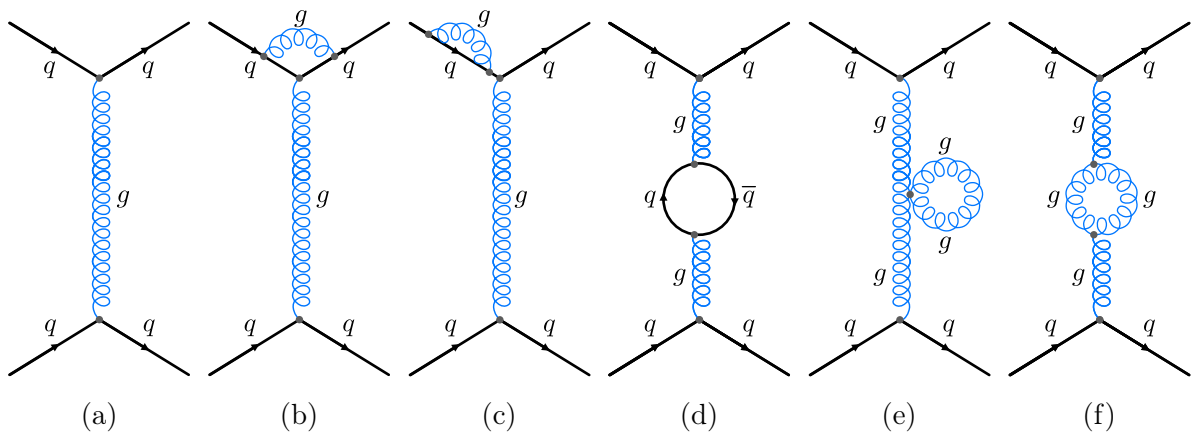


Figure 2.5. Leading order Feynman diagram for gluon exchange (a) corrections to the quark four-vector (b-c), and corrections to the gluon propagator (d-f).

335 When calculating the vertex of a Feynman diagram, any higher-order corrections can and
 336 will contribute to the process. For example, when considering the scattering of two quarks
 337 through the exchange of a gluon, the leading-order diagram is given by Fig. 2.5. However,
 338 the effective-strong coupling will be composed of the sum of all higher-order diagrams which
 339 include quark and gluon loops in the propagator known as the gluon self-energy terms or,

340 as hinted above, vacuum polarisation loops. Due to the Ward identity [12], such corrections
 341 associated with the quark cancel each other perfectly. These corrections include diverging
 342 four-momentum integrals that diverge in the *ultra-violet* as the four-momenta can take large
 343 values. These divergences are controlled through the introduction of a cut-off parameter known
 344 as *renormalization* [2]. This results in a running-coupling constant

$$\alpha_S(Q^2) = \left[\frac{11N_C - 2N_f}{12\pi} \ln \left(\frac{Q^2}{\Lambda^2} \right) \right]^{-1}, \quad (2.9)$$

345 where $N_C = 3$ is the number of colour charges, $N_f = 6$ is the number of quarks, Q^2 is the
 346 four-momentum transfer squared of the exchanged gluon, Λ is known as the QCD-energy-scale
 347 parameter, an experimentally determined parameter (~ 100 MeV) which marks the energy scale
 348 at which $\alpha_s(Q^2)$, starts to diverge asymptotically. Therefore, Λ loosely marks where perturbative
 349 methods are no longer applicable. A summary of strong-coupling constant measurements is
 shown in Fig. 2.6 as a function of Q .

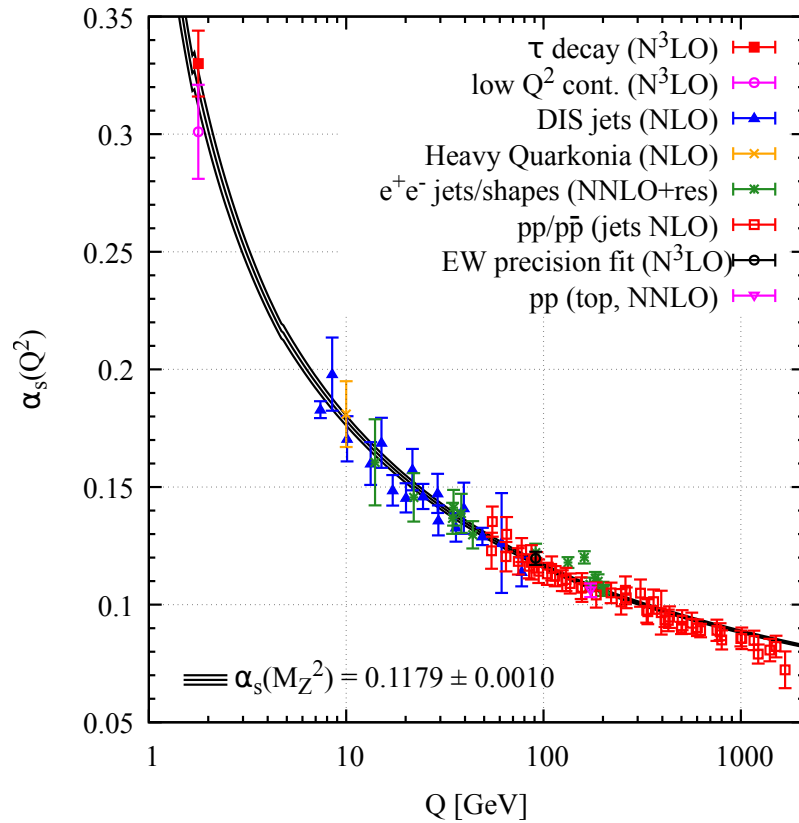


Figure 2.6. Summary of measurements of $\alpha_s(Q^2)$ as a function of the energy scale Q . Reproduced from [13].

351 2.1.4 Pomeron

352 In QCD and in this text, the word pomeron (\mathbb{P}) refers to a pair of gluons in a colour-singlet
 353 state such that they carry the quantum numbers of the vacuum [14]. That is, zero isospin
 354 $I = 0$, natural parity $P = +1$ (even), and even charge-conjugation $C = +1$. As a result, events
 355 mediated by a pomeron do not exchange quantum numbers in the reaction.

356 The word pomeron, coined in honour of the Russian physicist Isaak Yakovlevich Pomeranchuk
 357 [15], is inherited from a theoretical model, called Regge theory, developed by Italian physicist
 358 Tullio Regge, that predates QCD. Regge theory introduced the use of complex-angular momentum
 359 in quantum mechanics. The theory was particularly successful when extended to relativistic
 360 particle physics by Chew and Frautschi and then applied to high-energy hadron-hadron and
 361 photon-hadron interactions [16].

362 Regge theory is a t-channel model, depicted in Fig. 2.7 (centre), where the scattering process
 363 is mediated through a virtual particle. Following the example of the Yukawa hypothesis which
 364 states that long-range nucleon interactions are due to the exchange of pions [17], these t-channel
 365 interactions were generally modelled through the exchange of virtual mesons, such as the π
 366 and ρ mesons which have a definite spin. However, in Regge theory not only can the particles
 367 have complex-angular momentum but, to preserve unitarity, processes are mediated through
 368 the superposition of a family of resonances known as *Regge trajectories* or *Reggeons* [18]. To
 369 obtain agreement between the predicted cross-sections and experimental observations, a new
 370 Regge trajectory was added that carries the quantum numbers of the vacuum. This trajectory
 371 is what is known as the *pomeron* (\mathbb{P}).

372 2.2 Central exclusive production

373 Central exclusive production (CEP) [19–21] is an interesting phenomenon, where a system of
 374 one or two colour-singlet particles, X , are produced in a diffractive-elastic process such that the
 375 colliding protons, p , remain intact after the interaction and scatter at small angles. Essentially,
 376 the system X is produced in a *central* or near-zero rapidity region relative to that of the outgoing
 377 protons, and consists *exclusively* of its decay products and no other hadronic activity. Rapidity,
 378 y , is a quantity used to describe the polar coverage of accelerator physics, measured from the
 379 interaction point, that is invariant under longitudinal relativistic transformation. Rapidity is
 380 defined such that,

$$y = \frac{1}{2} \ln \left(\frac{E + p_z c}{E - p_z c} \right), \quad (2.10)$$

381 where E is the total energy of the particle, p_z is the momentum along the beam line, and c is
 382 the speed of light in vacuum. A particle with momentum perpendicular to the beam line will
 383 have a rapidity of zero, which will increase as the momentum becomes co-linear with the beam
 384 line. An alternative variable known as pseudorapidity, η , is calculated with the assumption that

385 the particle's momentum is much larger than its mass and is defined such that,

$$\eta = -\ln \tan\left(\frac{\theta}{2}\right) \quad (2.11)$$

386 where θ is the polar angle measured from the beam line.

387 These conditions result in a unique topology characterised by two large rapidity gaps, defined
388 as a volume of inactivity in the detector and denoted by \oplus , between each of the outgoing protons
389 and the system of interest, such that

$$p_1 \oplus p_2 \rightarrow p_3 \oplus X \oplus p_4, \quad (2.12)$$

390 where p_1 and p_2 are the incoming protons and p_3 and p_4 are the outgoing protons. Experimentally,
391 this implies that only the decay products of the produced object of interest are present in
392 an otherwise empty detector, as long as there are no pile-up events or secondary interactions
393 which might break the rapidity-gap criteria. Pile-up events have more than one interaction per
394 bunch crossing. As a result, CEP provides a clean environment in which to study the signal
395 while imposing strict kinematic and dynamic constraints, described in detail in Sec. 2.4, which
396 to a close approximation are independent of the central object produced. In addition, CEP
397 allows us to access spin and parity quantum-number information: a difficult task via inelastic
398 events [22]. Measurements of *standard candles* allow CEP predictions to be tested. When we
399 achieve confidence from the agreement between the theoretical and experimental predictions we
400 can then test properties of other states.

401 This makes CEP a powerful tool through which to study known resonant and non-resonant
402 Standard Model (SM) states. Additionally, this makes CEP an even more promising discovery
403 tool in the search for unobserved states predicted by the SM, such as the glueball [23], a bound
404 state composed purely of self-interacting gluons and no quarks, and odderon (O) [24], a t -channel
405 exchange of a colour-neutral system composed of an odd number of gluons, as well as states
406 predicted in Beyond the Standard Model (BSM) theories [25]. Not only does CEP provide access
407 to the system, but it also sheds light on the nature of the system and its quantum properties,
408 making CEP a very valuable probe for spectroscopy studies.

409 2.3 CEP production mechanisms

410 CEP events are mediated by the t -channel exchange of colour singlets. In t -channel interactions
411 one of the incoming protons can emit an intermediate particle that is absorbed by the second
412 proton. Alternatively, each of the incoming protons can emit an intermediate particle that
413 interact with one another. This allows for interactions where the outgoing protons remain
414 intact, something that is not possible in s -channel and u -channel interactions. Colour singlets
415 are particles, or a system of particles, with a total-colour charge of zero. This means there is
416 no exchange of charge or colour charge during the t -channel exchange. This, in turn, allows
417 the colliding protons to remain intact and preserve the rapidity gap of the final-state particles.

418 The Feynman diagram for t -channel scattering events is shown in Fig. 2.7 (centre), together
 419 with the s -channel (left) and u -channel (right) diagrams. There are three possible mediating
 420 mechanisms for CEP: double-photon exchange ($\gamma\gamma \rightarrow X$), photo-production ($IP\gamma \rightarrow X$), and
 421 double-pomeron exchange ($IP\mathbb{P} \rightarrow X$).

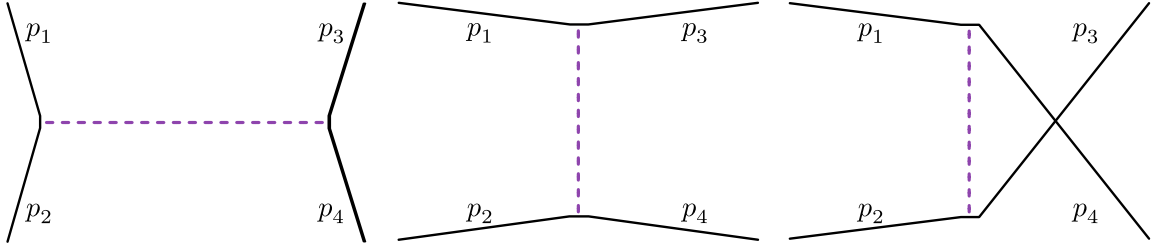


Figure 2.7. Feynman diagrams of different possible scattering channels in proton-proton collisions including the s -channel (left), t -channel (centre), and u -channel (right). Here p_1 and p_2 are incoming particles while p_3 and p_4 are outgoing particles. The exchange of intermediate particles is shown in dashed purple.

422 2.3.1 Double-photon exchange

423 In double-photon exchange, also known as two-photon fusion, the event is mediated by a
 424 theoretically well-understood Quantum Electrodynamics (QED) process, where each of the
 425 protons emits a quasi-real photon (low- Q^2) where q is the four-momentum transfer from the
 426 proton to the emitted photon that couples to the electromagnetic charge of the proton. The
 427 lowest-order Feynman diagram for this process is shown in Fig. 2.8 (left) for dimuon production.

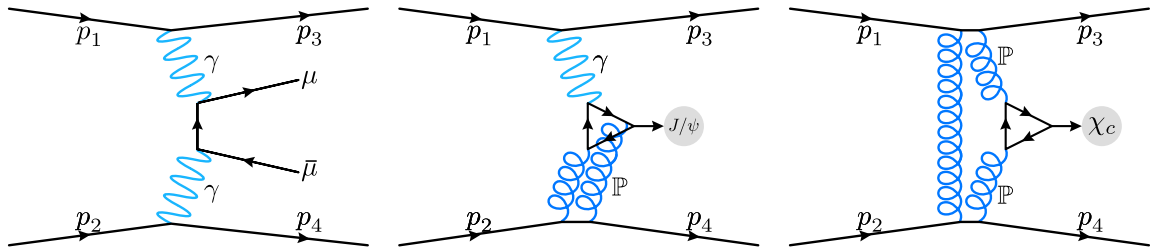


Figure 2.8. Lowest-order Feynman diagrams for three CEP mechanisms: double-photon exchange (left), photo-production (centre), and double-pomeron exchange (right).

428 Through double-photon exchange we are able to study non-resonant states such as light-
 429 by-light scattering ($\gamma\gamma \rightarrow \gamma\gamma$) [26], di-electron ($\gamma\gamma \rightarrow e^+e^-$) [27, 28] and di-muon ($\gamma\gamma \rightarrow$
 430 $\mu^+\mu^-$) [29, 30] production, as well as charged-electroweak-gauge boson pair production ($\gamma\gamma \rightarrow$
 431 W^+W^-) [31]. The CEP $\gamma\gamma$ channel can also be used to study meson production such as
 432 $\gamma\gamma \rightarrow \eta_c$ [32, 33] as well as double-hadron production ($\gamma\gamma \rightarrow hh$). The latter process is of
 433 particular interest as it has the potential to shed light on the nature of the odderon [34] as well
 434 as glueballs [35].

435 2.3.2 Photo-production

436 A second mechanism involves the exchange of a photon emitted by one of the protons and a
 437 pomeron from the other in a process known as photo-production or photon-pomeron fusion.
 438 The lowest-order Feynman diagram for J/ψ production is shown in Fig. 2.8 (centre).

439 The fusion of an odd-charge-conjugate photon and an even-charge-conjugate pomeron implies
 440 we are able to produce odd-charge-conjugate objects allowing for the study of spin-1 vector meson
 441 final states (1^{--}) such as $\gamma\mathbb{P} \rightarrow \rho^0$ [36–39]. This also allows for the study of heavy-quarkonia
 442 states ($c\bar{c}$ and $b\bar{b}$) such as $\gamma\mathbb{P} \rightarrow J/\psi$ [40–46], $\psi(2S)$ [41,43,46], and $\gamma\mathbb{P} \rightarrow \Upsilon(1S)$ [47–49] mesons.
 443 These states are particularly interesting as they cover a regime where perturbative QCD applies
 444 and serve as a probe of small Bjorken- x , the fraction of the proton momentum carried by the
 445 parton (quarks and gluons) involved in the interaction. Quarkonia studies are also of particular
 446 interest in searching for the odd-charge-conjugate odderon, O , as it is expected to contribute
 447 to the vector-meson-CEP cross-section via an odderon-pomeron interaction ($O\mathbb{P} \rightarrow X$). The
 448 contributions of the odderon can be determined by detecting an excess of these CEP events. In
 449 addition to the study of mesons, it is also possible to study the exclusive production of the Z^0
 450 boson via this process [28].

451 2.3.3 Double-pomeron exchange

452 The third CEP production mechanism, double-pomeron exchange (DPE) also known as pomeron-
 453 pomeron fusion, is mediated purely through QCD and is responsible for the production of
 454 $\chi_c(1P)$ mesons. The CEP of χ_c mesons is the main subject of this study and an introduction to
 455 the particle is detailed in Sec. 2.7 together with an exposition of previous relevant measurements
 456 of this meson. The lowest-order Feynman diagram for the double-pomeron channel for χ_c
 457 production is illustrated in Fig. 2.8 (right).

458 DPE provides a versatile framework through which to study properties of a wide range of
 459 SM and BSM physics. Since this channel involves the interaction of two even-charge-conjugate
 460 pomerons, it is possible to study the CEP of any even-charge-conjugate particle that couples to
 461 gluons. The unique dynamic constraints of CEP limit the process and allows it to behave as a
 462 quantum-number filter. The spin-selection rules associated with these production constraints
 463 are summarised in Sec. 2.5.3. As a result, this process allows for the study of particles with
 464 $J^{CP} = 0^{++}, 1^{++}, 2^{++}, \dots$ and isospin $I = 0$. For example, this channel is responsible for the
 465 production of χ_c mesons, a heavy-charmonium state ($c\bar{c}$). It is also possible to study the CEP
 466 χ_b mesons, the heavier bottomonium ($b\bar{b}$) counterparts of χ_c mesons, which are at an energy
 467 scale where pQCD predictions might also be more reliable.

468 DPE is also a promising production mechanism for particle discovery. For example, lattice
 469 QCD predicts the lightest glueball state to be a low-mass, ~ 1700 MeV, scalar with quantum
 470 numbers 0^{++} [23,50,51]. This makes $f_0(1500)(0^{++})$ and $f_0(1710)(0^{++})$ prime glueball candidates,
 471 and CEP an ideal tool for their study.

472 The interest of the physics community in CEP physics has been reignited thanks to its inherent
 473 ability to measure the spin of the central system and its application to the measurement of the
 474 spin for the Higgs boson. The CEP of the Higgs boson is mediated via the DPE [21,22,52–54]. For
 475 example, the Higgs boson can be reconstructed through a di-jet decay, $IP \rightarrow H^0 \rightarrow b[j] \bar{b}[j]$,
 476 a final state that can be produced directly through DPE, $(IP \rightarrow jj)$ [29]. As a result, the
 477 measurement of the cross-section for the CEP of di-jets is an important measurement with
 478 which to calibrate our theoretical prediction of the CEP of the Higgs boson. A similar incentive
 479 applied for the study of two-photon CEP via double-pomeron, $(IP \rightarrow \gamma\gamma)$ [55], as this is one
 480 of the final states used in the discovery of the Higgs boson by the CMS experiment [56].

481 It is important to highlight that observing even a few CEP Higgs events would confirm its
 482 0^{++} nature. As result, it is essential that we conduct measurements of other resonant states
 483 produced exclusively through this mechanism, such as the CEP χ_c mesons, in order to test our
 484 theoretical understanding of this process and guide us through these future measurements.

485 2.4 CEP kinematics and dynamics

486 2.4.1 Bjorken- x in deep inelastic scattering

487 In deep inelastic scattering [57], a high-energy-charged-probe particle is fired at a nucleon in
 488 order to probe the nucleon's internal structure via the exchange of a virtual gauge boson, with
 489 four-momentum q . The kinematics of deep inelastic scattering can be described in terms of a
 490 few relativistic-invariant quantities, one of which is known as Bjorken- x [58], defined by,

$$x \equiv \frac{Q^2}{2P \cdot q}, \quad (2.13)$$

491 where Q^2 is the square of the four-momentum of the gauge boson, such that

$$Q^2 = -q^2, \quad (2.14)$$

492 and P is the momentum of the incoming hadron. The resolving wavelength of the virtual gauge
 493 boson is inversely proportional to the magnitude of its four-momentum, as given by the de
 494 Broglie relation [59],

$$\lambda = \frac{h}{p}, \quad (2.15)$$

495 where λ is the wavelength associated with the particle, p is its momentum, and h is Planck's
 496 constant. At low- Q^2 values, the wavelength is long compared to the size of the proton. As the
 497 wavelength becomes comparable to the size of the proton, the photon begins to resolve the size
 498 of the proton. For high- Q^2 values, the wavelength is much shorter than the size of the proton,
 499 and is able to resolve the internal structure of the struck proton.

500 When Bjorken- x is plotted against the spectrum of the probe particle, the distribution has
 501 a consistent profile regardless of the collision energy. That is, the scattering process is not

502 determined by the collision energy and therefore the resolving power of the gauge boson. This
 503 is known as Bjorken scaling. The independence of the absolute-resolution scale suggests that
 504 hadrons behave as a collection of point-like constituents known as partons, quarks and gluons.

505 **2.4.2 Bjorken- x in double-pomeron exchange**

506 When the mass of the central system, m_X , is sufficiently large (*i.e.* in the high- Q^2 regime) the
 507 CEP mechanism via double-pomeron fusion can be successfully described by perturbative QCD
 508 (pQCD). Here, large m_X is loosely defined in relation to the QCD energy scale Λ_{QCD} such that
 509 $Q^2 \gg \Lambda_{\text{QCD}}^2$.

510 CEP calculations also involve low- Q^2 diffractive physics where perturbation theory breaks
 511 down. The physics in this regime is associated with secondary interactions that result in
 512 additional hadronic activity which breaks the CEP-double-rapidity-gap criteria, such as in
 513 rescattering corrections. CEP physics in this region can be calculated with Regge theory [60,61].
 514 These soft QCD calculations have a strong sensitivity to low- x and Q^2 gluon parton-distribution
 515 functions (PDF), which describe the probability of a parton having a fraction, x , of the proton's
 516 energy. These PDFs are extracted from data using global fits and have large uncertainties. The
 517 precision of these PDFs plays a fundamental role in studies of SM physics and BSM searches at
 518 hadron machines. The sensitivity of DPE to high- Q^2 as well as low- Q^2 physics makes it an ideal
 519 mechanism to put perturbative and non-perturbative theoretical frameworks of QCD to test.

520 The parton model is often formulated in a frame where the proton has very high energy.
 521 This allows us to neglect the proton mass such that the centre-of-mass energy, \sqrt{s} , is given by

$$\sqrt{s} = p_1 + p_2, \quad (2.16)$$

522 where p_1 and p_2 are the momenta of the colliding protons. In this reference frame, we can also
 523 neglect the mass of the quarks and the transverse momentum of the incident partons such that
 524 the four-momenta of the partons in the hadron-hadron centre-of-mass frame are given by

$$p_a = \frac{\sqrt{s}}{2} (x_a, 0, 0, x_a) \quad \text{and} \quad p_b = \frac{\sqrt{s}}{2} (x_b, 0, 0, -x_b), \quad (2.17)$$

525 where x_a and x_b are the fraction of energy carried by the parton from proton p_1 and p_2
 526 respectively. We apply this approximation to DPE. As a result we can write the square of the
 527 mass of the central system, m_X , in terms of the parton momentum such that,

$$m_X^2 = (p_a + p_b)^2 = x_a x_b s. \quad (2.18)$$

528 It is conventional to define the unitless quantity, τ , such that,

$$\tau = x_a x_b = m_X^2 / s. \quad (2.19)$$

529 We can write the rapidity of the central system in terms of the parton momentum fraction,

$$y = \frac{1}{2} \ln \left(\frac{E + p_z}{E - p_z} \right) = \frac{1}{2} \ln \left(\frac{E(x_a + x_b + x_a - x_b)}{E(x_1 + x_b - x_a + x_b)} \right) = \frac{1}{2} \ln \left(\frac{x_a}{x_b} \right), \quad (2.20)$$

530 where E is the energy of the central system and p_z is its longitudinal momentum. Making use
531 of Eq. 2.18, we can write the fractional momenta in terms of the centre-of-mass energy and the
532 central system's mass and rapidity such that,

$$x_a = \frac{m_X}{\sqrt{s}} e^{+y} \quad \text{and} \quad x_b = \frac{m_X}{\sqrt{s}} e^{-y}. \quad (2.21)$$

533 The forward topology of the LHCb experiment allows us to study central systems with a
534 rapidity range $2 < y < 4.5$, giving us access to two Bjorken- x regions that are not accessible
535 through zero rapidity central-barrel experiments: one at low- x and another at high- x . For
536 a central system of mass $m_X = 3.5$ GeV (approximately the mass of a χ_c meson) produced
537 in proton-proton (pp) collisions at a centre-of mass energy of $\sqrt{s} = 13$ TeV, we are able to
538 access fractional momenta (Bjorken- x) of the order 10^{-2} to 10^{-3} and 10^{-5} to 10^{-6} for the case
539 when the colliding gluon belongs to the proton moving in the positive and negative direction,
540 respectively. This provides a unique opportunity to obtain important constraints for PDF
541 fits. The kinematic coverage in (x, Q^2) phase space for pp collisions at a centre-of-mass energy
542 $\sqrt{s} = 13$ TeV for the LHCb experiment is shown in Fig. 2.9, together with the coverage of
543 other experiments including ATLAS, CMS, CDF/D0, HERA, and more generally, fixed-target
544 experiments. The rapidity coverage is shown in red-dashed-diagonal lines.

545 2.4.3 Characteristically low $p_T^2(X)$ in CEP

546 The CEP of mesons occurs via the t -channel exchange of a colourless object between the colliding
547 protons, see Fig. 2.7 (centre). In the case of χ_c meson production, this process occurs through a
548 DPE. The differential cross-section of elastic pp scattering as a function of the four-momentum
549 transfer squared at the proton vertex, t , also known as one of the three Mandelstam variables
550 (s , t , and u), falls with increasing values of $|t|$. The four-momentum transfer squared for the
551 t -channel is given by

$$t = (p_1 - p_3)^2 = (p_4 - p_2)^2, \quad (2.22)$$

552 where p_1 and p_2 are the four momenta of the incident protons and p_3 and p_4 are the four
553 momenta of the scattered protons. To a first approximation, the cross-section dependence on
554 the four-momentum transfer in elastic interactions can be parameterised as an exponential
555 function such that,

$$\frac{d\sigma}{dt} \propto e^{-b_{\text{CEP}}|t|}, \quad (2.23)$$

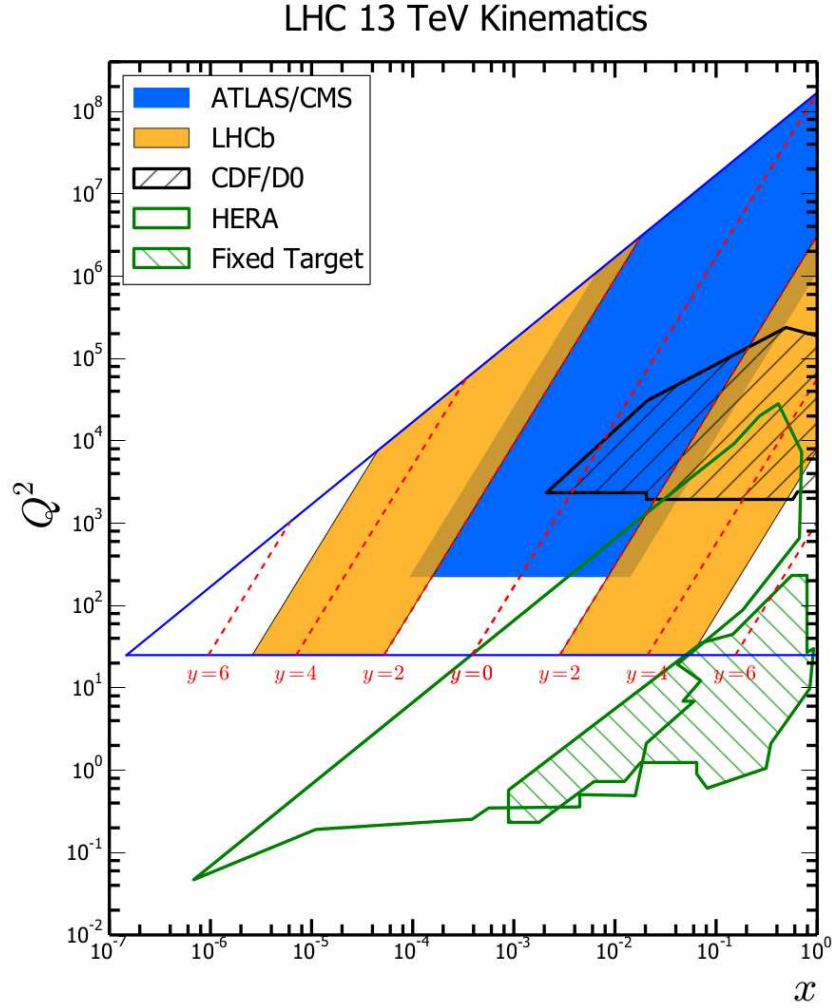


Figure 2.9. Kinematic coverage in (x, Q^2) phase space for pp collisions at a centre-of-mass energy $\sqrt{s} = 13$ TeV in comparison to ATLAS, CMS, CDF/D0, HERA and fixed-target coverage. Image reproduced from [62].

556 for small- $|t|$ values, $|t| < 0.5$ GeV/ c , and where b_{CEP} is the slope of the exponential, in this
 557 case related to the CEP mechanism. Similarly, the differential cross-section for inelastic events
 558 with proton dissociation falls as $|t|$ grows. However, it does so at a much lower rate. This is
 559 parameterised with a power-law function such that,

$$\frac{d\sigma}{dt} \propto \left(1 + \left(\frac{b_{\text{In.}}}{n}\right) |t|\right)^{-n}, \quad (2.24)$$

560 where n is the power law's exponent. For low- $|t|$ values, this can be approximated with an
 561 exponential that takes the same form as Eq. 2.23,

$$\frac{d\sigma}{dt} \propto e^{-b_{\text{In.}} |t|}, \quad (2.25)$$

562 where b_{In} is the slope of the exponential, in this case related to the inelastic mechanism.

563 Unfortunately, $|t|$ is not directly accessible experimentally but it can be estimated from the
564 transverse-momentum squared of the central system, X , in the laboratory frame, such that,

$$t \approx -p_{\text{T}}^2(X). \quad (2.26)$$

565 Therefore, although the invariant-mass distribution of $\chi_c \rightarrow J/\psi[\mu^+\mu^-]\gamma[e^+e^-]$ inelastic and
566 CEP events is expected to be similar, CEP events have a characteristically lower transverse-
567 momentum squared compared to their inelastic counterparts, which is a signature that can be
568 used to discriminate between signal and background. The low-momentum exchange between the
569 interacting protons, characteristic of CEP events, stems from the requirement that the protons
570 do not fragment. Therefore, the transverse-momentum squared of the object of interest, X , is
571 also small in CEP events. On the other hand, inelastic interactions result in the fragmentation
572 of one or both of the protons, which does not impose an upper constraint on the momentum
573 exchange, hence producing particles with larger $p_{\text{T}}^2(X)$ on average.

574 The low-momentum transfer constraint also manifests itself in the low-transverse momentum
575 of the outgoing protons, which typically have $p_T < 1$ GeV for CEP events [20]. In fact, with
576 information about the incoming proton, a measurement of the outgoing proton's kinematics, and
577 law of conservation of four momentum we are able to calculate the mass of the object of interest,
578 m_X , regardless of its decay. This technique is referred to as the missing-mass method [53]. As a
579 result, it is desirable for CEP studies to measure the kinematics of the outgoing proton with
580 high-rapidity spectrometers.

581 2.5 The Durham model

582 In this section, we present a summary of the formalism used to calculate the perturbative CEP
583 cross-section, known as the Durham model [20, 63–69]. Theoretical predictions of the cross
584 sections for the processes relevant for this thesis are presented in Chapter 7. The lowest order
585 Feynman diagram for the QCD contribution to CEP, DPE, is shown in Fig. 2.10. As mentioned
586 previously, this occurs through the t -channel exchange of two gluons: a gluon that couples
587 to the central system, X , and one that is present to ensure the colour singlet interaction
588 between the colliding partons, known as a *screening gluon*. Here p_1 and p_2 are the momenta of
589 the incoming protons, p_3 and p_4 are the momenta of the outgoing protons, q_1 and q_2 are the
590 momenta carried by each of the gluons that couples to the central system, corresponding to the
591 fractional momenta x_1 and x_2 associated with their respective protons, while x' is the fractional
592 momentum carried by the screening gluon. Q is the gluon-loop momentum, and μ and ν are
593 the Lorentz indices associated with their corresponding four-momenta vector.

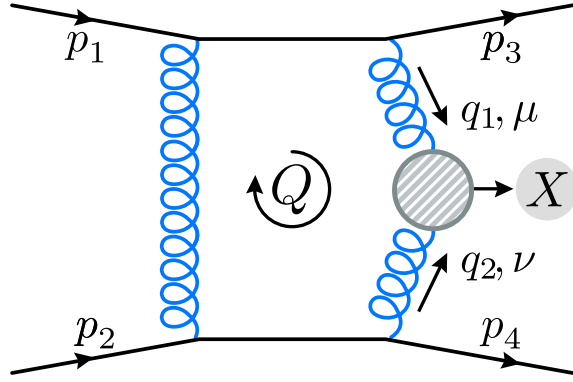


Figure 2.10. Lowest-order Feynman diagrams for the DPE CEP mechanisms for $p \oplus p \rightarrow p \oplus X \oplus p$ process in pQCD.

594 2.5.1 Hard process

595 The parton-level amplitude, A , of the CEP DPE production mechanism described by Fig. 2.10
 596 is given by

$$\frac{iA}{s} = \frac{8}{N_C^2 - 1} \alpha_s^2 C_F^2 \int \frac{d^2 Q_T}{Q_T^2 q_1^2 q_2^2} \overline{\mathcal{M}}, \quad (2.27)$$

597 where s is the centre-of-mass energy squared, $i = \sqrt{-1}$, N_C is the number of colour charges, and
 598 C_F is known as the colour factor which describes the relative weight of the vertex associated
 599 with gluon bremsstrahlung, or the radiation of a gluon from a quark line. In the case of SM
 600 QCD, $N_C = 3$ and $C_F = 4/3$. Q_T is the gluon-loop transverse momentum and q_1 and q_2 are
 601 the momentum of the fusing gluon, while α_s is the QCD running coupling. The colour-averaged,
 602 normalised sub-amplitude $\overline{\mathcal{M}}$ for the $gg \rightarrow X$ process is given by

$$\overline{\mathcal{M}} \equiv \frac{2}{m_X^2} \frac{1}{N_C^2 - 1} \sum_{a,b} \delta^{ab} q_{1T}^\mu q_{2T}^\nu V_{\mu\nu}^{ab}, \quad (2.28)$$

603 where m_X is the mass of the central system produced in the gluon-fusion vertex, $V_{\mu\nu}^{ab}$, associated
 604 with the coupling of the two gluons with the central object produced $gg \rightarrow X$, with q_{1T} and
 605 q_{2T} being the transverse momenta of the fusing gluons, given by

$$q_{1T} = Q_T - p_{3T} \quad \text{and} \quad q_{2T} = -Q_T - p_{4T}, \quad (2.29)$$

606 respectively, where p_{3T} and p_{4T} are the transverse momentum of the outgoing protons.

607 The integral over the momentum loop, in Eq. 2.27, diverges as Q_T approaches zero, which
 608 is known as an infrared divergence. This is corrected via higher-order virtual corrections to
 609 the leading-order process through the introduction of Sudakov form factors, T_g [70, 71]. The
 610 Sudakov form factors represent the poisson probability that the gluons involved in the hard
 611 process emit non-resolvable parton radiation that might break the exclusivity requirement, and

612 therefore the rapidity gap criteria. Assuming a fixed, strong-coupling constant α_s , for simplicity,
 613 the form factor is given by

$$T_g(Q_T^2, \mu^2 = m_X^2) = \exp\left(-\frac{\alpha_s N_c}{4\pi} \ln^2\left(\frac{Q_T^2}{m_X^2}\right)\right), \quad (2.30)$$

614 where μ is the hard scale at which the form factor is regularised. In this case, the regularisation
 615 occurs at the scale of the central system's mass, $\mu = m_X$. T_g goes to zero as Q_T goes to zero,
 616 thus keeping the momentum-loop integral finite and allowing the CEP amplitude in the infrared
 617 region to vanish. In the case of the production of χ_c mesons μ is approximately 3 GeV where a
 618 significant part of the cross-section calculation falls under the unstable, low- Q_T infrared regime.
 619 As a result, corrections described in Sec. 2.5.2 are included to account for these soft processes.
 620 The infrared contribution becomes less significant at higher energy scales, such as that of the
 621 Higgs boson, $\mu \simeq m_H \sim 125$ GeV [67].

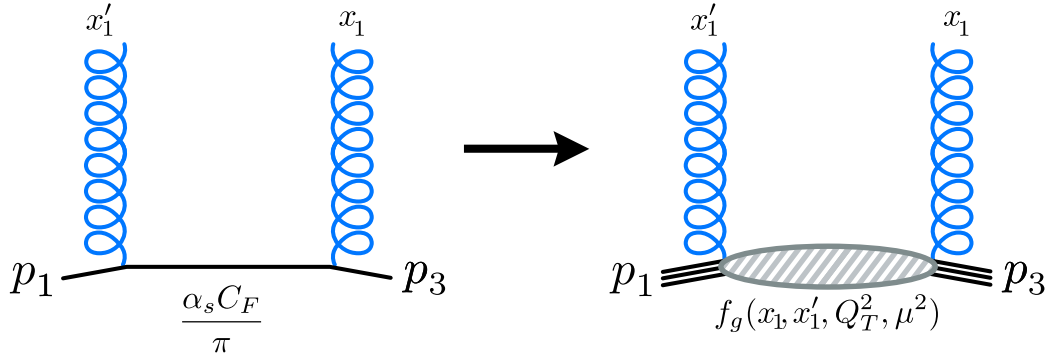


Figure 2.11. Pictorial representation of the replacement of a quark-level treatment, $\alpha_s C_F/\pi$, to a skewed, unintegrated, gluon PDF, $f_g(x, x', Q_T^2, \mu^2)$.

622 To convert the parton-level amplitude Eq. 2.27 to a hadron-level amplitude, we introduce
 623 the replacement of the coupling constant described by Fig. 2.11 as

$$\frac{\alpha_s C_F}{\pi} \rightarrow f_g(x_{1,2}, x', Q_T^2, \mu^2 = m_x^2), \quad (2.31)$$

624 where f_g is known as the skewed, unintegrated gluon PDF, which describes the probability
 625 of finding a gluon with a given momentum fraction, x' is the momentum fraction carried
 626 by the screening gluon, and x_i is the momentum fraction carried by the gluon fusing to the
 627 central system. Here the term skewed refers to the fact that the momentum fraction carried
 628 by the screening gluon can differ from that of the fusing gluon where $x' \ll x_i$ [72]. The final

629 perturbative CEP amplitude is given by,

$$T \equiv \frac{iA}{s} = \pi^2 \int \frac{d^2\vec{Q}_T \bar{\mathcal{M}}}{\bar{Q}_T^2 (\vec{Q}_T - \vec{p}_{1T})^2 (\vec{Q}_T + \vec{p}_{2T})^2} f_g(x_q, x'_1, Q_1^2, \mu^2) f_g(x_2, x'_2, Q_2^2, \mu^2) F_p(t_1) F_p(t_2), \quad (2.32)$$

630 where $F_p(t_1)$ and $F_p(t_2)$ are the proton elastic form factors for the corresponding proton in the
 631 interaction. The t dependence, where t corresponds to the t -channel Mandelstam variable, of
 632 the proton form factor is not well known and is taken from experimental soft hadronic data and
 633 is found to be in agreement with CEP J/ψ studies [40, 42–46, 73]. As hinted in Sec. 2.4.3, this
 634 takes the form of $F_p(t) = \exp(bt/2)$. The parameter b is taken from fits of soft hadronic data
 635 and is found to be $b \sim 4 \text{ GeV}^{-2}$ [74].

636 2.5.2 Soft-process corrections

637 The exclusivity requirement of CEP demands that the event is not accompanied by additional
 638 activity. One such source of activity comes from soft, non-perturbative secondary interactions.
 639 The Durham model considers two types of rescattering processes associated with the underlying
 640 event collectively known as *soft survival effects*, each of which measure the probability that the
 641 CEP double-rapidity-gap criteria will *survive* the scattering process.

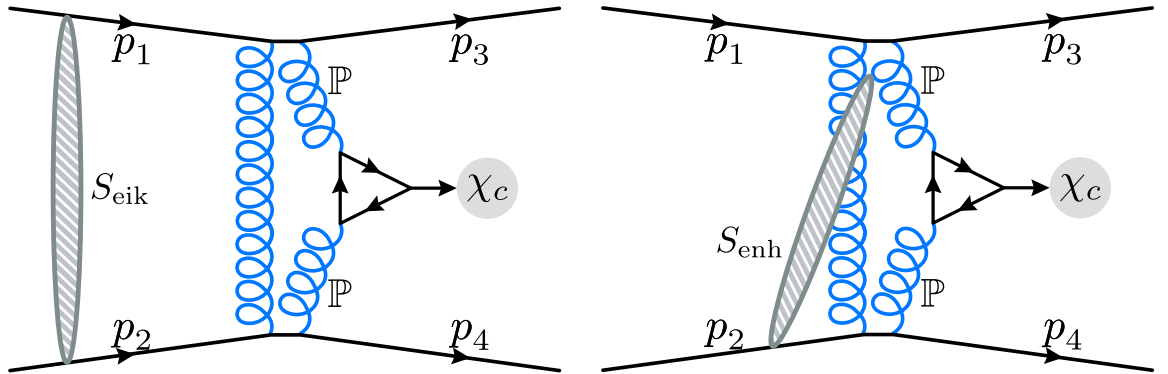


Figure 2.12. A schematic representation of the soft survival factors necessary to correct for soft-rescattering processes that break the rapidity gap including the eikonal survival factor S_{eik} (left) and enhanced survival factor S_{enh} (right).

642 The first soft survival effect, known as *eikonal survival factor*, S_{eik} , considers pp rescattering
 643 and is depicted in Fig. 2.12 (left). Although the survival factor is a soft process that cannot be
 644 calculated using perturbative methods, it is possible to measure it from soft hadronic data, such
 645 as in single and double diffraction studies [75]. The eikonal survival factor is dependent on the
 646 centre-of-mass energy and the transverse momentum of the colliding protons. The dependence
 647 on the protons' transverse momentum implies a dependence on the central object's spin and
 648 parity, which plays a greater role in the spin selection rules discussed in detail in Sec. 2.5.3.

649 Ignoring the internal structure of the proton, the expected eikonal suppression is given by

$$\langle S_{\text{eik}}^2 \rangle = \frac{\int d^2\vec{p}_{1T} d^2\vec{p}_{2T} |T(s, \vec{p}_{1T}, \vec{p}_{2T}) + T^{\text{res}}(s, \vec{p}_{1T}, \vec{p}_{2T})|^2}{\int d^2\vec{p}_{1T} d^2\vec{p}_{2T} |T(s, \vec{p}_{1T}, \vec{p}_{2T})|^2}, \quad (2.33)$$

650 where $\langle \dots \rangle$ denotes averaging over the proton's transverse momentum, T is the double-pomeron-
 651 CEP amplitude, and T^{res} is the pp rescattering amplitude. Although it has a large suppression
 652 effect on the CEP cross-section of about two orders of magnitude, there are significant uncer-
 653 tainties associated with its centre-of-mass energy dependence, highlighting the importance of
 654 putting our theoretical models to test with this and future studies. The expected suppression
 655 factors, $\langle S_{\text{eik}}^2 \rangle$, for χ_{c0} , χ_{c1} , and χ_{c2} at a centre-mass-energy $\sqrt{s} = 13$ TeV are expected to be
 656 0.029, 0.091, and 0.072, respectively [63].

657 The second soft survival effect considers the probability of an additional interaction between
 658 one of the protons and one of the partons within the gluon loop. This is known as an *enhanced*
 659 *survival effect*, denoted by S_{enh} , and depicted in Fig. 2.12 (right). Although the magnitude of
 660 this effect is not known precisely, it depends mostly on the transverse momentum of the parton
 661 and proton, as well as the available rapidity interval for rescattering, which in turn depends
 662 on the centre-of-mass energy, $y_X \sim \ln(s/m_X^2)$. The enhanced suppression is expected to have
 663 a much smaller effect than the eikonal survival factor described above, being about 0.25 at a
 664 centre-of-mass energy $\sqrt{s} = 14$ TeV for all $\chi_{c0,1,2}$ states [76].

665 The differential cross-section for the production of a central object X at rapidity y is given
 666 by

$$\frac{d\sigma}{dy} = \langle S_{\text{enh}}^2 \rangle \int d^2\vec{p}_{1T} d^2\vec{p}_{2T} \frac{|T(\vec{p}_{1T}, \vec{p}_{2T})|^2}{16^2 \pi^5} S_{\text{eik}}^2(\vec{p}_{1T}, \vec{p}_{2T}). \quad (2.34)$$

667 The final schematic of the Durham model is shown in Fig. 2.13, including representations for
 668 the soft survival factors, and gluon PDF. The CEP DPE cross-section has a dependence on
 669 the centre-of-mass energy since we expect higher gluon densities at low Bjorken- x to increase
 670 the frequency of double pomeron interactions. However, the soft survival effects decrease with
 671 centre-of-mass energies due to the increased proton opacity, the matter density of the proton,
 672 and the increased size of the rapidity gap available for the enhanced absorption.

673 2.5.3 Spin selection rules - spin filter

674 Due to the intact proton requirement, CEP processes satisfy special spin-selection rules that
 675 make CEP measurements sensitive to the quantum numbers of new states, particularly spin,
 676 parity, and charge conjugation [63], which are not easily accessible in diffractive and inclusive
 677 processes. While the production of states with quantum numbers $J_z^{PC} = 1^{++}$ and $J_z^{PC} = 2^{++}$
 678 are possible, DPE predominantly produces central objects with $J_z^{PC} = 0^{++}$ quantum numbers,
 679 where J_z is the projection of the objects' angular momentum on the z -axis. The origin of this
 680 selection rule is described below.

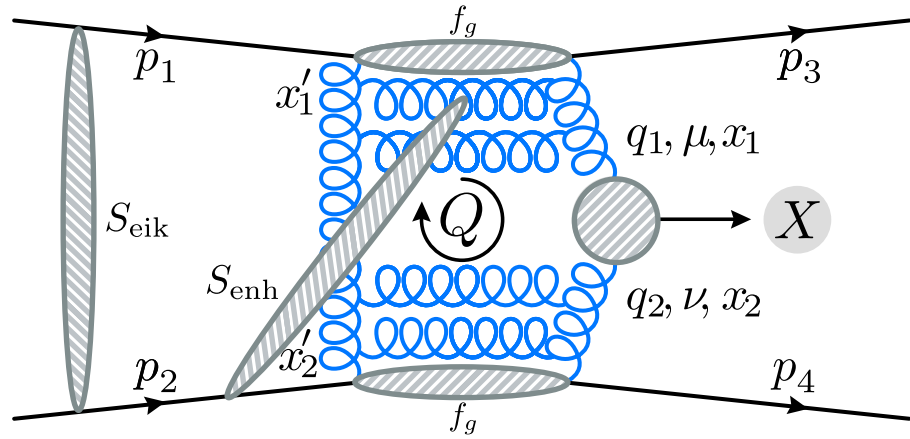


Figure 2.13. A schematic of the perturbative mechanism described by the Durham model for the CEP process $p_1 \oplus p_2 \rightarrow p_1 \oplus X \oplus p_2$ through the DPE channel. Here the gluon PDF f_g , the eikional survival factor S_{eik} , and the the enhanced survival factor S_{enh} are represented symbolically.

681 As mentioned earlier, DPE includes the interaction of two gluon pairs, one that fuses to the
 682 central system and another known as the screening gluon that guarantees the process occurs in
 683 a colour-singlet state, even under charge conjugation ($C = +1$). Therefore, the object produced
 684 must also be a colour-singlet object with $C = +1$.

685 In the limit where the protons have no transverse-momentum after the interaction ($p_{3T} =$
 686 $p_{4T} = 0$), there is no angular-momentum transfer between the two protons. Since the orbital-
 687 angular momentum of the two proton system is zero, $L_z = 0$, by conservation of angular
 688 momentum the central object produced must also have zero angular momentum along the z -axis,
 689 $J_z = 0$. In practice, however, there will very likely be some residual momentum transfer between
 690 the two colliding protons, such that the net $p_T \neq 0$: this will be small for central-exclusive-elastic
 691 reactions, and so will be a small correction to this selection rule. The transverse momentum
 692 of the fusing gluons forms part of the polarisation vectors of the on-shell $g(\lambda_1)g(\lambda_2) \rightarrow X$
 693 process described by the sub-amplitude, Eq. 2.27. Here, λ_1 and λ_2 are the polarisation modes
 694 of the fusing gluons associated with the incoming protons p_1 and p_2 respectively. For bosons of
 695 momentum

$$p_\mu = (p_0, |\vec{p}| \sin \theta \cos \phi, |\vec{p}| \sin \theta \sin \phi, |\vec{p}| \cos \theta), \quad (2.35)$$

696 where $\mu = \{0, 1, 2, 3\}$ is the Lorentz index of the four-momentum vector (index 0 corresponds
 697 to the particle energy p_0), θ and ϕ are the azimuthal and polar angles, the polarisation vector is
 698 given by

$$\varepsilon_\mu^\pm = \frac{1}{\sqrt{2}}(0, \cos \theta \cos \phi \mp i \sin \phi, \cos \theta \sin \phi \pm i \cos \phi, -\sin \theta). \quad (2.36)$$

699 Here, \pm are the polarisation modes λ_i , with $+$ corresponding to a right-handed (R) helicity and
 700 $-$ corresponding to a left-handed helicity (L), and the subscript i maps to the proton emitting

701 the gluon. We take the z -axis to be in the direction-of-motion of the gluons in the gg rest
 702 frame moving such that $\theta = 0$. In the on-shell approximation ($q^2 = q_T^2 = 0$), that is a process
 703 that satisfies the Einstein energy-momentum relation $E^2 = \vec{p}^2 + m^2$ such that the gluons have
 704 zero mass, the z -axis aligns with the beam line in the lab frame up to small corrections, order
 705 q_T^2/m_X^2 . Therefore, the momenta of the gluons simplifies to

$$p_\mu = (p_0, 0, 0, |\vec{p}|). \quad (2.37)$$

706 Similarly, the gluon polarisation vectors are

$$\begin{aligned} \varepsilon_{\mu 1}^+ &= \varepsilon_{\mu 2}^- = -\frac{1}{\sqrt{2}}(0, 1, i, 0) \\ \varepsilon_{\mu 1}^- &= \varepsilon_{\mu 2}^+ = \frac{1}{\sqrt{2}}(0, 1, -i, 0), \end{aligned} \quad (2.38)$$

707 where the subscripts $\{1, 2\}$ map to the proton emitting the corresponding gluon. We can then
 708 use the inverse of the polarisation vectors to write the gluon transverse-momentum vectors in
 709 terms of their helicity vectors, such that

$$q_{1T}^{\lambda_1} q_{2T}^{\lambda_2} \mathcal{M}_{\lambda_1 \lambda_2} = \begin{cases} -\frac{1}{2}(\vec{q}_{1T} \cdot \vec{q}_{2T}) (\mathcal{M}_{++} + \mathcal{M}_{--}) & (J_z^P = 0^+) \\ -\frac{i}{2}|(\vec{q}_{1T} \times \vec{q}_{2T})| (\mathcal{M}_{++} - \mathcal{M}_{--}) & (J_z^P = 0^-) \\ +\frac{1}{2}((q_{1T}^x q_{2T}^x - q_{1T}^y q_{2T}^y) + i(q_{1T}^x q_{2T}^y + q_{1T}^y q_{2T}^x)) \mathcal{M}_{-+} & (J_z^P = +2^+) \\ +\frac{1}{2}((q_{1T}^x q_{2T}^x - q_{1T}^y q_{2T}^y) - i(q_{1T}^x q_{2T}^y + q_{1T}^y q_{2T}^x)) \mathcal{M}_{+-} & (J_z^P = -2^+), \end{cases} \quad (2.39)$$

710 where $\mathcal{M}_{\lambda_1 \lambda_2}$ are the $g(\lambda_1)g(\lambda_2) \rightarrow X$ helicity amplitudes. The parity and angular-momentum-
 711 projection quantum numbers shown alongside follow from the possible helicity combinations.
 712 The parity eigenstates are given such that

$$\begin{aligned} \psi_+ &= RR + LL \quad (P = +1) \\ \psi_- &= RR - LL \quad (P = -1) \\ \psi_+ &= RL, LR \quad (P = +1), \end{aligned} \quad (2.40)$$

713 where R and L correspond to right-handed (+) and left-handed (-) helicity states. Similarly,
 714 the conditions for the J_z quantum numbers are detailed in Fig. 2.14.

715 According to the Landau-Yong theorem, spin-1 states cannot decay into two on-shell spin-1
 716 massless bosons [77]. Similarly, two on-shell spin-1 massless bosons cannot fuse into a spin-1 state.
 717 We see this reflected in the on-mass-shell calculation where we are missing an $J_z^P = 1^+$ term in
 718 Eq. 2.39, since the term is odd under Q_T and vanishes when integrating over Q_T . However, the
 719 Landau-Yang theorem is violated by off-shell virtual effects. As a result, the production of 1^{++}
 720 states such as χ_{c1} are not strictly forbidden but instead significantly suppressed.

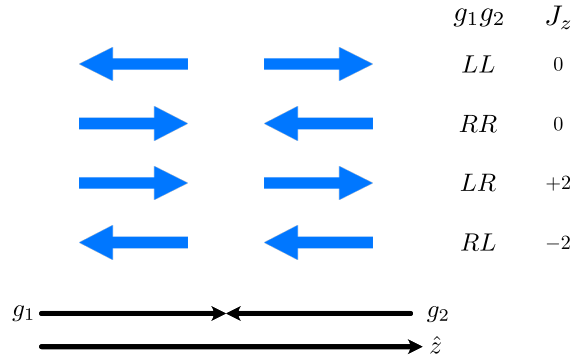


Figure 2.14. Schematic of determination of angular momentum along the z -axis, $J_z = 0$ of the project produced from the fusion of two spin-1 bosons travelling along the z -axis, where R and L corresponds to right-handed and left-handed helicity states.

721 In addition, when taking the $p_T \rightarrow 0$ limit we find that all terms in Eq. 2.39 vanish after the
 722 Q_T integral, with the exception of the $J_z^P = 0^+$ state, which results in the $J_z^{CP} = 0^{++}$ selection
 723 rule. However, this does not mean that χ_{c1} and χ_{c2} mesons are not produced in CEP DPE
 724 interactions, as the production of $J_z^{CP} = 1^{++}$ and $J_z^{CP} = 2^{++}$ systems are still possible due to
 725 the small-momentum exchange between the protons, which violates the $p_T \rightarrow 0$ assumption and
 726 results in small scattering angles. Consequently, CEP will produce predominantly $J_z^{CP} = 0^{++}$
 727 states, with $J_z^{CP} = 1^{++}$ and $J_z^{CP} = 2^{++}$ systems significantly suppressed.

728 By integrating and squaring the amplitudes \mathcal{M}_J we find rough estimates of the suppression
 729 relative to the production of χ_{c0} such that

$$|\mathcal{M}_0|^2 : |\mathcal{M}_1|^2 : |\mathcal{M}_2|^2 \sim 1 : \frac{\langle \vec{p}_T^2 \rangle}{m_X^2} : \frac{\langle \vec{p}_T^2 \rangle^2}{\langle \vec{Q}_T^2 \rangle^2} \sim 1 : \frac{1}{49} : \frac{1}{64}, \quad (2.41)$$

730 where $\langle \vec{Q}_T^2 \rangle$ can take values of a few GeV^2 , and we have taken $\langle \vec{Q}_T^2 \rangle \sim 2 \text{ GeV}^2$, $m_X = 3.5 \text{ GeV}$
 731 for the approximate mass of χ_{c1} , and $\langle p_T^2 \rangle \sim 0.25 \text{ GeV}^2$ is taken from the integral of the proton
 732 form factor $F_p(t_i)$. These results suggest we can expect the production of the χ_c mesons to
 733 follow a specific hierarchy, where the production of χ_{c1} and χ_{c2} is suppressed relative to that of
 734 χ_{c0} . The transverse-momentum dependence of the suppression factors can be exploited to select
 735 higher-purity samples of the desired spin system. Although these results provide us with an
 736 idea of the χ_c hierarchy and how the suppression scales, these are only approximations and do
 737 not take into account the soft-survival effects. The results for the full calculations are presented
 738 in Chapter 7 according to SuperChic, a Fortran-based Monte Carlo generator which implements
 739 the Durham model for CEP physics [78–80].

740 2.6 Rapidity-gap-breaking background

741 As mentioned previously, there are two critical requirements in CEP studies. The first demands
 742 that the central object is produced *exclusively* in the absence of any additional activity. The

743 second requires that the colliding protons remain intact after the interaction and continue their
744 trajectory down the beam line. Imposing both criteria implies that there will be two large-
745 rapidity gaps between the outgoing protons and the central object. However, there are processes
746 that mimic the CEP signature by breaking either the low-multiplicity or large-rapidity-gap
747 criterion, without leaving a signature of the proton dissociation or additional activity within
748 the detector acceptance. Here we introduce some of these rapidity-gap-breaking mechanisms.

749 Figure 2.15 depicts a series of Feynman diagrams for a number of processes considered
750 in this discussion, alongside a typical rapidity-coverage distribution for such events where the
751 forward and backward coverage of the LHCb main spectrometer is marked in green. In addition,
752 the extended rapidity coverage of the newly added HERSCHEL modules, described in Sec. 3.8,
753 is marked in blue. This sub-detector, installed for the data collection of Run 2, was designed
754 to detect particle showers at high-rapidity regions. The outgoing protons, if intact after the
755 interaction, are marked in red while the rapidity gaps present in the interaction are marked
756 (\oplus) and highlighted in grey. The interactions presented are all mediated through pomeron
757 exchange, with the exception of Fig. 2.15 (c), which represents a hard scattering process. For
758 example, Fig. 2.15 (a) corresponds to CEP through a DPE channel and Fig. 2.15 is elastic
759 proton scattering mediated through the exchange of a pomeron.

760 As a first example, we examine a central-exclusive-inelastic process where a central object is
761 produced, much like in CEP, but this time it is accompanied by gluon radiation in one or both
762 directions, as shown in Fig. 2.15 (d-f). This results in additional activity at high-rapidity values,
763 approximately $5 < \eta < 10$, thus falling outside the acceptance of the main spectrometer and
764 therefore leaving no trace of the rapidity break. However, the resulting particles may interact
765 with other accelerator components and induce showers detected by the HERSCHEL modules.
766 The presence of such soft interactions are accounted for in the Durham model through the
767 soft-survival factors, as described in Sec. 2.5.2.

768 If the momentum exchange between the interacting protons is high enough, the dissociation
769 of one or both of the interacting protons can occur in what is respectively known as single and
770 double diffraction, shown in Fig. 2.15 (h-l). As with gluon radiation, these interactions result in
771 high-rapidity fragments that can fall outside of the acceptance of LHCb's main spectrometer
772 since they carry a large-longitudinal fraction of the initial proton's momentum. The particles
773 resulting from the proton dissociation can have a broader rapidity coverage when compared to
774 gluon radiation, spanning between zero and ten in rapidity. Therefore, these processes cannot
775 always be excluded based solely on the no extra track and rapidity-gap requirement in the
776 LHCb experiment. However, the resulting particle showers can be detected by HERSCHEL.

777 Events with proton dissociation can come in the form of central-exclusive-inelastic production
778 where a central object is produced alongside proton dissociation, Fig. 2.15 (g-i), or without
779 the production of a central system, Fig. 2.15 (j-l). The latter is characterised by a single
780 large-rapidity gap, which implies an empty detector with signal on either of the HERSCHEL

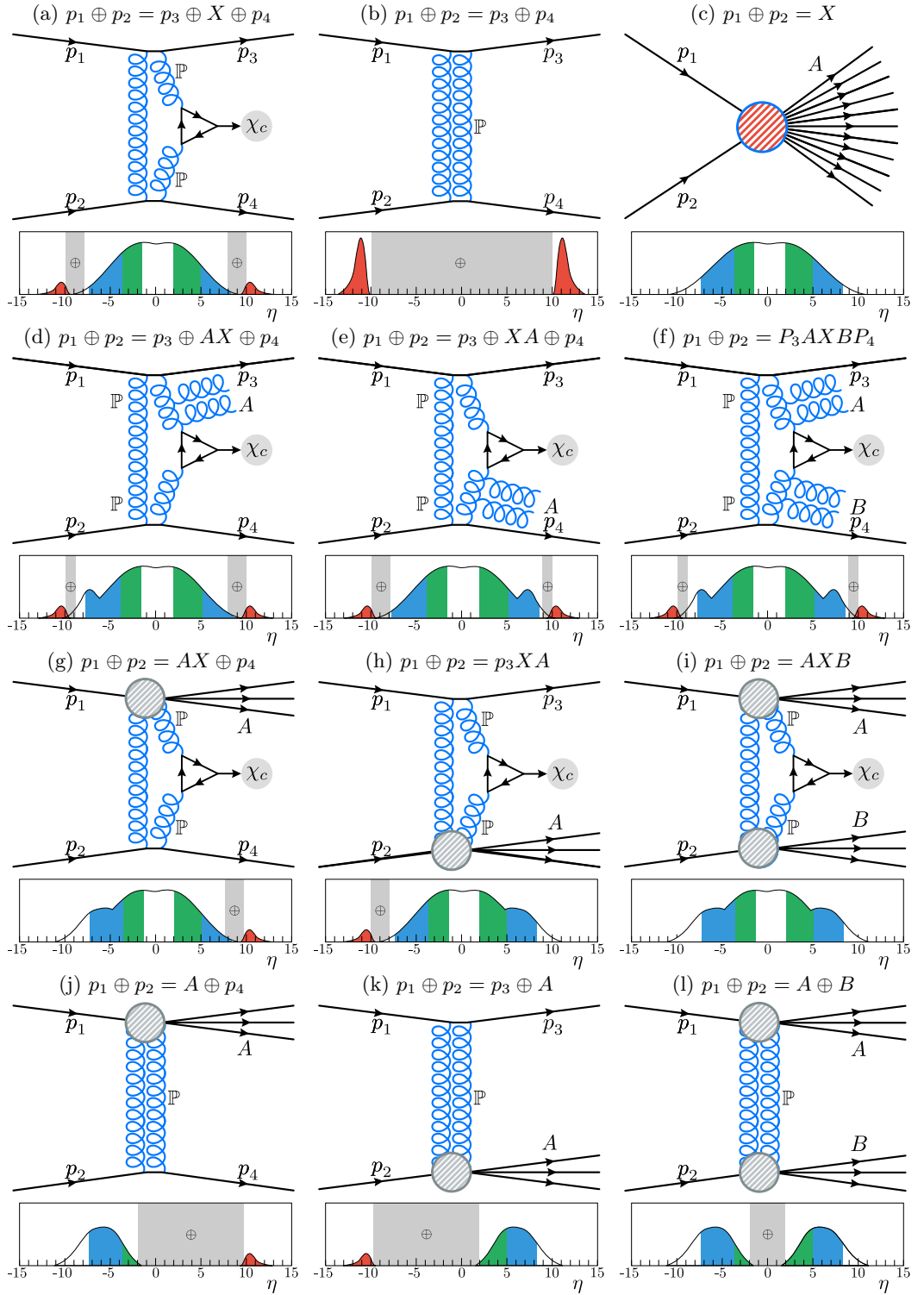


Figure 2.15. Feynman diagrams and pseudorapidity coverage depiction for (a) CEP (elastic), (b) proton scattering, (c) hard scattering, (d) CEP (inelastic) / gluon radiation (d, e, f), CEP (inelastic) / single (g, h) and double (i) proton dissociation, single (j, k) and double (l) diffraction for double pomeron exchange.

Table 2.1. Nominal-mass values for χ_c mesons, as given by the Particle Data Group [81] as well as (J^{CP}) quantum numbers, where I is the isospin, J is the spin, P is the parity and C is the charge-conjugation quantum number, their radiative-decay branching fractions (\mathcal{B}) into $\chi_c \rightarrow J/\psi\gamma$ and their corresponding Q -values.

Meson	$m(\chi_c)$ [MeV/ c^2]	Width	$I(J^{CP})$	$\mathcal{B}(\chi_c \rightarrow J/\psi\gamma)$	$m(\chi_c) - m(J/\psi)$ [MeV/ c^2]
χ_{c0}	3414.75 ± 0.31	10.8 ± 0.6	0 (0^{++})	1.27 ± 0.06 %	317.85 ± 0.31
χ_{c1}	3519.66 ± 0.07	0.84 ± 0.04	0 (1^{++})	33.9 ± 1.2 %	413.76 ± 0.07
χ_{c2}	3556.20 ± 0.09	1.97 ± 0.09	0 (2^{++})	19.3 ± 0.7 %	459.30 ± 0.09

781 modules. Although these events would not be selected directly due to the lack of the central
782 system, they may be selected alongside an elastic CEP event in the presence of pile-up events.
783 As a result, we might wrongly veto an elastic CEP event due to the dissociation of the secondary
784 event. Similarly, elastic CEP events might be wrongly vetoed if accompanied by any secondary
785 pile-up events that leave a signal in the main spectrometer.

786 2.7 χ_c meson

787 The $\chi_c(1P)$ particles are unstable-hadronic particles known as a meson, which are composed
788 of a quark-antiquark pair. The $\chi_c(1P)$ mesons belong to a subset of meson states known as
789 quarkonium, a special case where the quark and antiquark have the same flavour ($q\bar{q}$). In
790 particular, $\chi_c(1P)$ mesons are composed of a charm-anticharm quark pair ($c\bar{c}$) and are referred
791 to as charmonium. These characteristics make quarkonium mesons neutral as well as its own
792 anti-particle.

793 There are three $\chi_c(1P)$ mesons, known as $\chi_{c0}(1P)$, $\chi_{c1}(1P)$, and $\chi_{c2}(1P)$, which are close in
794 invariant mass to one another: their masses are 3414.75 ± 0.31 , 3519.66 ± 0.07 , and 3556.20 ± 0.09
795 MeV/ c^2 respectively, as given by the Particle Data Group [81]. The widths are 10.8 ± 0.6 ,
796 0.84 ± 0.04 , and 1.97 ± 0.09 MeV/ c^2 , respectively. In the following, we will refer to these states
797 as χ_{c0} , χ_{c1} , and χ_{c2} , and collectively as χ_c mesons. The nominal values for the invariant mass of
798 the χ_c mesons are summarised in Table 2.1 together with their quantum numbers, the branching
799 fractions of their radiative decay $\chi_c \rightarrow J/\psi\gamma$, and the χ_c and J/ψ mass difference.

800 2.7.1 Quantum numbers

801 The quarks that make up the χ_c mesons are fermions and have an intrinsic spin of $S = 1/2$. The
802 spins can either be unaligned, forming a spin-0 singlet (*i.e.* vector-length zero with a single-spin
803 projection $S_z = 0$) or the spins can be aligned, resulting in a spin-1 triplet (*i.e.* vector-length one
804 with three possible spin projections, $S_z = -1, 0, 1$). The χ_c mesons are an example of a spin-1
805 triplet. In addition, χ_c mesons have an orbital-angular-momentum quantum number $L = 1$,
806 which is associated with the angular momentum of their gluon composition. The quantum-
807 number combination of $S = 1$ and $L = 1$ makes the χ_c mesons a set of three ($1P$) excited-orbital
808 eigenstates of the $c\bar{c}$ system in the QCD potential. These three states are analogous to the

809 three configurations of the p -atomic-electron orbitals. The intrinsic-angular momentum and the
 810 orbital-angular momentum can be combined into the total-angular-momentum quantum number
 811 J such that it takes any value from $J = |L - S|$ to $J = |L + S|$ in increments of one, inclusive.
 812 As a result, χ_{c0} , χ_{c1} , and χ_{c2} mesons have a total-angular-momentum quantum number $J = 0$,
 813 $J = 1$, and $J = 2$, respectively.

814 The parity of the χ_c mesons, a symmetry associated with the sign change of spacial
 815 coordinates, is given by $P = (-1)^{L+1} = +1$ (P -even). The charge-conjugate quantum number,
 816 a symmetry under the exchange of quantum charges, is $C = +1$ (C -even) such that $|c\bar{c}\rangle = |\bar{c}c\rangle$.
 817 Quarkonium systems are also known as flavourless states, since all their quantum numbers
 818 associated with flavour are zero (strangeness $S = 0$, charm $C = 0$, bottomness $B = 0$, and
 819 topness $T = 0$), which have an isospin $I = 0$ as they have no u -quark or d -quark content. By
 820 convention, the notation $I(J^{CP})$ is used to summarise the quantum number of states, as detailed
 821 in Table 2.1. Mesons with $J^P = 0^+$, 1^+ and 2^+ such as χ_{c0} , χ_{c1} , and χ_{c2} are known as scalar
 822 mesons, pseudovector mesons, and tensor mesons respectively.

823 2.7.2 χ_c states as a CEP standard candle

824 As mentioned previously, CEP is a theoretically challenging process sensitive to non-perturbative
 825 soft effects, higher-order corrections, and PDF uncertainties. Therefore, it is essential to test our
 826 theoretical models, to set a benchmark for new searches and measurements of more exotic systems,
 827 and establish this field of study at the LHCb experiment. Naturally, low-mass objects have the
 828 largest cross-sections and are easier to access experimentally. In addition, the contribution of
 829 soft corrections becomes less significant and the use of perturbative QCD becomes justified when
 830 the hard scale is sufficiently high, $\mu \sim m_X \gg Q_T$, and the calculations become infrared stable.
 831 The hard-scale for χ_c mesons is approximately $\mu = m_{\chi_c} \sim 3.5$ GeV and sits at the border of the
 832 perturbative limit. In addition, the different χ_c states give us access to different J_z^P states and,
 833 as a result, the angular distributions of the forward protons and information about the violation
 834 of the $J_z = 0$ spin selection rule. This makes the χ_c meson an ideal candidate against which to
 835 test our theoretical models for the DPE CEP channel, and consequently is often regarded as
 836 the *standard candle* for this mechanism.

837 2.7.3 χ_c radiative decays

838 The $J/\psi(1S)$ particle is a neutrally charged $c\bar{c}$ vector meson, making it the second lightest
 839 charmonium state after the η_c meson. The J/ψ meson was simultaneously discovered at
 840 SLAC and Brookhaven National Laboratories, granting it its unique two-part name. It has a
 841 3096.900 ± 0.006 MeV/ c^2 mass, as given by the Particle Data Group [81], isospin $I = 0$, a total
 842 angular momentum $J = 1$, odd parity $P = -1$, and odd charge conjugation $C = -1$, such that
 843 $I(J^{CP}) = 0(1^{--})$. It can decay through either annihilation, or weakly through flavour-changing
 844 interactions. As a result, the J/ψ meson is a relatively long-lived particle with a narrow width
 845 of 92.9 ± 2.8 keV/ c^2 [81].

846 Of particular interest to this analysis is the decay of the J/ψ meson into a pair of muons
 847 which have a branching fraction of 5.961 ± 0.0033 . The CEP of J/ψ mesons has been studied
 848 at LHCb through this decay mode together with its excited state $\psi(2S)$ [42, 43]. $\psi(2S)$ is
 849 another quarkonium state that shares the same quantum numbers as J/ψ , has an invariant
 850 mass of 3686.10 ± 0.06 MeV/ c^2 and a width of 294 ± 8 MeV/ c^2 . Although J/ψ mesons can also
 851 decay into an electron pair with a similar branching fraction, $(5.971 \pm 0.032)\%$, the penetrating
 852 power of muons makes them easier to identify, they have low background, and tend to be better
 853 measured than their electron counterparts as they are less susceptible to energy loss through
 854 bremsstrahlung radiation.

855 χ_c mesons can decay to a J/ψ meson through radiative decay, $\chi_c \rightarrow J/\psi \gamma$. The branching
 856 fractions for χ_{c0} , χ_{c1} , and χ_{c2} are $1.27 \pm 0.06\%$, $33.9 \pm 1.2\%$, and $19.3 \pm 0.7\%$ [82]. Given the
 857 experience with the study of J/ψ mesons through the dimuon decay, as well as the benefits
 858 listed above, this study will focus on the reconstruction of the intermediate J/ψ meson through
 859 the dimuon decay. In addition, the well-understood CEP and inelastic production can be easily
 860 used to measure the efficiency of the HERSCHEL detector as described in Sec. 5.6.

861 Unfortunately, as it will be shown in Sec. 4.1.3, the invariant-mass resolution in LHCb of
 862 $\chi_c \rightarrow J/\psi [\mu^+ \mu^-] \gamma$ mesons reconstructed with calorimetric photons (*i.e.* photons that have not
 863 undergone pair production, $\gamma \rightarrow e^+ e^-$) is inadequate to cleanly resolve χ_{c1} and χ_{c2} states,
 864 which have means separated by approximately 50 MeV/ c^2 . However, separation can be achieved
 865 through the use of converted photons, $\gamma \rightarrow e^+ e^-$. This improves the invariant-mass resolution
 866 of the χ_c mesons significantly, making the separation of the resonances possible. As a result,
 867 this study will focus on the following decay:

$$\chi_c \rightarrow J/\psi [\mu^+ \mu^-] \gamma [e^+ e^-]. \quad (2.42)$$

868 2.8 Previous measurements

869 2.8.1 CDF II at Tevatron

870 The CEP of χ_c mesons was first observed in the Collider Detector at Fermilab II (CDF II)
 871 detector at the Tevatron, a proton-antiproton collider [41, 67, 83]. CDF was a general-purpose
 872 detector with a wide rapidity coverage. The central barrel had a pseudorapidity coverage of
 873 $|\eta| < 5.1$. In addition, CDF was equipped with scintillating pads along the beam line on both
 874 sides of the interaction point, extending the coverage to include $5.4 < |\eta| < 7.4$. These pads
 875 were designed to detect particle showers at high rapidities originating from proton dissociation.
 876 Finally, one side of the detector was equipped with a proton tagger, allowing for the direct
 877 detection of one of the emerging protons. The large rapidity coverage, and the ability to identify
 878 proton fragmentation, made CDF an excellent experiment with which to study CEP.

879 The CEP of χ_c mesons was studied in proton-antiproton collisions at centre-of-mass energies
 880 $\sqrt{s} = 1.96$ TeV in the $|\eta| < 0.6$ pseudorapidity region through its radiative decay into $J/\psi \gamma$.

881 This subset of the central barrel is instrumented with a tracking system and a drift chamber
 882 used to measure the muons from the $J/\psi \rightarrow \mu^+\mu^-$ decay. The cross-section was measured
 883 with an effective integrated luminosity of $\mathcal{L}_{\text{eff}} = 139 \pm 8 \text{ pb}^{-1}$, accounting for the percentage of
 884 bunch crossing with more than one interaction. Unfortunately, the invariant-mass resolution
 885 was not high enough to resolve the contributions of each of the χ_c states. The contributions
 886 of χ_{c1} and χ_{c2} were taken to be negligible due to the suppression associated with the $J_z = 0$
 887 spin-selection rule described in Chapter 3. Taking χ_{c0} as the only contribution, the cross-section
 888 was measured to be $\frac{d\sigma}{dy}|_{y=0}(\chi_{c0}) = 76 \pm 10 \pm 10 \text{ nb}$, where the first uncertainty is statistical
 889 and the second is systematic. These results were found to be in agreement with an adjusted
 890 theoretical prediction of 90 nb, as described in [84]. The measured cross-section and theoretical
 891 predictions are detailed in Table 2.2 together with other results.

892 2.8.2 LHCb at CERN

893 Two preliminary CEP χ_c analyses were performed at the LHCb experiment at CERN: one with
 894 pp data collected during 2010 and another with pp data collected during 2011. The LHCb
 895 detector, described in great detail in Chapter 3, is a single-arm forward spectrometer fully
 896 instrumented in the pseudorapidity range $2 < \eta < 5$. In 2015, LHCb was equipped with a set of
 897 scintillating modules that are sensitive to high-rapidity showers from particles originating in
 898 proton dissociation, extending the rapidity coverage of LHCb up to $\eta < 10$.

899 The first $\chi_c \rightarrow J/\psi[\mu^+\mu^-]\gamma$ analysis at LHCb was performed using pp collisions at a centre-
 900 of-mass energy $\sqrt{s} = 7 \text{ TeV}$ collected during 2010, exploiting a total integrated luminosity of
 901 37 pb^{-1} [85]. For this analysis, the photon and the dimuon from the J/ψ decay were required
 902 to be within the acceptance of LHCb's main spectrometer $2 < \eta < 4.5$. In this case, the mass
 903 resolution is sufficiently good to distinguish the contributions of each χ_c state but not good
 904 enough to obtain full resonant separation. The invariant-mass distribution of the $J/\psi\gamma$ system,
 905 shown in Fig. 2.16, is fitted using shapes extracted from SuperChic Monte Carlo. An additional
 906 shape (yellow) is added to account for background from $\psi(2S)$ feed-down, simulated using
 907 StarLight [86,87], a Monte Carlo simulator specialised in ultra-peripheral collisions mediated via
 908 two-photon or photonuclear interactions. A single exclusive purity of 0.39 ± 0.13 is calculated
 909 for the entire sample by fitting the transverse momentum of the χ_c candidates, thus taking
 910 advantage of the lower transverse momentum of CEP compared to inelastic processes. The
 911 cross-section-times-branching-fraction is determined to be $(9.3 \pm 4.5) \text{ pb}$, $(16.4 \pm 7.1) \text{ pb}$, and
 912 $(28.0 \pm 12.3) \text{ pb}$ for χ_{c0} , χ_{c1} and χ_{c2} , respectively. These are slightly higher than the SuperChic
 913 calculations of 4 pb, 10 pb, and 3 pb quoted in the study, which have an uncertainty factor of 4
 914 to 5 [67].

915 A second preliminary analysis was performed at LHCb, which repeated the previously
 916 mentioned measurement with a larger statistical sample corresponding to a total effective
 917 integrated luminosity of 222.3 pb^{-1} , collected during 2011 for pp collisions at a centre-of-mass
 918 energy of $\sqrt{s} = 7 \text{ TeV}$ [88]. The analysis was performed with the same acceptance criteria. This
 919 analysis measured a cross-section-times-branching-fraction of $(2.2 \pm 3.0) \text{ pb}$, $(4.3^{+7.6}_{-9.2}) \text{ pb}$, and

Table 2.2. Cross-section measurements for $\chi_c \rightarrow J/\psi[\mu^+\mu^-]\gamma$ CEP conducted in CDF II at Fermilab Tevatron at a centre-of-mass energy $\sqrt{s} = 1.96$ TeV in proton-antiproton [41, 67, 83] and cross-section- \times -branching-fraction at the LHCb experiment with a centre-of-mass energy $\sqrt{s} = 7$ TeV for pp collisions collected during 2010 [85] and 2011 [88], as well as theoretical predictions calculated with SuperChic (SC) quoted in each of the analysis [67].

Meson	\sqrt{s} [TeV]	η	$\sigma(\chi_{c0})$	$\sigma(\chi_{c1})$	$\sigma(\chi_{c2})$
CDF II	1.96	$-0.6 - 0.6$	$76 \pm 10 \pm 10$ nb	-	-
SC	1.96	$-0.6 - 0.6$	90 nb	-	-
Meson	\sqrt{s} [TeV]	η	$\mathcal{B} \times \sigma(\chi_{c0})$	$\mathcal{B} \times \sigma(\chi_{c1})$	$\mathcal{B} \times \sigma(\chi_{c2})$
LHCb 2010	7	2 – 4.5	9.3 ± 4.5 pb	16.4 ± 7.1 pb	28.0 ± 12.3 pb
LHCb 2011	7	2 – 4.5	2.2 ± 3.0 pb	$4.3_{-9.2}^{+7.1}$ pb	$25.0_{-9.2}^{+7.9}$ pb
SC	7	2 – 4.5	14 pb	9.8 pb	3.3 pb

920 $(25.0_{-9.2}^{+7.1})$ pb for χ_{c0} , χ_{c1} and χ_{c2} , respectively: fitting the transverse momentum of the dimuon
921 system, a purity of $23.8 \pm 3.3\%$ is found. Both sets of results suggest there is an enhancement
922 of the χ_{c2} relative to the production of χ_{c1} , in contrast to the expected theoretical hierarchy.
923 However, the cross-section measurements of χ_{c2} are consistent with the theoretical calculations
924 given the large uncertainties. This enhancement can result from the difficulties associated with
925 the invariant-mass and transverse-momentum fits necessary to determine the contribution of
926 the inelastic background and the CEP signal. The experimental and theoretical results for these
927 two analyses are summarised in Table 2.2.

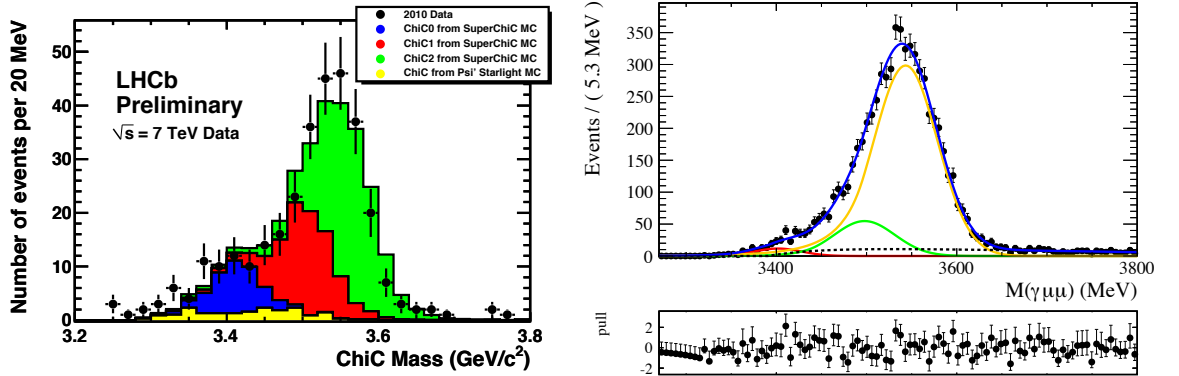


Figure 2.16. Invariant-mass distribution of $\chi_c \rightarrow J/\psi[\mu^+\mu^-]\gamma$ candidates from pp collisions at a centre-of-mass energy $\sqrt{s} = 7$ TeV from data collected in 2010 (left) and 2011 (right) at the LHCb experiment. Reproduced from Ref. [85] and Ref. [88], respectively.

CHAPTER 3

LHCb detector

928
929
930

931 Situated on the Franco-Swiss border at the European Organisation for Nuclear Research
932 (CERN), the Large Hadron Collider (LHC) [89] is the world’s largest and most powerful particle
933 accelerator, designed to collide protons, pp , at a centre-of-mass energy of $\sqrt{s} = 14$ TeV and
934 luminosity of $1 \times 10^{34} \text{ cm}^{-2} \text{ s}^{-1}$. Protons from ionised hydrogen are accelerated through multiple
935 stages of CERN’s accelerator complex, a schematic of which is shown in Fig. 3.1. In the final
936 stage of the acceleration the protons are split into two counter-rotating beams and injected into
937 the LHC at an energy of 450 GeV where they are accelerated to the desired collision energy
938 by eight 400 MHz superconducting-radiofrequency cavities cooled to 4.5 K with superfluid
939 helium. To achieve high-luminosity conditions, up to 2808 proton bunches are injected into
940 the LHC storage rings each with $\sim 1.2 \times 10^{11}$ protons. The beams are steered around the
941 26.7 km ring with 1232 superconducting copper-clad niobium-titanium dipole magnets and
942 focused with 392 quadrupoles. The beams are crossed at four interaction points where the
943 major LHC experiments are located: A Toroidal LHC ApparatuS (ATLAS), Compact Muon
944 Solenoid (CMS), A Large Ion Collider Experiment (ALICE), and the Large Hadron Collider
945 beauty experiment (LHCb).

946 So far the LHC has had two main periods of operation: Run 1 and Run 2. During Run
947 1, which took place between 2010 and 2012 collisions occurred at centre-of-mass energies of
948 $\sqrt{s} = 7$ and 8 TeV. In Run 2, which took place between 2015 and 2018, the collision energy
949 was $\sqrt{s} = 13$ TeV.

950 3.1 LHCb Experiment

951 LHCb [91, 92] is a single-arm forward spectrometer designed to study heavy-flavour physics
952 through the decay of beauty and charm hadrons. A schematic of LHCb is shown in Fig. 3.4.
953 LHCb adopts a right-handed coordinate system centred on the nominal-interaction point where
954 the positive z-axis points down the beam-line, in the direction of the spectrometer, and the y-axis
955 points upward. In proton collisions b quarks are dominantly produced via gluon fusion. It is
956 stochastically favourable for these interacting gluons to have asymmetric momentum. Therefore,
957 the $b\bar{b}$ pair is boosted along the beam-line. As a result, the main spectrometer is built in a
958 forward direction with a pseudorapidity coverage of $2 < \eta < 5$. This allows 25% of the $b\bar{b}$ quark
959 pairs produced fall within the acceptance of LHCb. Figure 3.2 shows the relative production

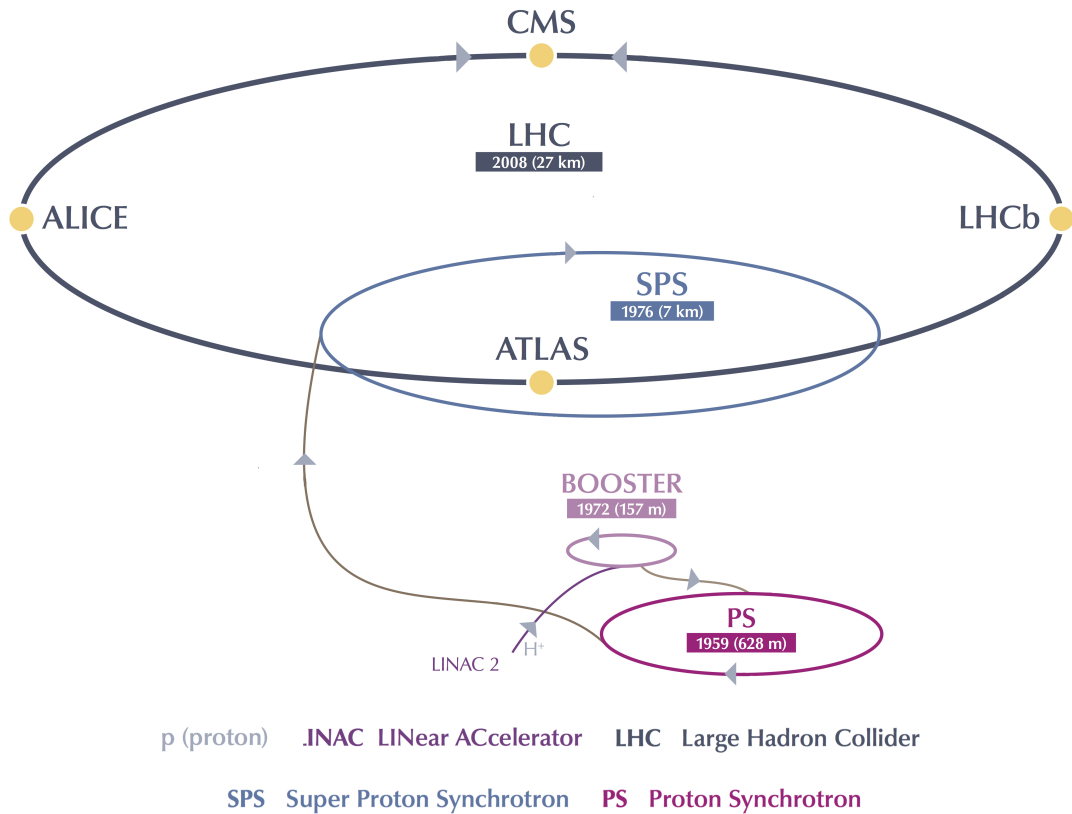


Figure 3.1. Schematic diagram of CERN's accelerator complex. Reproduced from Ref. [90]

960 cross-section of the produced $b\bar{b}$ pairs as a function of the polar angle of each quark, where the
 961 coverage of the LHCb experiment is highlighted in red.

962 The LHCb main spectrometer is equipped with a number of sub-detectors including the
 963 VERTex LOcator (VELO), two Ring Imaging CHerenkov detectors (RICH1 and RICH2), the
 964 Tracker Turicensis (TT), the dipole magnet, the inner and outer tracking stations (T1-T3),
 965 the Scintillating Pad Detector (SPD), the PreShower (PS), the Electromagnetic CALorimeter
 966 (ECAL), the Hadronic CALorimeter (HCAL), and the muon stations (M1-M5) [91,95]. The
 967 sub-detectors are discussed briefly in the following sections. In addition, the HeRsChel detector,
 968 a set of forward-scintillating counters designed to increase the coverage of the LHCb experiment,
 969 was installed in 2015. This detector will be described in detail in Sec. 3.8.

970 During the first period of operation (Run 1), from 2010 to the end of 2012, LHCb collected
 971 1.1 fb^{-1} of proton-proton (pp) collisions at $\sqrt{s} = 7 \text{ TeV}$ and 2.1 fb^{-1} at $\sqrt{s} = 8 \text{ TeV}$. During the
 972 second period of operation (Run 2), from 2015 to the end of 2018, LHCb collected 5.9 fb^{-1} of
 973 pp collisions at $\sqrt{s} = 13 \text{ TeV}$. The LHCb integrated luminosity for pp collisions is summarised in
 974 Fig. 3.3. The analysis presented in this thesis uses 2015 to 2017 data corresponding to 3.7 fb^{-1}
 975 of integrated luminosity. This data set is chosen for the capabilities provided by the newly
 976 installed HERSCHEL system.

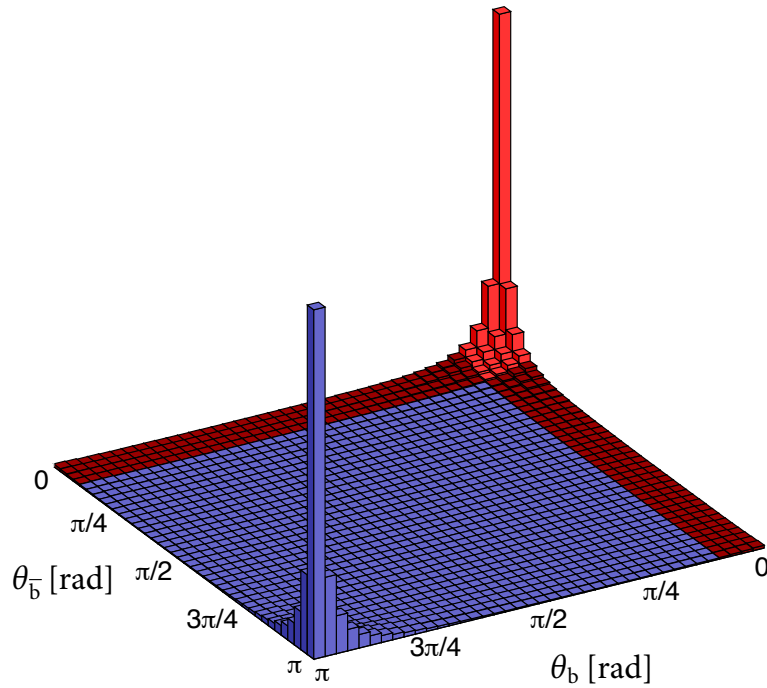


Figure 3.2. Simulation of the relative cross-section of $b\bar{b}$ pair production in pp collisions at $\sqrt{s} = 8$ TeV as a function of the angle between the quark trajectories and the z -axis, θ_1 and θ_2 . The LHCb acceptance is highlighted in red. Reproduced from Ref. [93].

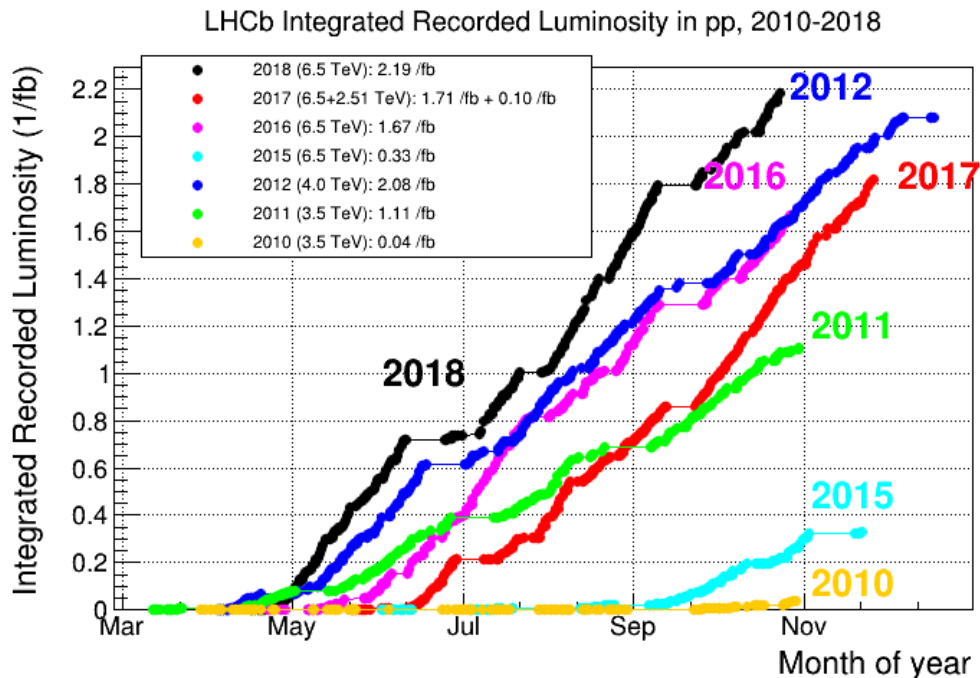


Figure 3.3. LHCb integrated luminosity for pp collisions for 2010 to 2018 runs. Reproduced from Ref. [94].

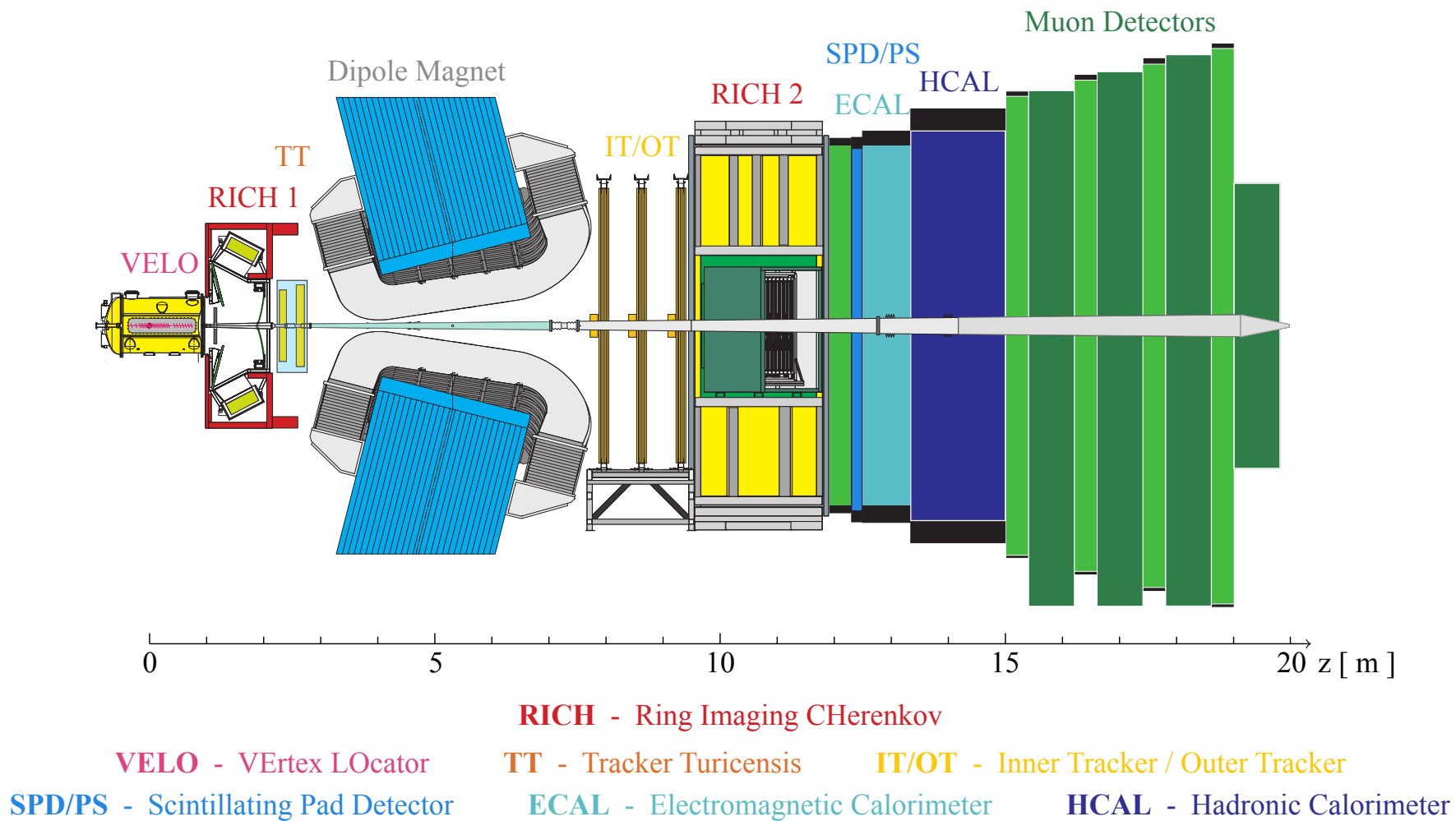


Figure 3.4. Vertical cross-section schematic of LHCb experiment. Reproduced from Ref. [92].

978 **3.2 Vertex Locator (VELO)**

979 The VELO is the detector closest to the pp interaction point [96,97]. It uses 21 semicircular-
 980 silicon-strip stations distributed along the z -axis to measure the coordinates of energy deposits
 981 left by charged particles in order to reconstruct their associated tracks, and from these their
 982 production and decay vertices. Figure 3.5 shows the layout of the VELO for, that makes clear
 the positioning of modules relative to the nominal interaction point.

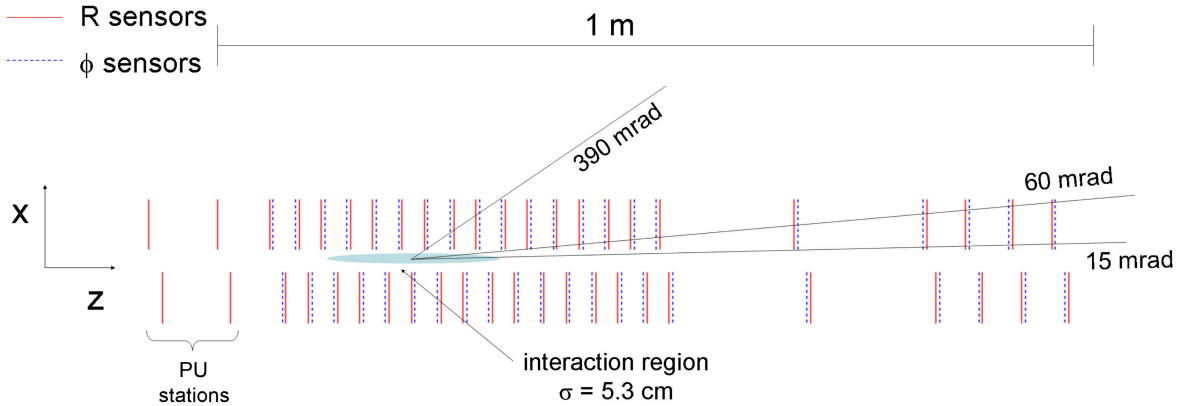


Figure 3.5. Schematic showing the cross-section of the VELO sub-detector and the pile-up system along the $y = 0$ plane showing the position of the silicon-strip modules along the z -axis. The R sensors are depicted in red and ϕ sensors are depicted in blue. Reproduced from Ref. [91].

983

984 Each of the modules consists of two sensors, as shown in Fig. 3.6, one with a concentric
 985 pattern used to measure the radial distance from the beam (R sensor) and one with a radial
 986 pattern designed to measure the azimuthal angle (ϕ sensor) of the track. The VELO provides a
 987 forward ($\eta > 0$) coverage of $1.6 < \eta < 4.9$ and a backward ($\eta < 0$) coverage of $-3.5 < \eta < -1.5$
 988 in pseudorapidity.

989 B mesons, have a typical flight distance of $\mathcal{O}(10)$ mm. Thus, LHCb needs to be able to
 990 resolve secondary vertices with high accuracy. To achieve this, the VELO sensors are placed
 991 8.2 mm away from the beam-line during data collection. The VELO is capable of tracking
 992 particles with a 10 μm resolution in the perpendicular direction to the beam-line and 50 μm in
 993 the parallel direction. The primary vertex resolution as a function of number of tracks, and the
 994 impact parameter as a function of $1/p_T$, is shown in Fig. 3.7 for the x -axis and y -axis. Here the
 995 impact parameter is defined as the distance between the track and its associated primary vertex.

996 The silicon sensors are placed inside a 0.3 mm thick vacuum-aluminium enclosure, known
 997 as the Radio Frequency foil (RF foil). This provides shielding against RF pick-up from the
 998 beams while protecting the beams' vacuum from VELO outgassing. The foil is corrugated to
 999 allow the sensors to overlap, eliminating inactive detector gaps. To minimise radiation damage,
 1000 the vertex modules are retracted to a position 35 mm away from the beam during injection and
 1001 periods of unstable beam and kept at -30°C with liquid CO_2 .

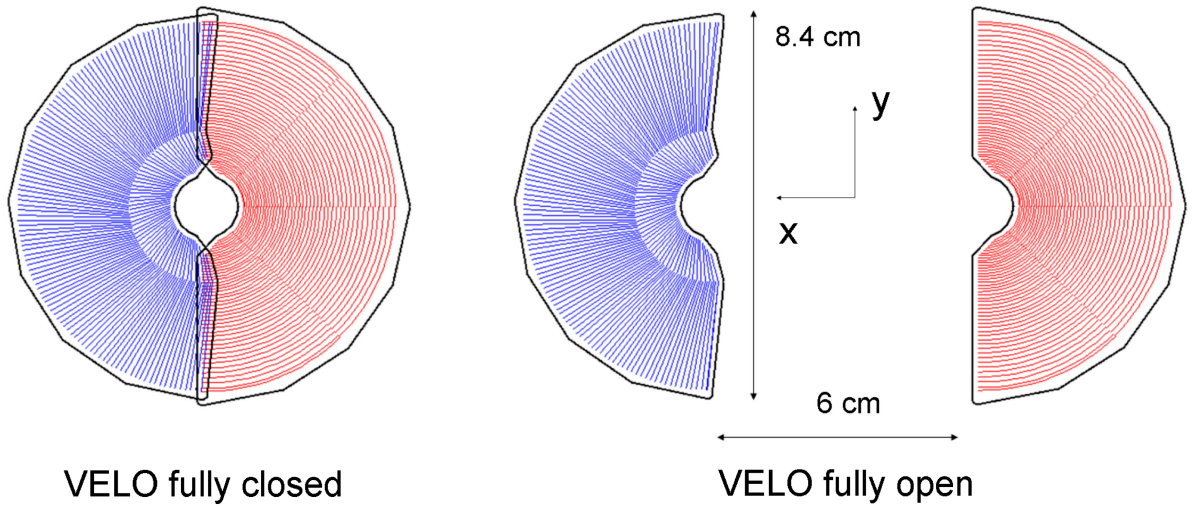


Figure 3.6. Schematic showing the silicon-strip modules in their closed (left) and open position (right). The R sensors are depicted in red and ϕ sensors are depicted in blue. Reproduced from Ref. [91].

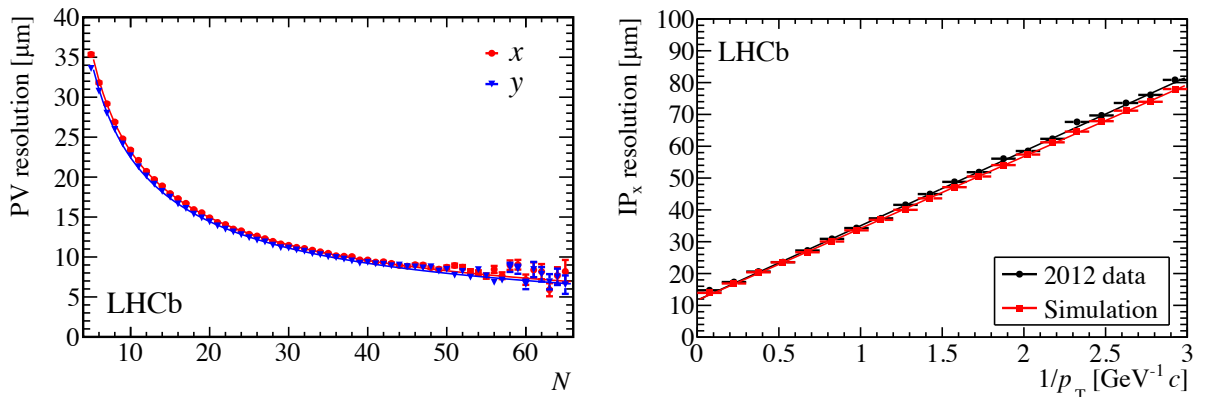


Figure 3.7. Primary vertex resolution as a function of track multiplicity (left) for the x-axis (red) and y-axis (blue) for 2012 data. Impact parameter resolution as a function of $1/p_T$ for 2012 data (data) and Monte Carlo (red). Reproduced from Ref. [95].

1002 In addition to the 21 stations that compose the main VELO detector, there are two modules
 1003 upstream of the VELO equipped only with R sensors that constitute the pile-up (PU) system
 1004 which is used to detect backwards tracks and estimate the number of interactions per bunch
 1005 crossing. These upstream stations are used to reject backwards tracks during the selection of
 1006 CEP candidates.

1007 3.3 Dipole magnet

1008 LHCb employs a dipole magnet [98] to curve charged particles in the horizontal plane to allow
 1009 for the measurement of momentum from each track's radius of curvature. The magnet is made
 1010 from two water-cooled, non-superconducting, aluminium coils shaped as a trapezoid. The

1011 magnet is aligned with the acceptance of the spectrometer and held in this wedge configuration
 1012 by a 1600 tonne window-frame iron yoke, see Fig. 3.8.

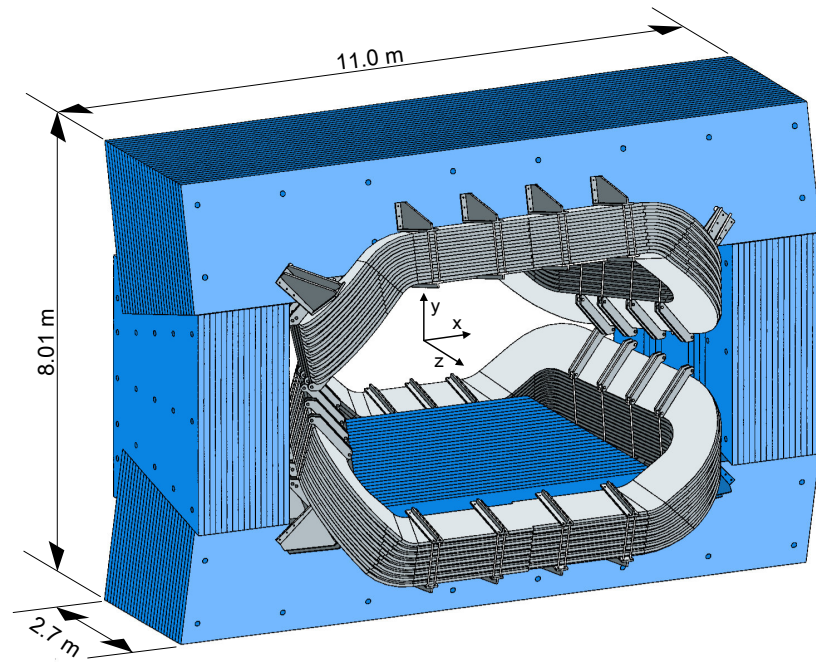


Figure 3.8. Perspective upstream view of the dipole magnet (grey) and yoke (blue). Reproduced from Ref. [98].

1012

1013 The magnet's integrated field is 4 Tm for a 10 m track. To improve the performance of
 1014 the tracking stations, both immediately before and after the magnet, the dipole is aligned with
 1015 the spectrometer with a precision of 1 mm and the magnetic field is known with a precision of
 1016 1×10^{-4} . The performance of the VELO and RICH detectors is sensitive to external magnetic
 1017 fields. Straight tracks in the VELO allow for better vertex reconstruction and event triggering.
 1018 Similarly, the image in the RICH photon detectors are distorted by the presence of a magnetic
 1019 field. For this reason, not only do both detectors have magnetic shielding but the magnet is
 1020 designed such that the magnetic field is minimal where these detectors are instrumented and
 1021 stronger near the tracking stations, see Fig. 3.9.

1022 The CP -violation studies at the LHCb experiment are sensitive to systematic biases from
 1023 charge asymmetries in the detector. Since positive and negative particles bend in opposite
 1024 directions within a magnetic field, the polarity of the magnet is periodically inverted to reduce
 1025 any detector biases.

1026 3.4 Tracking system

1027 The LHCb tracking system relies on the VELO, the Tracker Turicensis (TT), dipole magnet
 1028 and Tracking stations (T1–T3) to map the spatial trajectory of charged particles and measure
 1029 their momentum.

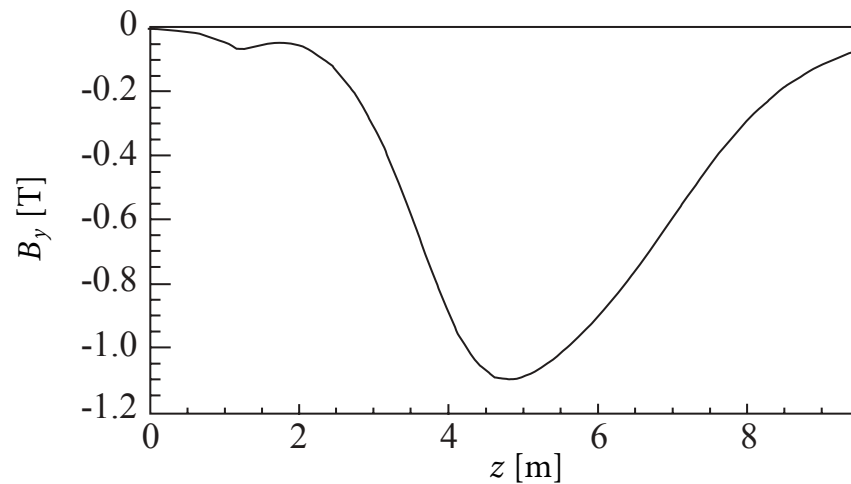


Figure 3.9. The y-component of the dipole-magnetic field as a function of distance along the z-axis of the detector. Reproduced from Ref. [95].

1030 3.4.1 Tracker Turicensis

1031 Located immediately before the dipole magnet, the TT is composed of four layers of silicon
 1032 micro-strip sensors with a single-hit spatial resolution of $50\ \mu\text{m}$ that spans the acceptance of the
 1033 spectrometer. The two inner layers are offset by -5° and $+5^\circ$ relative to the vertical along the
 1034 x-y plane to provide a *stereo angle* to give some sensitivity to the y-coordinate. A schematic
 of the third station is shown in Fig. 3.10 (left) illustrating this angular shift. The detector

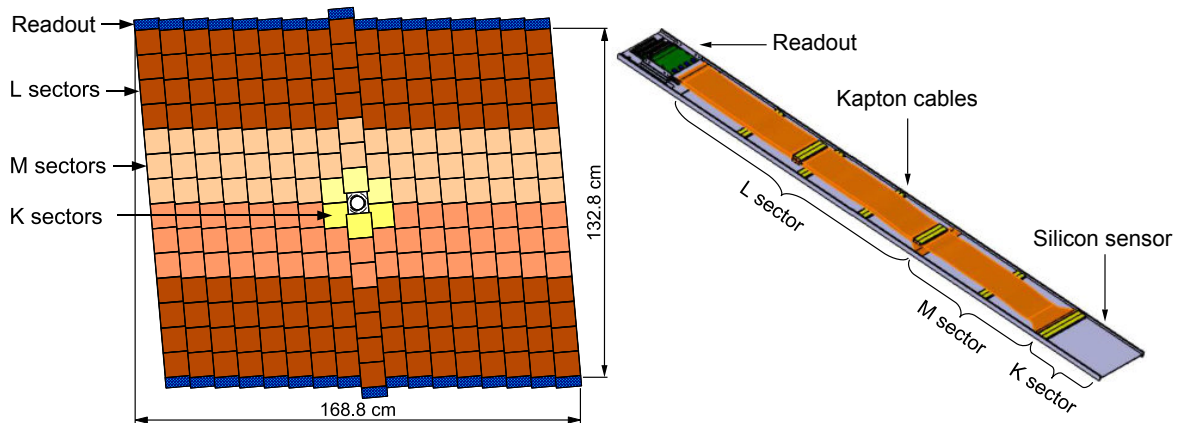


Figure 3.10. Schematic of the third layer of the TT (left). The readout electronics are highlighted in blue, the L sector in brown, the M sector in beige, and the K sector in yellow. A close up schematic of a single TT module (right). Reproduced from Ref. [91].

1035

1036 layers are bifurcated horizontally, and composed of seventeen modules with seven silicon sensors
 1037 each. The modules closest to the beam-line are separated into three sectors to accommodate
 1038 for high-track densities, sector L, M, and K. All other modules are separated into two sectors
 1039 only, sectors L and M. The readout electronics are located at the end of each of the modules.

1040 Fig. 3.10 (right) shows the schematic of a module located close to the beam-line. To reduce
 1041 inactive areas the modules are staggered with an overlap of one centimetre.

1042 3.4.2 Tracking stations

1043 Three Tracking stations (T1-T3) are located immediately after the dipole magnet. To account
 1044 for the higher track density near the beam-line, each of these stations is separated into an Inner
 1045 Tracker (IT) instrumented with the same crossed-silicon micro strips as the TT, and an Outer
 1046 Tracker (OT) instrumented with drift-tube detectors. Each station is composed of four layers
 1047 with the two internal layers rotated by -5° and $+5^\circ$ with respect to the vertical axis, and
 1048 overlapping adjacent modules by 4 mm in the z direction and 3 mm in the x direction. Similar
 1049 to the TT, this increasing the sensitivity of the detector in the y -coordinate. The layout of one
 1050 of the tracking stations is shown in Fig. 3.11 (left) together with a close up of the IT (left) and
 1051 the Inner Tracker (right). Reproduced from Ref. [99].

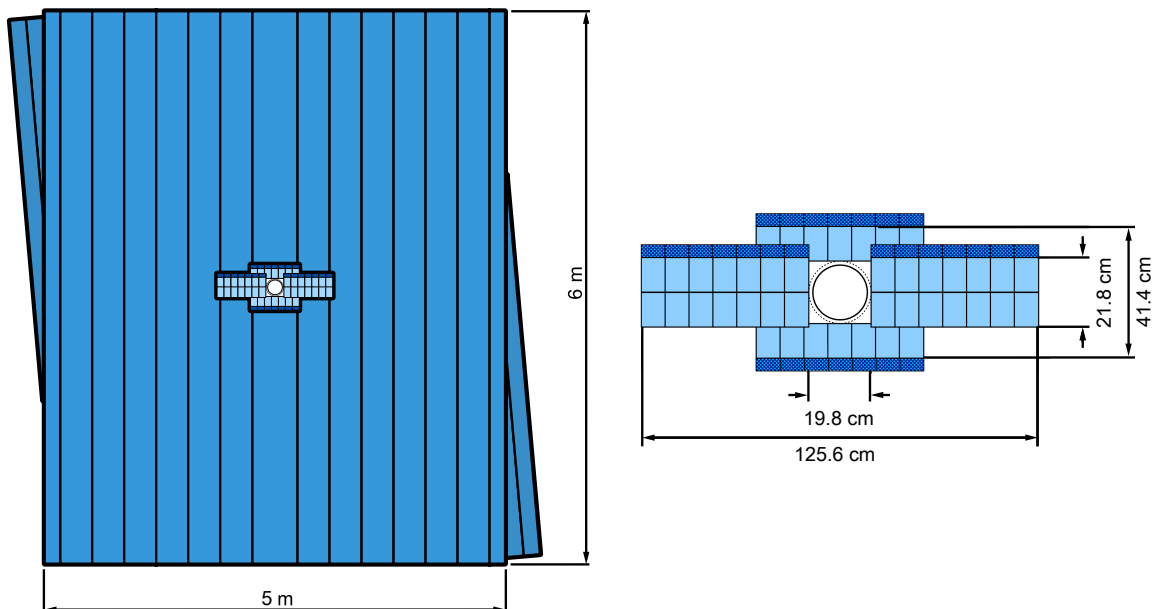


Figure 3.11. Schematic of the Outer Tracker (left) and close up of the Inner Tracker (right). Reproduced from Ref. [91].

1052 Each module of the OT is composed of two layers of the drift-tube detectors filled with a
 1053 gas mixture composed of 70% argon, 28.5% carbon dioxide and 1.5% oxygen. The OT shares
 1054 the same four-layer arrangement as the IT, has a drift-coordinate resolution of $200 \mu\text{m}$, and a
 1055 momentum resolution of $\delta p/p \approx 0.4\%$. The track reconstruction procedure is discussed further
 1056 in Sec. 3.10.1.

1057 3.5 Particle identification

1058 Particle identification (PID) is fundamental for the study of physics involving hadronic decays.
 1059 Two Ring-Imaging CHerenkov detectors (RICH1 and RICH2) [100] provide charged-particle

1060 identification, mainly used to discriminate between kaon, pion, and proton candidates. When a
 1061 particle passes through a material with refractive index $n > 1$, also known as a radiator, at a
 1062 velocity (v) greater than the phase velocity of light in the material, it emits a cone of photons
 1063 known as Cherenkov radiation. These detectors measure the angle of emission of Cherenkov
 1064 photons (θ_c) defined in Fig. 3.12. The velocity of the particle can then be determined by

$$v = \frac{c}{n \cos(\theta_c)}, \quad (3.1)$$

1065 where c is the speed of light in vacuum. The velocity is then combined with the momentum
 1066 measurement extracted from the radius of curvature of the tracks to determine the mass
 1067 hypothesis of the particle.

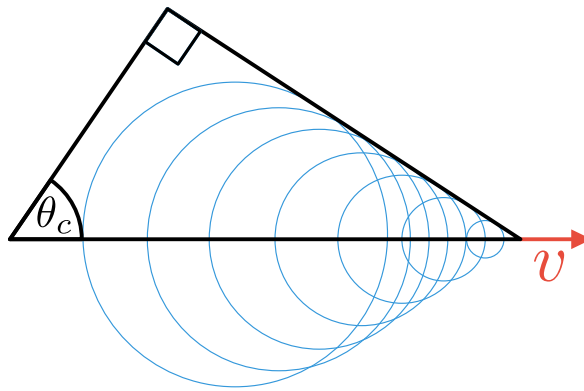


Figure 3.12. The geometry of Cherenkov radiation. The red arrow depicts the velocity of the particle and the blue rings depict the formation of the Cherenkov cone.

1068 Both RICH1 and RICH2 use concave mirrors to focus the Cherenkov rings onto a flat mirror
 1069 that reflects them onto two layers of Hybrid Photon Detectors (HPD) on either side of the
 1070 opening window. The HPD are sensitive in the 200 to 600 nm wavelength and enclosed in
 1071 mu-metal to reduce magnetic-field distortions. RICH1 is built in a vertical configuration while
 1072 RICH2 is built in a horizontal configuration, as indicated in Fig. 3.13.

1073 Three different radiator materials are used to provide mass-hypothesis discrimination capa-
 1074 bilities across a wide momentum range. Located before the magnet, RICH1 is equipped with an
 1075 aerogel and C_4F_{10} radiators resulting in optimal performance in the 1 – 60 GeV/ c momentum
 1076 range. The aerogel radiator, however, was removed before the start of Run 2, a change that only
 1077 had consequences for very low momentum PID. Since low-momentum particles tend to have
 1078 larger polar angles, RICH1 has the full coverage of the LHCb acceptance. Conversely, RICH2 is
 1079 located after the bending magnet and uses a CF_4 radiator optimised for the 50 – 100 GeV/ c
 1080 momentum range and has an acceptance of ± 25 mrad to ± 300 mrad in the horizontal and
 1081 ± 2500 mrad in the vertical.

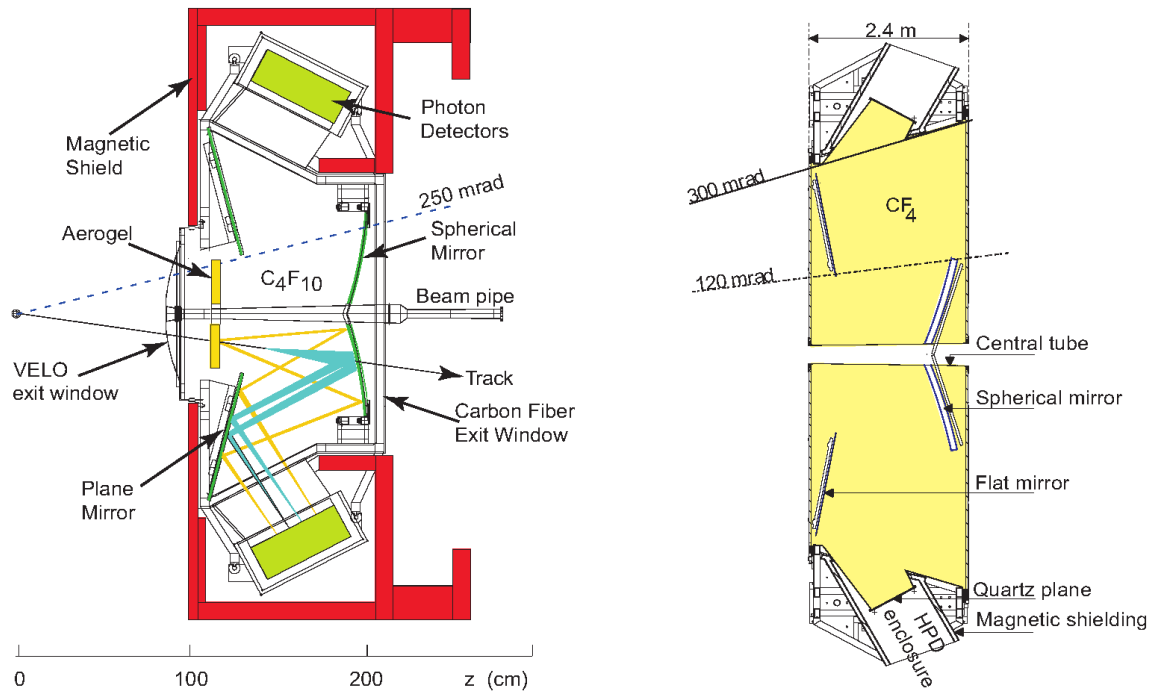


Figure 3.13. Side schematics view of RICH1 (left) and top schematic view of RICH2 (right). Reproduced from Ref. [91].

1082 Figure 3.14 shows the calculated Cherenkov angle as a function of momentum for the different
 1083 radiating materials used at LHCb (left) as well as the reconstructed distribution for the C_4F_{10}
 1084 radiator in RICH1 (right).

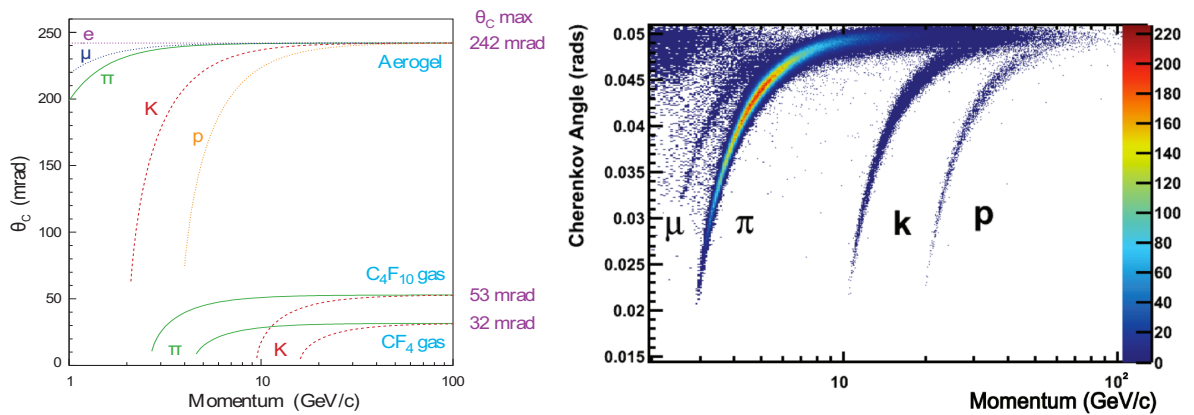


Figure 3.14. Calculated Cherenkov angle as a function of momentum for different RICH radiators: Aerogel, C_4F_{10} , and CF_4 (left). Reconstructed Cherenkov angle for isolated tracks in RICH1 C_4F_{10} radiator (right). The bands are shown for muons (μ), pions (π), kaons (K), protons (p), and electrons (e). Reproduced from Ref. [91] and Ref. [95] respectively.

1085 3.6 Calorimetry

1086 The calorimetry system [101] of LHCb plays an important role in the identification and re-
 1087 construction of electrons, photons, and neutral pions (π^0). In addition, it provides occupancy
 1088 and transverse energy (E_T) information that allows hadrons, electrons, and photons to fire the
 1089 hardware trigger. This is covered in greater detail in Sec. 3.9.1. Starting from the position closest
 1090 to the interaction point, the calorimeter system consists of the Scintillating Pad Detector (SPD),
 1091 the Pre-Shower (PS), the Electromagnetic Calorimeter (ECAL), and the Hadronic Calorimeter
 1092 (HCAL). The calorimeters are segmented into three regions in the case of the SPD, PS, and
 1093 ECAL, and two regions in the case of the HCAL with higher granularity towards the beam-line
 1094 to compensate for two orders of magnitude variation in occupancy along the active plane of the
 1095 detector. Figure 3.15 illustrates the layout of the SPD/PS and the HCAL.

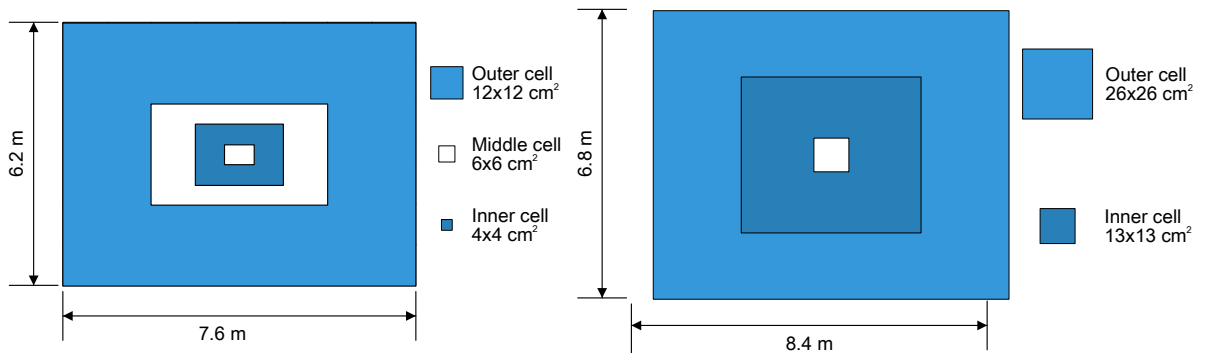


Figure 3.15. Schematic of the SPD (left) and HCAL (right). Each colour region represents a different cell side. The layout of the PS and ECAL are the same as the SPD but scale accordingly to maintain the same acceptance window.

1096 3.6.1 Scintillating Pad and Pre-Shower Detector

1097 The SPD and PS consist of an array of scintillator pads coupled to multi-anode photo multiplier
 1098 tubes separated by a 15 mm thick layer of lead. Only charged particles interact with the SPD.
 1099 However, when neutral particles interact with the lead converter a particle shower is induced,
 1100 leaving a signal in the PS and thus allowing one to distinguish energy depositions left by charged
 1101 and neutral particles in the ECAL and HCAL. This is exploited in the hardware trigger to
 1102 provide a rapid separation of electrons, and neutral pions. Figure 3.16 illustrates the detectors
 1103 involved in the energy measurement of electrons, hadrons, and photons. The hit multiplicity in
 1104 the SPD also provides a measure of the number of charged particles in an event and plays a
 1105 crucial role in the low-multiplicity trigger lines used to study CEP.

1106 3.6.2 Electromagnetic Calorimeter (ECAL)

1107 The ECAL is constructed with alternating layers of 2 mm thick lead absorbers and 4 mm
 1108 scintillators stacked along the z-axis. The cell size of the innermost region of the ECAL
 1109 ($4 \times 4 \text{ cm}^2$) is close to the Moliere radius, such that most of the shower can be contained in
 1110 a single cell. Wavelength shifting fibres connect the scintillators to photomultiplier tubes. A

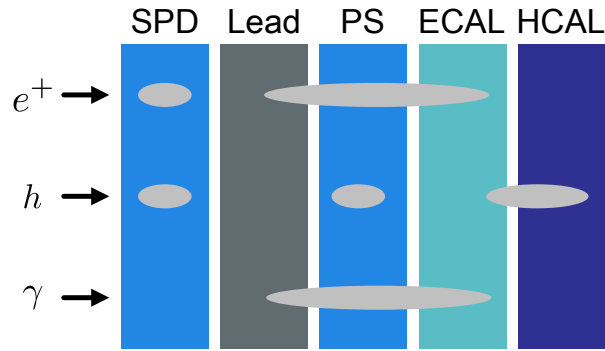


Figure 3.16. Schematic of energy depositions in the calorimetry system for electron, hadrons, and photons.

1111 schematic of an ECAL module is shown in Fig. 3.17 (left). The energy resolution for the ECAL
 1112 can be modelled as

$$\frac{\sigma_E}{E} = \frac{9\%}{\sqrt{E}} \oplus 0.8\% , \quad (3.2)$$

1113 where E is in GeV and the symbol \oplus indicates a quadratic sum. The first term on the right-hand
 1114 side describes the stochastic-resolution effect and the second term gives the energy-independent
 1115 contribution.

1116 3.6.3 Hadronic Calorimeter (HCAL)

1117 Similar to the ECAL, the HCAL is a sampling calorimeter with alternating 3 mm and 1 cm
 1118 iron absorbers connected to photomultiplier tubes via wavelength shifting absorbers. However,
 1119 the plates are placed perpendicular to the ECAL plates along the x-axis. Since hadronic showers
 1120 are larger, the granularity of the HCAL does not need to be as fine as that of the ECAL. A
 1121 schematic of an HCAL module is shown in Fig. 3.17 (right). The energy resolution for the
 1122 HCAL is described by

$$\frac{\sigma_E}{E} = \frac{69\%}{\sqrt{E}} \oplus 9\% , \quad (3.3)$$

1123 where E is in GeV. The first term on the right-hand side describes the stochastic-resolution
 1124 effect and the second term gives the energy-independent contribution.

1125 3.7 Muon system

1126 The muon system is composed of five stations (M1–M5). To keep the detector occupancy uniform,
 1127 the modules are segmented into four regions, R1 to R4, with R1 having the smallest granularity,
 1128 being the region closest to the beam-line. All stations are equipped with multi-wire proportional
 1129 counters (MWPC) with the exception of station M1 region R1, which is equipped with gas
 1130 electron multipliers (GEM). Figure 3.18 (left) shows a layout of the upper-right quadrant of M2.

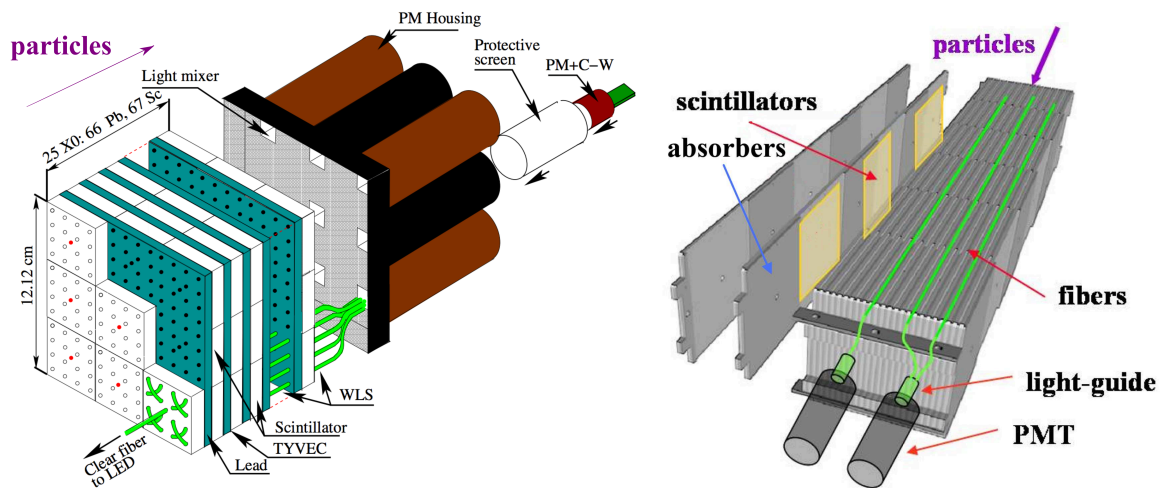


Figure 3.17. Blown-up schematic of an ECAL (left) and HCAL (right) module. The approximate direction of motion of incoming particles is indicated by a violet arrow. Reproduced from Fig. [91]

1131 The first module, M1 is located between RICH2 and the calorimetry system to improve
 1132 the transverse-momentum calculation in the earliest trigger level, while M2-M5 are located
 1133 at the end of the calorimetry system. The M2-M5 modules are each separated by an 80 cm
 1134 iron absorber preventing hadrons that punch through the HCAL from entering into the muon
 1135 system. This results in a momentum resolution of 20%. See Fig. 3.18 for a schematic of the
 1136 muon station positioning.

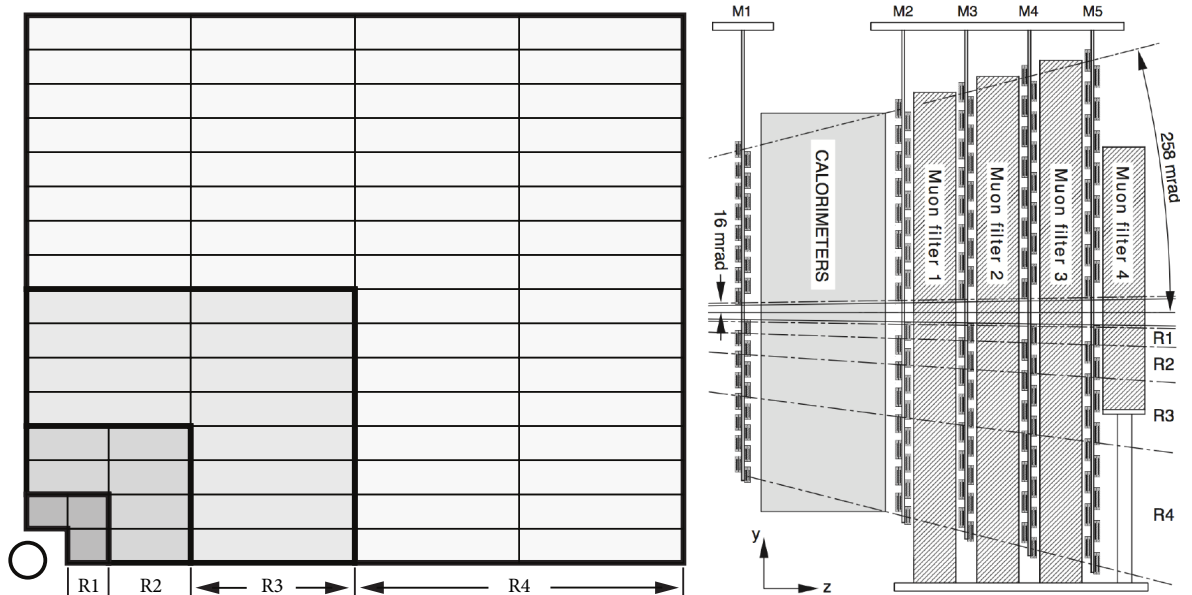


Figure 3.18. Layout schematic of the upper-right-hand corner of M3 (left) and muon stations (right). Reproduced from Ref. [91]

1137 **3.8 HERSCHEL**

1138 HERSCHEL (High Rapidity Shower Counter for LHCb) [102] is a sub-detector system installed
1139 for Run 2, which began in 2015. The modules are designed to detect particle showers induced
1140 by the interaction of high-rapidity particles, which fall outside the acceptance of the main
1141 spectrometer, with the beampipe as well as structural and machine elements of the particle
1142 collider. It is composed of five shower-counter modules, F0, F1, B0, B1, and B2, installed around
1143 the beamlines inside the accelerator tunnel: two in the forward direction of the interaction point,
1144 downstream, and three in the backwards direction, upstream. Each module is segmented into
1145 four quadrants of $300\text{ mm} \times 300\text{ mm} \times 20\text{ mm}$ EJ-200 [103] plastic scintillating pads tightly
1146 fitted around the beam pipe. EJ-200 has a peak emission wavelength of 425 nm and a yield
1147 of 10^4 photons per 1 MeV electron. Energy from incident particles is absorbed in the form of
1148 ionisation and released as light in the de-excitation process.

1149 To detect and amplify the scintillating light, each pad is equipped with a 51 mm diameter
1150 Hamamatsu R1828-01 photo-multiplier tube [104] connected to the scintillating pad via a
1151 fishtail-plexiglass light guide, which is read synchronously with the LHCb spectrometer. These
1152 PMTs are characterised by a high-response time of 1.3 ns necessary to keep up with the high
1153 collision rate of the LHC as well as a large range in gain. The latter allows for operation at
1154 high gain during calibration using single-particle cosmic-ray interactions as well as low gain
1155 necessary to cope with the high-multiplicity particle showers present during regular operation.
1156 For fire safety regulations, and as a means to shield the scintillators from external light leaks,
1157 each module is wrapped with a 1 mm thick aluminium sheet. A module schematic is shown in
1158 Fig. 3.19 together with the schematic of one of the stations.

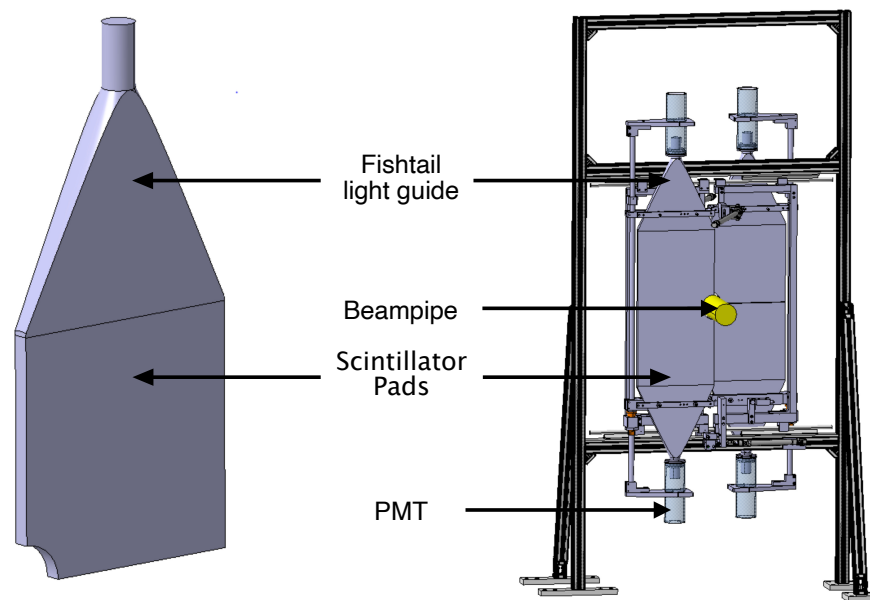


Figure 3.19. Schematic design of a scintillator and light guide of a single HERSCHEL quadrant (left) and a full station (right). Reproduced from Ref. [102]

1159 The stations are placed behind large and dense accelerator components, such as beam screens
 1160 and collimating magnets, where particle showers might be initiated. In the forward direction
 1161 (positive z relative to the interaction point), we find stations F1 and F2 at $z \sim 20.0$ m and
 1162 $z \sim 114.0$ m, respectively. In the backwards direction (negative z), we find stations B0, B1, and
 1163 B2 at $z \sim -7.5$ m, $z \sim -19.7$ m, and $z \sim 114.0$ m, respectively. Figure 3.20 shows a schematic
 1164 of the system. The HERSCHEL modules extend the sensitivity of the main spectrometer from
 1165 $2 < \eta < 5$, in the forward direction, and $-3.5 < \eta < -1.5$, in the backwards direction, to a
 1166 maximum pseudorapidity of ten on either side. A simulation of the energy deposits from forward
 1167 showers originating from proton dissociation in pp collisions is reproduced in Fig. 3.21, showing
 1168 the pseudorapidity coverage of each HERSCHEL module.

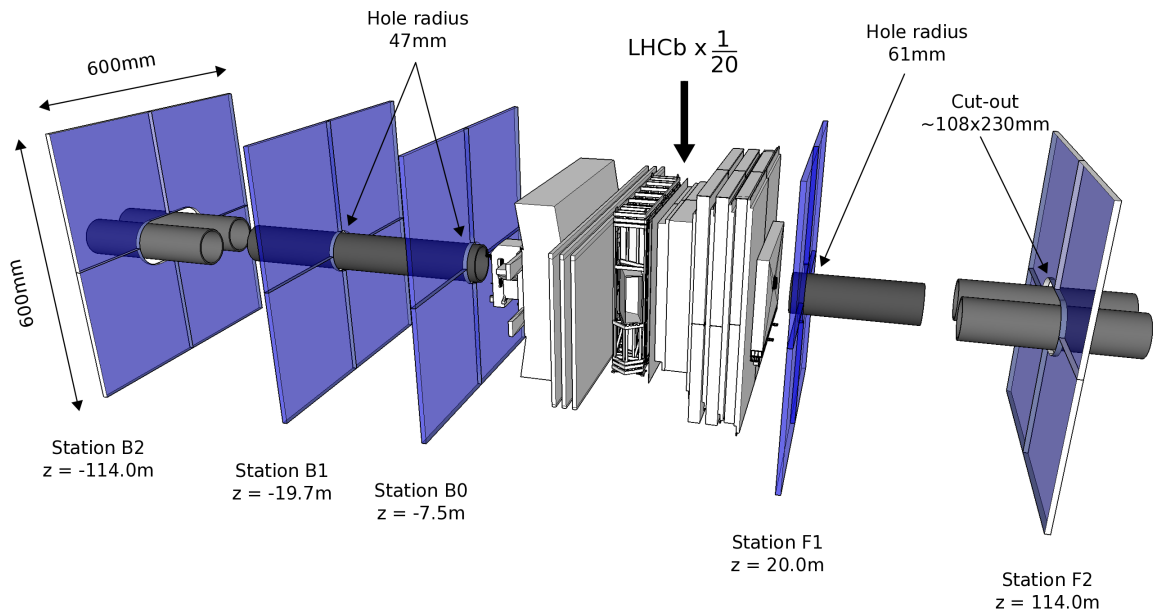


Figure 3.20. Layout of the active area of HERSCHEL stations. The stations are scaled by a factor of 20 and the z -axis is not to scale. Reproduced from Ref. [102]

1169 The increased sensitivity at high rapidities provides valuable information for the classification
 1170 of diffractive processes, such as single and double diffraction, by providing information about
 1171 the presence or absence of a rapidity gap. For example, in a CEP event and in the absence of
 1172 pile-up, the interacting protons would remain intact and continue their trajectory down the
 1173 beam line, resulting in a signature in the HERSCHEL modules consistent with background
 1174 noise. While in inelastic events, the primary background of CEP, the resulting high-rapidity
 1175 particles from the proton-dissociation interact with machine elements and produce particle
 1176 showers, breaking the rapidity gap and leaving an excess of signal in the HERSCHEL modules.
 1177 This signature allows us to use this information to veto the primary source of background
 1178 in CEP studies. In addition, HERSCHEL is also sensitive to the presence of inelastic events
 1179 originating from secondary interactions that can occur alongside a CEP event during pile-up.

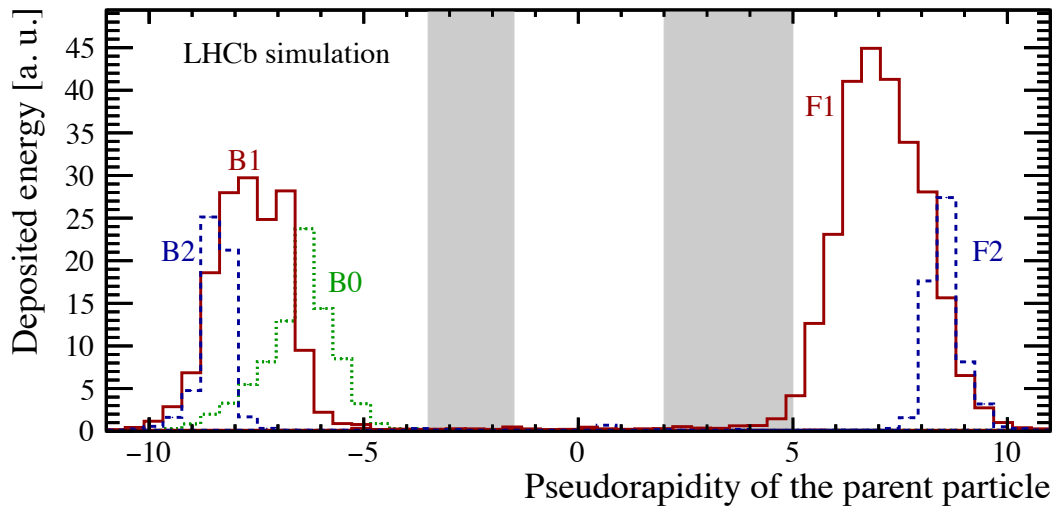


Figure 3.21. Energy deposits on HRC modules as a function of pseudorapidity. The pseudorapidity coverage of LHCb is highlighted in grey. Reproduced from Ref. [102]

1180 Although HERSCHEL is able to identify the presence of these rapidity-breaking showers it is
 1181 unable to distinguish their source.

1182 The integrated analogue signal from the PMT is digitised by a 10-bit analogue-to-digital
 1183 converter (ADC). A typical detector signal is shown in Fig. 3.22 for station B0 for the first 100
 1184 ADC counts. The pedestal, shown in red, corresponds to an empty detector and is representative
 1185 of the absence of activity we expect in CEP-like events. It is determined by reading the detector
 1186 during empty crossing following the last of a series of pp crossings known as a train. Events
 1187 with activity, shown in black, are read during pp crossings and are characterised by a long tail
 1188 at higher ADC counts. An efficiency study of the HERSCHEL module for 2015 and 2016 data
 1189 is detailed in Sec. 5.6 using dimuon continuum data.

1190 3.9 Trigger system

1191 The LHC bunch crossing frequency is 40 MHz. However, it is unfeasible to permanently store
 1192 every event. Composed of a hardware, Level-0 (L0), and a software component, High Level
 1193 Trigger (HLT), the trigger system [105] is a two stage process designed to identify and store
 1194 events containing signatures of interesting physics as well as select events for calibration.

1195 3.9.1 Level-0 trigger

1196 The earliest trigger level, L0, operates synchronously with LHC's 40 MHz bunch crossings and
 1197 reduces the data bandwidth to 1 MHz, the rate at which the entire detector can be read out.
 1198 Given how quickly the initial decision needs to be made, only a subset of the detectors are used
 1199 at this stage. This includes the Pile-Up, the calorimetry, and muon systems. The PU system
 1200 distinguishes events with multiple interactions by measuring the multiplicity of backward tracks.
 1201 The calorimetry provides multiplicity information in the forward direction and calculates the
 1202 total transverse energy, E_T , for electrons, photons, and hadrons in 2×2 cell clusters. The muon

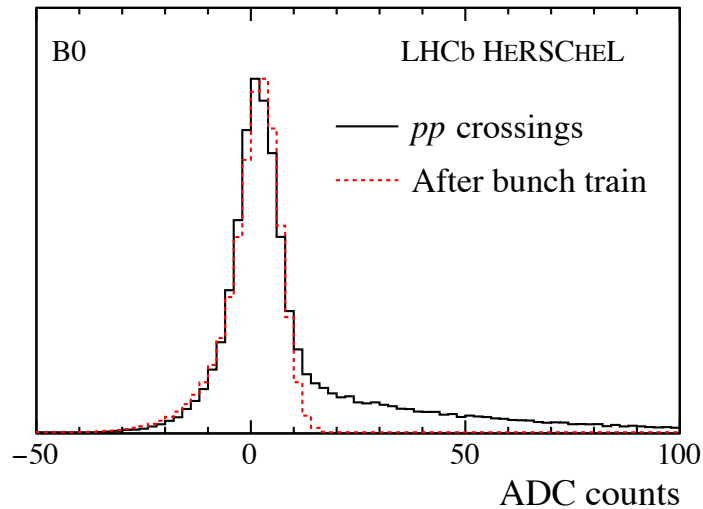


Figure 3.22. Example of HERSCHEL signal for station B0 for pp crossings (black) and for empty crossings following a pp crossing. Reproduced from Ref. [102]

1203 decision uses all five stations to calculate the transverse momentum, p_T , and selects the two
 1204 muons with the highest p_T per quadrant. This information is then combined and compared
 1205 with decision criteria or trigger lines. Those events that meet these criteria are placed in a
 1206 buffer to be processed by the hardware stage. Dedicated low-multiplicity trigger lines are used
 1207 for the study of CEP physics. The specific trigger lines used to collect the data for the analysis
 1208 presented in this thesis will be described in detail in Chapter 4.

1209 3.9.2 High Level Trigger (HLT)

1210 The second trigger level, HLT, is a software-based C++ application executed in the Event
 1211 Filter Farm (EFF), which is a large ensemble of CPUs, and employs information from the entire
 1212 detector to reduce the 40 MHz L0 output to a bandwidth of 12.5 kHz. This is achieved in two
 1213 steps: HLT1 where the event with tracks that have large impact parameters or matching hits
 1214 in the muon arm are reconstructed, and HLT2 where the event is fully reconstructed. During
 1215 HLT1, vertex tracks are reconstructed to calculate impact parameters as well as primary and
 1216 secondary vertices. These are combined with information of the tracking system to reconstruct
 1217 the entire track. The track reconstruction process is explained in detail in Sec. 3.10.1.

1218 3.10 Reconstruction

1219 3.10.1 Track reconstruction

1220 LHCb's data-processing software is centred around GAUDI, an event-processing framework for
 1221 particle physics experiments [106, 107]. As part of this framework, BRUNEL [108] is specialised
 1222 in track reconstruction and particle identification. During track reconstruction, the signal from
 1223 all the tracking sub-detectors are combined to determine each particle's trajectory. The process
 1224 starts with energy depositions from the VELO and the T stations. Since the magnetic field is
 1225 weakest for these stations, they have relatively straight tracks. A Kalman fitter is then used to

1226 account for multiple scattering, and energy loss as intermediate data points are iteratively added
 1227 to construct the track. The event display of a typical inelastic event is shown in Fig. 3.23 with
 1228 the overlapping tracks. HLT2 uses the fully reconstructed event and is able to apply kinematic
 1229 cuts to individual particles as well as combine tracks and apply cuts to mass and vertex fits.

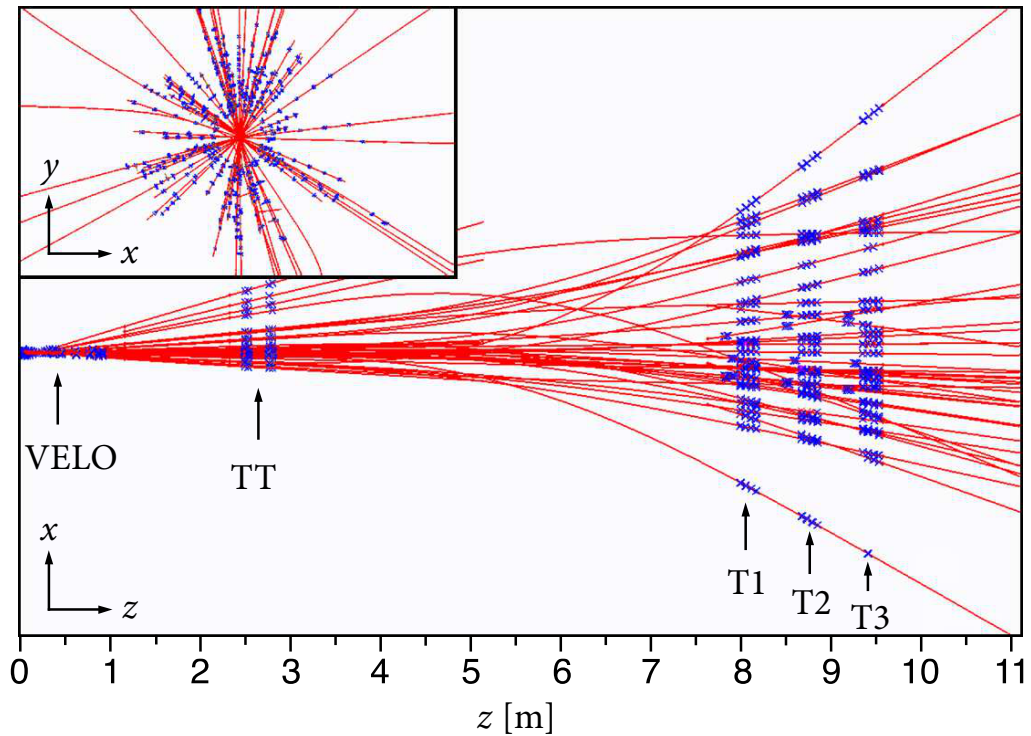


Figure 3.23. Reconstructed tracks (red) and energy detector hits (blue). Reproduced from Ref. [91]

1230 The tracks are then classified according to the detectors with energy deposits associated
 1231 with that track:

- 1232 • **VELO Tracks** traverse only the VELO, tend to have large angles relative to the horizontal,
 1233 and are normally used for vertex reconstruction.
- 1234 • **Upstream Tracks** traverse the VELO and TT, tend to be low momentum with poor
 1235 momentum resolution, and are deflected outside the acceptance of the spectrometer by the
 1236 bending magnet.
- 1237 • **Long Tracks** traverse all tracking stations and tend to have the best momentum resolution.
- 1238 • **Downstream Tracks** traverse the TT and T stations and tend to be decay products of
 1239 particles that decay outside of the VELO.
- 1240 • **T Tracks** traverse only the T station.

- 1241 • **Backwards Tracks** traverse through the VELO and PU. These particles have a negative
 1242 rapidity and do not make it into the mains spectrometer.

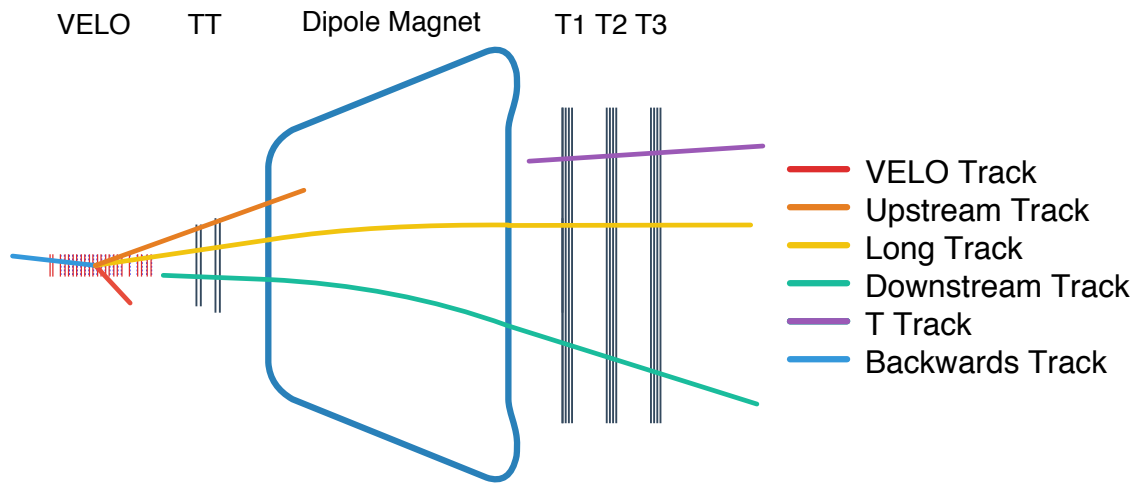


Figure 3.24. Schematic of the LHCb tracking system with representative examples of track types: VELO (red), upstream (orange), long (yellow), downstream (green), T (purple), and backward tracks (blue).

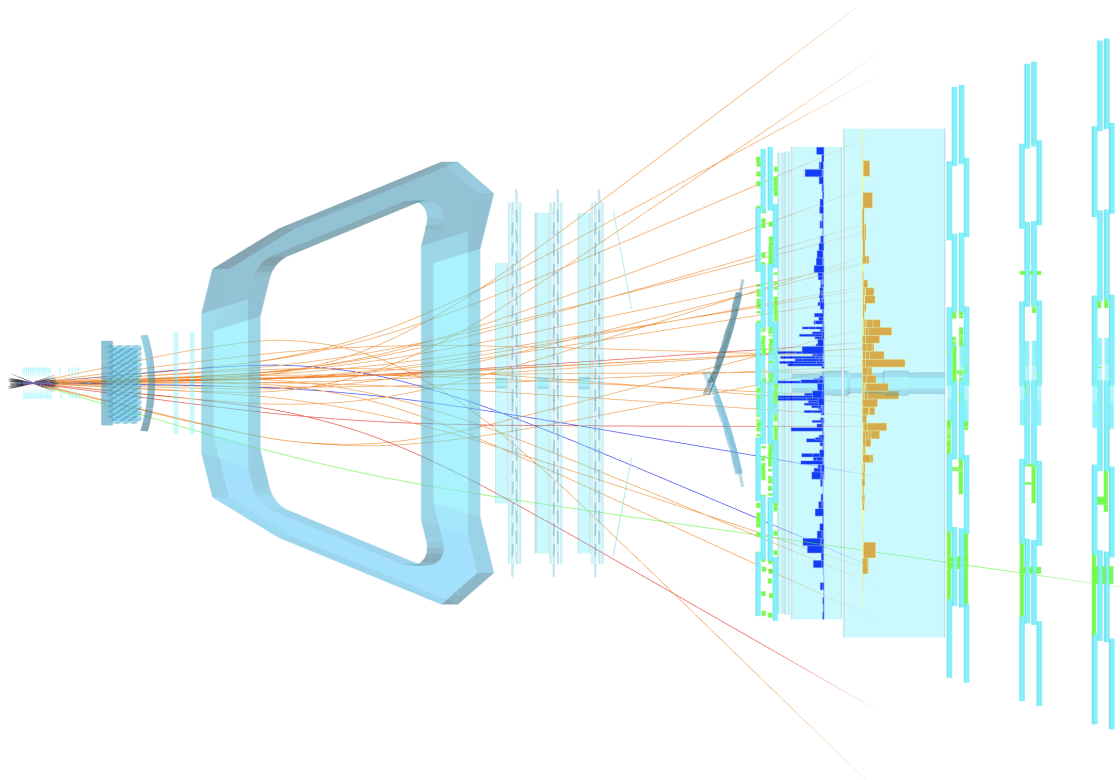


Figure 3.25. Event display top view of a typical event showing tracks for pions (orange), kaons (red), protons (violet), electrons (blue), and muons (green) together with energy depositions in the calorimeters and muon arm.

1243 3.10.2 Particle identification

1244 Neutrals

1245 Neutral particles are distinguished by the absence of tracks associated with energy depositions in
 1246 the calorimetry system. To identify neutral particles, all reconstructed tracks are extrapolated
 1247 to the calorimetry system and matched with a cluster. In the ECAL, a cluster is defined as
 1248 a 3×3 cell pattern centred around the cell with the largest energy deposit. The match is
 1249 evaluated by comparing the track and cluster coordinates at the energy-weighted centre of the
 1250 cluster along the z direction according to a χ_{2D}^2 metric,

$$\chi_{2D}^2 = (\vec{r}_{track} - \vec{r}_{cluster})^T (C_{track} + S_{cluster})^{-1} (\vec{r}_{track} - \vec{r}_{cluster}), \quad (3.4)$$

1251 where \vec{r}_{track} and $\vec{r}_{cluster}$ are the local coordinates of tracks and clusters respectively, C_{track} is
 1252 the covariant matrix of \vec{r}_{track} and $S_{cluster}$ is the cluster energy spread matrix. Neutrals are
 1253 identified as being associated to clusters with a large value of χ^2 . The isolation criteria for
 1254 photon candidates are satisfied by selecting events with $\chi_{2D}^2 > 4$.

1255 The energy of non-converted photons is calculated from the total energy deposition in the
 1256 ECAL and the PS. The photon direction is calculated according to its assumed point of origin.
 1257 Photons can also be reconstructed from electron-positron pairs when they convert before the
 1258 bending magnet. Electron-positron candidates within 3σ of cluster extent and 200 mm in the
 1259 vertical plane are paired and the energy is corrected by including associated bremsstrahlung
 1260 photons.

1261 Neutral pions are reconstructed with two well-separated photons. However, for transverse
 1262 momentum greater than 2 GeV the photon clusters tend to overlap with one another. The
 1263 energy deposited in overlapping cells is accounted for by fitting the energy distribution of the
 1264 two photons according to simulation. To prevent the misidentification of high-energy neutral
 1265 pions and photons a neural network trained on $B^0 \rightarrow K^{*0}\gamma$ is used to distinguish energy-deposit
 1266 patterns.

1267 Hadrons

1268 Charged hadrons are mainly identified through a global pattern-recognition algorithm that
 1269 matches the patterns left by Cherenkov radiation in the photo detectors of RICH1 and RICH2
 1270 with the expected signature of a reconstructed track under a given mass hypothesis. The mass
 1271 hypothesis with the highest likelihood is found by cycling through all potential candidates (pion,
 1272 kaon, proton, electron or muon) for all reconstructed tracks and finding the best match. For
 1273 each track, the log-likelihood difference is calculated relative to the pion mass hypothesis, the
 1274 most abundant hadron produced, such that

$$\Delta \log \mathcal{L}_{X-\pi} = \log \mathcal{L}_X - \log \mathcal{L}_\pi, \quad (3.5)$$

1275 where \mathcal{L}_X is the likelihood of a given mass hypothesis X and \mathcal{L}_π is the likelihood given the π
1276 mass hypothesis.

1277 Muons

1278 Muons are identified by extrapolating reconstructed tracks and associating them with signals
1279 recorded in the muon system. Signals are searched at each station within a window centred
1280 around the coordinates of the extrapolated reconstructed tracks. The window as well as the
1281 number of stations involved in the particle-identification algorithm are energy dependent since
1282 a minimum-momentum transverse momentum of 3 GeV is needed to reach the M2 and M3
1283 stations and 6 GeV to reach all five stations. Similarly to the ECAL cluster-track matching, a
1284 χ^2_{2D} metric that quantifies the cluster-track proximity is minimised.

1285 Combined particle identification

1286 Two methods are used to combine particle identification information from each subsystem to
1287 form a more powerful identification. The first adds the log likelihood of each sub-system linearly
1288 to obtain a combined likelihood $\Delta \log \mathcal{L}_{combined}(X - \pi)$. A second method uses Toolkit for
1289 Multivariate Data Analysis with ROOT (TMVA) [109] to combine PID information and other
1290 parameters to calculate the probability for a given mass hypothesis.

1291 3.10.3 Stripping and Turbo

1292 Stripping can be considered as an offline trigger. Pre-selections are applied to the recorded
1293 events, and the saved samples are grouped in streams according to their physics potential. In
1294 the stripping process, the latest alignments and calibrations are used to fully reconstruct the
1295 recorded events. This high-precision tracking, vertex, and PID information is used for the study
1296 of independent decay channels. The reconstruction of composite particles and loose selection
1297 criteria are specified in dedicated stripping lines. This first selection pass is designed to reduce
1298 the data set to a manageable size while maintaining flexibility of the selection criteria for a
1299 broad number of analyses.

1300 During the LHC long shut down, 2013 to 2014, the processing power and storage of the EFF
1301 computing system was upgraded allowing for a 5.2 PB of buffer space. This corresponds to
1302 about ten days of continuous data taking. As a result, the HLT decision can be postponed until
1303 after data taking, and fully calibrated events can be reconstructed, providing analysis-ready
1304 data to be used as part of the trigger decision. Turbo [110] is a class of output stream with
1305 fully reconstructed decay-specific dedicated streams immediately ready for analysis. Fig. 3.26
1306 depicts a direct comparison of the conventional trigger system (left) and the Turbo stream
1307 system (right).

1308 The data in the Turbo and Stripping streams are ready for analysis. Part of the analysis
1309 process is conducted with DAVINCI [111], a component of the GAUDI analysis framework where
1310 particles can be combined from the decay chain and a first pass of cuts can be applied. At
1311 this stage specialised tools and algorithms can be implemented and tailored for the analysis.

1312 The remainder of the analysis is done with custom software based around the ROOT analysis
 1313 framework [112].

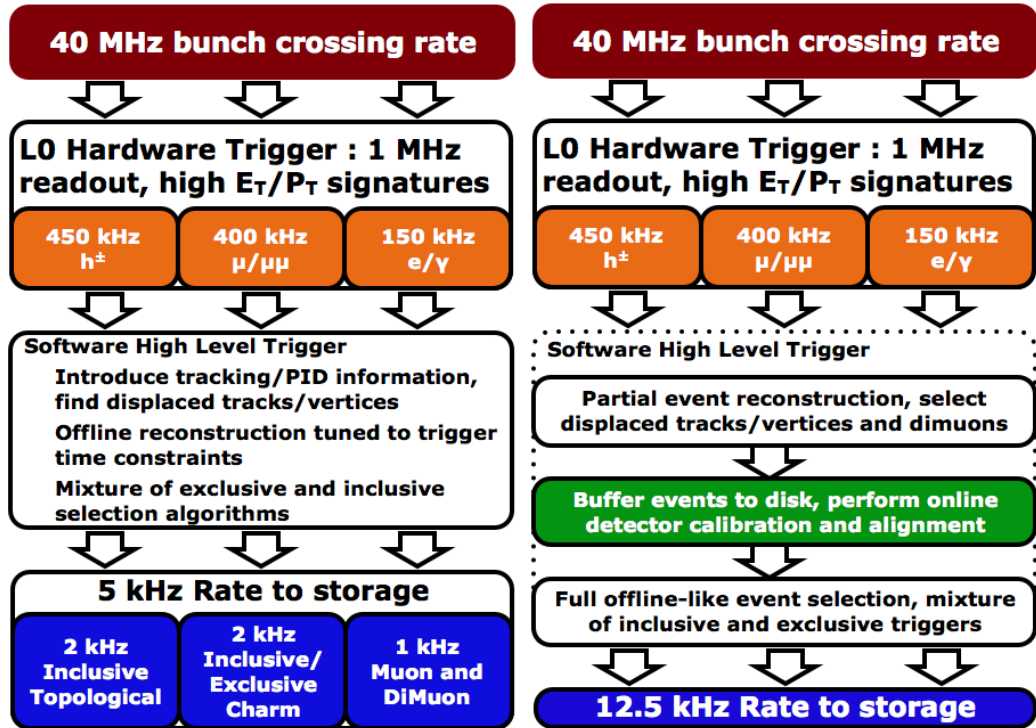


Figure 3.26. LHCb trigger decision flow for Run 1 (left) and Run 2 (right). Reproduced from Ref. [113].

1314 3.11 Simulation

1315 Monte Carlo studies play an essential role in the study of signal modes, efficiencies, detector
 1316 response, and background studies. The first stage of simulation is run using GAUSS [114–116].
 1317 This takes care of the generation and particle propagation. The analysis presented in this thesis
 1318 relies on SuperChic v2 [78] to generate χ_c signal samples as well as $\psi(2S)$ background samples.
 1319 The output of SuperChic v2 is incorporated in the simulation framework via a *particle gun*
 1320 method. This method generates χ_c particles by sampling the momentum distribution generated
 1321 by SuperChic v2 and decays them using EVTGEN [117] and models final-state radiation with
 1322 PHOTOS [118]. The decay particles are then propagated through the detector by GEANT4 [119],
 1323 which simulates multiple scattering throughout the detector material. The second generator
 1324 used is PYTHIA [120, 121], a pp collision simulator, that is fully implemented into the LHCb
 1325 simulation framework. BOOLE [122] models the detector response and front-end electronics.
 1326 The trigger software is then run, MOORE [123], to simulate the hardware and software triggers.
 1327 At this point, the Monte Carlo can be reconstructed with BRUNEL [108] and analysed with
 1328 DAVINCI in the same fashion as data.

CHAPTER 4

Event selection

1329

1330

1331

1332 In this chapter we present the selection of the collision data sets for the two major components
 1333 of this analysis: the CEP χ_c sample used for the cross-section measurements of CEP χ_{c1} and
 1334 χ_{c2} mesons as well as the D^{*0} sample necessary to measure the photon-conversion efficiency.
 1335 The trigger, stripping, and offline-selection criteria applied to each of the samples are outlined
 1336 in detail. Finally, we present the samples of Monte Carlo simulation data necessary for the
 1337 measurements.

1338 4.1 CEP χ_c study: data sets, selection criteria, and simulation

1339 4.1.1 CEP χ_c data sets

1340 This analysis is performed with pp collision data collected with the LHCb detector at a
 1341 centre-of-mass energy of $\sqrt{s} = 13$ TeV, during the 2015 and 2016 runs. The data collected
 1342 correspond to an integrated luminosity of $\mathcal{L}_{\text{int}}^{2015} = 328 \text{ pb}^{-1}$ and $\mathcal{L}_{\text{int}}^{2016} = 1665 \text{ pb}^{-1}$ for a total
 1343 of $\mathcal{L}_{\text{int}}^{2015+2016} = 1993 \text{ pb}^{-1}$. Only events where all sub-detectors were operational are used in
 1344 the analysis. However, due to commissioning downtime of the trigger lines and the newly
 1345 installed HERSCHEL detector during the early parts of the 2015 run, only 86.6% of the 2015
 1346 data meets the trigger lines and HERSCHEL requirements for this analysis while 98.2% of the
 1347 2016 data satisfies these requirements. In addition, to isolate CEP candidates the exclusivity
 1348 requirement demands that we examine events with a single interaction per bunch crossing, that
 1349 is, in the absence of pile-up. Approximately 35.7% of the total-integrated luminosity meets this
 1350 criterion. The determination of the effective integrated luminosity for single-interaction events
 1351 is described in Sec. 7.5. The reconstruction and stripping conditions used are summarised in
 1352 Table 4.1 together with the data pipeline utilised in the analysis. Each of the steps within the
 1353 data-selection process is described in detail in Sec. 4.1.2 and Sec. 4.1.3.

1354 It is worthwhile mentioning that there are two additional data samples of similar size to
 1355 the 2016 data set. The data collected during the 2017 and 2018 pp runs have an integrated
 1356 luminosity of $\mathcal{L}_{\text{int}}^{2017} = 1609 \text{ pb}^{-1}$ and $\mathcal{L}_{\text{int}}^{2018} = 2185 \text{ pb}^{-1}$, respectively. Although we have
 1357 conducted preliminary studies with the 2017 sample, these two data sets have been excluded
 1358 from this study as the data necessary to perform the photon-conversion-efficiency measurement
 1359 is missing for these two data sets. This is explained further in Sec. 4.2.1.

Table 4.1. Summary the trigger reconstruction and stripping information.

Data pipeline	
L0	L0DiMuon,lowMult L0Muon,lowMult
HLT1	Hlt1NoPVPassThrough
HLT2	Hlt2LowMultDiMuon Hlt2LowMultMuon
Stripping Line	LowMultDiMuonLine LowMultMuon

1360 4.1.2 CEP χ_c online-selection criteria

1361 L0 trigger criteria

1362 To be considered, the events must pass the requirements specified by either the `Muon,lowMult`
 1363 or `DiMuon,lowMult` lines in L0, the earliest hardware-trigger level. As the name suggests, these
 1364 trigger lines are designed to select events with one or two muons in a low-multiplicity environment.
 1365 The `Muon,lowMult` trigger requires a single muon with a transverse momentum above 400 MeV/ c
 1366 for 2015, and above 800 MeV/ c for 2016. The `DiMuon,lowMult` trigger requires two muons, each
 1367 with a transverse momentum above 200 MeV/ c .

1368 The low-multiplicity criteria are met by selecting events with less than 30 hits in the
 1369 SPD for 2015, and less than 20 hits for the 2016 data set. The distribution of SPD hits for
 1370 $\chi_c \rightarrow J/\psi [\mu^+ \mu^-] \gamma [e^+ e^-]$ is expected to have approximately one hit from each muon and slightly
 1371 over one hit for each electron, as bremsstrahlung radiation can result in additional hits. Other
 1372 than the hits from the final-state particles, we expect activity in the SPD from noise and
 1373 spillover. A study of this SPD requirement is presented in Sec. 5.1.6 and the L0 trigger criteria
 1374 are summarised in Table 4.2.

Table 4.2. Configuration for the `L0DiMuon,lowMult` and `L0Muon,lowMult` L0 trigger line.

Variable	Units	L0DiMuon,lowMult		L0Muon,lowMult	
Year	-	2015	2016	2015	2016
SPD hits	-	< 30	< 20	< 30	< 20
$\mu_1 p_T$	MeV/ c	> 200	> 200	> 400	> 800
$\mu_2 p_T$	MeV/ c	> 200	> 200	n/a	n/a
Prescale	-	1.0	1.0	1.0	1.0

1375 HLT trigger criteria

1376 Events that pass the hardware-line requirements are forwarded to the first software-trigger level,
 1377 HLT1. In this case, the events are evaluated by the `Hlt1NoPVPassThrough` trigger line, which
 1378 has two unique characteristics pertaining to CEP events. Firstly, since CEP events have a low
 1379 multiplicity, the resources required to process these events are low compared to typical inelastic
 1380 events and so they can therefore be processed directly by HLT2, in the lines `Hlt2LowMultDiMuon`

1381 or `Hlt2LowMultMuon`. The second is that this line, unlike those for inelastic events, does not
 1382 require the reconstruction of a primary vertex (PV).

1383 The `Hlt2LowMultDiMuon` line requires two muons with transverse momentum greater than
 1384 400 MeV/ c and the `Hlt2LowMultMuon` line requires a single muon. with transverse momentum
 1385 greater than 400 MeV/ c . The configurations for these HLT2 trigger lines are summarised in
 1386 Table 4.3.

Table 4.3. Configuration for `Hlt2LowMultDiMuon` and `Hlt2LowMultMuon` trigger lines.

Variable	Units	Hlt2LowMultDiMuon		Hlt2LowMultMuon	
Year	-	2015	2016	2015	2016
$\mu_1 p_T$	MeV/ c	> 400	> 400	> 400	> 400
$\mu_2 p_T$	MeV/ c	> 400	> 400	n/a	n/a
$m_{\mu^+\mu^-}$	MeV/ c^2	> 0.0	> 0.0	n/a	n/a
Prescale	-	1.0	1.0	1.0	1.0
Postscale	-	1.0	1.0	1.0	1.0

1387 4.1.3 CEP χ_c offline-selection criteria

1388 Approximately a fifth of the photons at the LHCb experiment convert into an electron-positron
 1389 pair before they reach the dipole magnet due to their interactions with detector material. These
 1390 photons are known as *converted photons*. More specifically, we categorised photons into three
 1391 subgroups. The first set is known as *long converted photons*, which undergo conversion in the
 1392 first part of the VELO. The electron tracks in this sub-group will leave energy deposits in the
 1393 VELO, TT, and T-stations and as a result will be classified as long tracks. In the second group,
 1394 known as *downstream converted photons*, the conversion occurs in the later portion of the VELO
 1395 or after the VELO, primarily in the TT. These electrons will leave energy deposits in the TT
 1396 and T-stations, and will be classified as downstream tracks. Finally, we define a third group,
 1397 *calorimetric photons*, composed of unconverted photons detected at the ECAL and photons that
 1398 convert into an electron-positron pair after the dipole magnet.

1399 The use of converted photons has two major consequences: a low reconstruction efficiency
 1400 and an improved energy resolution. The low reconstruction efficiency is due to the fact that
 1401 electrons with energies lower than 2 GeV are deflected outside of the detector acceptance by
 1402 the dipole magnet and never reach the ECAL. In addition, the electrons scatter en route to the
 1403 calorimeters and lose energy to bremsstrahlung radiation, reducing the reconstruction efficiency
 1404 further. On the other hand, there is a significant improvement in energy resolution in converted
 1405 photons. This stems from the added tracking information traversing most of the magnetic field.
 1406 Downstream tracks have an average momentum resolution of $\delta p/p \approx 0.43\%$, which compares
 1407 to an energy resolution of $\sigma_E/E \approx 9\%/\sqrt{E} \oplus 0.8\%$ from the ECAL [91]. The improvement in
 1408 energy resolution of the photons translates into a better invariant-mass resolution of particles
 1409 reconstructed with these converted photons, making it particularly appealing for studies such as

1410 that of the χ_c mesons, which require the χ_{c1} and χ_{c2} resonances to be resolved within $50 \text{ MeV}/c^2$
 1411 of each other. Throughout this analysis we use the difference between the reconstructed invariant
 1412 mass of the χ_c candidates and of the intermediate J/ψ meson such that,

$$\Delta m_{\chi_c} = m(J/\psi\gamma) - m(J/\psi). \quad (4.1)$$

1413 Using the Δm_{χ_c} , a quantity we shall sometimes refer to as *delta mass*, partially cancels the
 1414 experimental error in the reconstruction of the J/ψ meson and improves the mass resolution of
 1415 the χ_c candidates, therefore allowing us to better resolve the different χ_c resonances. The Δm_{χ_c}
 1416 distribution in 2016 data is shown in Fig. 4.1 for χ_c mesons using calorimetric and downstream
 1417 converted photons. The distributions are shown prior to the application of the exclusivity cuts
 1418 described later in the section to increase the sample size and better appreciate the differences
 1419 between the two photon-reconstruction methods. In the case of calorimetric photons, the signal
 1420 distributions for χ_{c1} and χ_{c2} mesons overlap completely, whereas they are easily distinguished
 1421 when we use downstream converted photons. As a result, we use converted photons in this
 1422 study.

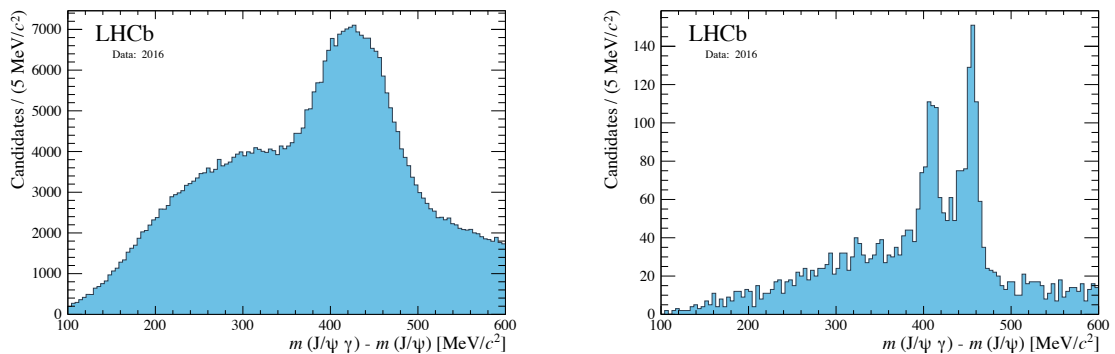


Figure 4.1. Invariant mass of χ_c candidates reconstructed with calorimetric photons (left) and downstream converted photons (right) in 2016 data.

1423 In particular, we prefer downstream converted photons over long converted photons since,
 1424 on average, the electrons from long converted photons have longer distances to traverse and
 1425 thus tend to radiate more secondary photons compared to downstream converted photons. The
 1426 higher sensitivity of long converted photons to bremsstrahlung effects make correcting for this
 1427 effect more difficult and, on average, results in poorer resolution. In addition, the electrons from
 1428 long converted photons are more likely to be deflected from the spectrometer acceptance by the
 1429 magnetic field making their detection and full reconstruction more difficult. The reconstruction
 1430 efficiency of long conversions is further hindered since the energy deposits from conversions that
 1431 occur early in the VELO can be reconstructed as a single VELO track. As a result, electron
 1432 pairs that should be reconstructed as two long tracks can be reconstructed as a single long track
 1433 and a downstream track. Such events are not considered as candidates. Overall, downstream
 1434 converted photons give rise to a better χ_c mass resolution, produce lower levels of background,

1435 and provide larger data samples compared to long converted photons. Consequently, we use
 1436 downstream converted photons in this study.

1437 CEP χ_c stripping-selection criteria

1438 Stripping, described in Sec. 3.10.3, provides another software-based mechanism for data reduction.
 1439 This level of selection allows for fine tuning in a non-destructive form, that is, the events that do
 1440 not pass the criteria set by a stripping line are not deleted. However, they are also not available
 1441 for analysis.

1442 We use the `LowMultDiMuonLine` and `LowMultMuon` stripping lines, which take in the output
 1443 of `Hlt2LowMultDiMuon` and `Hlt2LowMultMuon` trigger lines described above, respectively. In 2015
 1444 and 2016, these trigger lines did not impose new cuts to the HLT2 output. However, they do
 1445 run data-quality checks and make the data available for offline analysis. The decision not to
 1446 impose new cuts is possible with low-multiplicity muon events because of the data samples' size
 1447 and the simplicity of the muon experimental signature. In addition, this allows for the greatest
 1448 flexibility by expanding the range of applicability of these data sets.

1449 CEP χ_c offline-selection criteria

1450 The offline-selection criteria in this analysis focus on two main goals. The first is to select
 1451 $\chi_c \rightarrow J/\psi[\mu^+\mu^-]\gamma[e^+e^-]$ and the second is to ensure there are no signatures of additional
 1452 rapidity-gap-breaking activity.

1453 The intermediate J/ψ candidates are reconstructed using two oppositely charged long tracks
 1454 which are required to match energy deposits in the muon chambers and be consistent with the
 1455 muon hypothesis. We impose a cut, the *track ghost probability*, such that $P_{\text{Track}}^{\text{Ghost}} < 0.9$. This is
 1456 a discriminating variable based on a multivariate classifier used to reduce fake tracks [124, 125].
 1457 These tracks, commonly known as *ghost tracks*, are composed of mismatched hits and do not
 1458 correspond to a true particle.

1459 We require that both muons be within the acceptance of the main spectrometer, $2 <$
 1460 $\eta(\mu^+\mu^-) < 4.5$. To reduce contamination from dimuon-combinatorial background we ap-
 1461 ply a $100 \text{ MeV}/c^2$ J/ψ mass-window cut centred around the J/ψ nominal mass, which is
 1462 $3096.916 \text{ MeV}/c^2$ according to the PDG [81]. Figure 4.2 shows the invariant mass of the
 1463 J/ψ mesons in the χ_c sample as well as the selection mass window. The J/ψ mass distribution
 1464 is slightly skewed to the left due to the muons' loss of energy as they traverse the different
 1465 layers of the spectrometer. The combinatorial background and mass fit is addressed in detail in
 1466 Sec. 6.1.

1467 The J/ψ meson is then paired with a downstream converted photon, which is reconstructed
 1468 by selecting energy cluster pairs in the ECAL associated with downstream electron tracks of
 1469 opposite charge. The clusters must be at most 200 mm or within 3σ of each other in the
 1470 vertical direction. The tracks are then extrapolated and the vertex is reconstructed using
 1471 the *Runge-Kutta* method, which uses iterative-numeric integration to trace tracks through

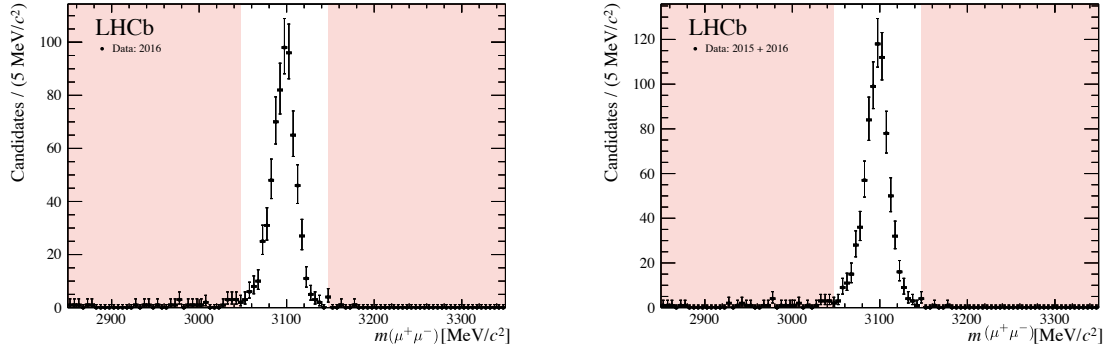


Figure 4.2. Invariant mass of J/ψ mesons from $\chi_c \rightarrow J/\psi[\mu^+\mu^-]\gamma[e^+e^-]$ candidates for 2016-only (left) and 2015 + 2016 (right) data. The veto mass windows are highlighted in red.

1472 non-uniform magnetic fields such as the one in LHCb [126]. Convergence is reached when the
 1473 vertex z -position, $z_{\gamma_{\text{conv}}}$, varies no more than 100 mm within two iterations.

1474 To account for the electrons' energy loss to bremsstrahlung radiation, we apply a recovery
 1475 procedure which systematically adds low-energy photons, $p_T(\gamma_{\text{Brem}}) > 75$ MeV/ c , detected in
 1476 the calorimeter. The ECAL clusters that fall between the linearly extrapolated energy deposits
 1477 in the TT from the dielectron pair are selected as bremsstrahlung candidates. The kinematic
 1478 restrictions on the electrons and photons are left as loose as possible.

1479 Another useful tool for background suppression is the two-dimensional distribution of the
 1480 di-electron invariant mass $m(e^+e^-)$ and $z_{\gamma_{\text{conv}}}$. A photon needs to interact with material in
 1481 order to convert into a pair of electrons. By allowing some dependence on $z_{\gamma_{\text{conv}}}$, we are able to
 1482 efficiently eliminate events with non-physical vertices, combinatorial background and poorly
 1483 reconstructed photons. For these reasons, events that satisfy one of the following requirements
 1484 are rejected:

$$m(e^+e^-) [\text{MeV}/c^2] - 0.00001 \left[\frac{\Delta \text{MeV}/c^2}{\Delta \text{mm}^2} \right] z_{\gamma_{\text{Conv}}}^2 [\text{mm}^2] > 20 [\text{MeV}/c^2] , \quad (4.2)$$

1485

$$m(e^+e^-) [\text{MeV}/c^2] - 0.04 \left[\frac{\Delta \text{MeV}/c^2}{\Delta \text{mm}} \right] z_{\gamma_{\text{Conv}}} [\text{mm}] > 20 [\text{MeV}/c^2] , \quad (4.3)$$

1486

$$m(e^+e^-) > 50 [\text{MeV}/c^2] . \quad (4.4)$$

1487 We will refer to these cuts collectively as the γ two-dimensional (2D) cut. The $m(e^+e^-)$ and
 1488 $z_{\gamma_{\text{conv}}}$ distribution is shown in Fig. 4.3 before and after the the γ two-dimensional cut is applied.
 1489 These same cuts are studied with the larger $D^*(2007)^0 \rightarrow D^0[K^\pm\pi^\mp]\gamma[e^+e^-]$ data set used to
 1490 calculate the photon-conversion efficiency, described in greater detail in Sec. 4.2.3.

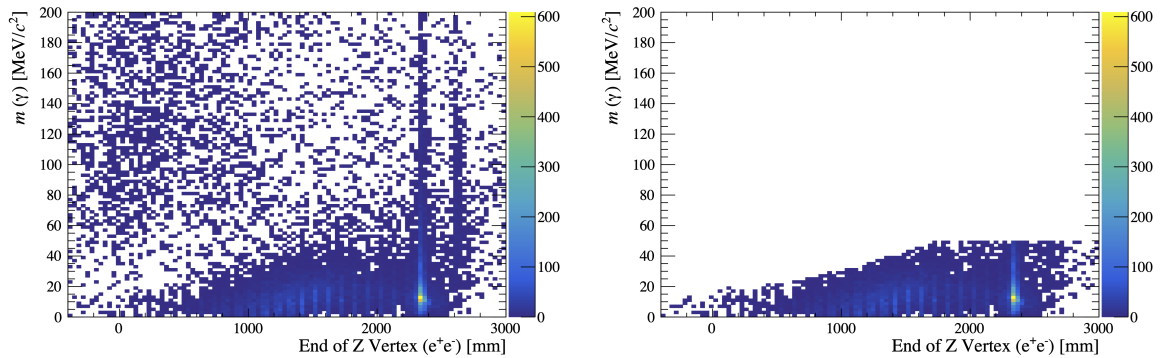


Figure 4.3. Downstream converted photon invariant-mass vs. photon Z-Vertex before (left) and after (right) the two-dimensional cut is applied.

1491 To meet the exclusivity CEP requirement in the main spectrometer, we select events that
 1492 have tracks associated with our final-state particles in an otherwise empty detector. This
 1493 enhances the CEP component of the sample by enforcing the rapidity-gap criteria within the
 1494 main spectrometer. We achieve this by selecting events with two oppositely charged, long muon
 1495 tracks necessary to reconstruct our intermediate J/ψ candidates and two downstream, oppositely
 1496 charged electron tracks used to reconstruct the converted photon. In addition, we request that
 1497 there are no tracks, backwards tracks, or track stubs in the VELO as well as no additional
 1498 long, muon or downstream tracks. The full set of offline-selection criteria are summarised in
 1499 Table 4.4.

1500 HERSCHEL selection

1501 As mentioned in Sec. 2.6, there are diffractive processes that can mimic the CEP signature where
 1502 one or both of the colliding protons dissociate outside of the main spectrometer's acceptance.
 1503 The HERSCHEL detector is thus employed to reduce this background. This is done via a
 1504 figure-of-merit variable, the HERSCHEL discriminant $\ln(\chi_{\text{HRC}}^2)$, which is related to the amount
 1505 of activity in each of the forty HERSCHEL modules. To account for spill-over effects, the
 1506 pedestal is characterised by extracting the mean (μ) and the root-mean-squared (σ) from the first
 1507 non-beam-beam event after a train of beam-beam collisions. With these calibration constants
 1508 we define the figure-of-merit value such that,

$$\ln(\chi_{\text{HRC}}^2) = \sum_{i=1}^{40} \left(\frac{x_i - \mu_i}{\sigma_i} \right)^2, \quad (4.5)$$

1509 where x_i is the HERSCHEL signal in channel i . CEP-like events will show little activity in the
 1510 HERSCHEL modules and as a result will have low values of $\ln(\chi_{\text{HRC}}^2)$ compared to events with
 1511 proton dissociation.

1512 The figure-of-merit is shown in Fig. 4.4 for the CEP $\chi_c \rightarrow J/\psi[\mu^+\mu^-]\gamma[e^+e^-]$ candidates in
 1513 2016, and combined 2015 and 2016 data. The distribution is shown before (left) and after (right)

Table 4.4. J/ψ candidate offline-selection criteria.

Variable	Cut	Units
$J/\psi [\mu^+ \mu^-]$		
$p(\mu^\pm)$	> 1000	MeV/ c
$P_{\text{Track}}^{\text{Ghost}}$	< 0.9	–
μ_1, μ_2 isMuon	True	–
$\eta(\mu_1), \eta(\mu_2)$	$\in [2, 4.5]$	–
J/ψ mass window	$ m_{J/\psi} - 3096.916 < 50$	MeV/ c^2
$\gamma[e^+e^-]$		
e^\pm track type	Downstream	–
ECAL position Δy	3σ	–
ECAL position Δy max	< 20	cm
$p_T(\gamma)$	$\in [0, 1600]$	MeV/ c
$p_T(e^\pm)$	> 0	MeV/ c
$p_T(\gamma_{\text{Brem}})$	> 75	MeV/ c
γ 2D cut	Eq. 4.2 Eq. 4.3 Eq. 4.4	–
CEP track criteria		
N^\ominus upstream tracks	0	–
N^\ominus VELO tracks	0	–
N^\ominus backward tracks	0	–
N^\ominus downstream tracks	2 (e^+e^-)	–
N^\ominus long tracks	2 ($\mu^+ \mu^-$)	–
HERSCHEL		
$\ln(\chi_{\text{HRC}}^2)$	< 5	–

1514 the rapidity-gap selection is applied. The distribution on the right corresponds to events with
 1515 the CEP-track selection applied: two long muon tracks and two downstream tracks. Before this
 1516 selection is applied we see that the sample is dominated by inelastic-like events which have high
 1517 values of $\ln(\chi_{\text{HRC}}^2)$. After the CEP criteria are applied, the mean of the distribution reduces
 1518 as the proportion of inelastic background is reduced. We select events with $\ln(\chi_{\text{HRC}}^2) < 5$.
 1519 The efficiency of the HERSCHEL figure-of-merit is studied in detail in Sec. 5.6. The Δm_{χ_c}
 1520 distribution of the final CEP χ_c selection is shown in Fig. 4.5 before and after the HERSCHEL
 1521 cut is applied.

1522 4.1.4 Simulation samples for the CEP χ_c analysis

1523 Monte Carlo simulations play an essential role in this analysis. They help us guide our decisions
 1524 on selection criteria, provide valuable information for background and signal modelling, and
 1525 help us to determine efficiencies and systematic uncertainties. More importantly, they give us
 1526 access to state-of-the-art theoretical predictions with which to compare our experimental results,

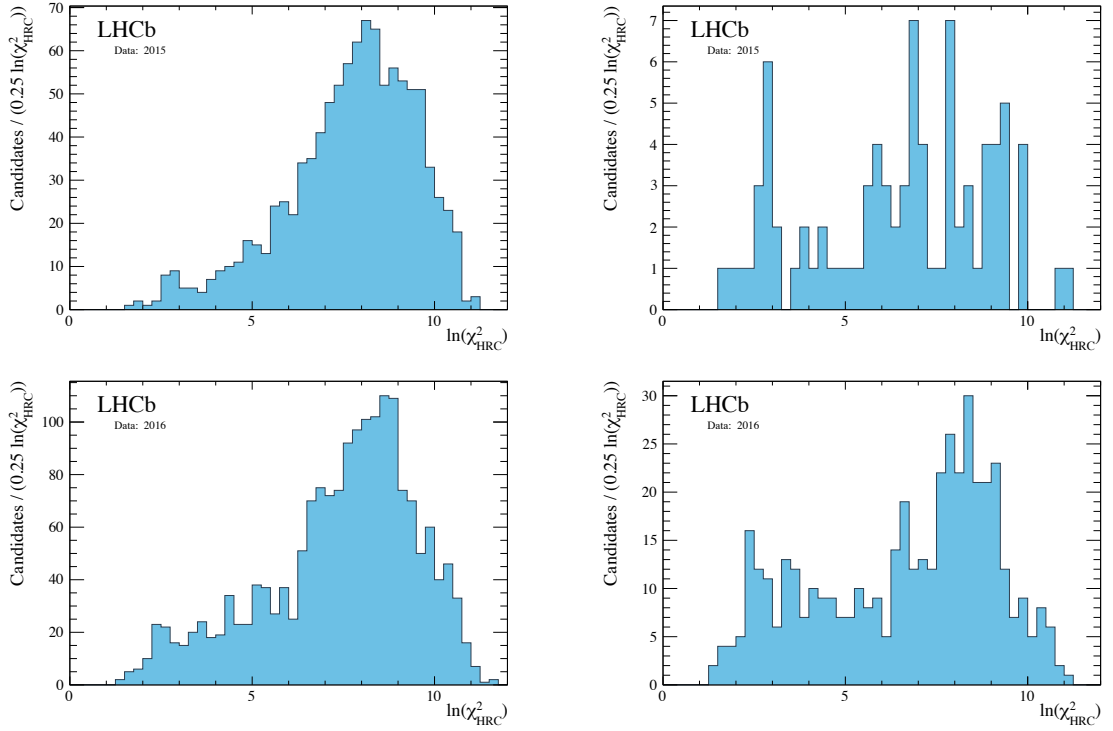


Figure 4.4. Logarithm distribution of the HERSCHEL discrimination variable, $\ln(\chi_{\text{HRC}}^2)$ for $\chi_c \rightarrow J/\psi [\mu^+ \mu^-] \gamma [e^+ e^-]$ candidates before (left) and after (right) the CEP-rapidity-gap-track selection is applied in 2015 (top) and 2016 (bottom).

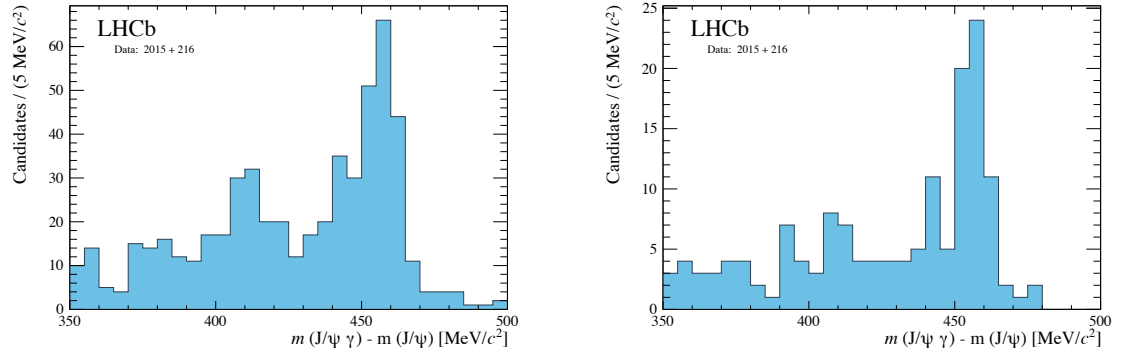


Figure 4.5. Delta-mass distribution of CEP χ_c selection before (left) and after (right) the HERSCHEL cut is applied.

1527 thus allowing us to put our understanding of fundamental physics to test. In this section, we
 1528 introduce the Monte Carlo samples used throughout this analysis.

1529 CEP χ_c Monte Carlo

1530 Approximately one million $\chi_{c1,2} \rightarrow J/\psi \gamma$ events were generated using the LHCb central-
 1531 production framework for Monte Carlo simulations for each of the χ_{c1} and χ_{c2} mesons, as well
 1532 as each of the magnet polarities using the *particle gun* (pGun) method. The number of events

1533 generated for each configuration are summarised in Table 4.5. This method is fully incorporated
 1534 into the LHCb simulations framework. It is capable of generating one or several particles
 1535 coming from the same vertex according to a specified PDG particle ID and a set of momentum
 1536 distributions taken as input. The vertex is randomly spread around the nominal-interaction
 1537 point according to a Gaussian distribution that is representative of a typical collision at LHCb.

Table 4.5. Summary of CEP $\chi_c \rightarrow J/\psi \gamma$ Monte Carlo production.

Magnet Polarity	Year	χ_{c1}	χ_{c2}
Up	2015	1,311,819	1,169,524
Up	2016	1,128,492	1,006,600
Down	2015	1,081,398	1,170,477
Down	2016	1,296,204	1,201,728

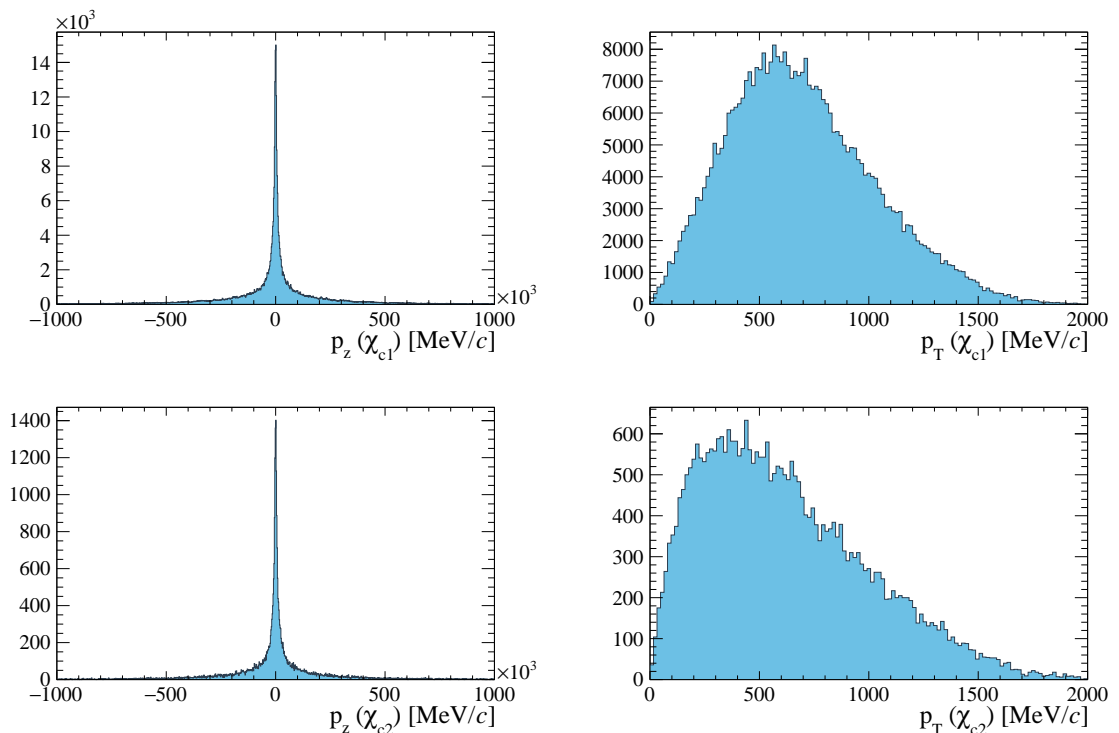


Figure 4.6. Generator-level p_z distribution (left), and p_T (right) for χ_{c1} (top), and χ_{c2} (bottom). These distributions were generated by SuperChic v2 for pp collisions with a centre-of-mass energy $\sqrt{s} = 13$ TeV.

1538 The momentum distribution of the χ_c mesons, show in Fig. 4.6, is calculated using
 1539 the SuperChic v2.03 [78–80,127] generator, described in Sec. 3.11, with the MMHT2014lo68cl
 1540 ($\alpha_S(M_Z^2) = 0.135$) [128] PDF set. We select a leading-order (LO) PDF to match the $gg \rightarrow \chi_c$
 1541 vertex calculation which is calculated to leading order by SuperChic. The generator implements
 1542 four versions of the two-channel eikonal model as described in Ref. [75] to describe proton disso-
 1543 ciation. The simulations are run with “soft-survival model four”, which describes the interaction

1544 via an effective pomeron and allows its coupling to the diffraction eigenstates to depend on the
 1545 collider energy. This model successfully describes diffraction into low and high-mass systems
 1546 at the LHC. The number of events generated for each of the run conditions is summarised in
 1547 Table 4.5.

1548 After the event generation, the χ_c mesons are forced to decay into a $J/\psi\gamma$ with the J/ψ
 1549 decaying into a pair of muons that fall within the acceptance of the main LHCb spectrometer.
 1550 The events are then propagated through the LHCb simulation framework, described in Sec. 3.11.
 1551 This includes the propagation of particles, material interactions, detector response and signal
 1552 digitisation. After digitisation the Monte Carlo can be treated as standard data and propagated
 1553 through the trigger and stripping pipe-line.

1554 $\psi(2S)$ feed-down Monte Carlo

1555 To calculate the contribution of $\psi(2S)$ feed-down background, we use a *cocktail* sample of
 1556 100,000 simulated CEP $\psi(2S) \rightarrow J/\psi X$ events generated with SuperChic for pp collisions at a
 1557 centre-of-mass energy $\sqrt{s} = 13$ TeV. Here X represents all possible decay products in a $\psi(2S)$
 1558 decays containing a J/ψ meson. The contribution of each decay is proportional to the decay
 1559 branching fractions, summarised in Table 4.6.

Table 4.6. Branching fractions of relevant $\psi(2S) \rightarrow J/\psi X$ decays, taken from the PDG [81].

Variable	Value
$\mathcal{B}(\psi(2S) \rightarrow \chi_{c0}\gamma)$	$(9.79 \pm 0.27) \%$
$\mathcal{B}(\psi(2S) \rightarrow \chi_{c1}\gamma)$	$(9.75 \pm 0.20) \%$
$\mathcal{B}(\psi(2S) \rightarrow \chi_{c2}\gamma)$	$(9.52 \pm 0.24) \%$
$\mathcal{B}(\psi(2S) \rightarrow J/\psi\gamma\gamma)$	$(3.1 \pm 1.0) \times 10^{-4}$
$\mathcal{B}(\psi(2S) \rightarrow J/\psi\eta)$	$(3.37 \pm 0.05) \%$
$\mathcal{B}(\psi(2S) \rightarrow J/\psi\pi^0)$	$(1.268 \pm 0.032) \times 10^{-3}$
$\mathcal{B}(\psi(2S) \rightarrow J/\psi\pi^0\pi^0)$	$(18.24 \pm 0.31) \%$
$\mathcal{B}(\chi_{c0} \rightarrow J/\psi\gamma)$	$(1.4 \pm 0.05) \%$
$\mathcal{B}(\chi_{c1} \rightarrow J/\psi\gamma)$	$(34.3 \pm 1.0) \%$
$\mathcal{B}(\chi_{c2} \rightarrow J/\psi\gamma)$	$(19.0 \pm 0.5) \%$
$\mathcal{B}(J/\psi(1S) \rightarrow \mu^+\mu^-)$	$(5.961 \pm 0.033) \%$
$\mathcal{B}(\eta \rightarrow \gamma\gamma)$	$(39.41 \pm 0.2) \%$
$\mathcal{B}(\pi^0 \rightarrow \gamma\gamma)$	$(98.823 \pm 0.034) \%$

1560 The $\psi(2S)$ mesons are generated according to the assumed shape for the hadronic form
 1561 factor, reflecting the size and shape of the proton described in Sec. 2.5.1. The $\psi(2S)$ mesons
 1562 are also produced according to a flat distribution in the azimuthal angle (ϕ), and restricted to
 1563 rapidities within the LHCb acceptance, $2 < \eta < 4.5$. The $\psi(2S)$ mesons are then decayed using
 1564 PYTHIA version 6.205, with the J/ψ forced to decay into a pair of muons. These events are
 1565 then processed by the LHCb detector simulation, digitisation, and reconstruction chain for 2015
 1566 run conditions.

1567 4.2 Converted-photon study: data sets, selection criteria, and simulation

1568 Having a good understanding of the photon-conversion efficiency is crucial for the success of the
 1569 CEP χ_c study. Moreover, the determination of this photon-conversion efficiency is particularly
 1570 challenging as we are dealing with low-momentum photons, a characteristic which stems from
 1571 the low-energy transfer required to avoid proton dissociation by CEP. As a result, we have
 1572 developed a new method through which we are able to measure the photon-conversion efficiency
 1573 of soft-photons at the LHCb using $D^{*0} \rightarrow D^0[K^\pm\pi^\mp]\gamma$ radiative decay, described in Sec. 5.1.
 1574 Although the approach is primarily data driven, simulation input is required for some aspects.
 1575 In the following sections we introduce the data and simulation samples required for this study,
 1576 followed by a description of the event-selection criteria. A schematic of the $D^{*0} \rightarrow D^0[K^\pm\pi^\mp]\gamma$
 1577 decay is shown in Fig. 4.7 depicting the characteristic displaced vertex of the long-lived D^0
 1578 meson.

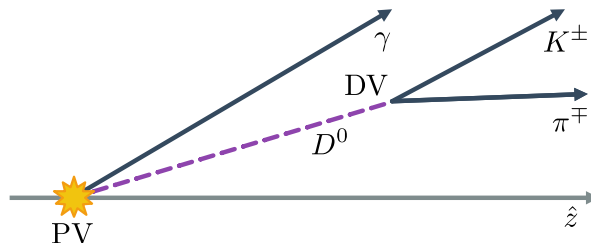


Figure 4.7. Schematic depicting the production of a $D^{*0} \rightarrow D^0[K^\pm\pi^\mp]\gamma$ meson including the primary vertex (PV) of the pp collision and the displaced vertex of the long lived D^0 .

1579 4.2.1 D^{*0} and D^0 data set

1580 We use pp collisions at a centre-of-mass energy $\sqrt{s} = 13$ TeV, collected during the 2016 run
 1581 comprising of a total integrated luminosity of $\mathcal{L}_{\text{int}}^{2016} = 1665 \text{ pb}^{-1}$. The photon-conversion
 1582 efficiency measurement requires both a $D^{*0} \rightarrow D^0[K^\pm\pi^\mp]\gamma$ and a $D^0[K^\pm\pi^\mp]$ inclusive sample.
 1583 In both samples, the D^0 candidates originate from the `Hlt2CharmHadD02KmPipTurbo` Turbo-stream
 1584 line and are selected identically. As a reminder, a Turbo stream is a data-processing stream that
 1585 uses fully reconstructed information as part of the event selection during the software-trigger
 1586 stage, as is described in Sec. 3.10.3. The online data selection pipe-line is summarised in
 1587 Table 4.7 and described in Sec. 4.2.2.

Table 4.7. Summary of the data set used in the photon-conversion-efficiency study.

Data pipeline	
L0	L0Hadron
HLT1	Hlt1TrackMVA Hlt1TwoTrackMVA
HLT2 /Turbo	Hlt2CharmHadD02KmPipTurbo

1588 The photon-conversion-efficiency study is performed exclusively with 2016 data since the
 1589 HLT2 line necessary for the study, `Hlt2CharmHadD02KmPipTurbo`, was not run during 2015. In

1590 addition, during 2016, if the requirements were met for a given trigger the entire event was
 1591 stored. Changes to the nature of the stored information means that this analysis cannot be
 1592 performed on the 2017 and 2018 data.

1593 4.2.2 D^{*0} and D^0 online-selection criteria

1594 To study the converted-photon reconstruction efficiency in an unbiased manner we make sure
 1595 that the trigger criteria are independent of the photon. The D^0 mesons are required to pass
 1596 the L0Hadron trigger decisions, either Hlt1TrackMVA or Hlt1TwoTrackMVA decision lines, and the
 1597 Hlt2CharmHadD02KmPipTurbo Turbo stream.

1598 D^{*0} and D^0 L0 trigger-selection criteria

1599 The L0Hadron trigger has two main criteria. The first selects events with a cluster in the hadronic
 1600 calorimeter, a group of 2×2 cells, with transverse energy greater than 3.7 GeV. This threshold
 1601 is chosen to meet the finite rate at which the detector channels can be read, and to select b - and
 1602 c -hadron decays, which have a characteristically high transverse energy. The threshold value
 1603 was adjusted slightly throughout the 2016 data collection period. At this stage, the transverse
 1604 energy is estimated by summing over the energy deposits, E_i , in the cluster's i^{th} cell and over all
 1605 calorimeter layers, while accounting for the polar angle, θ_i , which measured from the interaction
 1606 point such that

$$E_T = \sum_{i=1}^4 E_i \sin \theta_i. \quad (4.6)$$

1607 The second criterion limits the event multiplicity by placing a cap of 450 on the number of SPD
 1608 hits. The L0Hadron selection criteria are summarised in Table 4.8.

1609 D^{*0} and D^0 HLT1 trigger-selection criteria

1610 At the HLT1 level, the events must pass either the Hlt1TrackMVA or the Hlt1TwoTrackMVA trigger
 1611 lines [124]. In the case of Hlt1TrackMVA, at least one of the mesons from the $D^0 \rightarrow K^\pm \pi^\mp$ decay
 1612 is required to result in a well-reconstructed track, which is characterised by a large transverse
 1613 momentum and a significant impact parameter (IP) relative to the primary vertex (PV). A
 1614 schematic depicting the IP of a track is shown in Fig. 4.8 alongside other important parameters
 1615 to the discussion of the software trigger requirements.

1616 The track-reconstruction-quality requirement is met through two reconstruction-quality cuts:
 1617 $\chi_{\text{Track}}^2/\text{dof} < 2.5$ and $P_{\text{Track}}^{\text{Ghost}} < 0.2$. The former is the χ^2 per degrees-of-freedom associated
 1618 to the track fit. The latter is the probability that a track is fake, as previously described in
 1619 Sec. 4.1.3.

1620 The remainder of the criteria focuses on selecting tracks that are likely to originate from
 1621 long-lived particles, such as the D^0 meson. This is achieved by identifying potential displaced
 1622 vertices (DV). A fit of the PV is performed with and without the track considered and the
 1623 difference between these fits results in a χ_{IP}^2 value. Particles originating from secondary vertices

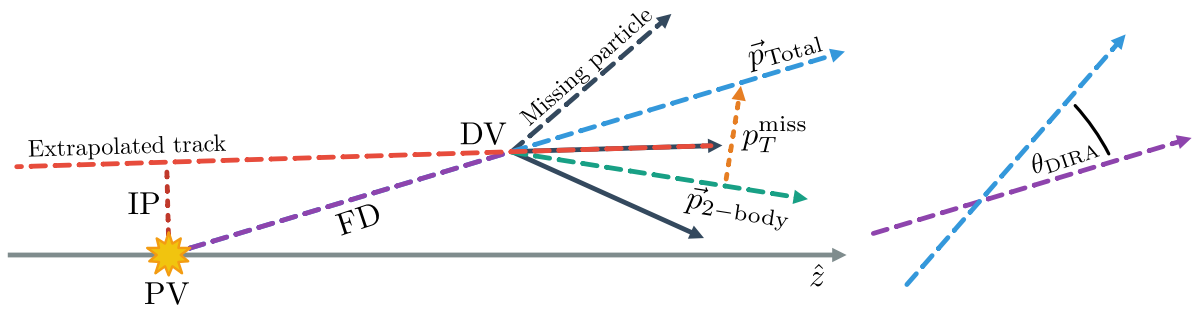


Figure 4.8. Schematic depicting parameters of events with long-lived particles produced at the primary vertex (PV in yellow), which decays after a flight distance (FD in dashed purple) into a three-particle final state (in black) with a summed four-momentum \vec{p}_{Total} and displaced vertex (DV). Two of the particles are reconstructed (solid black) with summed four-momentum $\vec{p}_{2\text{-body}}$ (dashed green) while one particle is not reconstructed (dashed black) with transverse momentum p_T^{miss} . The track of one of the reconstructed particles is extrapolated (dashed red) and the shortest distance to the PV, known as the impact parameter (IP), is marked (dashed-dark red). The angle between the \vec{p}_{Total} and the vector formed by the PV and the DV, known as the directional angle θ_{DIRA} , is shown on the right.

1624 tend to have large χ_{IP}^2 values. A two-dimensional cut of this variable is then performed in
 1625 tandem with the tracks' transverse momentum such that

$$p_T > 25 \quad \text{and} \quad \chi_{\text{IP}}^2 > 7.4, \quad (4.7)$$

1626 OR

$$1 < p_T < 25 \quad \text{and} \quad \chi_{\text{IP}}^2 > \ln(7.4) + \frac{1}{(p_T - 1)^2} + 1.2 \left(1 - \frac{p_T}{25}\right), \quad (4.8)$$

1627 where the transverse momentum is measured in GeV/c.

1628 Alternatively, both of the hadrons from the D^0 decay can meet the criteria of
 1629 Hlt1TwoTrackMVA, which requires two long, oppositely charged, well-reconstructed, high-
 1630 momentum tracks. We define well-reconstructed tracks according to the track fit χ^2 , requiring
 1631 $\chi_{\text{Track}}^2/\text{dof} < 2.5$. A cut is applied to the track momentum, $p > 5$ GeV/c, the transverse
 1632 momentum, $p_T > 500$ MeV/c, and the sum of the transverse momentum of the two tracks,
 1633 $\sum p_T = p_T(h^+) + p_T(h^-) > 2$ GeV/c. The two tracks are required to originate from a DV by
 1634 considering at their displacement relative to the PV, $\chi_{\text{IP}}^2 > 2.5$.

1635 A set of cuts is also applied to the combined h^+h^- system. The D^0 candidate is required to
 1636 have a rapidity within the acceptance of the main spectrometer, $2 < \eta < 5$. The mass of D^0
 1637 meson candidates, m_{D^0} , is corrected with respect to particle-flight direction such that

$$m_{\text{corr}} \equiv \sqrt{m_{D^0}^2 + |p_T^{\text{miss}}|^2 + p_T^{\text{miss}},} \quad (4.9)$$

1638 where p_T^{miss} is the missing momentum transverse to the direction of flight of the D^0 . This
 1639 correction is used to account for missing-transverse momentum from partially reconstructed

1640 decays, such as those that include neutrinos, which might result in a lower-mass reconstruction
 1641 of the parent particle. The directional angle, θ_{DIRA} , is the angle between the line drawn from
 1642 the PV to the DV, and the four-momentum sum of the D^0 candidate's decay products. We
 1643 expect θ_{DIRA} to be zero for particles originating from primary vertices, and non-zero for both
 1644 secondary decays and partially reconstructed decays. At this stage, the angle is simply expected
 1645 to be greater than zero which prevents the DV from being behind the PV. The quality of the
 1646 vertex fit using the two tracks is evaluated by requesting a $\chi_{\text{Vertex}}^2 < 10$.

1647 Additionally, a boosted-decision-tree (BDT) classifier is used with the following inputs: the
 1648 flight distance between the PV and the DV (χ_{FD}^2), $\sum p_{\text{T}}$, the number of tracks with $\chi_{\text{IP}}^2 > 16$,
 1649 and the χ_{DV}^2 of the displaced-vertex fit. A threshold of 0.96 is set on the BDT figure-of-merit.
 1650 The entire selection criteria of these trigger lines are specified in Table 4.8.

1651 D^{*0} and D^0 HLT2 trigger-selection criteria

1652 At the HLT2 level, events are selected by the Hlt2CharmHadD02KmPipTurbo line, which is designed
 1653 to identify and select $D^0 \rightarrow K^\pm \pi^\mp$ mesons with displaced vertices. This selection tightens the
 1654 minimum transverse-momentum requirement of the hadron tracks to 800 MeV/ c and one of the
 1655 daughters is required to have p_{T} larger than 1500 MeV/ c . Particle identification is applied to
 1656 the K^\pm and π^\pm candidates such that the log-likelihood difference relative to the pion hypothesis
 1657 (described in Eq. 3.10.2) is $\Delta \log \mathcal{L}_{K-\pi} > 5$ and $\Delta \log \mathcal{L}_{K-\pi} < 5$, respectively. The efficiency
 1658 and fake rate for this cut is shown in Fig. 4.9 as a function of the meson's momentum.

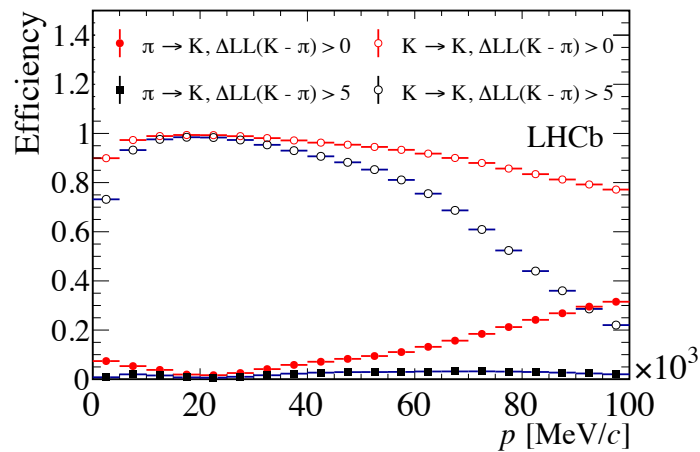


Figure 4.9. Efficiency and fake rate of the RICH identification for 2016 data. Reproduced from [124].

1659 A series of cuts associated with the D^0 DV is then applied. The χ^2 distance between a track
 1660 and the PV is expected to be greater than four, the distance of closest approach (DOCA) of each
 1661 track to the DV is required to be within 0.1 mm, and the minimum χ_{FD}^2 -distance between the
 1662 PV and the DV is required to be greater than 25. The contribution of secondary charm mesons
 1663 produced from B -meson decays is low and is reduced to negligible levels by requiring that the D^0

Table 4.8. Summary of the trigger-level-selection criteria used for the reconstruction of $D^0 \rightarrow K^\pm \pi^\mp$ and $D^*(2007)^0 \rightarrow D^0[K^\pm \pi^\mp] \gamma[e^+ e^-]$ decay modes for 2016 data .

Variable	Cuts	Units
L0Hadron		
$E_T(h^\pm)$	> 3.7	GeV
SPD Hits	< 450	–
Prescale	1	–
HLT1TrackMVA		
$p_T(h^\pm), \chi_{\text{IP}}^2$	Eq. 4.7 Eq. 4.8	GeV/c, –
$\chi_{\text{Track}}^2/\text{DoF}$	< 2.5	–
$P_{\text{Track}}^{\text{Ghost}}$	< 0.2	–
HLT1TwoTrackMVA		
$p(h^\pm)$	> 5000	MeV/c
$p_T(h^\pm)$	> 500	MeV/c
χ^2 track distance to PV	> 4	–
$\Delta \log \mathcal{L}_{K-\pi}(K^\pm)$	> 5	–
$\Delta \log \mathcal{L}_{K-\pi}(\pi^\pm)$	< 5	–
χ_{IP}^2	> 2.5	MeV/c
$\chi_{\text{Track}}^2/\text{DoF}$	> 4.0	MeV/c
$\eta(h^+ h^-)$	$\in [2, 5]$	–
m_{corr}	$\in [1, 10^6]$	GeV/c ²
θ_{DIRA}	> 0	–
Σp_T	> 2	GeV/c
Vertex χ^2	< 10	–
BDT threshold	0.96	–
HLt2CharmHadD02KmPipTurbo		
$p(h^\pm)$	> 5000	MeV/c
$p_T(h^\pm)$	> 800	MeV/c
$p_T(h^+) \parallel p_T(h^-)$	> 1500	MeV/c
$K^\pm \pi^\mp$ pair DOCA	< 0.1	mm
χ^2 track distance to PV	> 4	–
$D^0 \chi_{\text{FD}}^2$	> 25	–
$\cos(\theta_{\text{DIRA}})$	< 17.3	mrاد
Vertex χ^2	< 10	–
$p_T(D^0)$	> 2000	MeV/c
$m(D^0)$	$\in [1715, 2015]$	MeV/c ²

1664 candidate point back to the primary vertex. To this end, the cosine of the angle θ_{DIRA} (described
1665 above) is capped at 17.3 mrad. Finally, the minimum transverse momentum of the D^0 candidate
1666 is set at 2 GeV/c and its invariant-mass window is limited to the $1715 < m(D^0) < 2015$ MeV/c²
1667 range. The selection criteria of these trigger lines are specified in Table 4.8.

1668 4.2.3 D^{*0} and D^0 offline-selection criteria

1669 Unlike the CEP χ_c sample, events processed by Turbo are directly available for analysis and
 1670 stripping is not required. To ensure that the data sample is not biased, we require that the
 1671 trigger decision is based on the D^0 meson, or three daughter hadrons, and is independent of
 1672 the photon reconstruction for all L0 and HLT1 physics lines. The offline-selection criteria are
 1673 summarised in Table 4.9.

1674 The D^0 invariant-mass is restricted to a $50 \text{ MeV}/c^2$ window centered around the D^0 nominal
 1675 mass. The transverse momentum of the D^0 mesons is constrained within the range of 2 to 15
 1676 GeV/c and a fiducial cut is applied such that the D^0 mesons have a pseudorapidity between 2
 1677 and 4.5. At this point the D^0 selection is complete and approximately 139 million D^0 candidates
 1678 pass the selection. Their invariant-mass distribution is shown in Fig. 4.10. However in the case
 1679 of D^{*0} we apply an additional set of selections associated with the photon and the reconstructed
 1680 D^{*0} candidate.

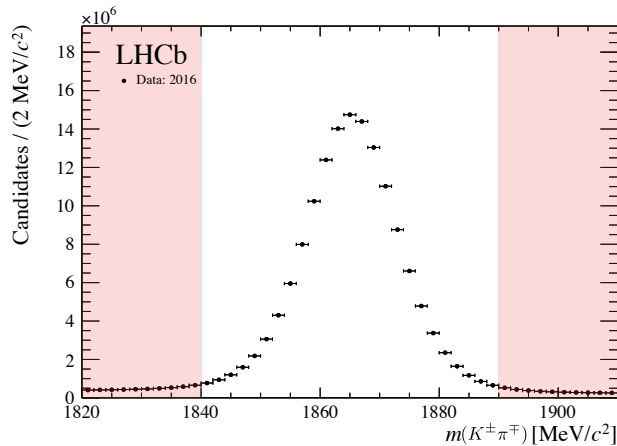
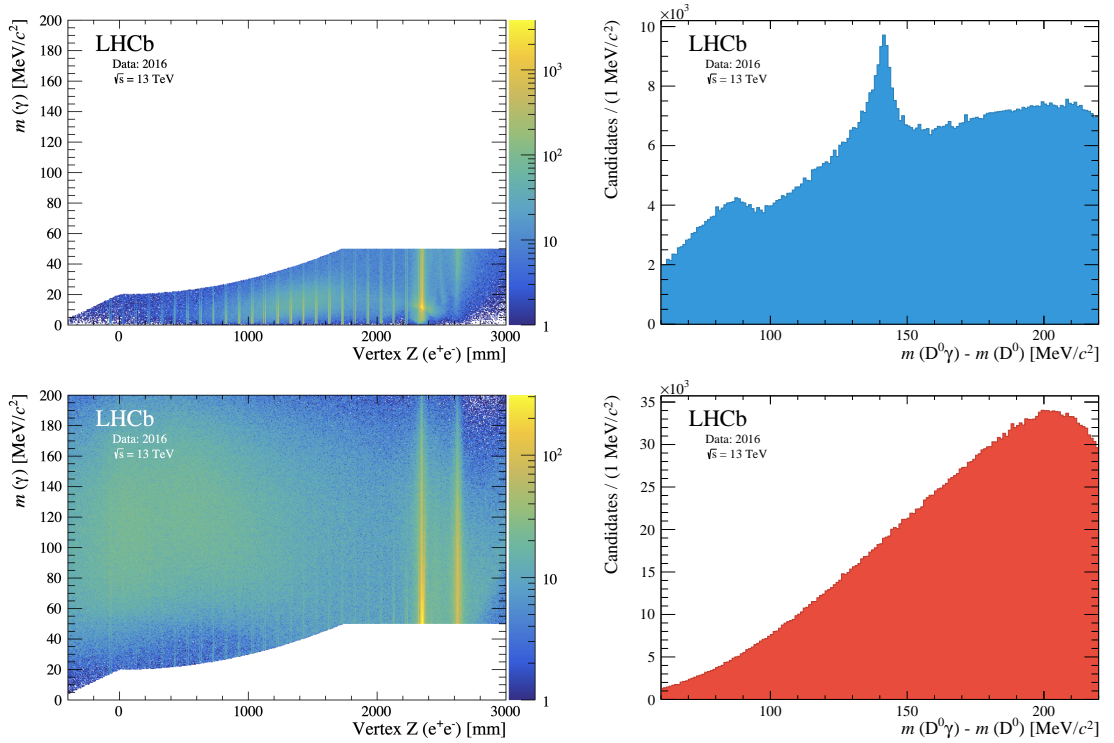


Figure 4.10. Invariant-mass distribution of D^0 candidates. The veto windows are highlighted in red.

1681 To form the D^{*0} candidates, the converted photons are selected and reconstructed with
 1682 the same requirements as the CEP χ_c meson analysis, see Sec. 4.1.3. The effects of the two-
 1683 dimensional cuts are shown in Fig. 4.11, along with the accepted (blue) and rejected (red)
 1684 $m(D^0\gamma) - m(D^0)$ distributions showing that this cut is effective at removing background.
 1685 The two vertical lines around 2300 and 2600 mm correspond to the two TT tracker planes,
 1686 where most of the conversions occur. Events to the left of the nominal interaction point
 1687 are clearly non-physical and tend to have large measurement uncertainties. A comparison of
 1688 truth-matched Monte Carlo and data shows that events with high $m(e^+e^-)$ and $z_{\gamma\text{Conv}}$ are
 1689 combinatorial background. High $m(e^+e^-)$ values correspond to background or they must be
 1690 poorly reconstructed signal. The transverse momentum of the converted photons is capped at
 1691 a maximum of 1600 MeV/c , which fully covers the kinematic range of the photons in the χ_c
 1692 sample.

Table 4.9. Offline-selection criteria for $D^{*0} \rightarrow D^0[K^\pm\pi^\mp]\gamma[e^+e^-]$ and $D^0 \rightarrow K^\pm\pi^\mp$ samples.

Variable	Cut	Units
$D^0[K^\pm\pi^\mp]$		
$p_T(D^0)$	$\in [2, 15]$	GeV/c
$\eta(D^0)$	$\in [2, 4.5]$	–
$m(D^0)$	$\in [1840, 1890]$	MeV/c ²
$\gamma[e^+e^-]$		
e^\pm track type	Downstream	–
ECAL position Δy	3σ	–
ECAL position Δy max	< 20	cm
$p_T(e^+e^-)$	< 1600	MeV/c
$p_T(e^\pm)$	> 0	MeV/c
γ 2D cut	Eq. 4.2 Eq. 4.3 Eq. 4.4	–
D^{*0}		
$m(D^{*0})$	$\in [1900, 2100]$	MeV/c ²

**Figure 4.11.** Two dimensional cut of the di-electron invariant mass vs. photon Z-Vertex (left) and delta-mass distribution (right) of selected (top) and rejected (bottom) D^{*0} meson candidates from the 2016 data set, based on a two-dimensional cut.

1693 4.2.4 Simulation samples for converted-photon study

1694 This photon-conversion-efficiency calculation requires three different Monte Carlo samples. The
 1695 first sample consists of a centrally produced D^{*0} Monte Carlo generated with PYTHIA 6 [120] for
 1696 pp collisions at a centre-of-mass energy $\sqrt{s} = 13$ TeV under 2015 run conditions for each of the
 1697 magnet polarities. In this sample the D^{*0} mesons are forced to decay into $D^0\pi^0$ and $D^0\gamma$ but
 1698 only the latter component is used for this study. Meanwhile, the D^0 mesons are forced to decay
 1699 into $K^\pm\pi^\mp$. The sample consists of 5,840,161 events, of which 2,943,685 are simulated with
 1700 the magnetic field of the di-pole magnet pointing up and 2,896,476 events with the magnetic
 1701 field pointing down. This sample is used to validate the method by which we calculate the
 1702 photon transverse-momentum dependence of the total number of D^{*0} mesons, described in
 1703 Sec. 5.1.5.

1704 Two additional D^{*0} Monte Carlo samples are produced with the pGun method, described
 1705 in Sec. 4.1.4. The kinematic phase space for the D^{*0} mesons was calculated using PYTHIA 8
 1706 for its production in pp collisions at a centre-of-mass energy of $\sqrt{s} = 13$ TeV. The events are
 1707 decayed with EvtGen and then processed by the LHCb simulation framework under 2016 run
 1708 conditions. The first D^{*0} Monte Carlo sample consists of 64 million events containing the decay
 1709 $D^{*0} \rightarrow D^0[K^\pm\pi^\mp]\gamma$, with equal proportions for each magnet polarity setting. Although, we
 1710 already have the centrally produced Monte Carlo sample with this decay mode described above,
 1711 it is statistically limited. As we will see, the photon-conversion efficiency for low-momentum
 1712 photons is very low. As a result, we are unable to use that sample to extract reliable invariant-
 1713 mass-difference distributions for different photon transverse-momentum ranges. We also use the
 1714 generator-level information to model the photon transverse-momentum dependence of the total
 1715 number of D^{*0} mesons, as described in Sec. 5.1.5. The second sample consists of 84 million
 1716 $D^{*0} \rightarrow D^0[K^\pm\pi^\mp]\pi^0[\gamma\gamma]$ events, with equal parts for each magnet polarity setting. This sample
 1717 is used to model the background for our $D^{*0} \rightarrow D^0[K^\pm\pi^\mp]\gamma$ selection where one of the photons
 1718 from the π^0 decay is not reconstructed.

CHAPTER 5

Efficiency determination

1719

1720

1721

1722 In this chapter we present a series of studies used to determine reconstruction and selection
 1723 efficiencies at different stages of the CEP χ_c analysis. In Sec. 5.1 we present the photon-
 1724 conversion-efficiency study as a function of the transverse momentum of the photon as well as its
 1725 dependence on the event multiplicity, followed by the study of the efficiency associated with the
 1726 muon reconstruction and selection in Sec. 5.2. The efficiency of the J/ψ mass-window and the
 1727 χ_c mass-difference-window cut are discussed in Sec. 5.3 and Sec. 5.4, respectively. The efficiency
 1728 of the low-multiplicity requirement at the hardware-trigger level is discussed in Sec. 5.5, followed
 1729 by a study of the performance of the HERSCHEL figure-of-merit in Sec. 5.6.3.

1730 5.1 Determination of the photon-conversion efficiency

1731 Although the combined conversion probability and reconstruction efficiency of photons ($\epsilon_{\gamma \rightarrow e^+e^-}$)
 1732 at the LHCb experiment has been studied in the past, a couple of factors make the determination
 1733 for photons from CEP events non-trivial. Previous $\epsilon_{\gamma \rightarrow e^+e^-}$ studies have not been performed for
 1734 photons with transverse momenta as low as those observed in the CEP χ_c selection. Furthermore,
 1735 $\epsilon_{\gamma \rightarrow e^+e^-}$ has a significant dependence on the transverse momentum of the photon, which makes
 1736 the extrapolation of previous measurements into our soft regime unreliable. Previous studies
 1737 have been performed on hard-scattering events [129, 130]. Although these types of events provide
 1738 a statistical advantage, they are characterised by a high detector occupancy. In comparison, the
 1739 low-multiplicity of CEP events provides a favourable environment for the reconstruction of the
 1740 electron tracks associated with the photon, which should result in a higher efficiency for a given
 1741 photon's transverse momentum.

1742 5.1.1 Strategy for the determination of the photon-conversion efficiency

1743 The probability for a photon conversion to occur and the efficiency for it to be reconstructed by
 1744 the LHCb spectrometer can be written as follows:

$$\epsilon_{\gamma \rightarrow e^+e^-} = \frac{N_{\gamma \rightarrow e^+e^-}}{N_{\gamma \text{All}}}, \quad (5.1)$$

1745 where $N_{\gamma \rightarrow e^+e^-}$ is the number of photons within a sample that undergo photon conversion into
 1746 an electron-positron pair and are fully reconstructed by LHCb, while $N_{\gamma \text{All}}$ is the initial number
 1747 of photons in the same data sample, whether or not they have converted.

1748 To take advantage of LHCb's excellent performance at reconstructing charmed mesons, we
 1749 use a data-driven approach using $D^*(2007)^0$ mesons to calculate the photon-conversion efficiency.
 1750 In particular, we use $D^*(2007)^0 \rightarrow D^0[K^\pm\pi^\mp]\gamma[e^+e^-]$ decays. Henceforth, D^{*0} should be taken
 1751 to mean $D^*(2007)^0$ mesons, and when we speak of D^{*0} candidates it should be assumed that
 1752 we speak of $D^{*0} \rightarrow D^0[K^\pm\pi^\mp]\gamma$ decays. Of course, there is some inefficiency associated with
 1753 the reconstruction of the $D^0 \rightarrow K^\pm\pi^\mp$ decay itself. Thus, we seek to measure

$$\epsilon_{\gamma \rightarrow e^+e^-} = \frac{N_{\text{Conv}}(D^{*0})}{N_{\text{All}}(D^{*0}|D^0)}, \quad (5.2)$$

1754 where $N_{\text{Conv}}(D^{*0})$ denotes the number of reconstructed and selected D^{*0} mesons using down-
 1755 stream converted photons, and $N_{\text{All}}(D^{*0}|D^0)$ denotes the number of D^{*0} decays in which the D^0
 1756 mesons would be reconstructed and selected given the criteria presented in Sec. 4.2, independent
 1757 of the photon detection.

1758 To calculate the number of D^{*0} mesons produced in our sample, we invoke isospin symmetry
 1759 and take advantage of the results from a previous LHCb measurement of $D^{*+} \rightarrow D^0[K^\pm\pi^\mp]\pi^+$
 1760 and $D^0 \rightarrow K^\pm\pi^\mp$ production at $\sqrt{s} = 13$ TeV [131]. By isospin symmetry we expect the same
 1761 number of D^{*0} as D^{*+} to be produced in the LHCb detector. Therefore, we can use the number
 1762 of all D^0 mesons in the sample $N(D^0)$ to calculate $N_{\text{All}}(D^{*0}|D^0)$ within the LHCb acceptance
 1763 such that,

$$N_{\text{All}}(D^{*0}|D^0) = N(D^0) \cdot \frac{\mathcal{B}(D^{*0} \rightarrow D^0\gamma)}{\mathcal{B}(D^{*+} \rightarrow D^0\pi^+)} \cdot r(D^{*+}/D^0), \quad (5.3)$$

1764 where $\mathcal{B}(D^{*0} \rightarrow D^0\gamma) = (35.3 \pm 0.9)\%$ and $\mathcal{B}(D^{*+} \rightarrow D^0\pi^+) = (67.7 \pm 0.5)\%$ are the branching
 1765 fractions of their corresponding decays as given by the PDG [81], and $r(D^{*+}/D^0)$ is the ratio of
 1766 the cross-sections times their corresponding branching fraction of $D^{*+} \rightarrow D^0[K^\pm\pi^\mp]\pi^+$ and
 1767 $D^0 \rightarrow K^\pm\pi^\mp$ as calculated in the LHCb paper referenced above.

1768 The ratio $r(D^{*+}/D^0)$ has been measured in bins of the charmed meson rapidity, in the
 1769 $2.0 < y < 4.5$ range, and its transverse momentum, in the $p_T < 15$ GeV/ c range. These results
 1770 are tabulated in Table 5.1 and are plotted in Fig. 5.1. Here we observe evidence of significant
 1771 variation with the transverse momentum of D^0 , but less so with its rapidity. We weight these
 1772 $r(D^{*+}/D^0)$ values by the transverse momentum and rapidity distributions of the D^0 mesons in
 1773 our inclusive D^0 selection, to calculate a $r(D^{*+}/D^0)$ central value that is representative of our
 1774 sample.

1775 The average transverse momentum of a photon in $D^{*0} \rightarrow D^0\gamma$ decays is higher than that
 1776 of photons from CEP $\chi_c \rightarrow J/\psi\gamma$ decays. Since the kinematics of the photon in D^{*0} decays
 1777 are strongly correlated to the kinematics of the D^0 meson, we are able to better match the
 1778 kinematics of the D^{*0} photons to those in our CEP χ_c sample by placing an upper limit cut on
 1779 the transverse momentum of the D^0 . As a result, we require that the transverse momentum of

Table 5.1. The ratios of differential production cross-section-times-branching-fraction for prompt D^{*+} and D^0 mesons in bins of (p_T, y) . The first uncertainty is statistical and the second is systematic. All values are given in percent [131].

p_T [GeV/c]	y				
	[2.0, 2.5]	[2.5, 3.0]	[3.0, 3.5]	[3.5, 4.0]	[4.0, 4.5]
[0.0 – 1.0]	-	-	-	-	$21.9^{+3.0+6.7}_{-3.0-6.3}$
[1.0 – 1.5]	-	$18.3^{+0.8+2.0}_{-0.8-2.0}$	$22.6^{+0.3+1.3}_{-0.3-1.6}$	$20.3^{+0.3+1.4}_{-0.3-1.5}$	$25.5^{+0.8+3.7}_{-0.8-3.1}$
[1.5 – 2.0]	-	$26.3^{+0.5+1.8}_{-0.4-1.6}$	$26.4^{+0.2+1.3}_{-0.2-1.9}$	$24.7^{+0.3+1.5}_{-0.3-1.9}$	$25.5^{+0.6+2.5}_{-0.6-2.0}$
[2.0 – 2.5]	$26.8^{+2.4+5.7}_{-2.4-6.0}$	$26.5^{+0.3+1.9}_{-0.3-1.1}$	$27.4^{+0.2+1.3}_{-0.2-1.8}$	$25.7^{+0.2+1.6}_{-0.2-1.6}$	$25.5^{+0.5+2.6}_{-0.5-2.1}$
[2.5 – 3.0]	$26.8^{+0.9+2.9}_{-0.9-3.1}$	$27.1^{+0.3+1.2}_{-0.3-1.7}$	$27.0^{+0.2+1.6}_{-0.2-1.5}$	$26.0^{+0.2+1.7}_{-0.3-1.7}$	$26.6^{+0.6+1.8}_{-0.6-2.0}$
[3.0 – 3.5]	$27.2^{+0.7+2.2}_{-0.7-2.5}$	$28.3^{+0.2+1.2}_{-0.2-1.9}$	$28.6^{+0.2+1.7}_{-0.2-1.4}$	$25.5^{+0.3+1.8}_{-0.3-1.8}$	$25.9^{+0.6+2.7}_{-0.6-2.2}$
[3.5 – 4.0]	$28.9^{+0.6+2.1}_{-0.6-2.5}$	$29.8^{+0.3+1.4}_{-0.3-2.1}$	$28.9^{+0.2+1.8}_{-0.2-1.4}$	$27.2^{+0.3+1.9}_{-0.3-1.7}$	$27.9^{+0.8+2.7}_{-0.8-2.7}$
[4.0 – 5.0]	$28.8^{+0.4+1.4}_{-0.4-2.3}$	$29.2^{+0.2+1.3}_{-0.2-2.0}$	$28.5^{+0.2+1.6}_{-0.2-1.4}$	$28.2^{+0.3+2.0}_{-0.3-1.5}$	$30.2^{+0.9+2.3}_{-0.9-2.2}$
[5.0 – 6.0]	$27.3^{+0.4+1.3}_{-0.4-2.3}$	$29.4^{+0.2+1.4}_{-0.2-2.0}$	$29.9^{+0.3+1.7}_{-0.3-1.3}$	$32.2^{+0.4+2.3}_{-0.5-1.6}$	$31.5^{+2.1+4.1}_{-2.0-3.7}$
[6.0 – 7.0]	$30.9^{+0.5+1.8}_{-0.5-2.6}$	$30.8^{+0.3+1.6}_{-0.3-2.1}$	$29.8^{+0.4+1.7}_{-0.4-1.5}$	$29.5^{+0.6+2.2}_{-0.6-2.2}$	$38.0^{+10.0+24}_{-8.0-17.0}$
[7.0 – 8.0]	$33.1^{+0.7+2.0}_{-0.7-2.9}$	$29.6^{+0.4+1.7}_{-0.4-2.3}$	$31.7^{+0.5+2.2}_{-0.5-1.6}$	$36.8^{+1.3+4.4}_{-1.2-4.3}$	-
[8.0 – 9.0]	$32.3^{+0.8+2.2}_{-0.8-2.9}$	$29.9^{+0.5+1.9}_{-0.5-2.3}$	$31.4^{+0.7+2.8}_{-0.7-1.7}$	$28.0^{+1.8+4.1}_{-1.7-3.4}$	-
[9.0 – 10.0]	$21.8^{+0.7+1.2}_{-0.7-1.7}$	$30.9^{+0.7+1.6}_{-0.7-2.1}$	$30.2^{+0.8+1.6}_{-0.8-1.5}$	$40.6^{+4.8+6.1}_{-4.3-7.0}$	-
[10.0 – 11.0]	$31.8^{+1.2+1.6}_{-1.1-2.2}$	$32.1^{+0.9+1.6}_{-0.9-2.1}$	$34.6^{+1.4+1.8}_{-1.3-1.8}$	$34.0^{+10.0+13.0}_{-8.0-11.0}$	-
[11.0 – 12.0]	$30.8^{+1.3+1.6}_{-1.4-2.5}$	$30.16^{+1.1+1.4}_{-1.1-2.0}$	$31.2^{+1.8+1.6}_{-1.7-1.7}$	-	-
[12.0 – 13.0]	$33.0^{+1.8+2.1}_{-1.8-3.1}$	$32.2^{+1.4+1.6}_{-1.4-2.2}$	$32.8^{+2.5+2.2}_{-2.4-1.8}$	-	-
[13.0 – 14.0]	$34.0^{+2.1+1.8}_{-2.1-3.0}$	$27.6^{+1.6+1.5}_{-1.6-2.0}$	$41.2^{+4.7+3.1}_{-4.3-3.4}$	-	-
[14.0 – 15.0]	$29.7^{+2.5+1.9}_{-2.4-2.4}$	$34.0^{+2.5+2.3}_{-2.3-2.5}$	$27.8^{+5.6+6.7}_{-4.8-5.7}$	-	-

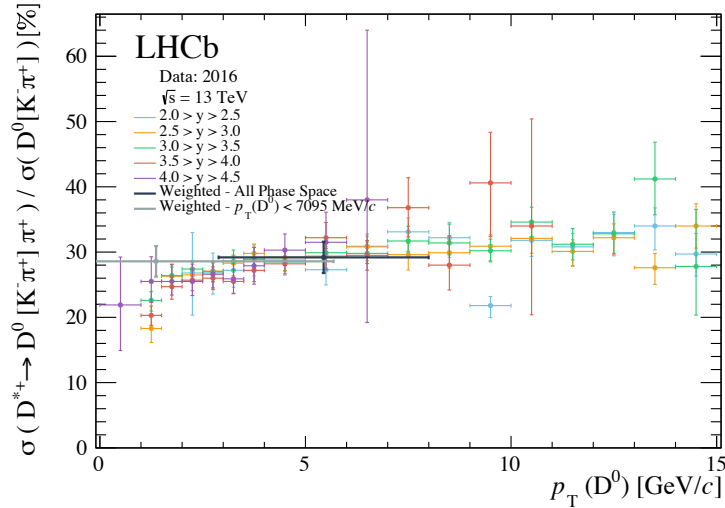


Figure 5.1. The ratios of differential production cross-section-times-branching-fraction for prompt D^{*+} and D^0 mesons as a function of the D^0 meson's transverse momentum and rapidity [131].

1780 the D^0 mesons used in the ratio calculation be less than 7.095 GeV/c in order to match the
 1781 mean of the transverse-momentum distribution of the photons in the χ_c sample.

1782 In a few cases, near the edge of phase space, the uncertainties in the measured cross-section
 1783 ratios are larger than ten percent. To reduce the effect of these larger uncertainties, we average
 1784 the value of that (p_T, η) bin with that of the nearest bin in p_T , then merge the result into
 1785 a single larger bin. Any event with kinematics for which a ratio has not been calculated is
 1786 assigned the value of the nearest neighbour in p_T .

1787 This procedure results in a value of $r(D^{*+}/D^0) = (28.6 \pm 2.3)\%$, which then can be used in
 1788 Eq. 5.3 as part of the photon-conversion efficiency calculation. The value is marked in Fig. 5.1
 1789 in grey. Here we assign a systematic uncertainty of a relative eight percent which is the same
 1790 as determined for the average ratio quoted in the prompt-charm paper. (This compares to
 1791 $(29.19 \pm 2.4)\%$, marked in Fig. 5.1 in black, where the ratio is averaged over the entire D^0 p_T
 1792 kinematic range, 1.8 to 15.0 GeV/c. In this figure, the error bar along the x -axis for these two
 1793 values are set by the root-mean-squared value of the D^0 transverse-momentum distribution used
 1794 in each calculation.)

1795 5.1.2 Study of the photon acceptance in the calibration and signal samples

1796 To ensure photons in our D^{*0} calibration sample are representative of those in our CEP χ_c
 1797 sample in all phase space, we compare the density plots of the photons' pseudorapidity and
 1798 the logarithm of the photons' transverse momentum. We start with the photons in the D^{*0}
 1799 sample in Fig. 5.2 (top left) where we observe a clear boundary in the photons' phase space.
 1800 Low-momentum electrons tend to be deflected out of the spectrometer's acceptance. The
 1801 electrons closest to the detector's edge are more likely to be expelled from the detector. This
 1802 boundary can be described empirically with a line overlaid in red such that,

$$\log(p_T(\gamma)) = -0.46 \cdot \eta(\gamma) + 4.1. \quad (5.4)$$

1803 From the χ_c signal sample (top right), we see that all events fall above this boundary and
 1804 their phase space is well represented by the calibration sample. We observe the same in fully
 1805 reconstructed and truth-matched Monte Carlo events for χ_{c1} (middle left) and χ_{c2} (middle right)
 1806 mesons. The differences in the density-plot distributions between the CEP χ_c data sample and
 1807 the Monte Carlo are attributed to both reconstruction and resolution differences between data
 1808 and Monte Carlo, specifically due to the bremsstrahlung correction and the contribution of
 1809 inelastic background events in the data which typically have higher energies. In addition, we
 1810 look at the generator-level phase-space distribution of the photon in Monte Carlo within our
 1811 fiducial acceptance, given the reconstruction of a J/ψ . To do this, we reconstruct only the J/ψ
 1812 mesons from the CEP χ_c Monte Carlo using the same criteria pertaining to the J/ψ from the
 1813 CEP χ_c selection and save the generator-level information of the accompanying photon. The
 1814 phase-space-density plots of these photons are shown in Fig. 5.2 for χ_{c1} (bottom left) and χ_{c2}
 1815 (bottom right) Monte Carlo, from which we find that approximately 46 (49) percent of χ_{c1} (χ_{c2})
 1816 events fall below this phase space boundary.

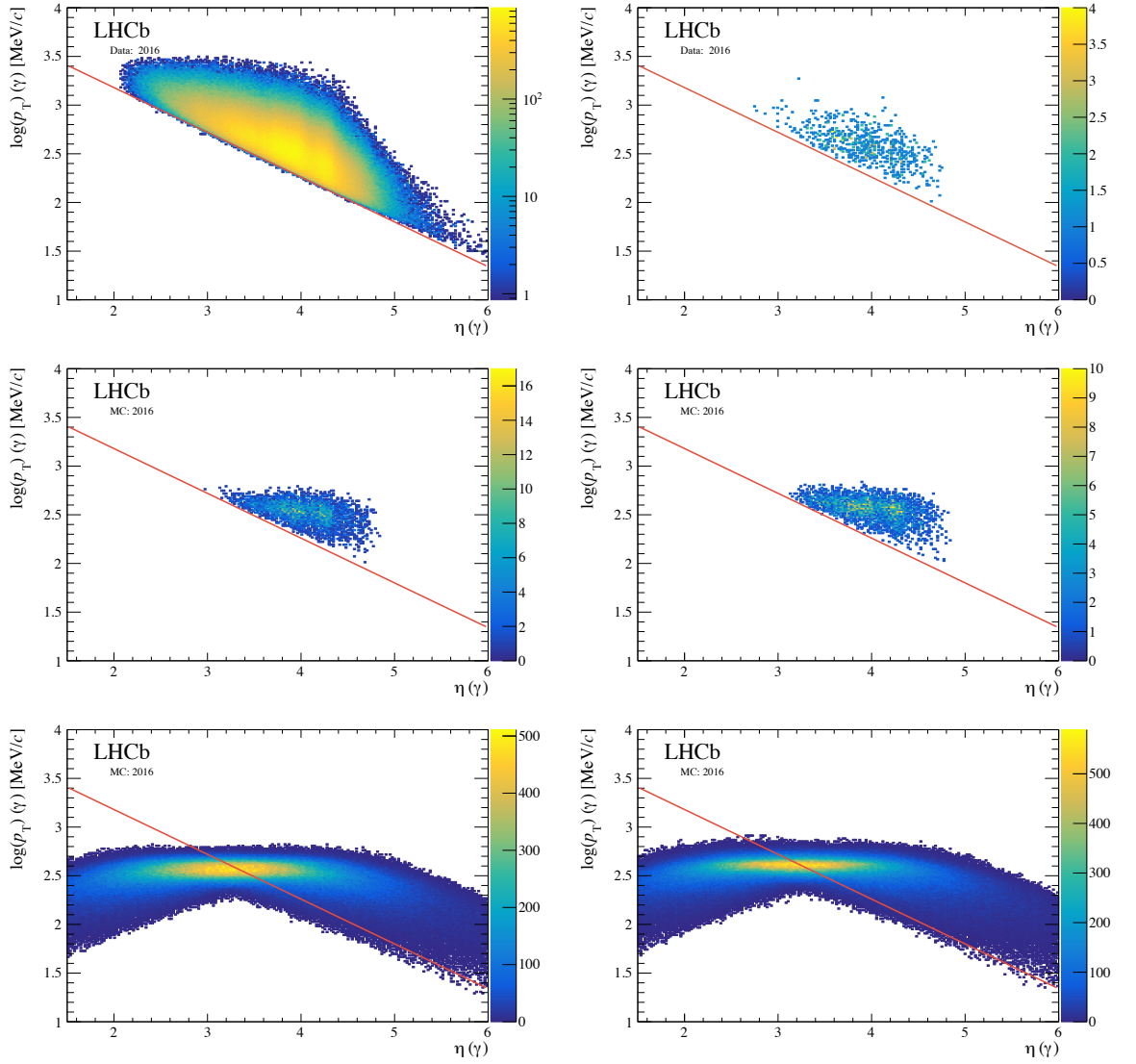


Figure 5.2. Density plots of the photons' pseudorapidity and the logarithm of its transverse momentum for photons from $D^{*0} \rightarrow D^0[K^\pm\pi^\mp]\gamma[e^+e^-]$ candidates (top left), χ_c candidates (top right), χ_{c1} reconstructed Monte Carlo (middle left), χ_{c2} reconstructed Monte Carlo (middle right), χ_{c1} generator-level Monte Carlo (bottom left), and χ_{c2} generator-level Monte Carlo (bottom right). A linear fit is overlaid to show the kinematic limit for the reconstruction of photons in red.

1817 5.1.3 Determination of D^0 yields

1818 To calculate $N(D^0)$ for Eq. 5.3, we fit the mass distribution of $D^0 \rightarrow K^\pm\pi^\mp$ candidates in the
 1819 $1820 < m(D^0) < 1910 \text{ MeV}/c^2$ mass range. For the signal we use two Gaussian distributions,
 1820 which share the same mean parameter, and we use a first-order Chebyshev polynomial for the
 1821 background. The fit results are shown in Fig. 5.3 and the parameter values are detailed in
 1822 Table 5.2. As is evident from the distribution, this sample has very low combinatoric background,
 1823 however to suppress it further we count the number of D^0 candidates within a window of ± 25
 1824 MeV/c^2 around its nominal mass value given by the PDG, $1864.83 \pm 0.05 \text{ MeV}/c^2$. From the fit

1825 we find $139,404,920 \pm 14931$ signal and $8,616,519 \pm 5628$ background events within the mass
 1826 window, which corresponds to a purity of 94.18 ± 0.01 %.

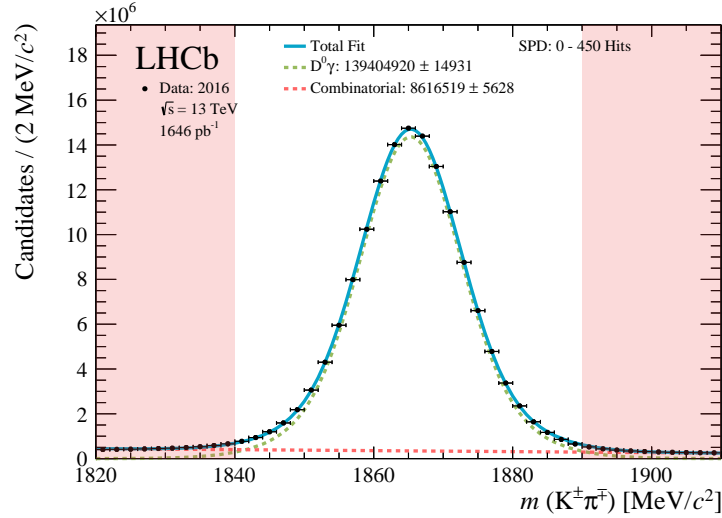


Figure 5.3. Invariant-mass distribution of $D^0 \rightarrow K^\pm \pi^\mp$ mesons for pp collisions at a centre-of-mass energy $\sqrt{s} = 13$ TeV from 2016 data. The D^0 signal is fitted with two Gaussian distributions with a common mean in green and the background is fitted with a first-order Chebyshev polynomial in red. The total fit is shown in blue. The region excluded by the mass-window cut is highlighted in red.

Table 5.2. Fit parameters for D^0 invariant-mass fit for 2016 data where μ is the mean shared by the two Gaussian distributions, σ_1 and σ_2 are their widths, Y_1/Y_2 is the fraction of the yields of the Gaussian distributions, Y_{Signal} is the number of D^0 candidates, a_0 is the parameter of the first-order Chebyshev polynomial, and $Y_{\text{Background}}$ is the number of background events.

Parameter	Value	Units
μ	1865.3266 ± 0.0008	MeV/ c^2
σ_1	11.35 ± 0.01	MeV/ c^2
σ_2	6.751 ± 0.003	MeV/ c^2
Y_1/Y_2	0.507 ± 0.003	-
Y_{Signal}	$139,404,919 \pm 14930$	-
a_1	-0.2885 ± 0.0005	-
$Y_{\text{Background}}$	$8,616,519 \pm 5627$	-

1827 5.1.4 Determination of D^{*0} yields

1828 We use the difference between the reconstructed invariant mass of the D^{*0} candidates and the
 1829 intermediate D^0 meson throughout this analysis to partially cancel out the experimental error
 1830 in the reconstruction of the D^0 meson such that,

$$\Delta m_{D^{*0}} = m(D^0 \gamma) - m(D^0). \quad (5.5)$$

1831 **Modelling $D^{*0} \rightarrow D^0[K^\pm\pi^\mp]\gamma[e^+e^-]$ invariant-mass difference**

1832 The shape of the $\Delta m_{D^{*0}}$ distribution is determined from the large, fully reconstructed Monte
 1833 Carlo described in Sec. 4.2.4. The same selection criteria used in the D^{*0} data are applied to the
 1834 Monte Carlo sample. After truth-matching the Monte Carlo a double-sided Crystal Ball [132] is
 1835 used to fit the $\Delta m_{D^{*0}}$ distribution, shown in Fig. 5.4, where all the parameters are left floating
 1836 during the fit. A double-sided Crystal Ball has a Gaussian core with two different power-law
 1837 tails, which allow for an adequate description of the asymmetric $\Delta m_{D^{*0}}$ shape. This shape has a
 1838 total of six free parameters: a mean (μ), a width (σ), two parameters that describe the distance
 1839 to the left (α_{Left}) and right (α_{Right}) of the mean where the Gaussian core becomes a power law,
 1840 and two parameters for the exponent of the power-law component of each tail (n_{Left} and n_{Right}).
 1841 We then separate the sample in $p_T(\gamma)$ bins of 200 MeV/c, and fit the $\Delta m_{D^{*0}}$ distribution in each
 1842 range up to 1600 MeV/c. These fits are shown in Fig. 5.5 and their fitting-parameter values are
 1843 summarised in Table 5.3.

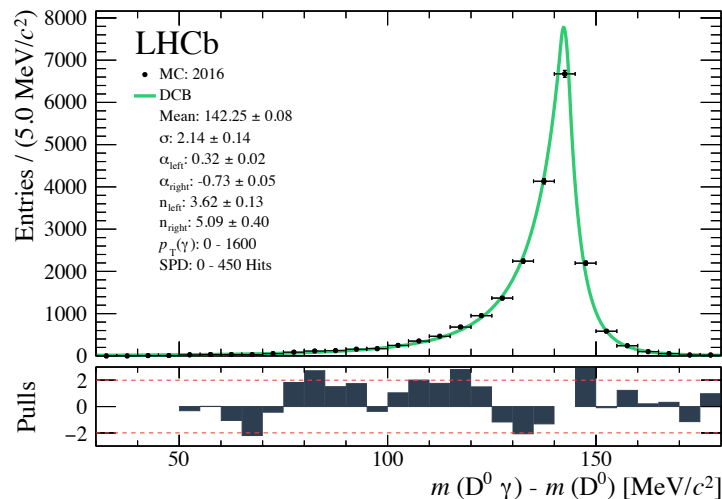


Figure 5.4. Fit of the $\Delta m_{D^{*0}}$ distribution of truth-matched $D^{*0} \rightarrow D^0[K^\pm\pi^\mp]\gamma[e^+e^-]$ mesons for pp collisions at a centre-of-mass energy $\sqrt{s} = 13$ TeV from 2016 Monte Carlo for converted photons with transverse momentum in the 0 to 1600 MeV/c range. The distribution is fitted with a double-sided Crystal Ball with all parameters floated (green).

1844 **Modelling $D^{*0} \rightarrow D^0[K^\pm\pi^\mp]\pi^0[\gamma\gamma]$ background**

1845 D^{*0} mesons can decay into a $D^0\pi^0$ pair with a branching fraction of $64.7 \pm 0.9\%$, where the π^0
 1846 decays into a pair of photons $98.923 \pm 0.034\%$ of the time. This compares to the $35.3 \pm 0.9\%$
 1847 branching fraction of $D^{*0} \rightarrow D^0\gamma$ decays. $D^0\pi^0$ events reconstructed with a single missing
 1848 photon have a lower invariant-mass signature than $D^0\gamma$ events, with the majority of events
 1849 falling between 50 and 100 MeV/c² in the $\Delta m_{D^{*0}}$ distribution. Due to the negative-skewed
 1850 distribution of the $D^0\gamma$, the tails overlap slightly and, as a result, it is important to include this
 1851 lower-mass region as part of the data fit.

Table 5.3. Fit parameters and yields for D^{*0} invariant-mass fit for Monte Carlo in bins of $p_T(\gamma)$.

Parameter	Unites	Value				
		0 – 1600	0 – 200	200 – 400	400 – 600	600 – 800
$p_T(\gamma)$	MeV/c					
μ	MeV/c ²	142.25 ± 0.08	142.4 ± 0.7	143.0 ± 0.2	142.30 ± 0.02	142.1 ± 0.2
σ	MeV/c ²	2.1 ± 0.1	2.11 ± 0.5	1.4 ± 0.5	1.56 ± 0.01	2.5 ± 0.3
α_{Left}	-	0.32 ± 0.02	0.13 ± 0.05	0.11 ± 0.04	0.21 ± 0.01	0.40 ± 0.05
α_{Right}	-	-0.73 ± 0.05	-0.6 ± 0.2	-0.4 ± 0.1	-0.50 ± 0.01	-0.9 ± 0.1
n_{Left}	-	3.6 ± 0.1	2.12 ± 0.7	5.8 ± 0.8	5.1 ± 0.2	5.6 ± 0.7
n_{Right}	-	5.09 ± 0.4	3.0 ± 1.6	9.8 ± 3.1	6.5 ± 0.4	4.3 ± 0.7
$p_T(\gamma)$	MeV/c		800 – 1000	1000 – 1200	1200 – 1400	1400 – 1600
μ	MeV/c ²		142.2 ± 0.2	142.1 ± 0.3	142.3 ± 0.2	142.4 ± 0.3
σ	MeV/c ²		2.2 ± 0.3	2.8 ± 0.5	0.7 ± 0.5	3.4 ± 0.3
α_{Left}	-		0.44 ± 0.07	0.5 ± 0.1	0.2 ± 0.1	0.7 ± 0.1
α_{Right}	-		-0.9 ± 0.2	-1.4 ± 0.3	-0.5 ± 0.3	-2.0 ± 0.3
n_{Left}	-		4.4 ± 0.5	5.7 ± 1.3	3.7 ± 0.7	5.7 ± 2.7
n_{Right}	-		3.7 ± 0.9	2.5 ± 0.7	2.8 ± 0.7	1.0 ± 0.5

1852 To model this background, we use the $D^{*0} \rightarrow D^0\pi^0$ Monte Carlo sample described in
1853 Sec. 4.2.4. The fully reconstructed events are processed with the same selection criteria as the
1854 D^{*0} data. As with the D^{*0} signal model, we need to understand how the $D^0\pi^0$ background
1855 changes with the photon's transverse momentum. The $\Delta m_{D^{*0}}$ shape of this background varies
1856 significantly with $p_T(\gamma)$. As a result, we use a one-dimensional *kernel estimation* (KE) PDF [133],
1857 a flexible, non-parametric method which models each data point as a Gaussian kernel. The
1858 width of the Gaussian is proportional to the local density of events and contributes to $1/N$ of
1859 the total integral, where N is the total number of events in the distribution. The fit for photons
1860 with a transverse momentum in bins of 200 MeV/c is shown in Fig. 5.6. The fit results are
1861 saved as templates for later use in the data fits.

1862 D^{*0} combinatorial-background model

1863 The combinatorial background in the $\Delta m_{D^{*0}}$ distribution has a characteristic shape which goes
1864 to zero at threshold. To model the combinatorial background, where D^0 mesons are wrongly
1865 matched with a photon, we use a density function designed to model $D^{*0} \rightarrow D^0 X$ decays as
1866 follows,

$$f(\Delta m_{D^{*0}}) = \begin{cases} 0 & \Delta m_{D^{*0}} - \Delta m_0 \leq 0 \\ r^A \left[1 - \exp\left(\frac{-(\Delta m_{D^{*0}} - \Delta m_0)}{C}\right) \right] + B(r - 1) & \Delta m_{D^{*0}} - \Delta m_0 > 0, \end{cases} \quad (5.6)$$

1867 where Δm_0 is the invariant-mass difference threshold under which the function is set to zero, r is
1868 the ratio of the delta mass and the $\Delta m_{D^{*0}}$ threshold, $\Delta m_{D^{*0}}/\Delta m_0$, and A , B , and C are shape
1869 parameters. The first term, r^A , assures that the distribution tends to zero for small $\Delta m_{D^{*0}}$

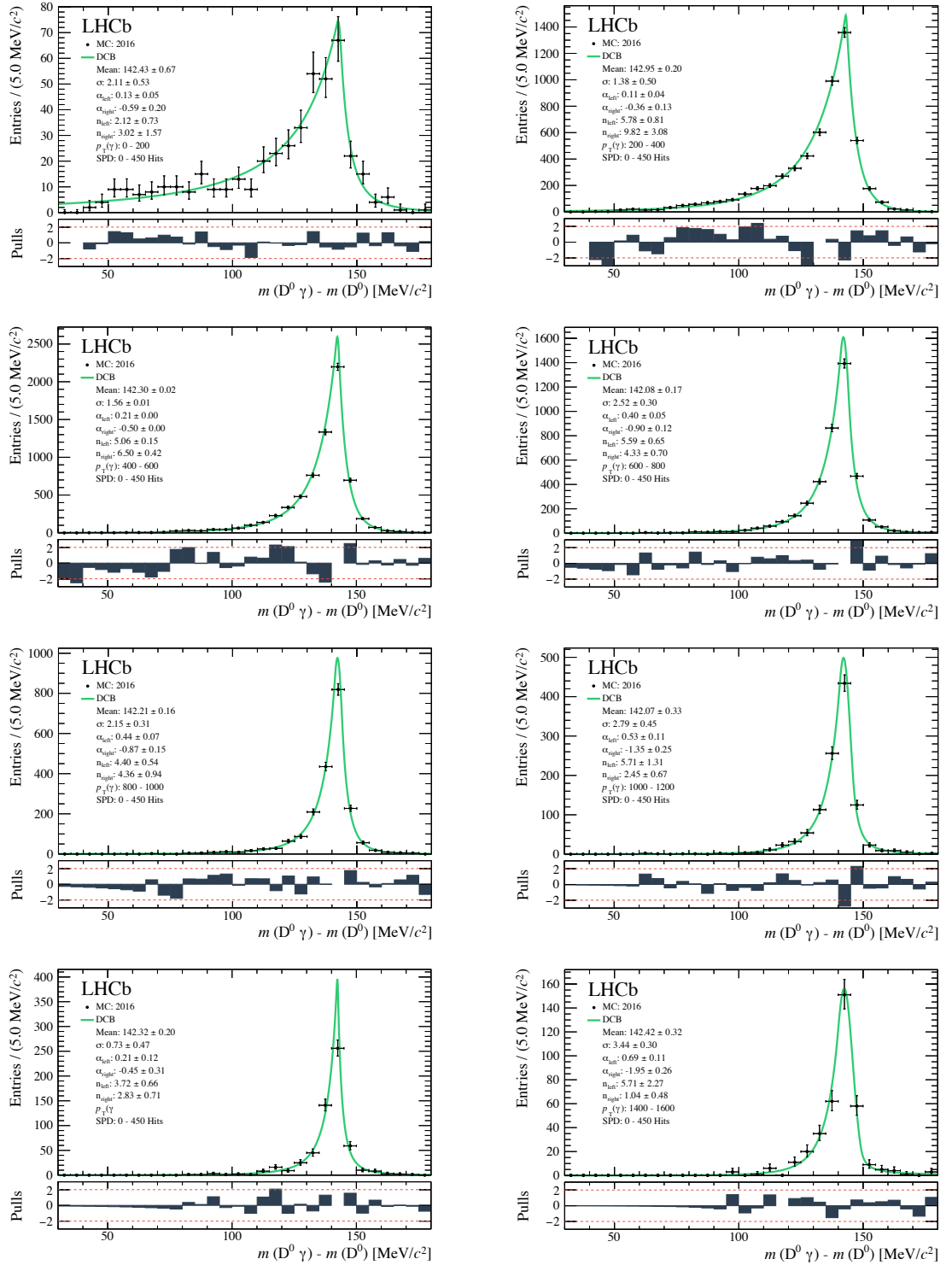


Figure 5.5. Fit of the $\Delta m_{D^{*0}}$ distribution of truth-matched $D^{*0} \rightarrow D^0[K^\pm\pi^\mp]\gamma[e^+e^-]$ Monte Carlo for pp collisions at a centre-of-mass energy $\sqrt{s} = 13$ TeV for 2016 data in increments of 200 MeV/c in $p_T(\gamma)$ from left to right. The distributions are fitted with a double-sided Crystal Ball with all parameters floated.

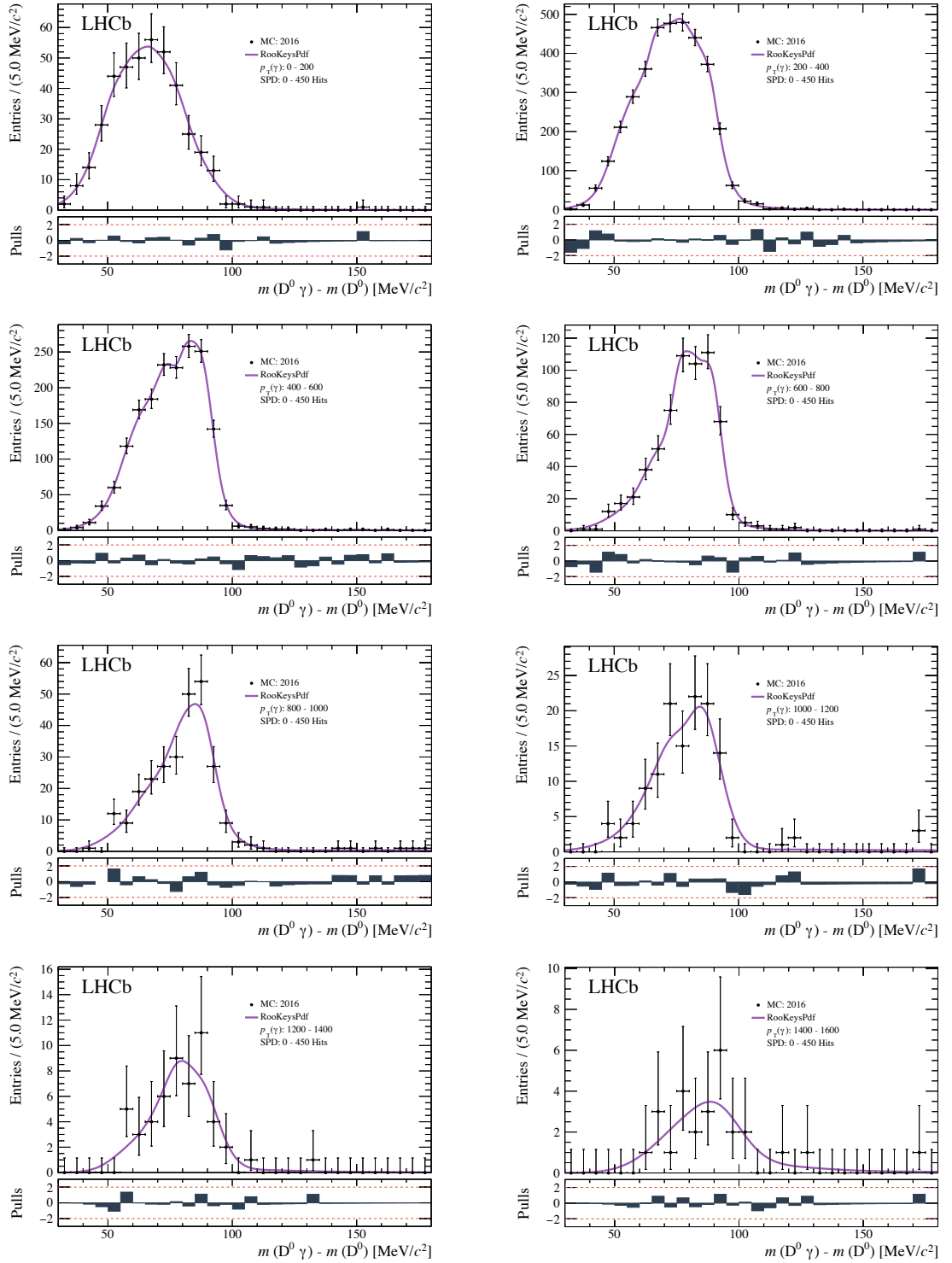


Figure 5.6. Fit of the $\Delta m_{D^{*0}}$ distribution of truth-matched $D^{*0} \rightarrow D^0[K^\pm\pi^\mp]\gamma[e^+e^-]$ events reconstructed from $D^{*0} \rightarrow D^0[K^\pm\pi^\mp]\pi^0[\gamma\gamma]$ Monte Carlo for pp collisions at a centre-of-mass energy $\sqrt{s} = 13$ TeV for 2016 data run conditions in increments of 200 MeV/c in $p_T(\gamma)$ from left to right. The distributions are fitted with a kernel-estimator PDF.

1870 values. The second exponential term, $1 - \exp\left(\frac{-(\Delta m_{D^{*0}} - \Delta m_0)}{C}\right)$, insures that the distribution
 1871 tends to zero for large $\Delta m_{D^{*0}}$ values, where C effectively controls the overall width of the
 1872 distribution. The last term is a linear correction. For $B < 0$ the function can be negative
 1873 at large $\Delta m_{D^{*0}}$ values. This regime is never reached within the analysis. All parameters are
 1874 floated during the fit.

1875 D^{*0} data fit

1876 To fit the $\Delta m_{D^{*0}}$ distribution in the 2016 calibration data, we fix the $D^0\gamma$ signal parameters
 1877 associated with the tails of the double-sided Crystal Ball to match the results of the Monte
 1878 Carlo fits for each $p_T(\gamma)$ range, while allowing the mean value to float. In addition, we use a
 1879 Gaussian convolution on the signal shape as an empirical correction to account for differences
 1880 in resolution between data and Monte Carlo. We allow the mean and width of the Gaussian to
 1881 float in the fit of the data spanning a wide photon kinematic range, 0 to 1600 MeV/ c , and fix
 1882 the parameters according to these results for the fits in 200 MeV/ c bin intervals. The KE PDFs
 1883 of the $D^0\pi^0$ background is used for the corresponding $p_T(\gamma)$ selection. This background has a
 1884 much wider distribution than that of the $D^0\gamma$ signal and, as a result, is not as susceptible to
 1885 the resolution effects. Therefore, no additional correction is applied to the shapes extracted
 1886 from Monte Carlo. Finally, we allow all the combinatorial-background parameters to float.
 1887 The fit result in the $p_T(\gamma) < 1600$ MeV/ c range is shown in Fig. 5.7 and for the individual
 1888 200 MeV/ c bin increments in Fig. 5.8. The peak of D^{*0} candidates is barely visible at low values
 1889 of $p_T(\gamma)$ and steadily grows with higher $p_T(\gamma)$. The corresponding yields and fit parameters
 1890 are summarised in Table 5.4. The D^{*0}_{Yield} or $N_{\text{Conv}}(D^{*}(2007)^0)$ is plotted as a function of the
 1891 photon's transverse momentum in Fig. 5.9. This is the numerator of our efficiency calculation
 1892 described in Eq. 5.2.

1893 5.1.5 Efficiency denominator

1894 D^0 kinematic re-weight method and validation

1895 We now discuss the calculation of the denominator of Eq. 5.2, $N_{\text{all}}(D^{*0}|D^0)$. As has been
 1896 explained, the cross-section measurements, $\sigma(pp \rightarrow D^{*+}X)$ and $\sigma(pp \rightarrow D^0X)$ [131], are used
 1897 together with the inclusive D^0 sample to provide a normalisation. However, we also need the
 1898 $p_T(\gamma)$ dependence of $N_{\text{all}}(D^{*0}|D^0)$. The selection requirements imposed on the D^0 will of course
 1899 change the $p_T(\gamma)$ distribution, even if there are no requirements imposed on the photon. These
 1900 changes are driven by correlations in the kinematics, and can be reproduced by considering the
 1901 changes in the $\eta(D^0)$ and $p_T(D^0)$ distributions with respect to the distributions unbiased from
 1902 selection and reconstruction effects.

1903 To obtain the $p_T(\gamma)$ dependence, we use the centrally produced $D^{*0} \rightarrow D^0[K^\pm\pi^\mp]\gamma$ Monte
 1904 Carlo described in Eq. 5.1.4 and weight the generator-level events such that their $\eta(D^0)$ and
 1905 $p_T(D^0)$ distributions are aligned with those observed in the data. By using these weights, we
 1906 then obtain the distribution of $p_T(\gamma)$ before selection and reconstruction effects of the photon.

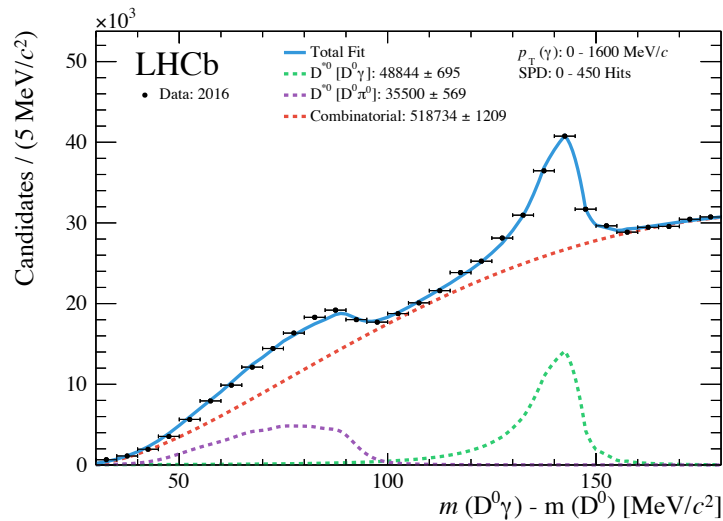


Figure 5.7. Fit of the $\Delta m_{D^{*0}}$ distribution of $D^{*0} \rightarrow D^0[K^\pm\pi^\mp]\gamma[e^+e^-]$ candidates for 2016 data with photons with transverse momentum between 0 to 1600 MeV/c. The D^{*0} signal is fitted with a double-sided Crystal Ball convoluted with a Gaussian (green), the $D^{*0} \rightarrow D^0[K^\pm\pi^\mp]\pi^0[\gamma\gamma]$ background is fitted with a KE template from Monte Carlo (purple), and the combinatorial background is fitted with Eq. 5.6.

1907 This procedure is tested with Monte Carlo to check the assumption that reweighting in
 1908 $\eta(D^0)$ and $p_T(D^0)$ is sufficient to reproduce the distribution of the p_T of the unselected photons.
 1909 To do this, Monte Carlo events are selected with the requirement that the D^0 is reconstructed,
 1910 and with no requirement on the reconstruction of a photon. Using the Monte Carlo truth
 1911 information, we check if the D^0 is associated with a $D^{*0} \rightarrow D^0[K^\pm\pi^\mp]\gamma$ decay. If it is, then the
 1912 truth information of the photon is saved.

1913 We re-weight unbiased generator-level Monte Carlo to match the kinematics of the D^0
 1914 mesons in the fully reconstructed Monte Carlo. It is checked and shown in Fig. 5.10 that $\eta(D^0)$
 1915 (top left), $p_T(D^0)$ (top right), and $p(D^0)$ (bottom left) are brought into agreement by this
 1916 procedure, as expected. The photon momentum of the re-weighted generator-level Monte Carlo
 1917 is then compared with the truth information of the photons that were saved along with the
 1918 reconstructed D^0 candidates. This is shown in Fig. 5.10 (bottom right), where good agreement
 1919 is seen between the two distributions, indicating that the method works.

1920 D^0 kinematic re-weight and efficiency calculation

1921 With the method validated, we next re-weight the generator-level Monte Carlo to now match
 1922 the kinematics of all the D^0 mesons in the inclusive D^0 sample. The comparison between
 1923 re-weighted Monte Carlo and the data is shown in Fig. 5.11. After this procedure, the $p_T(\gamma)$ of
 1924 the re-weighted, generator-level Monte Carlo gives the $p_T(\gamma)$ dependence of $N_{\text{All}}(D^{*0}|D^0)$. After
 1925 normalising it using Eq. 5.3, we have obtained the denominator of our efficiency calculation,
 1926 shown in Fig. 5.12.

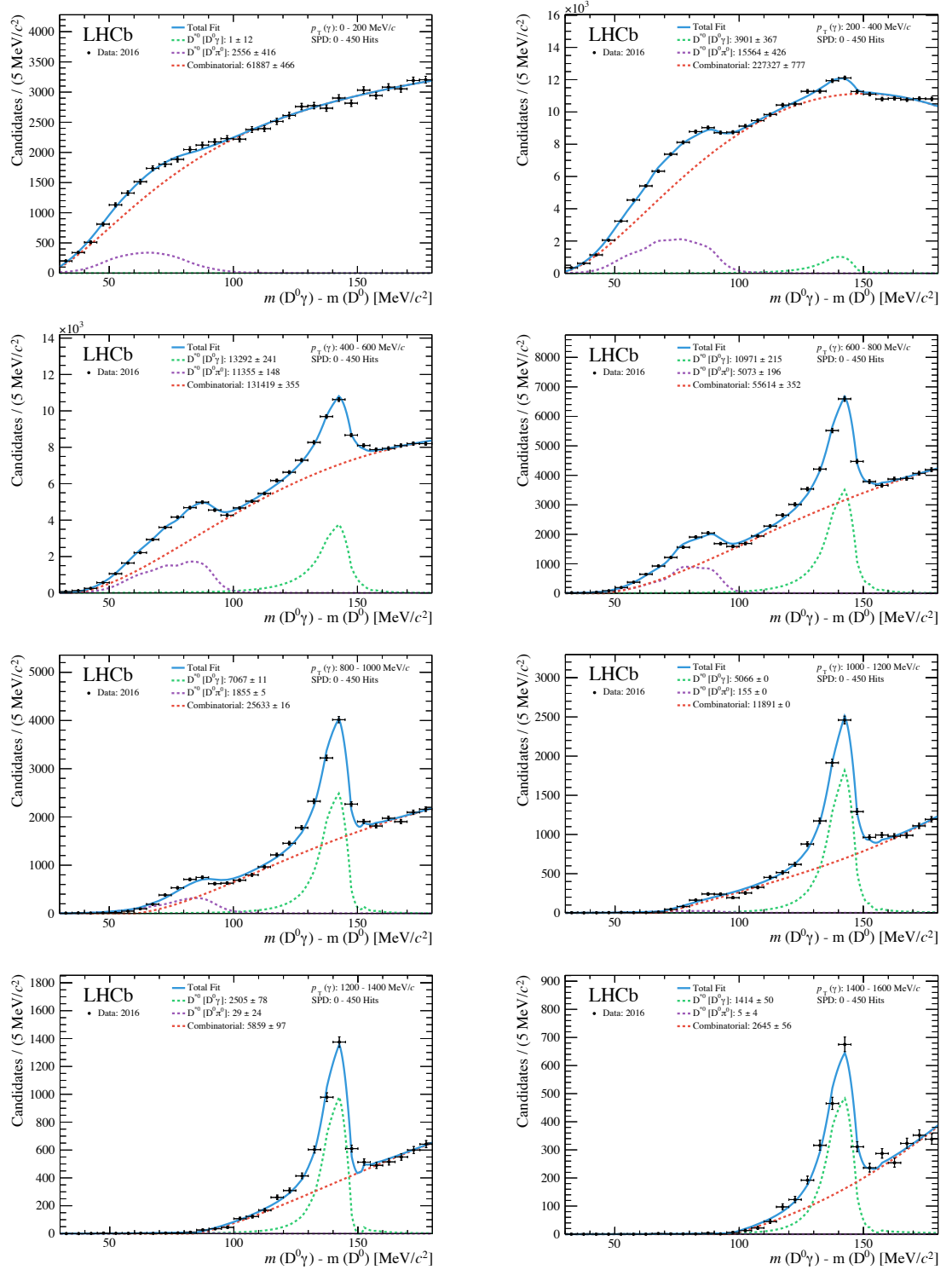


Figure 5.8. Fit of the $\Delta m_{D^{*0}}$ distribution of $D^{*0} \rightarrow D^0[K^\pm\pi^\mp]\gamma[e^+e^-]$ candidates for 2016 data in increments of 200 MeV/c in $p_T^2(\gamma)$. The D^{*0} signal is fitted with a double-sided Crystal Ball convoluted with a Gaussian (green), the $D^{*0} \rightarrow D^0[K^\pm\pi^\mp]\pi^0[\gamma\gamma]$ background is fitted with a KE template from Monte Carlo (purple), and the combinatorial background is fitted with Eq. 5.6.

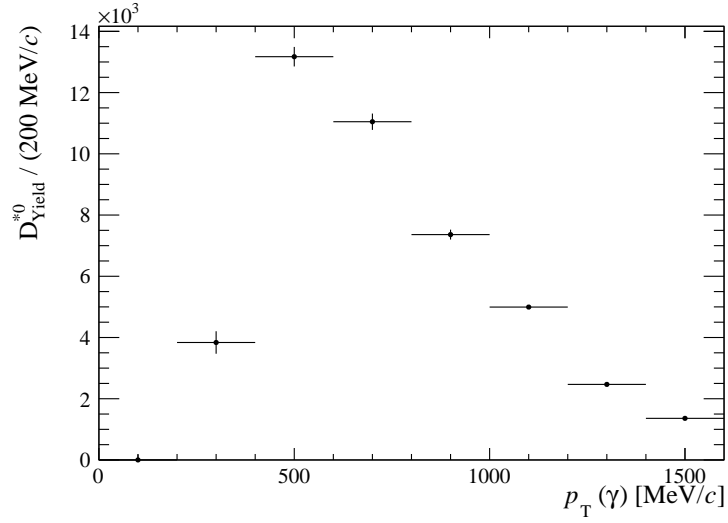


Figure 5.9. D^{*0} Y_{Yield} in 200 MeV/c bins of the photon's transverse momentum.

Table 5.4. Fit parameters and yields for $\Delta m_{D^{*0}}$ mass fit for 2016 data for photons with transverse momentum in the 0 to 1600 MeV/c range and in increments of 200 MeV/c. The μ_{Gauss} and σ_{Gauss} parameters are related to the Gaussian convolution to the signal used to apply the empirical correction to the data.

Para.	Units	Value				
$p_T(\gamma)$	MeV/c	0 – 1600	0 – 200	200 – 400	400 – 600	600 – 800
μ_{Gauss}	MeV/c ²	0.002 ± 0.0005	-	-	-	-
σ_{Gauss}	MeV/c ²	0.12 ± 0.01	-	-	-	-
μ_{Signal}	MeV/c ²	142.9 ± 0.2	140 ± 6	141.6 ± 0.4	143.6 ± 0.1	142.8 ± 0.2
Y_{Signal}	-	48843 ± 695	1 ± 179	3901 ± 367	13292 ± 241	10970 ± 215
m_0	MeV/c ²	26.0 ± 0.3	25 ± 0.5	25.8 ± 0.7	31 ± 2	45.95 ± 0.04
A	-	0.486 ± 0.002	0.93 ± 0.07	0.57 ± 0.02	0.641 ± 0.004	0.62 ± 0.02
B	-	-0.263 ± 0.001	-0.73 ± 0.14	-0.39 ± 0.02	-0.42527 ± 0.00004	-0.42 ± 0.02
C	-	99.4 ± 0.4	28 ± 4	67 ± 3	76.909 ± 0.008	97 ± 3
Y_{Bkg}	-	518734 ± 1209	61887 ± 465	227327 ± 777	131419 ± 355	55613 ± 352
Y_{π^0}	-	35499 ± 569	2556 ± 415	15563 ± 426	11355 ± 148	5073 ± 196
$p_T(\gamma)$	MeV/c		800 – 1000	1000 – 1200	1200 – 1400	1400 – 1600
μ_{Signal}	MeV/c ²		142.03 ± 0.02	143.011 ± 0.001	142.03 ± 0.09	142.1 ± 0.2
Y_{Signal}	-		7066 ± 11	5065 ± 0.01	2505 ± 78	1414 ± 50
m_0	MeV/c ²		49 ± 2	42.2645 ± 0.00002	55 ± 6	29 ± 5
A	-		1.17 ± 0.04	1.4113 ± 0.0002	1.03 ± 0.06	1.715 ± 0.007
B	-		-1.0341 ± 0.0006	-2.1000 ± 0.0002	-1.04 ± 0.03	-3.27 ± 0.04
C	-		53.0145 ± 0.0008	24 ± 18	66 ± 3	19 ± 13
Y_{Bkg}	-		25633 ± 15	11891.5 ± 0.01	5859 ± 97	2645 ± 56
Y_{π^0}	-		1854 ± 5	155.472 ± 0.002	29 ± 24	5 ± 4

1927 By dividing the reconstructed $N(D^{*0})$, shown in Fig. 5.9, and $N_{\text{All}}(D^{*0}|D^0)$ in bins of
 1928 the photon's transverse momentum, we obtain the efficiency of detecting a photon through

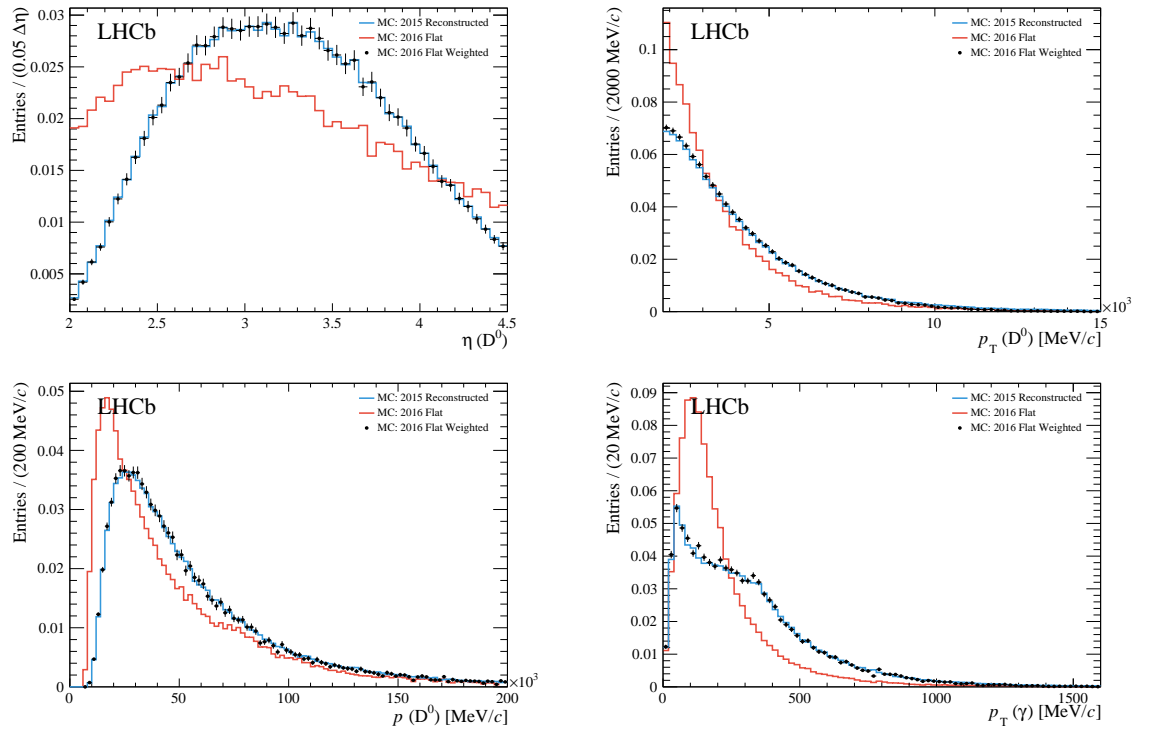


Figure 5.10. $D^0 \rightarrow K^\pm \pi^\mp$ kinematics in the fully reconstructed Monte Carlo (black markers) and generator-level $D^{*0} \rightarrow D^0[K^\pm \pi^\mp] \gamma$ before (red) and after re-weighting (blue). Weights are applied to D^0 transverse momentum (top left) and η (top right) that successfully reproduce the D^0 momentum distribution (bottom left) and the photon's transverse momentum (bottom right).

1929 conversion versus $p_T(\gamma)$, shown in Fig. 5.13. The efficiency is compatible with zero below
 1930 200 MeV/ c and rises steadily to 1% at around 1300 MeV/ c .

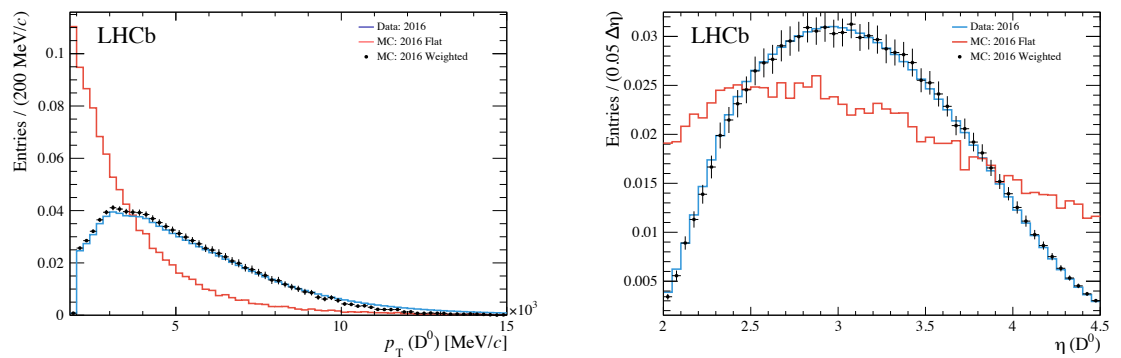


Figure 5.11. $D^0 \rightarrow K^\pm \pi^\mp$ kinematics in the fully reconstructed Monte Carlo (black markers) and generator level $D^{*0} \rightarrow D^0[K^\pm \pi^\mp] \gamma$ before (red) and after re-weighting (blue). Weights are applied to the D^0 transverse momentum (left) and pseudorapidity (right).

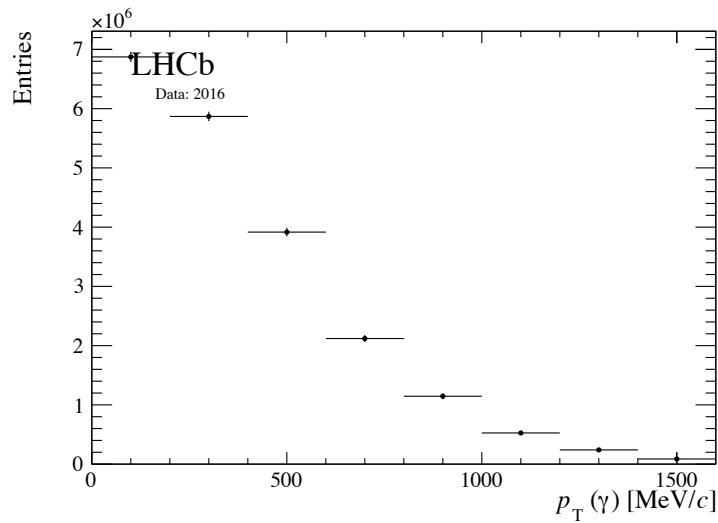


Figure 5.12. $N_{\text{All}}(D^{*0}|D^0)$ as a function of the photon's transverse momentum. The distribution is normalised according to the number of reconstructed D^0 mesons and the ratio of $pp \rightarrow D^{*+}$ and $Xpp \rightarrow D^0 X$ cross-sections.

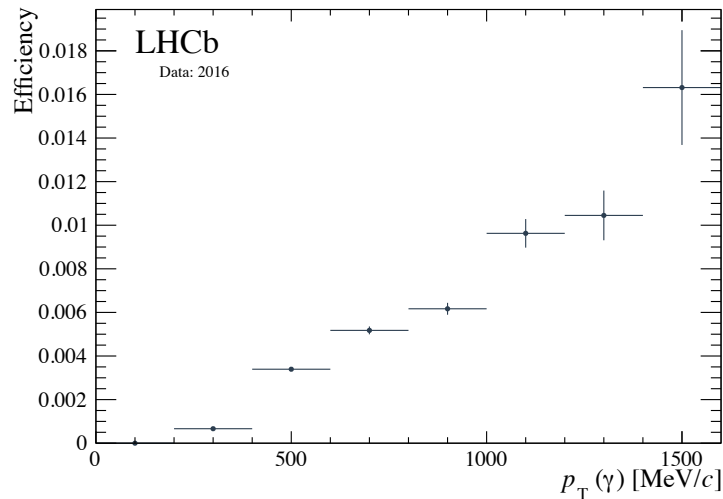


Figure 5.13. Photon-conversion efficiency as a function of photon's transverse momentum in bins of 200 MeV/c for 2016 run conditions.

1931 5.1.6 Dependence of efficiency on detector occupancy

1932 The detector environment for events in the D^{*0} samples is not properly representative of the
 1933 CEP environment, where we expect to see only particles associated with our decay mode in an
 1934 otherwise empty detector. As detector occupancy can affect pattern-reconstruction efficiency
 1935 in the tracking, we expect this difference to have consequences for the photon-reconstruction
 1936 efficiency. The amount of activity in the detector can be estimated using the number of hits
 1937 in the SPD. A typical CEP event, after accounting for spill over, will have less than 20 or 30
 1938 SPD hits, depending on the decay's final state. In contrast, the D^{*0} and D^0 events used for the

1939 calibration studies are generally produced in inelastic collisions where the the detector occupancy
 1940 is much higher: see Fig. 5.14 for a comparison of the SPD distribution from CEP χ_c and inelastic
 1941 D^{*0} events from 2016 data. It is expected that the reconstruction efficiency will vary as a
 1942 function of the detector occupancy, as tracking and vertex reconstruction tends to improve with
 1943 lower multiplicities. Therefore, to better understand the effect of the detector occupancy on
 1944 $\varepsilon_{\gamma \rightarrow e^+e^-}$, we repeat the procedure detailed above and calculate the photon-conversion efficiency
 1945 in bins of SPD hits.

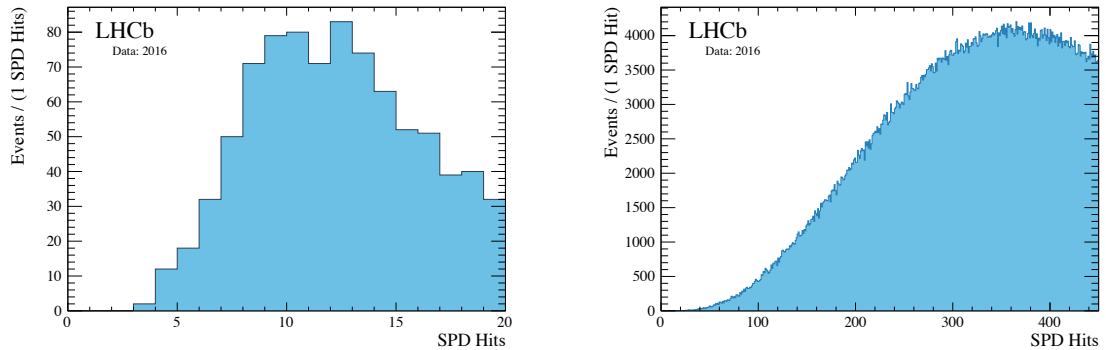


Figure 5.14. Distribution of the number of SPD hits in the χ_c sample (left) and the D^{*0} (right) sample for 2016 data.

1946 The D^0 and D^{*0} data set is further separated into subsets of SPD bins while keeping the
 1947 whole converted-photon transverse momentum range, 0 to 1600 MeV/ c , and their invariant
 1948 mass distributions are fitted to calculate the efficiency normalisation. For systematic checks
 1949 several binning schemes are considered: SPD bins of 75, 90, 112.5, and 150 SPD hit increments.
 1950 The efficiency results for these four data sets are shown in Fig. 5.15.

1951 As expected, from these distributions we learn that the photon-conversion efficiency increases
 1952 with a lower detector occupancy. However, the overall shape of the distribution with respect to
 1953 $p_T(\gamma)$ appears to be essentially independent of SPD multiplicity. We demonstrate this by fitting
 1954 the efficiency calculated over the entire SPD range, 0 to 450, with a quadratic polynomial,

$$a + b \cdot p_T + c \cdot p_T^2, \quad (5.7)$$

1955 with all parameters floating. We then apply the same fit, with all parameters fixed, except
 1956 for the normalisation constant a , to each of the efficiencies using the 75 SPD hit interval
 1957 subsets. These fits are shown in Fig. 5.16. In these fits the first bin with data is excluded as
 1958 its inclusion leads to instabilities in the lower statistics samples. It is seen that the shape of
 1959 the efficiency distribution fitted on the inclusive sample describes all of the sub-samples well,
 1960 indicating that it is reasonable to factorise $p_T(\gamma)$ and multiplicity dependence when measuring
 1961 the photon-conversion efficiency.

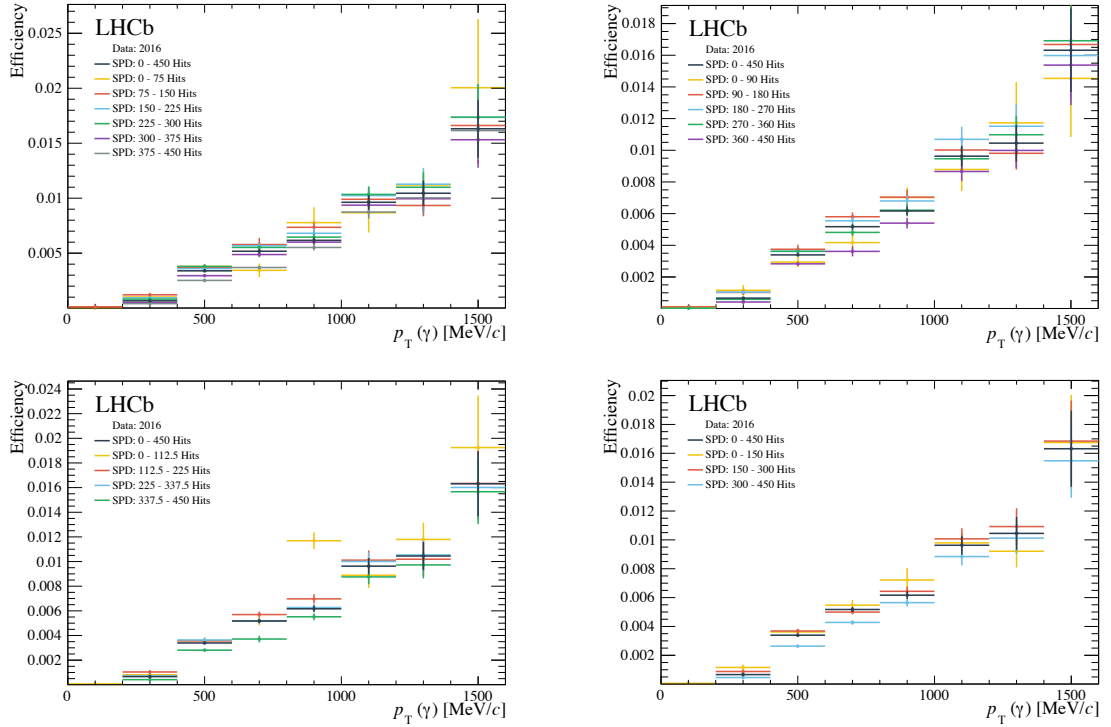


Figure 5.15. Photon-conversion efficiency as a function of the photon's transverse momentum in bins of 200 MeV/c for 2016 run conditions for 75 (top left), 90 (top right), 112.5 (bottom left), and 150 (bottom right) SPD hit increments.

1962 To extrapolate the photon-conversion efficiency to the low-multiplicity regime of CEP events
 1963 we take the sample of CEP candidates and correct for the photon-conversion efficiency according
 1964 to the transverse momentum of the photon candidate to calculate the number of candidates
 1965 prior to photon conversion. We repeat this exercise using the efficiency results evaluated in
 1966 different bins of SPD multiplicity, taking as a baseline the 75 SPD hits bin width sample. The
 1967 results are plotted in Fig. 5.17 (first two rows). The points are plotted at the mean of the SPD
 1968 distribution for each range, with an error bar corresponding to the RMS of this distribution. As
 1969 expected, the dependence of the photon-conversion efficiency on event multiplicity means that
 1970 the corrected number of candidates is not constant, but rather falls with multiplicity, reflecting
 1971 the higher efficiency in low-multiplicity events. Also shown is a point corresponding to the
 1972 number of candidates calculated with the inclusive distribution, which appears at around 300
 1973 SPD hits and is consistent with the binned distribution.

1974 To deduce the true number of CEP candidates we fit the binned distribution and extrapolate
 1975 to zero multiplicity, which is representative of CEP conditions. We then fit a quadratic function
 1976 over the entire SPD range, 0 to 450, with the minimum fixed at zero SPD hits: $a + b \cdot x^2$. The fit
 1977 results are shown in Fig. 5.17 (first row) and the fit parameters are summarised in Table 5.5. We
 1978 obtain the expected number of efficiency corrected χ_c candidates from the intercept parameter
 1979 a . To correct for the difference in multiplicity between the calibration and CEP samples we

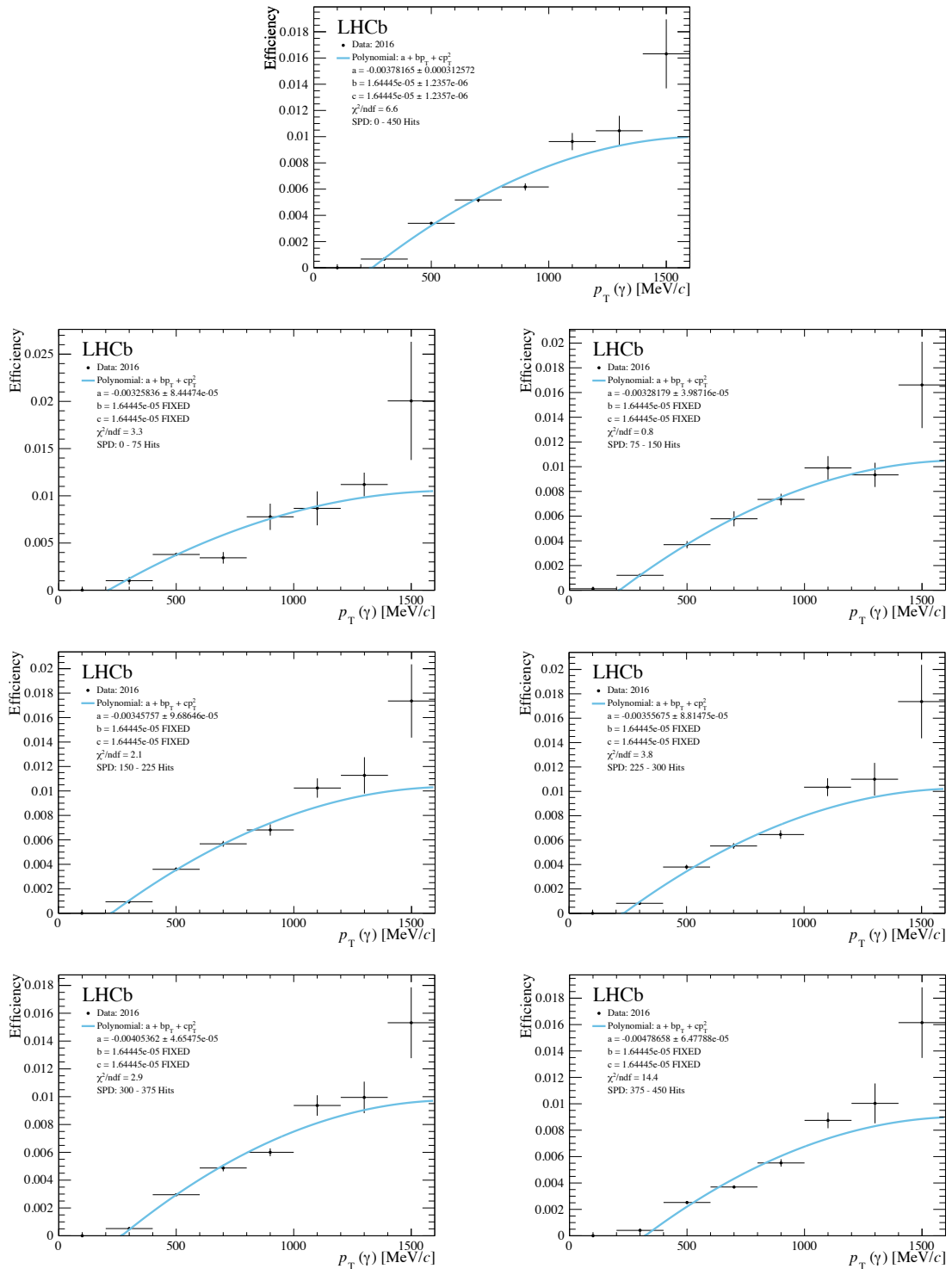


Figure 5.16. Photon-conversion efficiency as a function of the photon's transverse momentum in bins of 200 MeV/c for 2016 run conditions in 75 SPD hit increments. The distributions are fitted with a quadratic polynomial (blue). The top plot shows the results for the inclusive distribution.

1980 take the ratio between our extrapolation into low SPD, a , and the total number of expected χ_c
 1981 candidates as calculated using the whole SPD range, $Y_{\text{All SPD}}$.

1982 As a systematic check, we repeat the fit using the quadratic model over the first four points,
 1983 0 to 300 SPD hits, which are both well measured and lie closest to the CEP regime. This fit is
 1984 shown in Fig. 5.17 (second row) for the 2016-only, and combined 2015 and 2016 data. The fit
 1985 model is also substituted for a first-order polynomial and the fit is performed over both the first
 1986 four points and the entire range, see Fig. 5.18 (first two rows). In addition, we split the data
 1987 into five and four SPD bins then repeat the quadratic, Fig. 5.17, and linear, Fig. 5.18, fits. The
 1988 fit parameters are summarised in Table 5.5. From considering the precision of these fits, and
 1989 inspecting the variation in central values, we estimate a correction factor of 0.50 ± 0.10 .

Table 5.5. Summary of the fit parameters used to extrapolate the number of expected χ_c candidates corrected for photon conversions for linear and quadratic fits at two SPD intervals for 2016-only, and combined 2015 and 2016 data.

Model	SPD Hits	SPD Bins	Parameter	2016	2015 + 2016
$a + b \cdot x^2$	0 - 450	6	a	194058 ± 10051	232315 ± 12020
			b	-43449 ± 0.4	-43470 ± 0.4
			a/Y_{AllSPD}	0.54 ± 0.05	0.54 ± 0.05
$a + b \cdot x^2$	0 - 300	6	a	201154 ± 8913	240831 ± 10664
			b	-36353 ± 0.6	-36309 ± 0.4
			a/Y_{AllSPD}	0.56 ± 0.05	0.56 ± 0.05
$a + b \cdot x^2$	0 - 450	5	a	196430 ± 18634	235213 ± 22208
			b	-57300 ± 0.4	-57345 ± 0.4
			a/Y_{AllSPD}	0.55 ± 0.07	0.55 ± 0.07
$a + b \cdot x^2$	0 - 450	4	a	204667 ± 23953	245022 ± 28547
			b	-47500 ± 0.4	-47535 ± 0.4
			a/Y_{AllSPD}	0.57 ± 0.08	0.57 ± 0.08
$a + b \cdot x$	0 - 450	6	a	136542 ± 34248	163734 ± 40886
			b	704 ± 215	839 ± 257
			a/Y_{AllSPD}	0.38 ± 0.10	0.38 ± 0.10
$a + b \cdot x$	0 - 300	6	a	161827 ± 32124	193994 ± 38339
			b	506 ± 226	602 ± 269
			a/Y_{AllSPD}	0.45 ± 0.10	0.45 ± 0.10
$a + b \cdot x$	0 - 450	5	a	152999 ± 55386	183558 ± 66021
			b	571 ± 294	680 ± 350
			a/Y_{AllSPD}	0.43 ± 0.16	0.43 ± 0.16
$a + b \cdot x$	0 - 450	4	a	138579 ± 69566	166289 ± 82928
			b	724 ± 331	862 ± 394
			a/Y_{AllSPD}	0.39 ± 0.20	0.39 ± 0.20

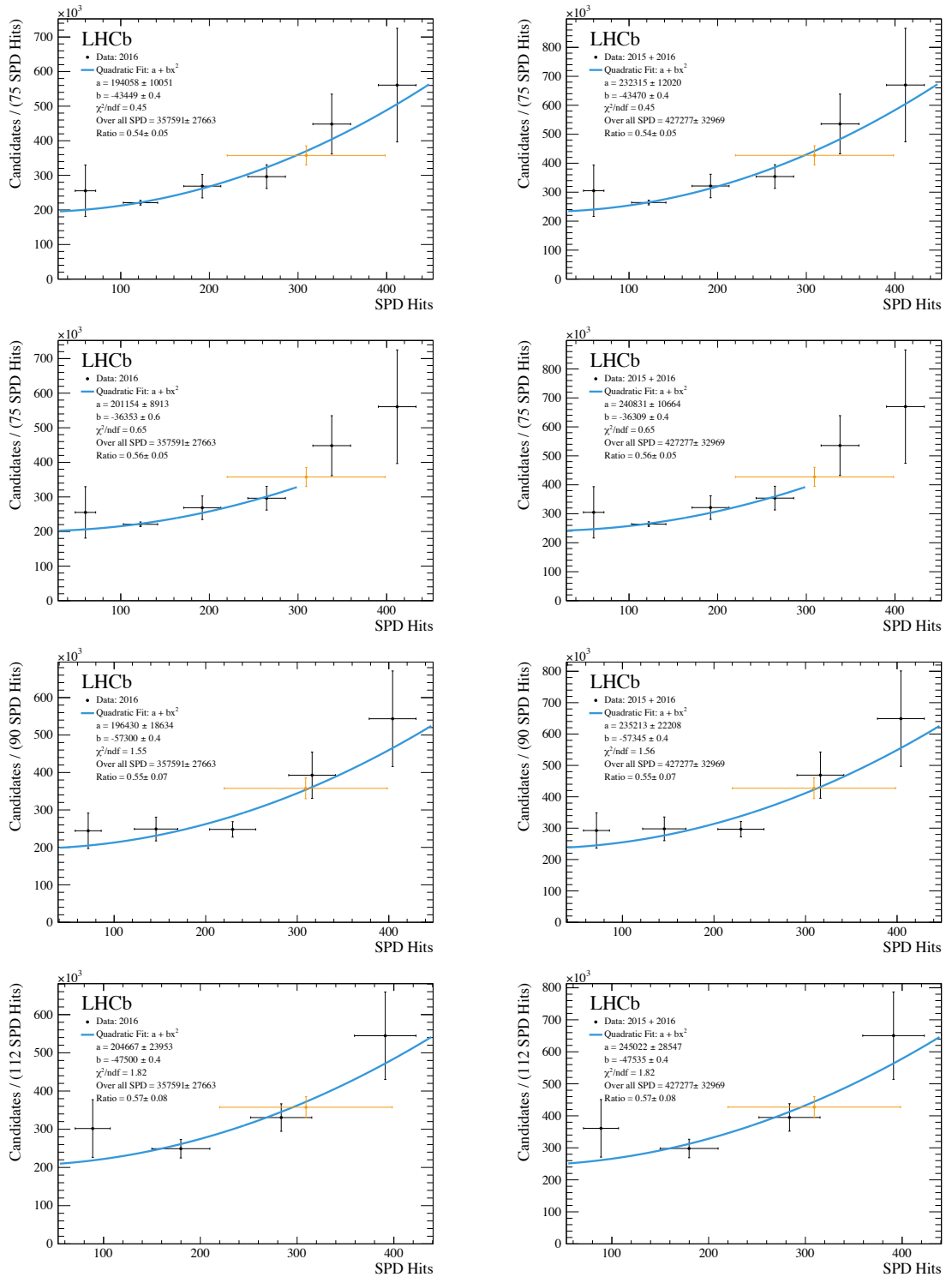


Figure 5.17. Number of χ_c candidates corrected for the photon-conversion efficiency as a function of SPD hits for the 2016-only (left), and combined 2015 and 2016 (right) data. The distributions are fitted with a quadratic function centred at zero, $a + b \cdot x^2$. In the first and second row, the data are separated into six bins but the fit is performed using the full SPD range and the first four points, respectively. In the third and fourth row, the fit is performed using the full SPD range but the data are separated into five and four bins, respectively. The number of expected candidates calculated over the entire SPD range is overlaid in yellow.

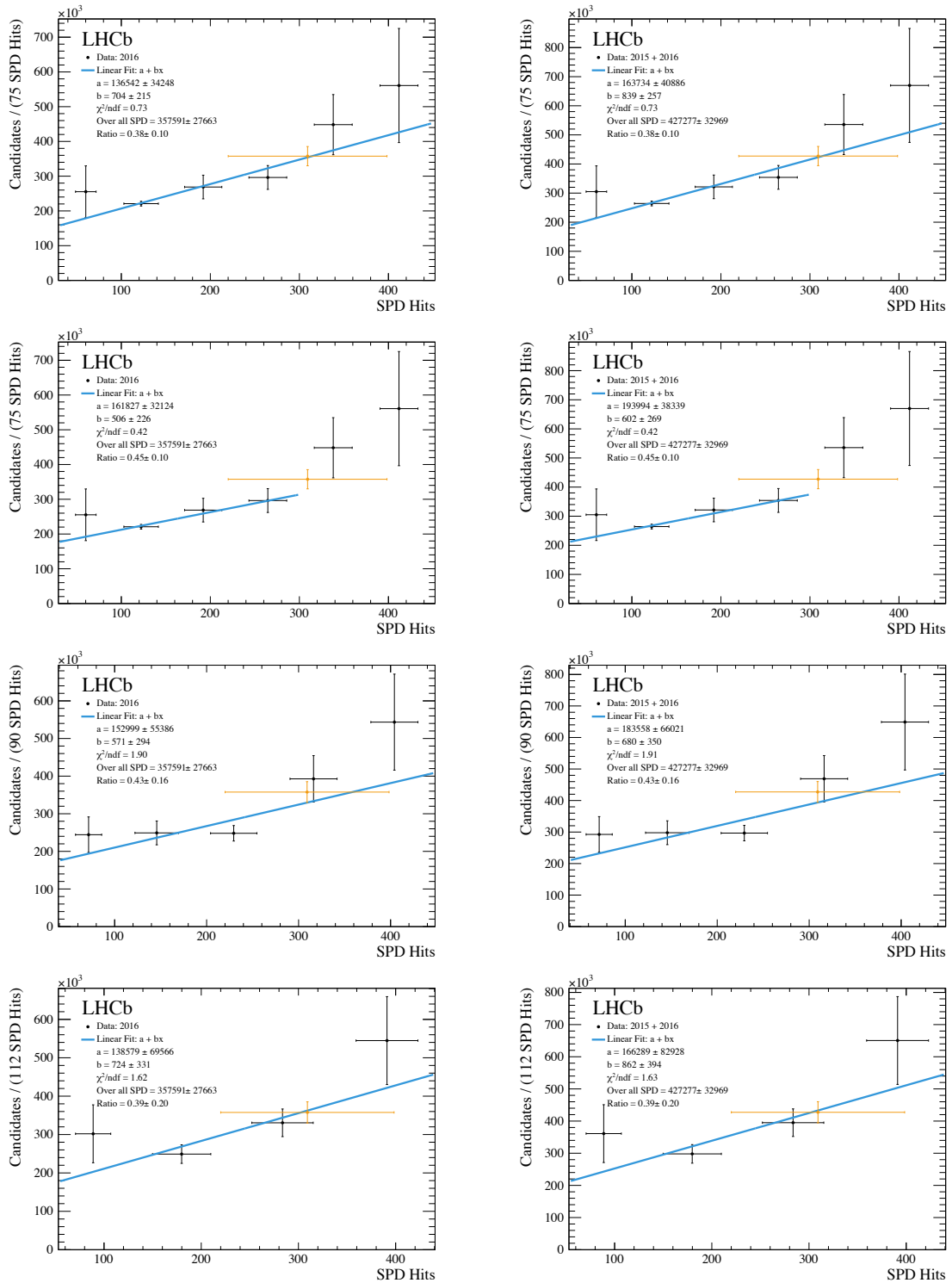


Figure 5.18. Number of χ_c candidates corrected for the photon-conversion efficiency as a function of SPD hits for the 2016-only (left), and combined 2015 and 2016 (right) data. The distributions are fitted with a first-order polynomial, $b + m \cdot x$. In the first and second row, the data are separated into six bins but the fit is performed using the full SPD range and the first four points, respectively. In the third and fourth row, the fit is performed using the full SPD range but the data are separated into five and four bins, respectively. The number of expected candidates calculated over the entire SPD range is overlaid in yellow.

1990 5.1.7 Summary of photon-conversion efficiency studies

1991 By studying the photons from $D^{*0} \rightarrow D^0[K^\pm\pi^\mp]\gamma$ decays we have been able to calculate
 1992 the photon-conversion efficiency (defined to be the product of the conversion probability and
 1993 reconstruction efficiency) for downstream tracks in bins of the photon's transverse momentum,
 1994 $p_T(\gamma)$. A significant dependence on $p_T(\gamma)$ is observed, with negligible efficiency below \sim
 1995 300 MeV/c, rising steeply thereafter. This behaviour affects the reconstruction of χ_{c0} mesons the
 1996 most, for which the photons in CEP events are very soft. As a result, we conclude our sample
 1997 in the χ_{c0} mass region is background dominated and have excluded it from the study.

1998 To account for the unique low-multiplicity environment conditions of CEP, we have studied
 1999 the effect of the detector occupancy on the photon-conversion efficiency. By determining the
 2000 evolution of the efficiency in bins of event multiplicity, quantified in the number of SPD hits, we
 2001 are able to extrapolate the performance into the low-multiplicity regime of CEP physics.

2002 In conclusion, we shall correct our observed χ_{c1} and χ_{c2} CEP signal by the photon-conversion
 2003 efficiency vs. $p_T(\gamma)$ distribution of Fig. 5.13. The dominant systematic uncertainty in this
 2004 procedure is a relative $\pm 8\%$ associated with the knowledge of the produced number of D^{*0}
 2005 mesons in the sample. We shall then apply a further correction factor to the corrected yield
 2006 of 0.50 ± 0.10 to account for the difference in multiplicity between the calibration and signal
 2007 samples.

2008 5.2 Muon-reconstruction efficiencies

2009 The muon-pair reconstruction efficiencies have been calculated for CEP conditions using 2015
 2010 data in an earlier study of J/ψ and $\psi(2S)$ production [43]. This study employed the same muon
 2011 trigger lines and muon fiducial cut, $2 < \eta < 4.5$, used in our CEP χ_c analysis. In the CEP J/ψ
 2012 and $\psi(2S)$ study, the reconstruction efficiency, ε_{Rec} , is defined such that,

$$\varepsilon_{\text{Rec}} = \varepsilon_{\text{Track}} \times \varepsilon_{\mu\text{Acc}} \times \varepsilon_{\mu\text{ID}} \times \varepsilon_{\text{Trig}} \times f_{\text{Rec}}, \quad (5.8)$$

2013 where $\varepsilon_{\text{Track}}$ is the tracking efficiency for two tracks to be reconstructed inside the fiducial
 2014 region, $2 < \eta < 4.5$, $\varepsilon_{\mu\text{Acc}}$ is the efficiency for both of the tracks to be inside the muon chamber
 2015 acceptance, $\varepsilon_{\mu\text{ID}}$ is the muon-identification efficiency, given by the fraction of muons traversing
 2016 the muon chamber that are reconstructed as muons, and $\varepsilon_{\text{Trig}}$ is the trigger efficiency, which is
 2017 defined as the fraction of events with two identified muons that fire the relevant hardware and
 2018 software triggers. Throughout this study, we will refer to the product of these efficiencies as the
 2019 *dimuon efficiency*. In Ref. [43] these efficiencies were calculated as a function of the J/ψ rapidity
 2020 using simulation and were then corrected to bring Monte Carlo and data into agreement using a
 2021 rapidity-dependent scale factor, f_{Rec} , obtained from a ‘tag-and-probe’ study performed on data.
 2022 The efficiencies and correction factors are tabulated in Table 5.6, with their distributions shown
 2023 in Fig. 5.19. We use this 2015 efficiency as a reference point in our analysis. However, we must
 2024 adjust this measurement slightly to be suitable for the conditions of the 2015 and 2016 χ_c study.

Table 5.6. Summary of the track ($\varepsilon_{\text{Track}}$), muon-chamber acceptance ($\varepsilon_{\mu\text{Acc}}$), muon identification ($\varepsilon_{\mu\text{ID}}$), and trigger ($\varepsilon_{\text{Trig}}$) efficiencies calculated using SuperChic Monte Carlo of exclusive J/ψ production for 2015 run conditions, and the scaling factor (ε_{Rec}) applied to the simulation in order to match data and calculate the muon data-reconstruction efficiency (ε_{Rec}). These values are reproduced from Ref. [43]. There follow quantities determined in the current analysis: R_N , which is the measured ratio of J/ψ events between 2015 and 2016 data samples, and $\varepsilon_{\mu\mu15}$ and $\varepsilon_{\mu\mu16}$, which are the total dimuon efficiencies in data (including all the contributions above) for 2015 and 2016, respectively.

y	[2.0, 2.25]	[2.25, 2.5]	[2.5, 2.75]	[2.75, 3.0]	[3.0, 3.25]
$\varepsilon_{\text{Track}}$	0.624 ± 0.018	0.770 ± 0.009	0.812 ± 0.007	0.861 ± 0.005	0.877 ± 0.005
$\varepsilon_{\mu\text{Acc}}$	0.789 ± 0.019	0.860 ± 0.009	0.896 ± 0.006	0.907 ± 0.005	0.887 ± 0.005
$\varepsilon_{\mu\text{ID}}$	0.986 ± 0.006	0.979 ± 0.004	0.966 ± 0.004	0.952 ± 0.004	0.944 ± 0.004
$\varepsilon_{\text{Trig}}$	0.790 ± 0.022	0.797 ± 0.011	0.805 ± 0.008	0.797 ± 0.007	0.820 ± 0.006
f_{Rec}	1.070 ± 0.063	1.016 ± 0.042	0.981 ± 0.032	0.952 ± 0.026	0.934 ± 0.024
ε_{Rec}	0.410 ± 0.031	0.524 ± 0.024	0.555 ± 0.020	0.564 ± 0.017	0.562 ± 0.016
$f_{\mu\varepsilon15}$	0.973 ± 0.086	0.930 ± 0.042	0.955 ± 0.034	1.004 ± 0.030	1.044 ± 0.029
R_N	0.143 ± 0.007	0.151 ± 0.004	0.148 ± 0.003	0.158 ± 0.003	0.165 ± 0.003
$\varepsilon_{\mu\mu15}$	0.399 ± 0.046	0.488 ± 0.032	0.530 ± 0.027	0.566 ± 0.024	0.586 ± 0.023
$\varepsilon_{\mu\mu16}$	0.485 ± 0.061	0.562 ± 0.039	0.622 ± 0.034	0.622 ± 0.029	0.617 ± 0.026
y	[3.25, 3.5]	[3.5, 3.75]	[3.75, 4.0]	[4.0, 4.25]	[4.25, 4.5]
$\varepsilon_{\text{Track}}$	0.897 ± 0.004	0.916 ± 0.004	0.925 ± 0.005	0.913 ± 0.007	0.900 ± 0.013
$\varepsilon_{\mu\text{Acc}}$	0.871 ± 0.005	0.850 ± 0.006	0.818 ± 0.007	0.779 ± 0.011	0.763 ± 0.020
$\varepsilon_{\mu\text{ID}}$	0.935 ± 0.004	0.932 ± 0.004	0.921 ± 0.006	0.905 ± 0.009	0.888 ± 0.017
$\varepsilon_{\text{Trig}}$	0.869 ± 0.006	0.902 ± 0.005	0.925 ± 0.006	0.935 ± 0.008	0.950 ± 0.012
f_{Rec}	0.924 ± 0.023	0.915 ± 0.024	0.911 ± 0.026	0.914 ± 0.030	0.893 ± 0.037
ε_{Rec}	0.587 ± 0.016	0.599 ± 0.017	0.587 ± 0.019	0.550 ± 0.021	0.517 ± 0.029
$f_{\mu\varepsilon15}$	1.030 ± 0.029	1.068 ± 0.032	1.099 ± 0.096	1.065 ± 0.122	1.126 ± 0.099
R_N	0.166 ± 0.003	0.171 ± 0.003	0.171 ± 0.003	0.164 ± 0.004	0.171 ± 0.008
$\varepsilon_{\mu\mu15}$	0.604 ± 0.023	0.639 ± 0.027	0.645 ± 0.060	0.586 ± 0.071	0.583 ± 0.061
$\varepsilon_{\mu\mu16}$	0.633 ± 0.027	0.650 ± 0.029	0.657 ± 0.0624	0.622 ± 0.077	0.592 ± 0.068

2025 By comparing the yield of J/ψ events we select in 2015, $N(J/\psi)_B$, with those of the
2026 earlier analysis, $N(J/\psi)_A$, we are able to determine the efficiency of our selection, since the
2027 muon-reconstruction efficiency for our 2015 sample is given by $\varepsilon_{\mu\mu15} = f_{\mu\varepsilon15} \times \varepsilon_{\text{Rec}}$, where
2028 $f_{\mu\varepsilon15} = N(J/\psi)_B/N(J/\psi)_A$. The selection criteria in the earlier paper are summarised in
2029 Table 5.7. In our analysis we replace the software trigger requirements, which are conditional on
2030 the state of the low-multiplicity hadron trigger decision called `L0Hadron`, `lowMult`, with a pass on
2031 either the `Hlt2LowMultDimuon` or `Hlt2LowMultMuon` trigger line detailed in Table 4.3 in order to
2032 match our χ_c analysis requirement. In performing this study we also need to reproduce as closely
2033 as possible the HERSCHEL working point adopted in the earlier analysis. The aforementioned
2034 paper used a different method and calibration to calculate $\ln(\chi_{\text{HRC}}^2)$. Therefore, using our
2035 HERSCHEL figure-of-merit efficiency results presented later in Sec. 5.6, we select a threshold
2036 of $\ln(\chi_{\text{HRC}}^2) < 5$. This is the same requirement used in the main χ_c analysis, which has an

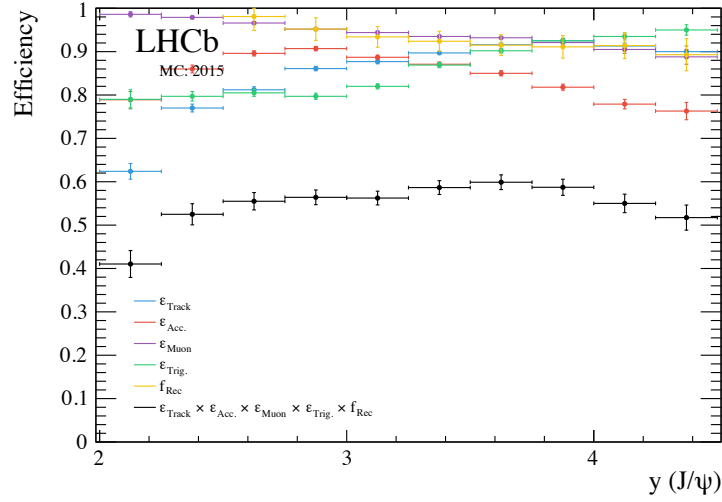


Figure 5.19. Track ($\varepsilon_{\text{Track}}$ in blue), muon chamber acceptance ($\varepsilon_{\mu\text{Acc}}$ in red), muon identification ($\varepsilon_{\mu\text{ID}}$ in purple), and trigger efficiencies calculated ($\varepsilon_{\text{Trig}}$ in green) using SuperChic Monte Carlo of exclusive J/ψ production for 2015 run conditions and the global scaling factor (f_{Rec} in yellow) applied to the simulation in order to match data and calculate the muon data-reconstruction efficiency (ε_{Rec} in black).

2037 efficiency of 0.704 ± 0.018 (see Sec. 5.6), to match the $\ln(\chi_{\text{HRC}}^2) < 3.5$ cut used in the CEP J/ψ
 2038 analysis, which in turn has an efficiency of 0.723 ± 0.008 .

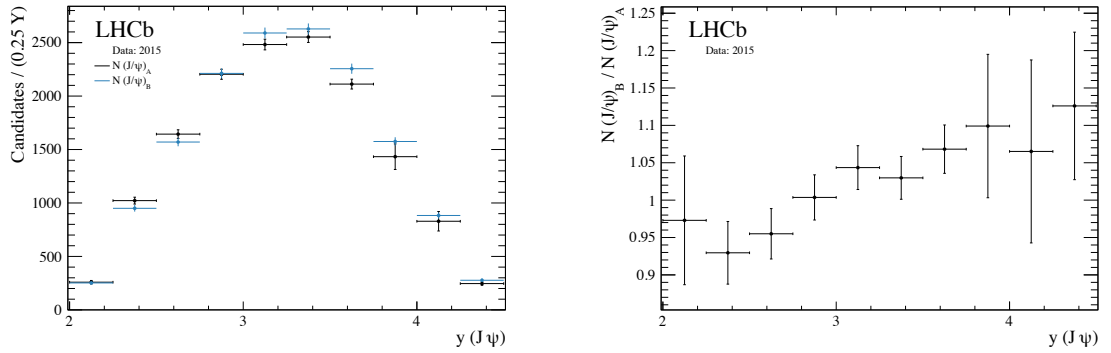


Figure 5.20. J/ψ yield as a function of rapidity (left) from CEP J/ψ results [43], $N(J/\psi)_A$ in black, together with the results from our modified selection, $N(J/\psi)_B$ in blue, for 2015 data, run numbers 164524 to 167136. Correction factor for 2015 data, $f_{\mu\varepsilon 15}$ (right).

2039 The J/ψ yields, $N(J/\psi)_B$ and $N(J/\psi)_A$, are shown in Fig. 5.20 in bins of rapidity alongside
 2040 their ratio and their values are tabulated in Table 5.6. We see that there is a difference
 2041 in the total selection efficiency between the two analyses that varies with rapidity and does
 2042 not exceed 10%. Globally, the yields integrated over all rapidity bins for each sample is
 2043 $N(J/\psi)_A \text{ Total} = 14783 \pm 122$ and $N(J/\psi)_B \text{ Total} = 15193 \pm 123$, making our selection more
 2044 efficient. The corrected muon-reconstruction efficiency for 2015 is shown in Fig. 5.21 (black).

Table 5.7. Selection criteria used in CEP J/ψ analysis from Ref. [43], selection criteria applied to 2015 data to compare with results from the CEP J/ψ paper, and selection criteria applied to both 2015 and 2016 data used to compare muon-reconstruction efficiency between the two years.

Trigger Level	J/ψ paper	2015 J/ψ	2016 J/ψ	
L0 Trigger	L0Muon, lowMult or L0DiMuon, lowMult	L0Muon, lowMult or L0DiMuon, lowMult	L0Muon, lowMult or L0DiMuon, lowMult	
HLT1	Pass through	Pass through	Pass through	
HLT2	If !L0Hadron, lowMult then Hlt2LowMultMuon If L0Hadron, lowMult then Hlt2LowMultChiC2HH	Hlt2LowMultMuon or Hlt2LowMultDiMuon	Hlt2LowMultMuon or Hlt2LowMultDiMuon	
Variable	Units	Cut		
$m_{\mu^+\mu^-}$ window	MeV/ c^2	$ m_{\mu^+\mu^-} - 3097 < 65$	$ m_{\mu^+\mu^-} - 3097 < 65$	$ m_{\mu^+\mu^-} - 3097 < 50$
N^{O} photons	-	0 with $E_T > 200$ MeV	0 with $E_T > 200$ MeV	0 with $E_T > 200$ MeV
N^{O} upstream tracks	-	0	0	0
N^{O} VELO tracks	-	0	0	0
N^{O} backward tracks	-	0	0	0
N^{O} downstream tracks	-	0	0	0
N^{O} long tracks	-	2 ($\mu^+\mu^-$)	2 ($\mu^+\mu^-$)	2 ($\mu^+\mu^-$)
N^{O} muon tracks	-	2 ($\mu^+\mu^-$)	2 ($\mu^+\mu^-$)	2 ($\mu^+\mu^-$)
Muon ID	-	True	True	True
$p_{\text{T}}^2(\mu^+\mu^-)$	[GeV/ c] 2	< 0.8	< 0.8	< 0.5
$\eta(\mu)$	-	$\in [2, 4.5]$	$\in [2, 4.5]$	$\in [2, 4.5]$
$\ln(\chi_{\text{HRC}}^2)$	-	< 3.5	< 5	< 5
$p_{\text{T}}(\mu)$	MeV/ c	-	-	> 200 or Max > 800
N^{O} SPD Hits	-	-	-	< 20

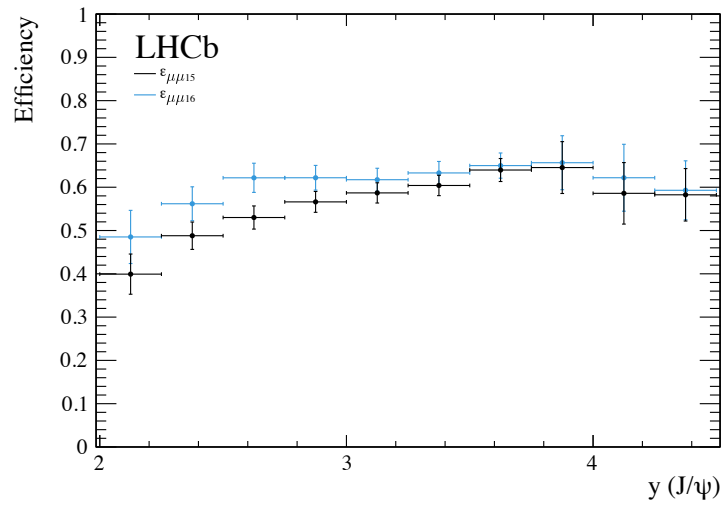


Figure 5.21. Dimuon-reconstruction efficiency for 2015 (black), $\epsilon_{\mu\mu15}$, and 2016 (blue), $\epsilon_{\mu\mu16}$, run conditions.

2045 It is now necessary to understand whether there are differences between the selection
 2046 efficiency for 2015 and 2016. To determine if this is the case, we apply the same nominal
 2047 selections to both years and compare the ratio of reconstructed CEP-like J/ψ events between
 2048 the years with the ratio of their integrated luminosities. If the efficiency is the same, we expect
 2049 these ratios to be the same. To account for any differences, the dimuon efficiency for 2016 is
 2050 given by $\varepsilon_{\mu\mu 16} = \varepsilon_{\mu\mu 15} \times R_{\mathcal{L}} / R_N$, where $R_{\mathcal{L}}$ is the integrated-luminosity ratio of 2015 to 2016
 2051 data of single interaction crossings¹, and R_N is the J/ψ yield ratio from 2015 and 2016 data.

2052 We use a similar selection as the one detailed above with a few exceptions: we tighten the
 2053 J/ψ mass-window cut to match the one used in our χ_c study, and we tighten the upper cut on the
 2054 $p_T^2(J/\psi)$ to increase the CEP purity of the sample. In addition, some changes were implemented
 2055 to the hardware trigger for the 2016 runs. This included the tightening of the number of SPD
 2056 hit requirements from < 30 to < 20 hits for both `L0DiMuon, lowMult` and `L0Muon, lowMult` trigger
 2057 lines. The `L0Muon, lowMult` trigger line requires a muon with a momentum greater than 800
 2058 MeV/ c compared to 400 MeV/ c . As a result, we apply these tighter cuts on the 2015 sample to
 2059 have a uniform selection between samples. The J/ψ selection is summarised in Table 5.7.

2060 We find that the global value of R_N is 0.1624 whereas $R_{\mathcal{L}}$ is 0.1739. Hence the 2016 efficiency
 2061 is seen to be 7% more efficient than 2015. The J/ψ yield for 2015 and 2016 is shown in Fig. 5.22
 2062 alongside their ratio in bins of J/ψ rapidity. As the rapidity dependence is significant, we apply
 2063 the correction factor to go from 2015 to 2016 efficiency in bins of this quantity. The corrected
 2064 muon reconstruction efficiency for 2016 is shown in Fig. 5.21 and the values are tabulated in
 2065 Table 5.6.

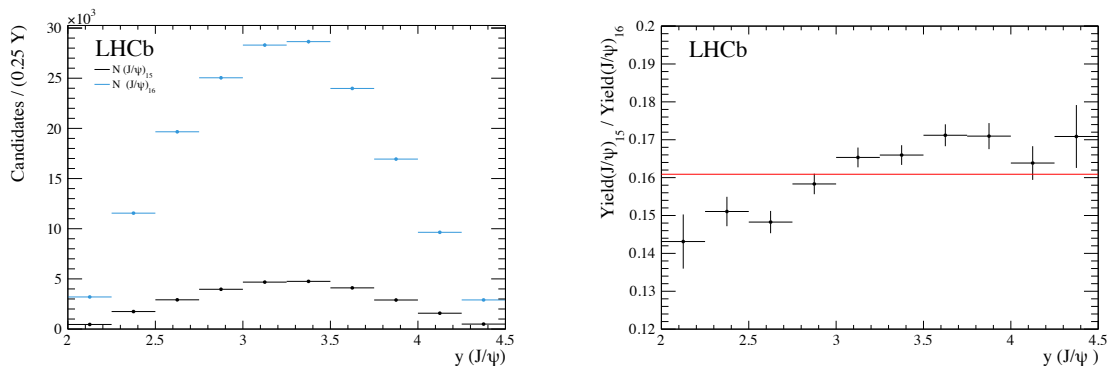


Figure 5.22. J/ψ yield as a function of rapidity (left) for two muon-track events for 2015, $N(J/\psi)_{15}$ in black, and 2016, $N(J/\psi)_{16}$ in blue, together with their ratio (right) R_N .

2066 To calculate a global dimuon efficiency, which accounts for the distribution in rapidity, we
 2067 correct each χ_c signal candidate for efficiency according to its rapidity bin, and then divide
 2068 the number of candidates in the original sample by the corrected total. This yields a global
 2069 dimuon efficiency of 0.611 (0.635) with the HERSCHEL cut applied for 2015 (2016) data and

¹We assume there is negligible uncertainty on this ratio, as the bulk of the luminosity systematic will be fully correlated between years.

2070 0.607 (0.635) without. This corresponds to a global dimuon efficiency of 0.631 for the combined
 2071 data set both with and without the HERSCHEL cut applied, once these individual numbers are
 2072 weighted by the integrated luminosities of each year.

2073 The systematic uncertainty on the trigger and dimuon efficiency as determined in Ref. [43]
 2074 is 0.2% and 0.4%, respectively. However, the uncertainty we assign is necessarily larger, and is
 2075 dominated by the change in efficiency between 2015 and 2016, which is not fully understood.
 2076 We assign the full value of this change as a systematic uncertainty in the 2016 analysis, which
 2077 then corresponds to an uncertainty of 5% on the combined 2015 and 2016 analysis.

2078 5.3 J/ψ mass-window efficiency

2079 We apply a J/ψ mass-window cut, $|m(J/\psi) - 3096.916| < 50 \text{ MeV}/c^2$, to reduce contamination
 2080 from di-muon continuum background. Since there is a slight difference in the J/ψ mass resolution
 2081 in Monte Carlo and data, we use a data-driven method to calculate the efficiency associated
 2082 with this cut, $\varepsilon_{m(J/\psi)}$. We employ a similar J/ψ selection as the one used for the 2015 and 2016
 2083 muon-reconstruction efficiency comparison tabulated in Table 5.7. However, we omit the SPD
 2084 and muon transverse-momentum requirements, since these cuts were only intended to make a
 2085 one-to-one comparison between 2015 and 2016 data samples and are not part of the χ_c analysis.
 2086 Similarly, we omit the photon cut as we expect to see extra photons in $\chi_c \rightarrow J/\psi [\mu^+ \mu^-] \gamma [e^+ e^-]$
 2087 events from bremsstrahlung radiation.

2088 To fit the J/ψ mass distribution, we use a Gaussian and a double-sided Crystal Ball with a
 2089 shared mean value. The ratio of the Gaussian yield and the double-sided Crystal Ball yield
 2090 is fixed according to the results of these fits on CEP $\chi_{c1,2} \rightarrow J/\psi [\mu^+ \mu^-] \gamma [e^+ e^-]$ Monte Carlo
 2091 described in Sec. 4.1 while keeping all other parameters free. Applying this constraint, we
 2092 perform an unbinned-maximum-likelihood fit of the data samples over the 2750 to 3450 MeV
 2093 mass range, the results of which are shown in Fig. 5.23. The fit does a good job at describing
 2094 the slightly skewed shape of the J/ψ resonance. The normalised integral of the J/ψ signal shape
 2095 within our selection mass window is 0.954 ± 0.002 (0.955 ± 0.002) for 2016 (2015 and 2016).

2096 As a systematic check, we repeat the fit using a single double-sided Crystal Ball to model the
 2097 J/ψ signal while maintaining a single exponential to model the background. The fit results are
 2098 shown in Fig. 5.23 for 2016-only, and the combined 2015 and 2016 data samples. The normalised
 2099 integral of the J/ψ signal shape over our selection mass window is 0.958 ± 0.002 (0.958 ± 0.002) for
 2100 2016 (2015 and 2016). We take the difference between the two sets of results as the systematic
 2101 uncertainty, corresponding to 0.4% (0.3%) for the 2016 (2015 and 2016) data.

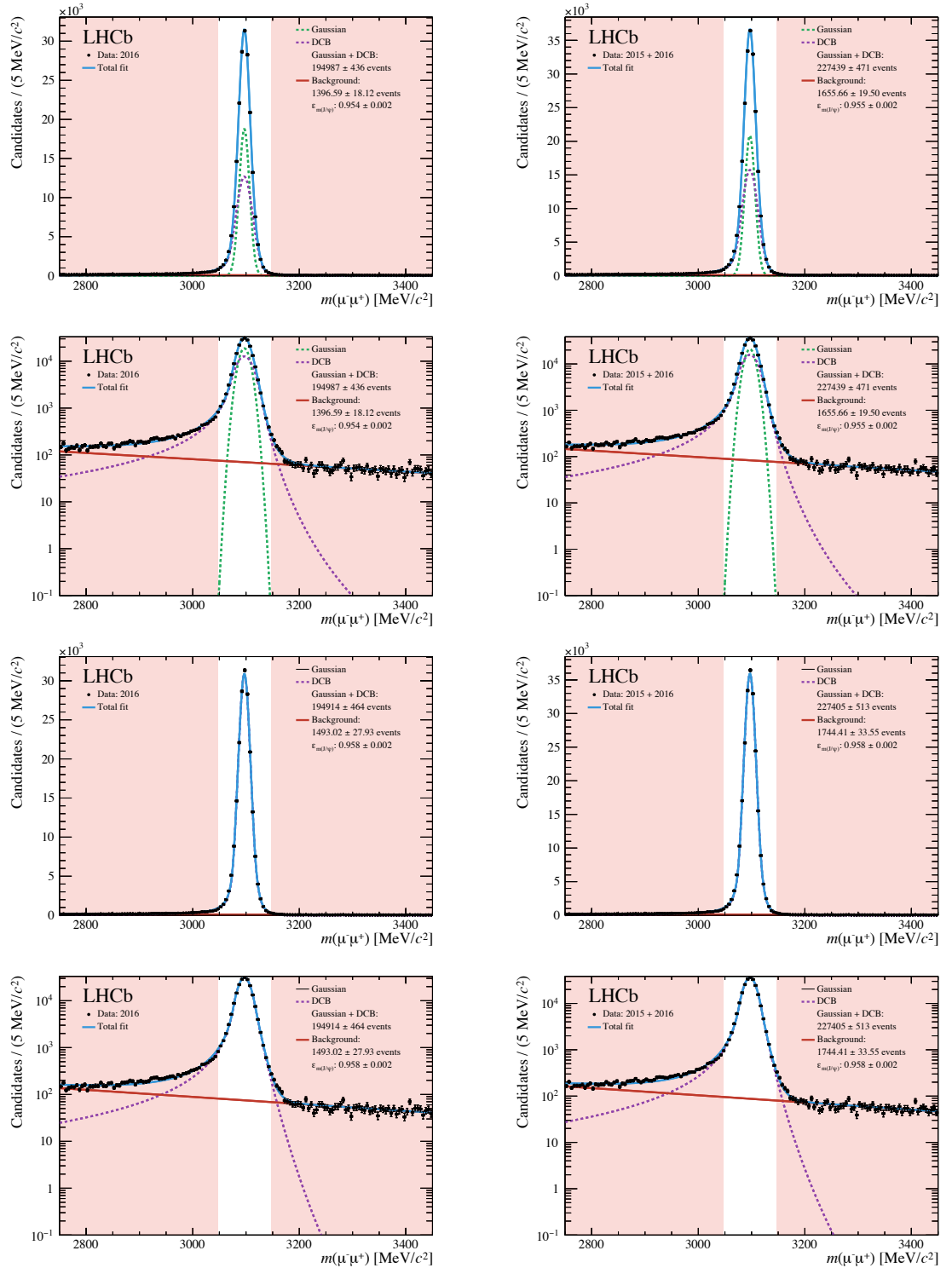


Figure 5.23. Invariant mass of CEP like $J/\psi \rightarrow \mu^+\mu^-$ mesons from proton-proton collisions at a centre-of-mass energy $\sqrt{s} = 13$ TeV for the 2016-only (left), and combined 2015 and 2016 (right) data in linear (first and third row) and logarithmic (second and fourth row) scale. In the first and second row the signal is fitted with the combination of double-sided Crystal Ball (dashed purple) and a Gaussian (dashed green) while in the third and fourth row it is fitted with a double-sided Crystal Ball. The continuum-combinatorial background is fitted with an exponential (dotted red). Integrals for events within our selection mass window are shown and the veto region is highlighted in red.

2102 5.4 χ_c invariant-mass-difference window-selection efficiency

2103 As part of our analysis, we apply a cut to the mass difference between the χ_c candidate and the
 2104 intermediate J/ψ meson, $350 < \Delta m_{\chi_c} < 500$. Therefore, when measuring the χ_{c1} and χ_{c2} yields
 2105 we have to account for the cut efficiency for each meson, $\varepsilon_{\Delta m_{\chi_{c1}}}$ and $\varepsilon_{\Delta m_{\chi_{c2}}}$ respectively. To
 2106 calculate the efficiency, we use the reconstructed CEP χ_c Monte Carlo, described in Sec. 4.1.4,
 2107 with our CEP χ_c selection applied. The Δm_{χ_c} distribution of the selected events is shown
 2108 in Fig. 5.24 for the 2016-only, and combined 2015 and 2016 run conditions together with the
 2109 delta-mass vetoed regions highlighted in red.

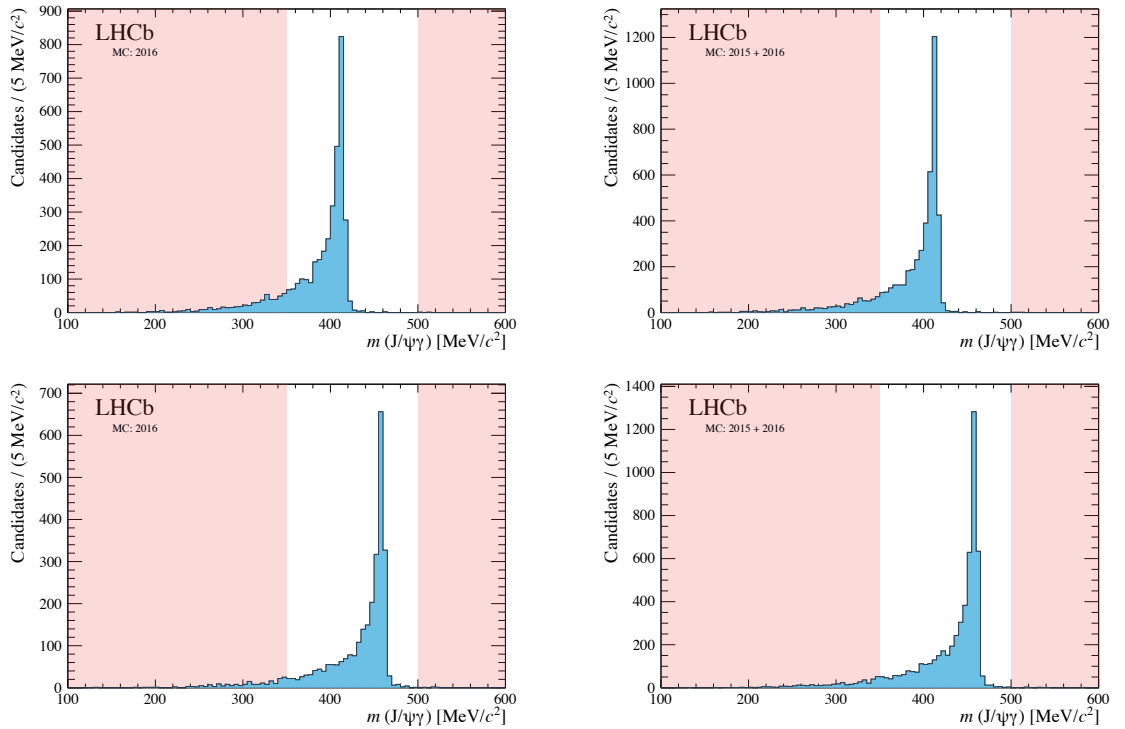


Figure 5.24. Delta-mass distribution from reconstructed CEP χ_{c1} (top) and χ_{c2} (bottom) Monte Carlo generated with SuperChic v2 for the 2016-only, and combined 2015 and 2016 run conditions. The delta-mass veto region is highlighted in red.

2110 It is important to note that these distributions correspond to reconstructed events, and it is
 2111 possible for the reconstruction efficiency of converted photons to be different in Monte Carlo
 2112 and data. The efficiency of the photon reconstruction varies with transverse momentum. If
 2113 the p_T distribution of those events below the cut in delta mass is different from those events
 2114 within the window, and if the dependence of the reconstruction efficiency with p_T is different
 2115 between data and Monte Carlo, then the determination of the window-selection efficiency will
 2116 be biased. To account for any differences, we calculate the photon-conversion efficiency using
 2117 the Monte Carlo, the distributions of which are shown as a function of the photon's transverse
 2118 momentum in Fig. 5.25 for 2016-only, and combined 2015 and 2016 run conditions. The photon-
 2119 conversion efficiency determined from data grows more steeply than that of the Monte Carlo.

2120 We then correct the delta-mass distribution for the Monte Carlo photon-conversion efficiency
 2121 and apply the efficiency determined using the data-driven method described in Sec. 5.1, such
 2122 that the distribution is now representative of that reconstructed in data. By integrating the
 2123 Δm_{χ_c} distribution within our selection window we determine the cut to have an efficiency of
 2124 0.885 ± 0.017 (0.892 ± 0.015) for χ_{c1} mesons and 0.944 ± 0.021 (0.948 ± 0.015) for χ_{c2} for the
 2125 2016-only (combined 2015 and 2016) data.

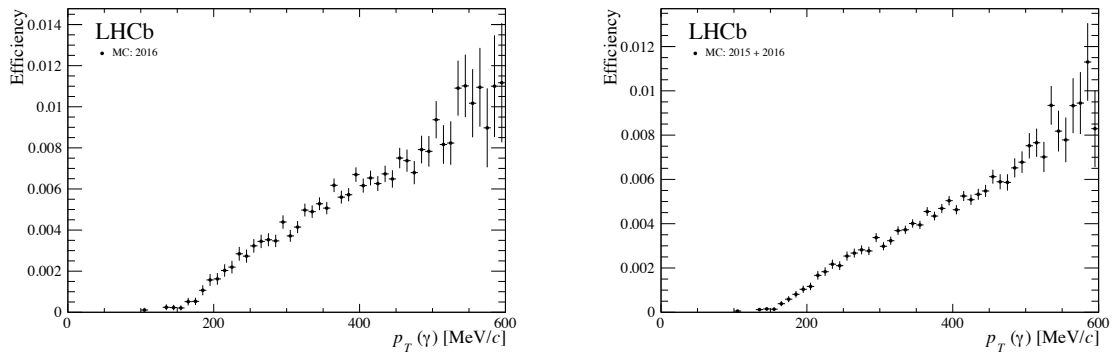


Figure 5.25. Photon-conversion efficiency as a function of the photon's generator-level transverse momentum using combined CEP χ_{c1} and χ_{c2} Monte Carlo for the 2016-only (left), and combined 2015 and 2016 (right) run conditions.

2126 As a systematic check we determine the mass-window efficiency directly from Monte Carlo,
 2127 that is with the photon-reconstruction efficiencies displayed in Fig. 5.25. By taking the fraction
 2128 of events that fall within our selection window we determine the window cut efficiency to be
 2129 0.851 ± 0.014 (0.856 ± 0.012) for χ_{c1} mesons and 0.928 ± 0.017 (0.923 ± 0.012) for χ_{c2} for the
 2130 2016-only (combined 2015 and 2016) data. As a result, we assign an uncertainty of 3.8% (4.0%)
 2131 for χ_{c1} and 1.7% (2.7%) for χ_{c2} for the 2016-only (combined 2015 and 2016) data.

2132 A further source of possible bias would be if the χ_c resolution of the Monte Carlo is
 2133 significantly different from that in the data. This is not the case, as can be seen in Fig. 5.26,
 2134 where we compare the function fitted to the data with the χ_{c1} and χ_{c2} Monte Carlo distributions.
 2135 Although the fit undershoots the Monte Carlo at the core, the tail is well described. Nonetheless,
 2136 exercises are performed in which additional smearing is introduced to the Monte Carlo, such
 2137 that the agreement with data remains tolerable. No significant change in the fraction of events
 2138 in the veto region is observed.

2139 5.5 SPD efficiency

2140 As part of the low-multiplicity hardware trigger lines, we use the number of SPD hits as an
 2141 indicator of the detector occupancy. Characteristically, CEP events have a low number of
 2142 final-state particles and will leave few SPD hits. However, due to the short 25 ns bunch spacing,
 2143 this detector is sensitive to remnant signatures from collisions of adjacent beam crossings, known
 2144 as spill-over and pre-spill. The `L0Muon`, `lowMult` and the `L0DiMuon`, `lowMult` hardware trigger lines
 2145 require less than thirty SPD hits for 2015 data and less than twenty for 2016. To estimate the

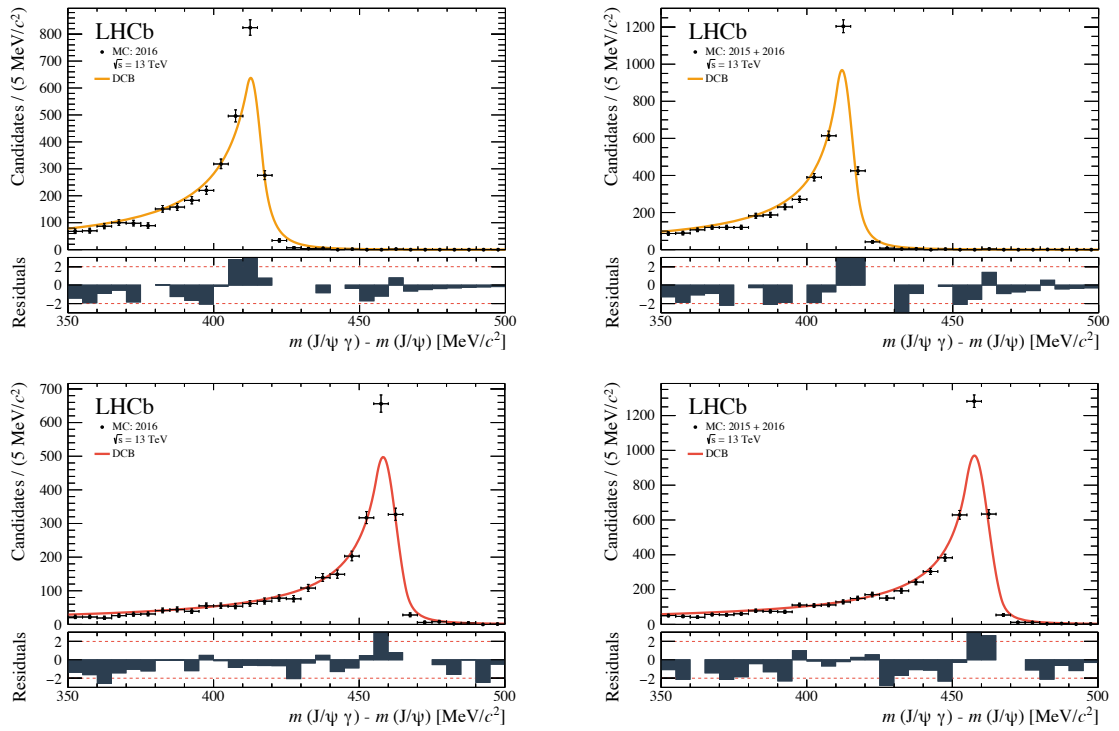


Figure 5.26. Delta-mass distribution from χ_{c1} (top) and χ_{c2} (bottom) Monte Carlo for the 2016-only (left), and combined 2015 and 2016 (right) run conditions. The distributions are fitted with the functions fitted to data.

2146 impact of the SPD cut on the efficiency of our χ_c selection, we model the SPD distribution
 2147 of an empty detector, as well as the separate contribution of muons from the J/ψ decay and
 2148 electrons from the photon conversion.

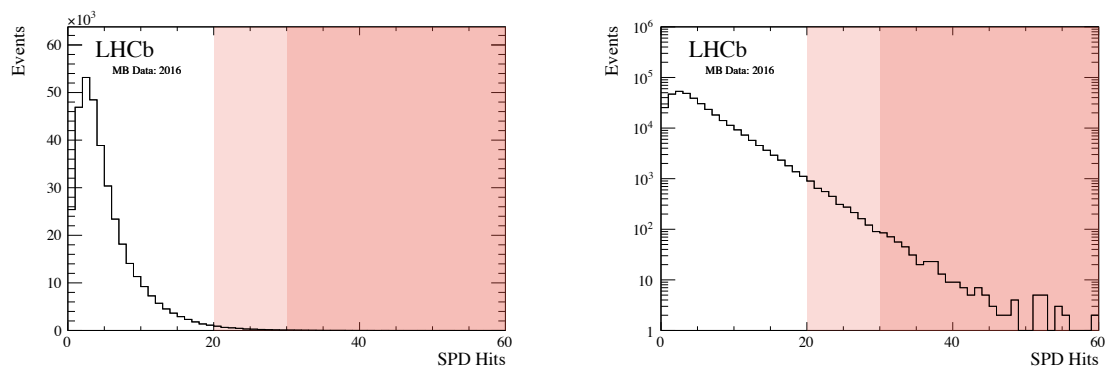


Figure 5.27. Distribution of SPD hits in randomly triggered empty events with zero tracks and photons in linear (left) and logarithmic scale (right) for 2016 data. The SPD veto regions for the $L0\mu\text{Muon}$, $low\text{Mult}$ and $L0\text{DiMuon}$, $low\text{Mult}$ trigger lines is highlighted in red for 2015 and pink for 2016 run conditions.

2149 To estimate the extra activity in the detector (detector noise, spill-over, and pre-spill), we
 2150 use randomly-triggered events and select those with zero reconstructed tracks and photons.

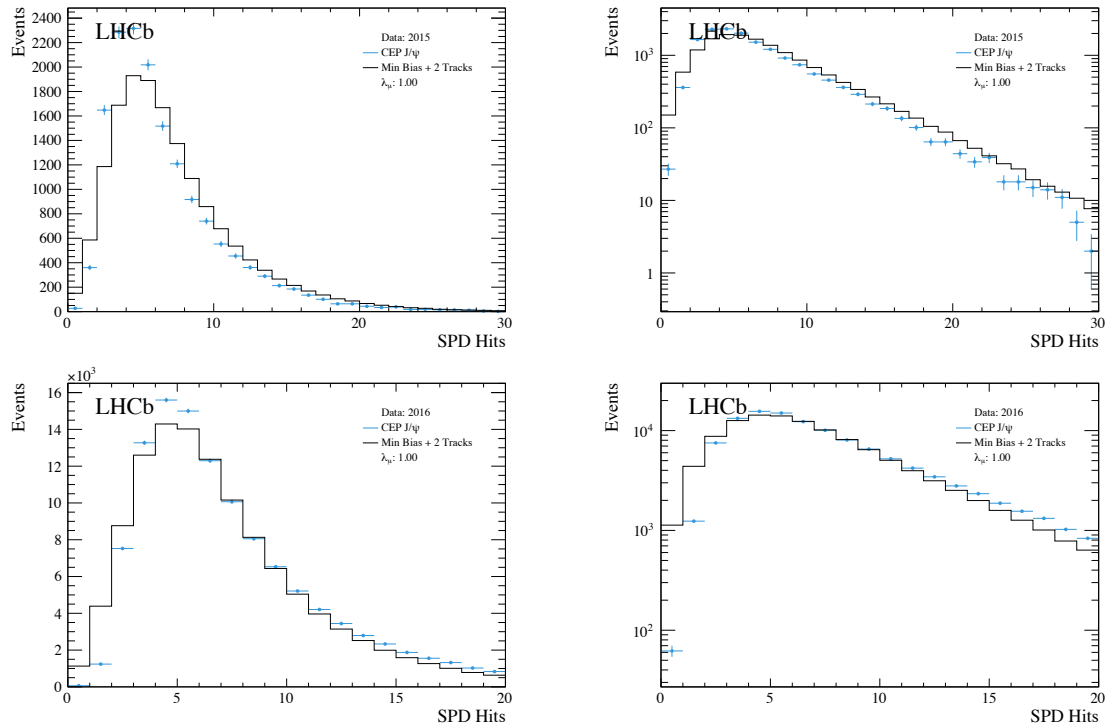


Figure 5.28. Distribution of SPD hits of CEP J/ψ candidates (blue) and of randomly triggered events with zero tracks and photons, added to a simple model that describes the interaction of muons assuming a Poisson distribution with a mean of one ($\lambda_\mu = 1$) for 2015 (top) and 2016 (bottom) data shown in linear (left) and logarithmic (right) scale.

2151 The SPD distribution for these empty events is shown in Fig. 5.27 for 2016 data in linear and
 2152 logarithmic scale. We expect muons to leave about one hit in the SPD. To model this, we
 2153 assume a Poisson distribution with a mean of one ($\lambda_\mu = 1$) for each muon and add it to the
 2154 noise distribution extracted from the minimum-bias sample. We check the model against the
 2155 CEP J/ψ sample used to compare the muon reconstruction efficiency of 2015 and 2016 data
 2156 described in Table 5.7 but with the additional requirement that there are no photons in the
 2157 event. The SPD distribution of this sample and our SPD model are shown in Fig. 5.28. This
 2158 method adequately models the right tail region, where our interest lies, although less well so for
 2159 lower SPD hit values.

2160 We expect electrons to generate more hits on the SPD than muons because of bremsstrahlung
 2161 radiation and material interactions. We can estimate the number of hits expected from electrons
 2162 using Monte Carlo, where we expect this aspect of the SPD response to be adequately described.
 2163 We use the truth matched $\chi_{c1,2} \rightarrow J/\psi[\mu^+\mu^-]\gamma[e^+e^-]$ Monte Carlo, described in Sec. 4.1, with
 2164 our CEP χ_c selection applied. The SPD distribution for this selection is shown in Fig. 5.29.
 2165 Note that this distribution has less of a spillover tail than that of Fig. 5.28 due to the absence
 2166 of noise, pre spill, and spill over in the simulated sample. Given our previous determination

2167 of approximately one SPD hit per muon, we estimate an additional average of two hits per
 2168 electron is required to model the distribution.

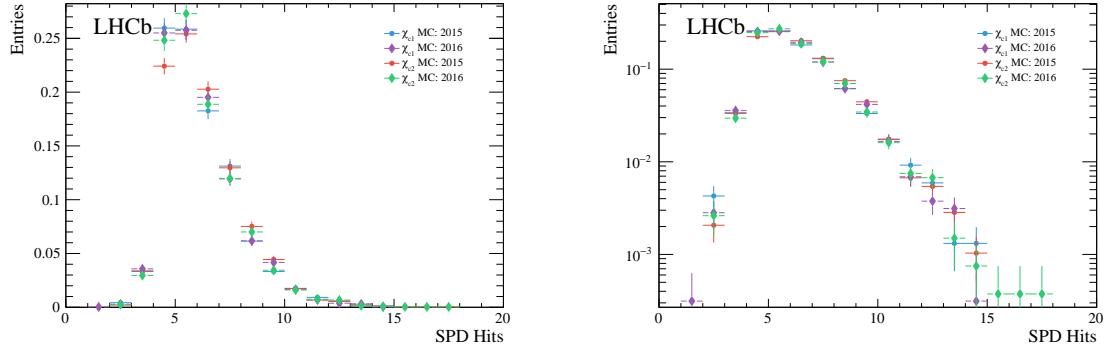


Figure 5.29. Normalised distribution of SPD hits of CEP χ_{c1} (blue and purple) and χ_{c2} (red and green) candidates from 2015 (dots) and 2016 (diamonds) Monte Carlo with CEP χ_c selections applied.

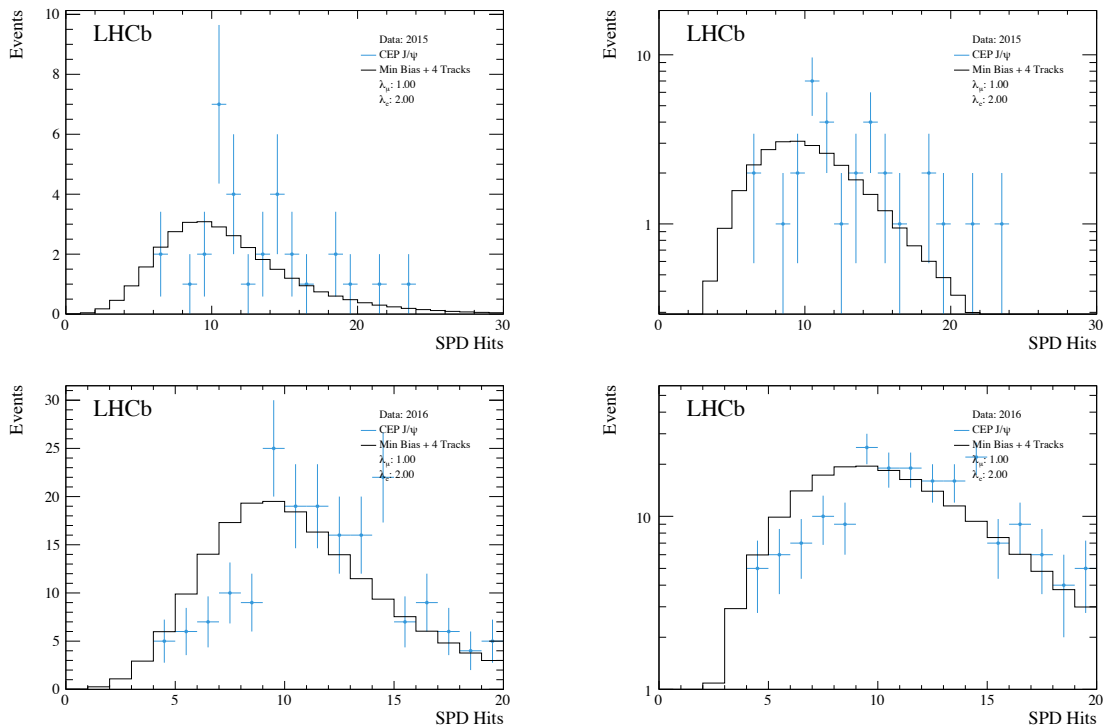


Figure 5.30. Distribution of SPD hits of CEP χ_c candidates (blue) and a model composed of randomly triggered 2016 events with zero tracks and photons added to a model that describes the interaction of muons assuming a Poisson distribution with a mean of one (black), and that of electrons with a Poisson distribution with a mean of two for 2015 (top) and 2016 (bottom) data shown in linear (left) and logarithmic (right) scale.

2169 With this in mind, we repeat the procedure detailed above and add a Poisson distribution
 2170 with a mean of two ($\lambda_e = 2$) for each electron in the χ_c decay to the J/ψ plus additional-activity

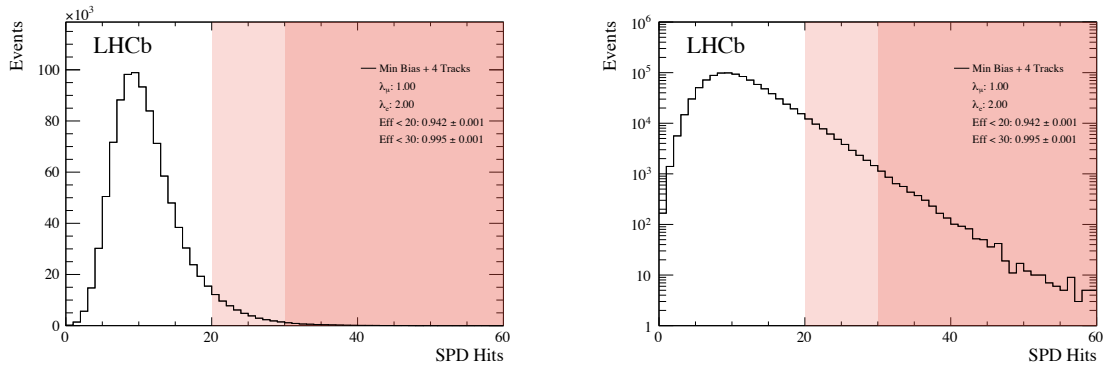


Figure 5.31. Distribution of SPD hits model based on randomly triggered 2016 events with zero tracks and photons added to a model that describes the interaction of muons assuming a Poisson distribution with a mean of one (black), and that of electrons with a Poisson distribution with a mean of two in linear (left) and logarithmic (right) scale.

Table 5.8. SPD efficiencies for the reconstruction of CEP-like χ_c events using different λ_μ and λ_e values in our SPD distribution model for 2015 and 2016 hardware trigger requirements.

λ_μ	λ_e	< 20 SPD Hits	< 30 SPD Hits
	1	0.970 ± 0.001	0.997 ± 0.001
0.75	2	0.949 ± 0.001	0.995 ± 0.001
	3	0.914 ± 0.001	0.992 ± 0.001
	1	0.966 ± 0.001	0.997 ± 0.001
1	2	0.942 ± 0.001	0.994 ± 0.001
	3	0.902 ± 0.001	0.991 ± 0.001
	1	0.961 ± 0.001	0.996 ± 0.001
1.25	2	0.933 ± 0.001	0.994 ± 0.001
	3	0.888 ± 0.001	0.989 ± 0.001

2171 model. The resulting model for χ_c events is presented together with the SPD hit distribution
 2172 from χ_c data for 2015 and 2016 samples, shown in Fig. 5.30. We obtain a reasonable description
 2173 of the right tail. We then generate a large sample with one million events, shown in Fig. 5.31,
 2174 and take a normalised integral from zero to thirty (twenty) to calculate an SPD efficiency, ε_{SPD} ,
 2175 of 0.994 ± 0.001 (0.942 ± 0.001) for 2015 (2016). We weight the efficiency of each year by its
 2176 corresponding single-interaction luminosity, the calculation of which is described in Sec. 7.5, to
 2177 yield a SPD efficiency of $\varepsilon_{\text{SPD}} = 0.950 \pm 0.001$ for the combined 2015 and 2016 data set.

2178 As a systematic check we vary the mean number of hits for muons by ± 0.25 and electrons
 2179 by ± 1 , the results for which are summarised in Table 5.8. We assign a systematic uncertainty
 2180 of ± 0.005 (± 0.05) for 2015 (2016) data. This corresponds to a combined uncertainty of ± 0.04
 2181 for the combined 2015 and 2016 data set.

2182 5.6 HERSCHEL efficiency

2183 To combine the response of all twenty HERSCHEL counters, four for each of the five modules, we
 2184 construct a figure-of-merit quantity, $\ln(\chi_{\text{HRC}}^2)$, as defined in Eq. 4.5, where low values correspond
 2185 to CEP-like events and high values correspond to non-CEP background. To better understand
 2186 the efficiency of the figure-of-merit, ε_{HRC} , and inform the placement of an upper limit for the
 2187 χ_c analysis, we study the efficiency with a continuum-dimuon sample as it offers a large CEP
 2188 data set. The dimuon CEP is mediated through two-photon exchange.

2189 5.6.1 Dimuon-data selection

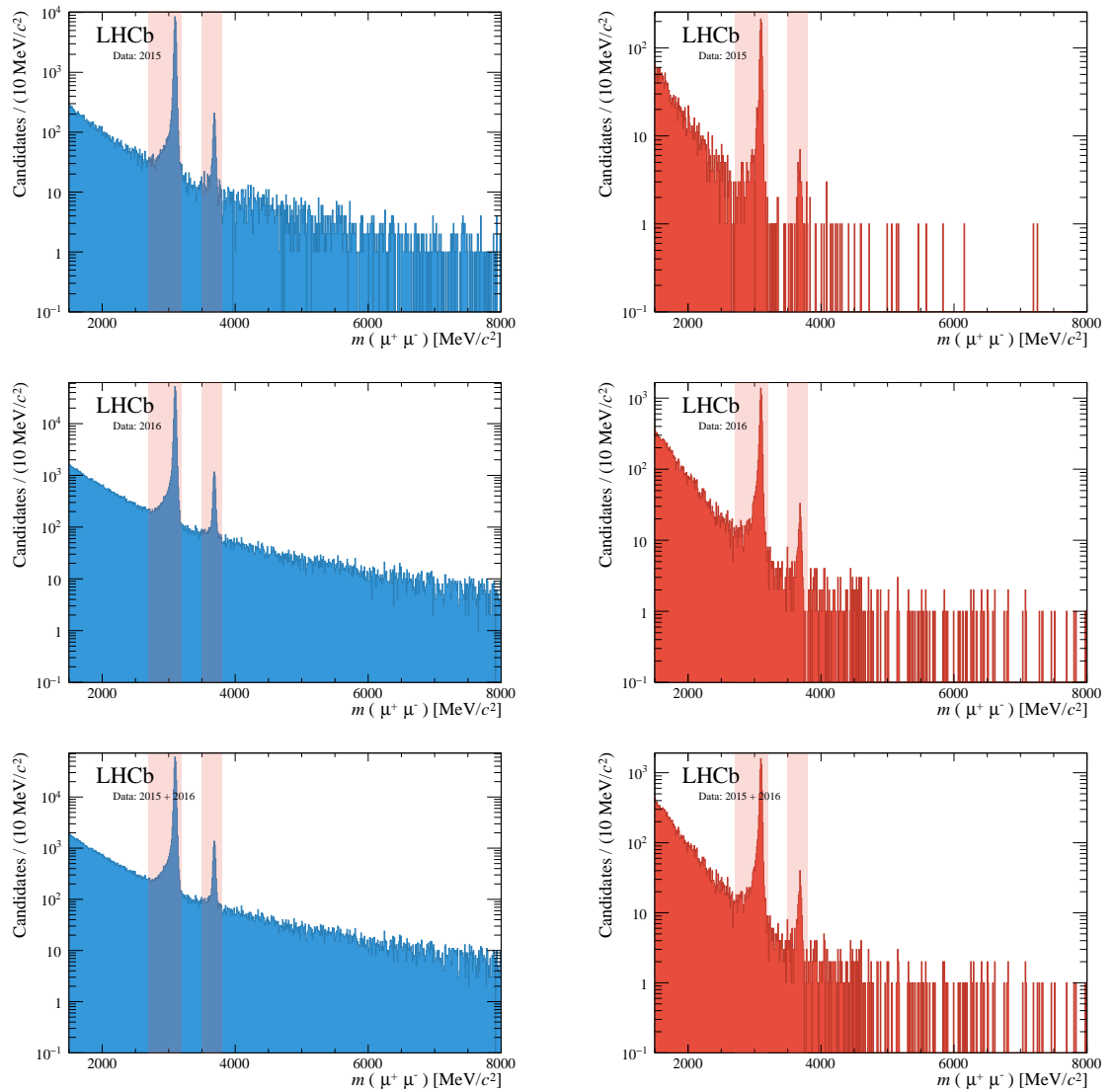


Figure 5.32. Dimuon invariant-mass distribution for the CEP (left) and non-CEP (right) dimuon selection for the 2015 (top), 2016 (middle), and combined 2015 and 2016 (bottom) data in logarithmic scale. The veto region of resonant J/ψ and $\psi(2S)$ mesons is highlighted in red.

2190 For this efficiency study, we select two samples: one with a high-CEP purity and another
 2191 inelastic sample that breaks the rapidity-gap criteria. Henceforth, these samples will be

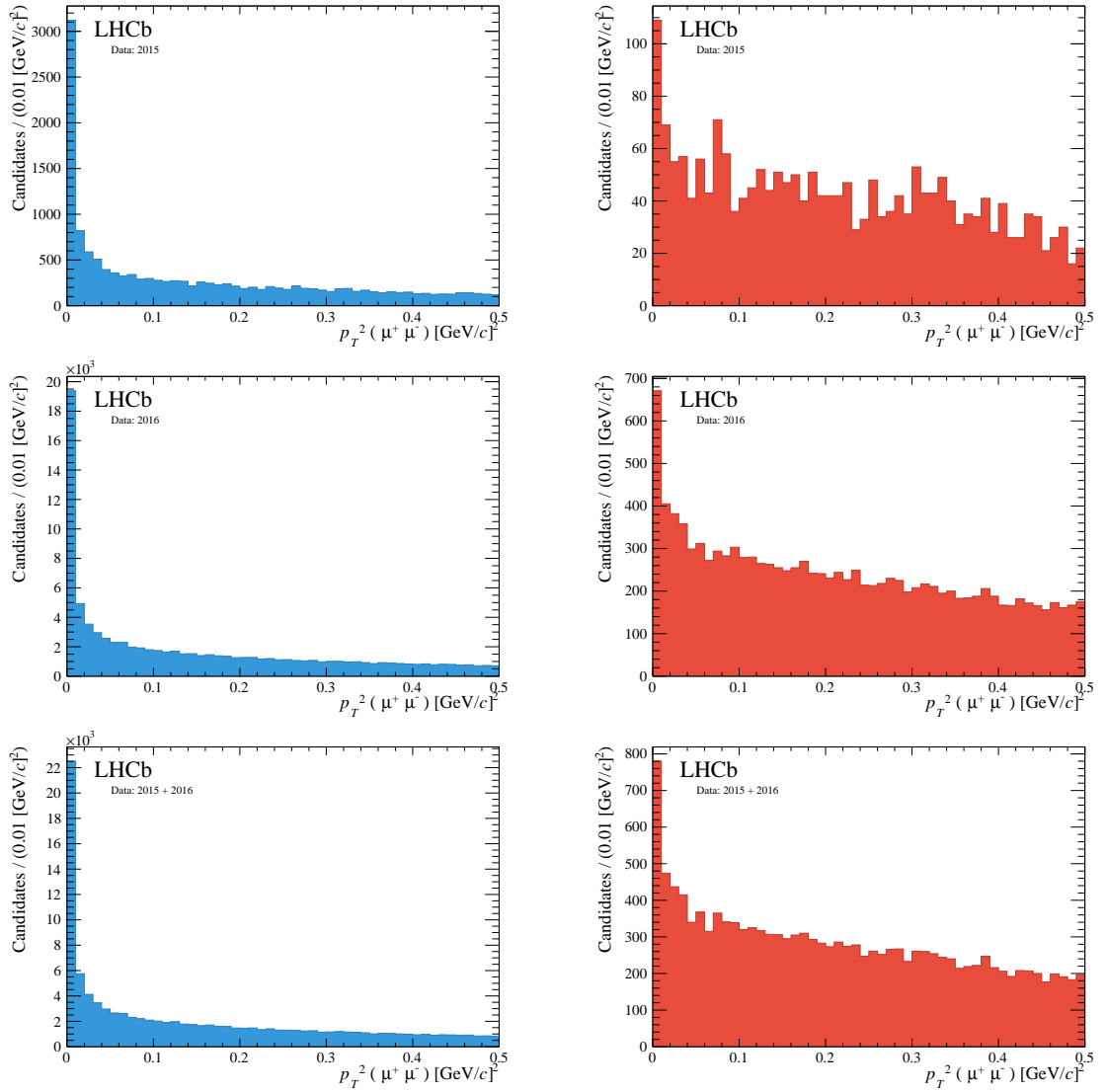


Figure 5.33. Dimuon transverse-momentum-squared distribution for the CEP (left) and non-CEP (right) dimuon selection for the 2015 (top), 2016 (middle), and combined 2015 and 2016 (bottom) data.

2192 referred to as the CEP-dimuon and non-CEP-dimuon samples. For the high-CEP purity
 2193 sample we use a similar selection as the one presented in Table 5.7 for the comparison of
 2194 the J/ψ yield between 2015 and 2016 data sets. However, we omit the SPD and muon
 2195 transverse-momentum requirements, since these cuts were only intended to make a one-to-one
 2196 comparison between the two data sets. In addition, the dimuon invariant mass is limited to
 2197 the window $1500 < m(\mu^+\mu^-) < 8000$ MeV/ c^2 where the resonant-mass windows of the J/ψ ,
 2198 $2700 < m(J/\psi) < 3200$ MeV/ c^2 , and $\psi(2S)$, $3500 < m(\psi(2S)) < 3800$ MeV/ c^2 , are excluded
 2199 from the study. We choose to exclude these resonant contributions because CEP J/ψ and
 2200 $\psi(2S)$ meson production is mediated by a different mechanism, photon-pomeron exchange, than
 2201 that of CEP-dimuon production, which is mediated by DPE. The veto-windows around the
 2202 resonant peaks are asymmetric in width to fully exclude the tail associated with energy loss

2203 via bremsstrahlung radiation. A total of 14,357 and 86,918 events pass the selection for 2015
 2204 and 2016 data respectively. The statistics for this sample are summarised in Table 5.9. The
 2205 invariant-mass distribution for this sample is shown in Fig. 5.32 (left) for 2015 and 2016 data
 2206 sets, where the vetoed resonance regions are highlighted in red. The transverse-momentum
 2207 distribution, excluding data from the invariant-mass-veto regions, is shown in Fig. 5.33 (left).

2208 For the non-CEP-dimuon sample, the track selection is modified to break the rapidity-gap
 2209 criteria by requesting that the event has at least one extra track or any type of photon activity
 2210 in the calorimeter. This assures the sample corresponds to non-CEP background. A total
 2211 of 2,158,100 and 2,712,653 events survive the selection for 2015 and 2016 data respectively,
 2212 summing to a total of 4,870,753 events. The statistics for this sample are also summarised in
 2213 Table 5.9. The invariant-mass distribution for the non-CEP-dimuon sample is shown in Fig. 5.32
 2214 (right) for the 2015, 2016, and combined 2015 and 2016 data sets. The transverse-momentum
 2215 distribution, excluding data from the invariant-mass-veto regions, is shown in Fig. 5.33 (right).
 2216 We use these histograms as templates for the PDF of the transverse-momentum-squared
 2217 distributions of non-CEP-dimuon production, which is necessary to describe the background of
 2218 our CEP-dimuon sample.

Table 5.9. Summary of CEP and non-CEP dimuon samples for the 2015, 2016, and combined 2015 and 2016 data as well as the LPair dimuon Monte Carlo for 2016.

Mechanism	2015	2016	2015 + 2016
CEP	14,357	86,981	101,275
Non-CEP	2,158,100	2,712,653	4,870,753
MC	-	18,166	-

2219 5.6.2 Dimuon transverse-momentum fit model

2220 To model the signal we use LPair [134], a Monte Carlo generator devoted to the process of
 2221 electromagnetic production of lepton pairs, to generate 100,000 CEP-dimuon events for 13 TeV
 2222 proton-proton collisions. After the reconstruction process, we apply the same selection criteria as
 2223 in the CEP-dimuon data sample and use generator-level information to check we reconstructed
 2224 the correct muons. A total of 18,166 events pass our selection. The invariant-mass distribution of
 2225 the dimuon system is shown in Fig. 5.34 where the veto-mass windows corresponding to the J/ψ
 2226 and $\psi(2S)$ resonance regions have been highlighted in red and the transverse-momentum-squared
 2227 distribution of the dimuon system is shown in Fig. 5.35. The events in the veto have been
 2228 excluded from this distribution. We can now use the transverse-momentum-squared histogram
 2229 as a PDF for the CEP signal in the fit of our CEP-dimuon sample.

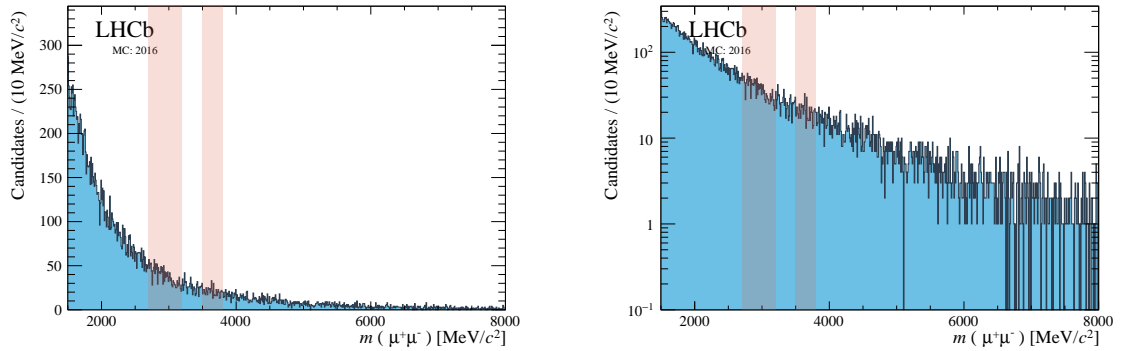


Figure 5.34. Dimuon invariant-mass distribution for the CEP-dimuon Monte Carlo for proton-proton collisions at a centre-of-mass energy $\sqrt{s} = 13$ TeV for 2016 run conditions in linear (left) and logarithmic scales (right). The veto region of resonant J/ψ and $\psi(2S)$ mesons is highlighted in red.

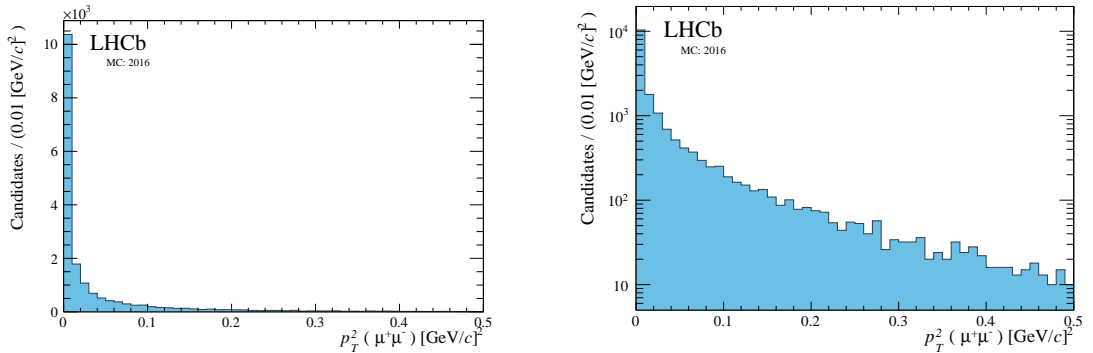


Figure 5.35. Dimuon transverse-momentum-squared distribution for the CEP dimuon Monte Carlo for proton-proton collisions at a centre-of-mass energy $\sqrt{s} = 13$ TeV for 2016 run conditions in linear (left) and logarithmic scales (right).

2230 5.6.3 HERSCHEL efficiency calculation

2231 The $\ln(\chi^2_{\text{HRC}})$ distribution is shown in Fig. 5.36 for the CEP (blue) and non-CEP (red) sample.
 2232 To better showcase the discriminatory power of the HERSCHEL detector, we tighten the

2233 transverse-momentum-squared cut of the CEP sample, such that $p_{\text{T}}^2(\mu^+\mu^-) < 0.01$ GeV/c, to
 2234 increase the CEP purity. Similarly, we can increase the inelastic purity of the non-CEP sample
 2235 by requiring that there are more than five long tracks in the main spectrometer. The $\ln(\chi_{\text{HRC}}^2)$
 2236 distributions for these enhanced purity samples are shown alongside our nominal selection in
 2237 Fig. 5.36. The non-CEP samples have a tail which extends to low $\ln(\chi_{\text{HRC}}^2)$ values: these are
 2238 background events where all additional activity associated with proton dissociation or secondary
 2239 interactions lies outside the HERSCHEL acceptance. Similarly, the CEP enhanced-purity sample
 2240 has a small fraction of events that have high $\ln(\chi_{\text{HRC}}^2)$ values: we attribute this feature to small
 2241 levels of residual background and also occasions where secondary proton interactions may occur,
 2242 producing activity outside of the main spectrometer but within that of HERSCHEL. Prior to
 2243 October 1st 2015, HERSCHEL was under commission. As a result, the HERSCHEL response
 2244 was less stable during this period, thus explaining the worse separation compared to 2016.

2245 To measure a signal efficiency for a given $\ln(\chi_{\text{HRC}}^2)$ cut we perform an unbinned-maximum-
 2246 likelihood fit on the dimuon-transverse-momentum-squared distribution of our CEP-dimuon
 2247 sample with the $\ln(\chi_{\text{HRC}}^2)$ cut applied. The fit enables us to determine how the true signal
 2248 content of the CEP sample varies with p_{T}^2 . We use a PDF composed of a CEP-signal shape
 2249 extracted from the LPair Monte Carlo, and a non-CEP-background shape extracted from data,
 2250 as described above. An example of such a fit is shown in Fig. 5.37 for $\ln(\chi_{\text{HRC}}^2) < 5$. The signal
 2251 peaks at low p_{T}^2 values, a feature characteristic of CEP events, while the background has a
 2252 much wider profile and extends to higher p_{T}^2 values.

2253 The effect of the HERSCHEL activity on a CEP-dimuon sample can be quantified by an
 2254 efficiency given by the ratio of the CEP-signal yield after the $\ln(\chi_{\text{HRC}}^2)$ cut is applied to the CEP-
 2255 signal yield prior to the $\ln(\chi_{\text{HRC}}^2)$ cut. Similarly, we are able to calculate the effect HERSCHEL
 2256 activity has on the non-CEP background surviving the cut. The background rejection rate
 2257 is given by subtracting the background-efficiency rate from one. The CEP-dimuon-signal
 2258 efficiency distribution and the non-CEP-background rejection are shown Fig. 5.38. The efficiency
 2259 distributions are shown for the interval of greatest change in efficiency, $2 < \ln(\chi_{\text{HRC}}^2) < 5$,
 2260 alongside the full-range versions. The uncertainties are calculated from the fit-yield uncertainties.
 2261 while the values and uncertainties between intervals are linearly interpolated. The signal-
 2262 efficiency and background-rejection values are tabulated in Table 5.10.

2263 Our working $\ln(\chi_{\text{HRC}}^2)$ upper limit for the χ_c analysis, marked in Fig. 5.38 by a grey-vertical-
 2264 dashed line, is $\ln(\chi_{\text{HRC}}^2) < 5$. With this cut the signal efficiency is $70.4 \pm 1.8\%$, $85.1 \pm 0.8\%$, and
 2265 $83.0 \pm 0.8\%$ for 2015, 2016, and combined 2015 and 2016 data respectively, while the background
 2266 rejection is $71.9 \pm 2.1\%$, $67.6 \pm 0.8\%$, and $68.2 \pm 0.7\%$. It should be stressed, however, that the
 2267 proportion of background that is suppressed is dependent on the exact nature of the background,
 2268 and so the values found are not necessarily representative of the background in the χ_c analysis
 2269 sample. As stated previously, the difference in performance between 2015 and 2016 is due to a
 2270 period of commissioning during 2015.

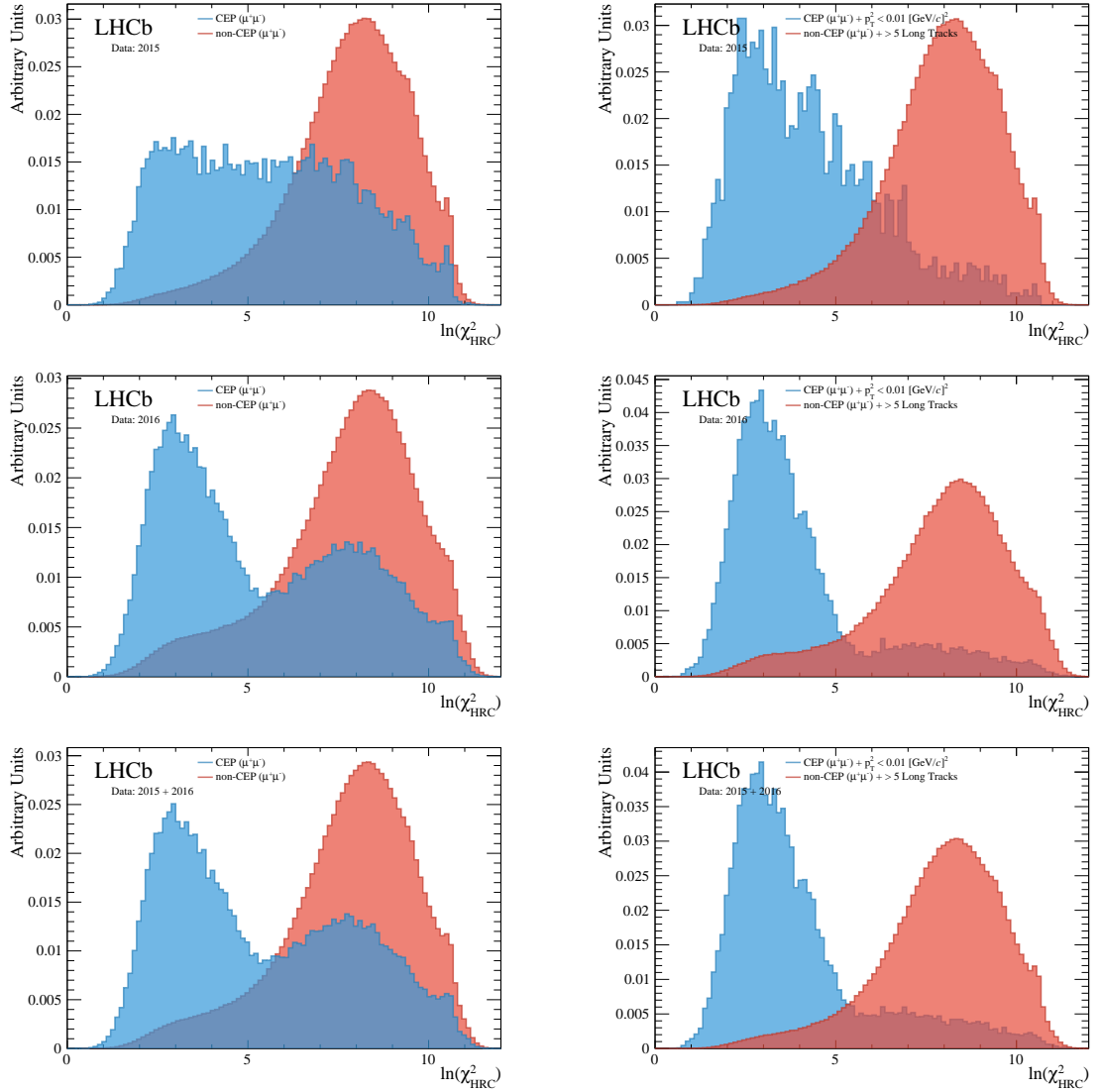


Figure 5.36. Distribution, normalised to unit area, of the discriminating $\ln(\chi_{\text{HRSHEL}}^2)$ variable that is related to the activity in HERSCHEL for the 2015 (top), 2016 (middle), and combined 2015 and 2016 (bottom) data. The response is shown for the CEP (blue) and non-CEP (red) sample in the left column and again on the right column with tighter CEP, $p_T^2(\mu^+\mu^-) < 0.01 \text{ GeV}/c^2$, and non-CEP, number of long tracks ≥ 6 , requirements respectively.

2271 To assess the systematic uncertainty associated with the dimuon transverse-momentum fit
 2272 used to calculate the HERSCHEL efficiency, we independently vary the background and signal
 2273 fit model, then recalculate the efficiency at our working point $\ln(\chi_{\text{HRSHEL}}^2) < 5$ for each of the new
 2274 configurations. As an alternative model of the background we use a shape suggested in a HERA
 2275 analysis [135] associated with the inelastic proton form factor, which takes the form

$$B(p_T^3) = \frac{p_0}{(1 + (a/n)p_T^2)^n}, \quad (5.9)$$

2276 where n and a are free parameters and the $n = 1.79$ is fixed to the experimental value taken
2277 from the HERA paper. The fit results are shown in Fig. 5.39 in linear and logarithmic scale.
2278 With this model we obtain an efficiency of $(85.5 \pm 0.8)\%$ and $(83.6 \pm 0.7)\%$ for the 2016-only,
2279 and combined 2015 and 2016 data, respectively. This corresponds to a difference of 0.4% and
2280 0.7%, respectively, with respect to the default fit.

2281 Similarly, we replace the signal shape for the sum of two exponentials while keeping the
2282 background shape model unchanged such that

$$p_0 e^{p_1 p_i^2} + p_2 e^{p_3 p_i^2}. \quad (5.10)$$

2283 As before, we repeat the fit procedure, the fits for which are shown in Fig. 5.39, and find an
2284 efficiency of $(80.2 \pm 1.1)\%$ and $(78.9 \pm 1.0)\%$ for the 2016-only, and combined 2015 and 2016 data.
2285 This corresponds to a difference of 5.7% and 4.9%, respectively, with respect to the default fit.
2286 We take the largest effect as the systematic uncertainty, and assign a 6% to both the 2016-only
2287 and 5% for the combined 2015 and 2016 data.

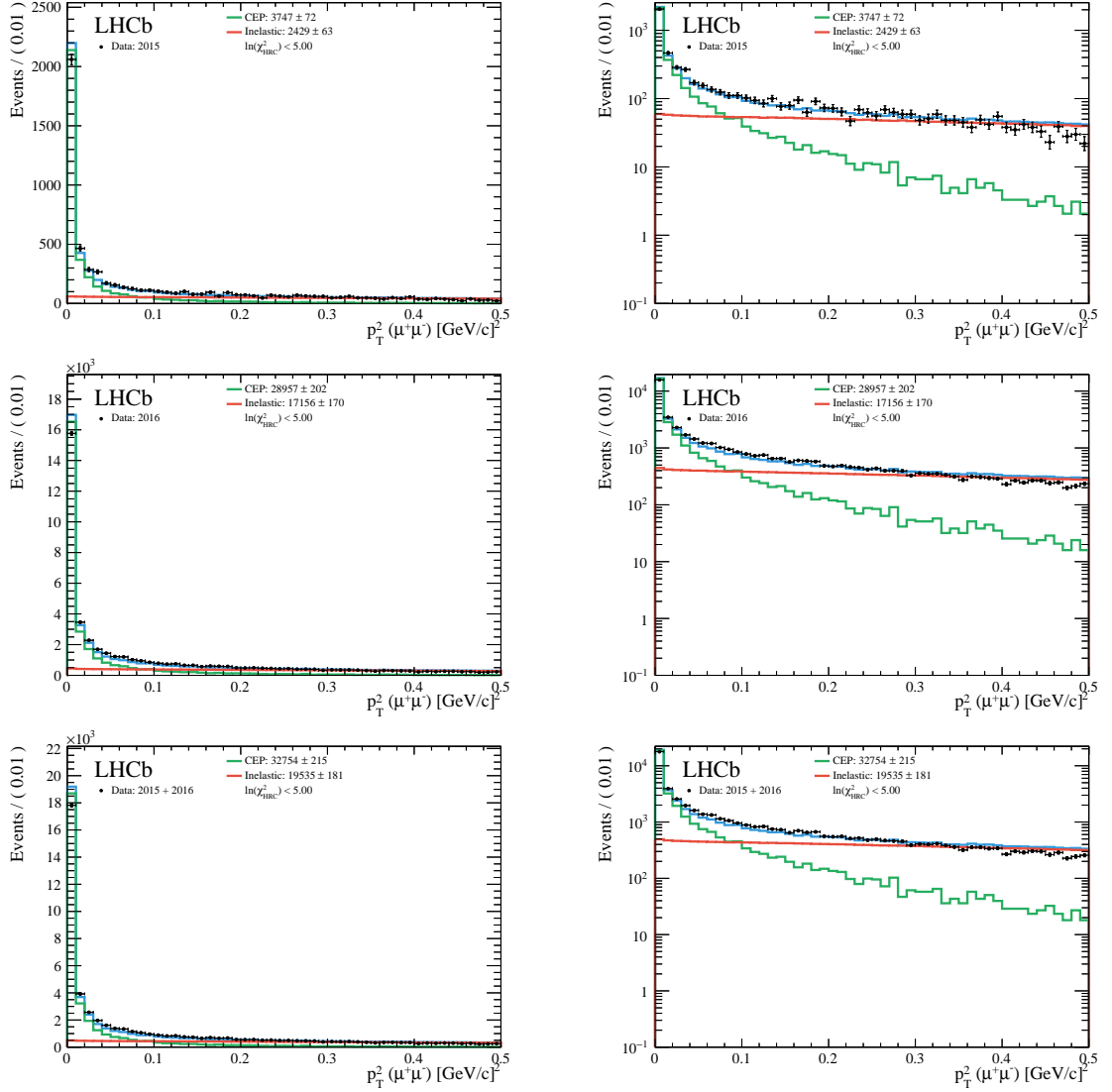


Figure 5.37. An example for the dimuon transverse-momentum-squared fits with a $\ln(\chi_{\text{HRC}}^2) < 5$ cut applied for the 2015 (top), 2016 (middle), and combined 2015 and 2016 (bottom) data in linear (left) and logarithmic (right) scale. The CEP component is fitted with a template extracted from Monte Carlo (green) while the inelastic non-CEP component is fitted with a template extracted from inelastic data (red).

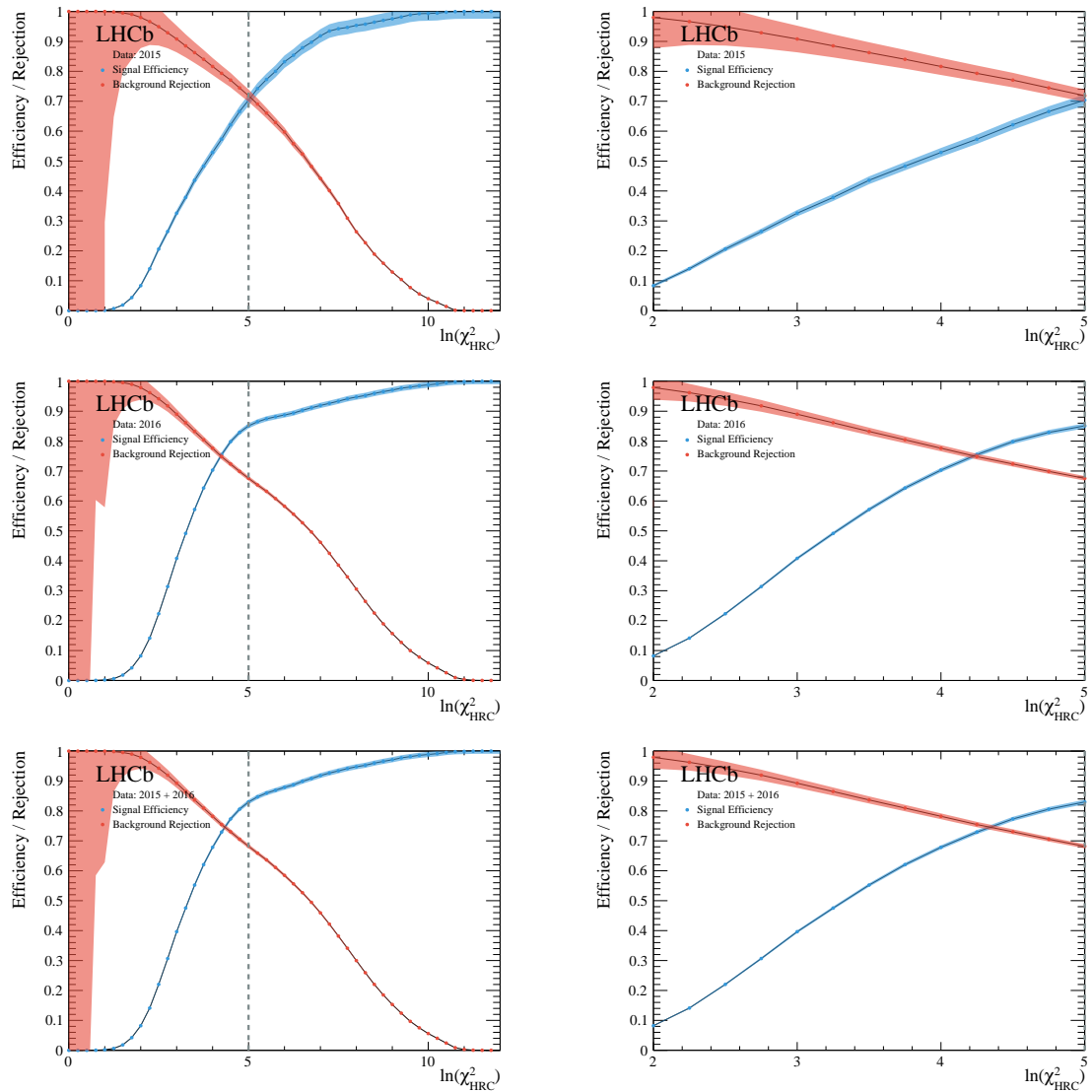


Figure 5.38. CEP-signal efficiency (blue) and background rejection (red) for dimuon production as a function of the limit chosen for $\ln(\chi^2_{\text{HRC}})$ for the 2015 (top), 2016 (middle), and combined 2015 and 2016 (bottom) data. The distribution is reproduced for the range where $\ln(\chi^2_{\text{HRC}})$ has the largest variation (right), $2 < \ln(\chi^2_{\text{HRC}}) < 5$.

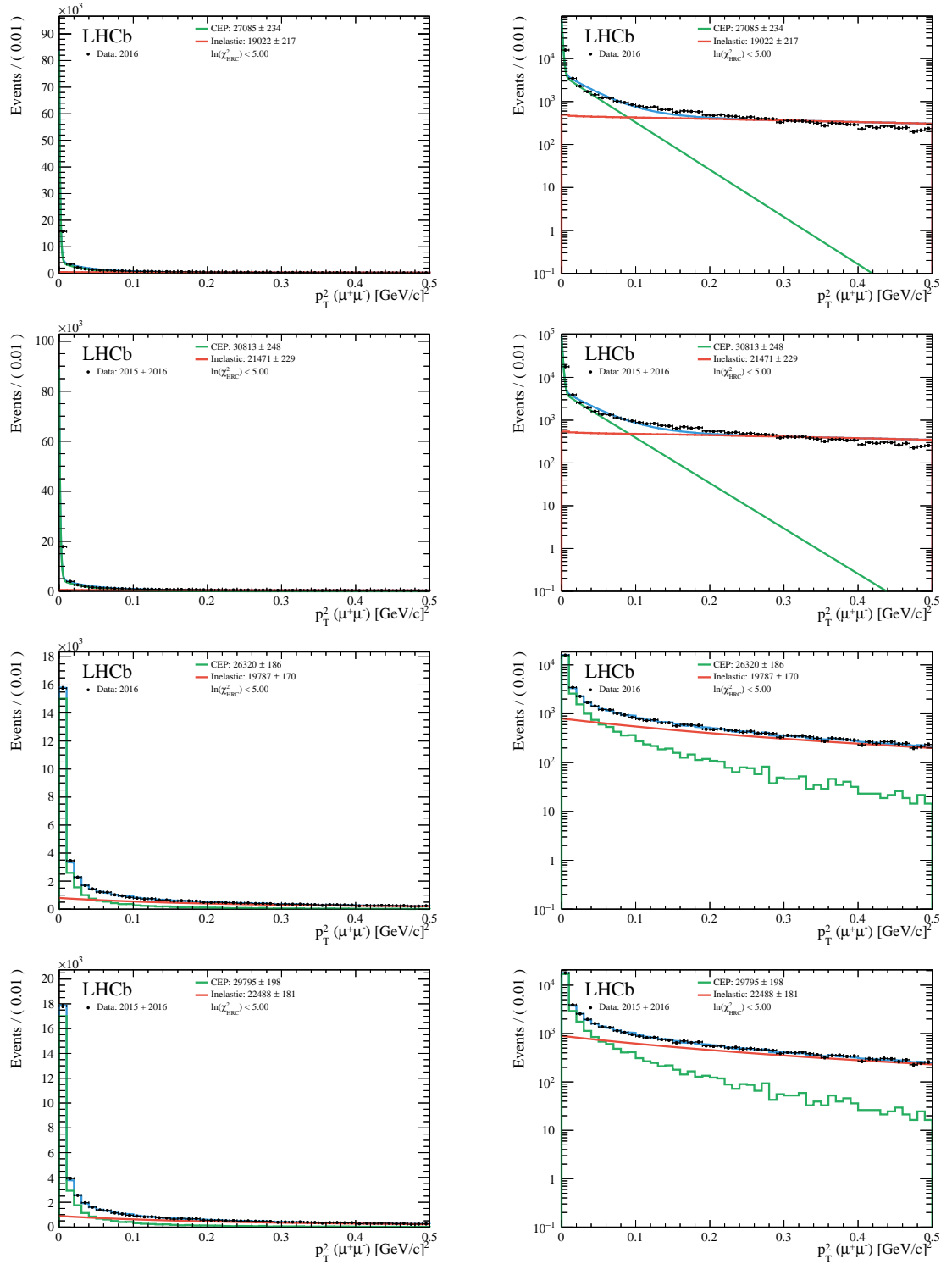


Figure 5.39. Dimuon transverse-momentum-squared fits with a $\ln(\chi_{\text{HRC}}^2) < 5$ cut applied for the 2016-only (first and third row), and combined 2015 and 2016 (second and fourth row) data in linear (left) and logarithmic (right) scale. In the first and second row, the CEP component is fitted with a template extracted from Monte Carlo (green) while the inelastic non-CEP component with Eq. 5.9 (red). In the second and third row, the CEP component is fitted with the sum of two exponentials (green) while the inelastic non-CEP component is fitted with a template extracted from inelastic data (red).

Table 5.10. Summary of $\ln(\chi_{\text{HRC}}^2)$ efficiency and background rejection.

$\ln(\chi_{\text{HRC}}^2)$ <	Efficiency [%]			Background Rejection [%]		
	2015	2016	2015 + 2016	2015	2016	2015 + 2016
0.25	0.0 ± 0.01	0.0 ± 0.002	0.0 ± 0.002	-	-	-
0.50	0.0 ± 0.01	0.004 ± 0.004	0.003 ± 0.003	-	100 ± 134	100 ± 134
0.75	0.019 ± 0.009	0.03 ± 0.01	0.03 ± 0.01	-	100 ± 40	100 ± 42
1.00	0.12 ± 0.05	0.2 ± 0.03	0.2 ± 0.02	100.0 ± 70.3	100 ± 42	100 ± 37
1.25	0.7 ± 0.1	0.6 ± 0.05	0.6 ± 0.05	99.8 ± 35.1	99.8 ± 14.4	99.8 ± 13.4
1.50	1.9 ± 0.2	1.8 ± 0.09	1.8 ± 0.08	99.5 ± 19.6	99.5 ± 8.8	99.5 ± 8.0
1.75	4.4 ± 0.3	4.2 ± 0.1	4.2 ± 0.1	99.1 ± 15.0	99.0 ± 5.9	99.0 ± 5.5
2.00	8.4 ± 0.5	8.2 ± 0.2	8.2 ± 0.2	98.0 ± 10.2	97.9 ± 4.1	97.9 ± 3.8
2.25	14.0 ± 0.6	14.2 ± 0.3	14.1 ± 0.2	96.6 ± 7.8	96.2 ± 3.0	96.3 ± 2.8
2.50	20.6 ± 0.8	22.3 ± 0.3	22.0 ± 0.3	94.9 ± 6.3	94.2 ± 2.4	94.3 ± 2.2
2.75	26.5 ± 0.9	31.4 ± 0.4	30.7 ± 0.4	92.9 ± 5.2	91.8 ± 2.0	91.9 ± 1.8
3.00	32.6 ± 1.1	40.8 ± 0.5	39.6 ± 0.4	90.8 ± 4.4	89.0 ± 1.7	89.3 ± 1.6
3.25	37.8 ± 1.2	49.1 ± 0.6	47.5 ± 0.5	88.5 ± 3.9	86.1 ± 1.4	86.5 ± 1.3
3.50	43.6 ± 1.3	57.1 ± 0.6	55.2 ± 0.6	86.2 ± 3.5	83.2 ± 1.3	83.7 ± 1.2
3.75	48.3 ± 1.4	64.3 ± 0.7	62.1 ± 0.6	84.0 ± 3.1	80.4 ± 1.1	81.0 ± 1.1
4.00	52.9 ± 1.5	70.3 ± 0.7	67.8 ± 0.7	81.6 ± 2.8	77.6 ± 1.0	78.2 ± 1.0
4.25	57.3 ± 1.6	75.5 ± 0.8	72.9 ± 0.7	79.3 ± 2.6	74.8 ± 0.9	75.5 ± 0.9
4.50	62.1 ± 1.7	79.8 ± 0.8	77.3 ± 0.7	77.1 ± 2.4	72.4 ± 0.9	73.0 ± 0.8
4.75	66.6 ± 1.8	82.9 ± 0.8	80.6 ± 0.7	74.5 ± 2.2	69.9 ± 0.8	70.5 ± 0.8
5.00	70.4 ± 1.8	85.1 ± 0.8	83.0 ± 0.8	71.9 ± 2.1	67.6 ± 0.8	68.2 ± 0.7
5.25	74.2 ± 1.9	86.5 ± 0.8	84.7 ± 0.8	69.0 ± 1.9	65.4 ± 0.7	65.9 ± 0.7
5.50	77.3 ± 2.0	87.5 ± 0.9	86.0 ± 0.8	66.0 ± 1.7	63.2 ± 0.7	63.6 ± 0.6
5.75	80.0 ± 2.0	88.1 ± 0.9	86.9 ± 0.8	62.9 ± 1.6	60.8 ± 0.6	61.1 ± 0.6
6.00	$83.2 \pm 2.$	88.7 ± 0.9	87.9 ± 0.8	59.7 ± 1.5	58.2 ± 0.6	58.5 ± 0.5
6.25	85.4 ± 2.1	89.4 ± 0.9	88.7 ± 0.8	55.8 ± 1.3	55.6 ± 0.5	55.6 ± 0.5
6.50	87.9 ± 2.1	90.3 ± 0.9	89.9 ± 0.8	52.4 ± 1.2	52.7 ± 0.5	52.7 ± 0.5
6.75	89.7 ± 2.2	91.1 ± 0.9	90.9 ± 0.8	48.2 ± 1.1	49.6 ± 0.5	49.4 ± 0.4
7.00	91.8 ± 2.3	91.9 ± 0.9	91.8 ± 0.8	44.2 ± 1.0	46.2 ± 0.4	45.9 ± 0.4
7.25	93.5 ± 2.3	92.6 ± 0.9	92.7 ± 0.8	40.1 ± 0.8	42.5 ± 0.4	42.2 ± 0.3
7.50	94.2 ± 2.3	93.3 ± 0.9	93.4 ± 0.8	35.8 ± 0.7	38.5 ± 0.3	38.2 ± 0.3
7.75	94.7 ± 2.3	94.2 ± 0.9	94.2 ± 0.8	30.9 ± 0.6	34.6 ± 0.3	34.1 ± 0.3
8.00	95.3 ± 2.3	94.7 ± 0.9	94.8 ± 0.9	26.4 ± 0.5	30.6 ± 0.2	30.0 ± 0.2
8.25	95.8 ± 2.3	95.2 ± 0.9	95.3 ± 0.9	22.7 ± 0.4	26.4 ± 0.2	25.9 ± 0.2
8.50	96.4 ± 2.4	96.0 ± 0.9	96.0 ± 0.9	18.9 ± 0.4	22.5 ± 0.2	22.0 ± 0.2
8.75	97.0 ± 2.4	96.5 ± 0.9	96.6 ± 0.9	15.8 ± 0.3	18.9 ± 0.1	18.5 ± 0.1
9.00	97.6 ± 2.4	97.1 ± 0.9	97.1 ± 0.9	12.9 ± 0.2	15.7 ± 0.1	15.3 ± 0.1
9.25	98.2 ± 2.4	97.7 ± 0.9	97.7 ± 0.9	10.4 ± 0.2	12.7 ± 0.1	12.41 ± 0.09
9.50	98.9 ± 2.4	98.1 ± 1.0	98.2 ± 0.9	7.7 ± 0.1	10.0 ± 0.07	9.67 ± 0.07
9.75	99.2 ± 2.4	98.5 ± 1.0	98.6 ± 0.9	5.6 ± 0.1	7.8 ± 0.06	7.51 ± 0.05
10.00	99.3 ± 2.4	98.8 ± 1.0	98.9 ± 0.9	4.01 ± 0.07	5.9 ± 0.04	5.60 ± 0.04
10.25	99.4 ± 2.4	99.1 ± 1.0	99.2 ± 0.9	2.75 ± 0.05	4.2 ± 0.03	4.02 ± 0.03
10.50	99.8 ± 2.4	99.5 ± 1.0	99.6 ± 0.9	1.41 ± 0.03	2.5 ± 0.02	2.42 ± 0.02
10.75	99.9 ± 2.4	99.8 ± 1.0	99.8 ± 0.9	$(139 \pm 2)10^{-3}$	$(978 \pm 7)10^{-3}$	$(860 \pm 6)10^{-3}$
11.00	100.0 ± 2.4	99.9 ± 1.0	99.9 ± 0.9	$(312 \pm 6)10^{-4}$	$(333 \pm 2)10^{-3}$	$(290 \pm 2)10^{-3}$
11.25	100.0 ± 2.4	100.0 ± 1.0	100.0 ± 0.9	-	$(544 \pm 4)10^{-4}$	$(468 \pm 3)10^{-4}$
11.50	100.0 ± 2.4	100.0 ± 1.0	100.0 ± 0.9	-	$(909 \pm 7)10^{-5}$	$(781 \pm 5)10^{-5}$
11.75	100.0 ± 2.4	100.0 ± 1.0	100.0 ± 0.9	-	-	-
12.00	100.0 ± 2.4	100.0 ± 1.0	100.0 ± 0.9	-	-	-

CHAPTER 6

Background and fit model

2288

2289

2290

2291 In this chapter, we construct the simultaneous-fit model of the Δm_{χ_c} and p_T^2 distributions of
 2292 selected CEP χ_c candidates, with and without the HERSCHEL cut applied. The final result for
 2293 our χ_c cross-section measurement is obtained with the HERSCHEL cut applied, which suppresses
 2294 the inelastic background. However, in order to understand the effect of the HERSCHEL detector
 2295 and as a systematic check we present the results of both samples along side one another. We
 2296 start by introducing a series of background studies through which we quantify and model each
 2297 background contribution for later use in the fit of CEP χ_c candidates. In Sec. 6.1 we present
 2298 studies of *combinatorial* background, where erroneously combined particles are matched to
 2299 emulate our decay signal. In Sec. 6.2 we describe *feed-down* background where the decay chains
 2300 of heavier particles, in particular those of $\psi(2S)$ mesons, may contain the final-state particles
 2301 from our signal-decay mode. The Δm_{χ_c} of many of these decays fall around the range of our
 2302 signal events, making it an important source of background to model and quantify. The last
 2303 source of background, discussed in Sec. 6.3, comes from the production of χ_c mesons by *inelastic*
 2304 processes where we fail to detect rapidity-breaking signatures such as proton dissociation or
 2305 gluon radiation. Finally, we discuss the fit parameterisation of our CEP χ_c signal and provide a
 2306 summary of all the fit components in Sec. 6.5.

2307 6.1 Combinatorial background

2308 There are two sources of combinatorial background. Firstly, non-resonant dimuon production
 2309 from photon-photon fusion can be wrongly matched with a random converted-photon candidate.
 2310 We will refer to this background as *dimuon* or *continuum combinatorial*. Secondly, a genuine
 2311 J/ψ meson can be wrongly matched with a random converted photon and mimic our signal.
 2312 We will refer to this background as J/ψ *combinatorial*.

2313 6.1.1 Continuum-combinatorial background

2314 We estimate the continuum-combinatorial background by fitting the invariant mass of the
 2315 $\mu^+\mu^-$ system of the events that pass our CEP χ_c selection criteria. This distribution contains
 2316 contributions from genuine J/ψ mesons and a dimuon continuum that falls with increasing
 2317 invariant mass. A fraction of this dimuon continuum falls within our 100 MeV/ c^2 wide J/ψ
 2318 mass window centred around the nominal invariant-mass value of the J/ψ , which is set at

2319 $m_{J/\psi} = 3096.900 \pm 0.006 \text{ MeV}/c^2$ according to the Particle Data Group [81]. We estimate this
 2320 contribution by fitting the distribution outside the window.

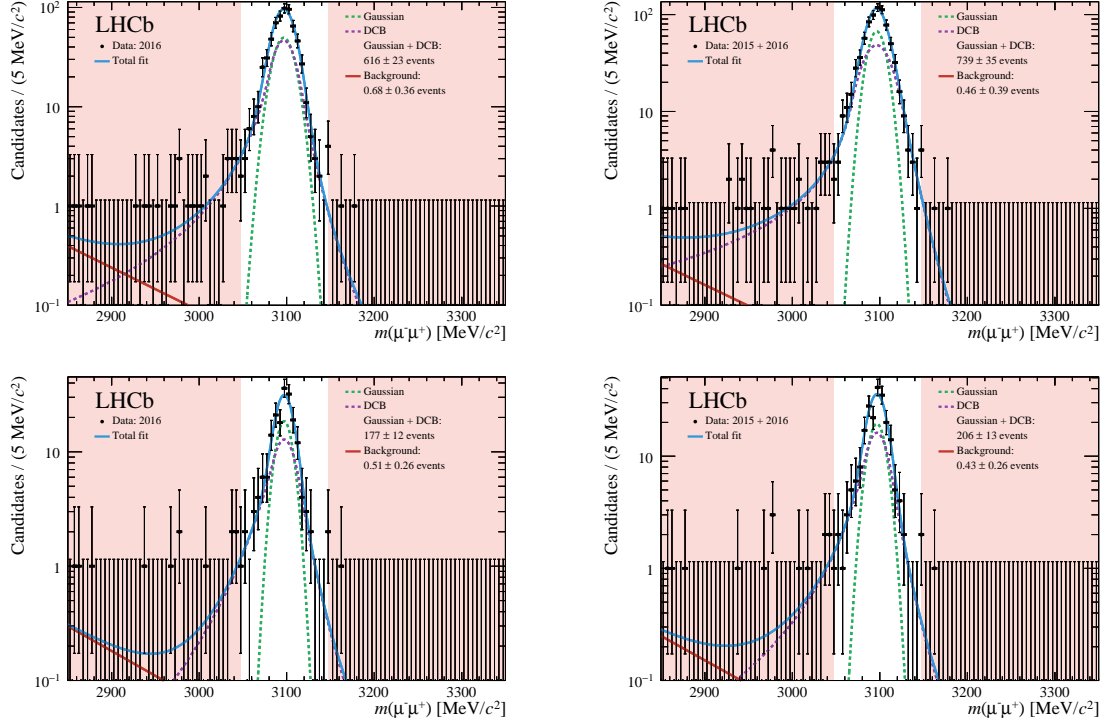


Figure 6.1. Invariant mass of J/ψ mesons from $\chi_c \rightarrow J/\psi [\mu^+ \mu^-] \gamma [e^+ e^-]$ for proton-proton collisions at a centre-of-mass energy $\sqrt{s} = 13 \text{ TeV}$ data in logarithmic scale before (top) and after (bottom) the HERSCHEL cut is applied, $\ln(\chi_{\text{HRC}}^2) < 5$, for the 2016-only (left), and combined 2015 and 2016 (right) data sets. Events within a 100 MeV mass window around the J/ψ nominal mass are selected. The complementary rejection windows are highlighted in red. A double-sided Crystal Ball (dashed purple) together with a Gaussian is used for the J/ψ candidates (dashed green) and the continuum-combinatorial background is fitted with an exponential (dashed red).

2321 The continuum contribution is modelled with a single exponential,

$$A \cdot e^{-\lambda p_T^2}. \quad (6.1)$$

2322 where A is a normalisation parameter and λ is the slope of the exponential. To fit the J/ψ
 2323 resonance we use a combination of a double-sided Crystal Ball [132] and a Gaussian with a
 2324 shared mean parameter, which is the same model used for the comparison of the 2015 and 2016
 2325 J/ψ yields presented in Sec. 5.3. As before, the yield ratio of the double-sided Crystal Ball and
 2326 a Gaussian is fixed to values extracted from CEP χ_c Monte Carlo. Applying this constraint, we
 2327 perform an unbinned-maximum-likelihood fit of the data samples, the results of which are shown
 2328 in Fig. 6.1 with and without the HERSCHEL cut applied for the 2016-only, and combined 2015
 2329 and 2016 data samples. The final values of the fit parameters are detailed in Table 6.1.

Table 6.1. Parameter values of J/ψ mass fit from CEP χ_c Monte Carlo and data for 2016-only, and combined 2015 and 2016 data sets. Fixed parameters are marked by *.

Variable	Units	Without HERSCHEL		With HERSCHEL	
		2016	2015 + 2016	2016	2015 + 2016
μ	MeV/ c^2	3096.7 ± 0.6	3096.4 ± 0.5	3097.2 ± 0.9	3096.6 ± 0.9
α_{Left}	-	1.26 ± 0.09	1.70 ± 0.20	0.90 ± 0.97	1.03 ± 0.13
α_{Right}	-	-1.58 ± 0.16	-1.85 ± 0.23	-1.41 ± 0.26	-1.45 ± 0.25
n_{Left}	-	4.32 ± 2.00	1.36 ± 0.20	4.32 ± 2.00	2.72 ± 0.76
n_{Right}	-	5.83 ± 2.60	11.50 ± 12.33	6.34 ± 4.70	6.26 ± 4.31
σ_{DCB}	MeV/ c^2	13.38 ± 0.88	12.84 ± 1.45	13.24 ± 1.65	12.84 ± 1.45
σ_{Gauss}	MeV/ c^2	12.07 ± 0.84	9.91 ± 1.33	9.31 ± 1.33	9.91 ± 1.33
$Y_{\text{Gauss}}/Y_{\text{DCB}}$	-	* 0.818 ± 0.501	* 0.748 ± 0.408	* 0.818 ± 0.501	* 0.748 ± 0.408
λ	[MeV/ c^2] $^{-1}$	-0.009 ± 0.007	-0.010 ± 0.008	-0.009 ± 0.008	-0.009 ± 0.008

2330 By integrating the background component of our data fit within our J/ψ selection window,
 2331 $m_{J/\psi} \pm 50$ MeV/ c^2 , we estimate 0.46 ± 0.39 (0.43 ± 0.26) continuum-combinatorial-background
 2332 events in the combined 2015 and 2016 data, and 0.68 ± 0.36 (0.51 ± 0.26) in the 2016-only data
 2333 without (with) the HERSCHEL cut applied. This demonstrates we have a very clean J/ψ signal
 2334 with a minimal amount of continuum-combinatorial background. This background is assumed
 2335 to have a flat Δm_{χ_c} profile.

2336 6.1.2 J/ψ -combinatorial background

2337 J/ψ -combinatorial background comes from the association of genuine J/ψ mesons and a converted
 2338 photon from another process, or from noise in the calorimeter wrongly interpreted as a photon.
 2339 To precisely determine the amount of J/ψ -combinatorial background we study a Δm_{χ_c} region
 2340 where we know the signal is dominated by J/ψ -combinatorial background. From the CEP
 2341 χ_c Monte Carlo we know not to expect any χ_c signal in the Δm_{χ_c} region above 500 MeV/ c^2 .
 2342 From the feed-down study that will be presented in Sec. 6.2, we also know to expect minimal
 2343 feed-down background in this right-hand side-band. Therefore, any events above this threshold
 2344 are dominated by J/ψ -combinatorial background with slight contamination from continuum-
 2345 combinatorial background. We are able estimate the amount J/ψ -combinatorial background in
 2346 our sample by fitting events in this right-tail region and extrapolating into our selection window.

2347 To perform the extrapolation we first need to know the shape of the J/ψ -combinatorial
 2348 background along the entire Δm_{χ_c} range. We model it through a data-driven approach where
 2349 we mismatch a J/ψ meson from one event with a converted photon from a different event in
 2350 the CEP χ_c data set. The resulting Δm_{χ_c} distribution falls gently to either side of our signal
 2351 window as shown in Fig. 6.2, with and without the HERSCHEL cut applied. We will refer to
 2352 this as the *artificial*-combinatorial background. To fit the distribution, we use a double-sided
 2353 Crystal Ball to accommodate the tail asymmetry in an unbinned-maximum-likelihood fit where

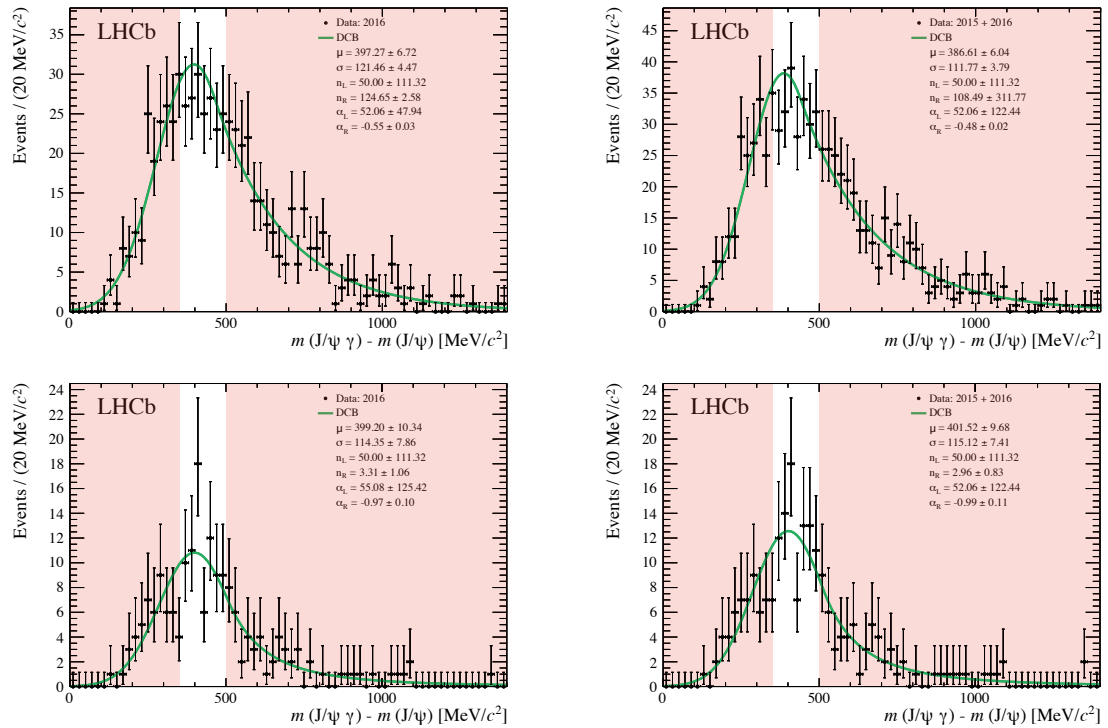


Figure 6.2. Fit of Δm_{χ_c} distribution of artificial-combinatorial model before (top) and after (bottom) the HERSCHEL cut is applied from the 2016-only (left), and combined 2015 and 2016 (right) data. The distribution is fitted with a double-sided Crystal Ball in green. The vetoed ranges in our CEP χ_c selection are highlighted in red.

2354 all parameters are left floating. The fit is overlaid on Fig. 6.2, and the final-parameter values
 2355 are summarised in Table 6.2.

2356 In addition to the J/ψ -combinatorial shape described above, we add a uniform distribution
 2357 for the sub-dominant continuum-combinatorial background such that its integral around our
 2358 selection window matches the results presented above. In determining the absolute background
 2359 level from the CEP χ_c sample, the size of the J/ψ -combinatorial background is determined
 2360 exclusively by the candidates to the right of the signal window. The fit shape of the J/ψ
 2361 combinatorial is then extrapolated into lower- Δm_{χ_c} values. The maximum-likelihood-fit results
 2362 of the combinatorial component are shown in Fig. 6.3, with and without the HERSCHEL cut
 2363 applied. The data in the resonant region are not shown as this is signal dominated and not
 2364 described by the fit model. The fit does not describe the low- Δm_{χ_c} -veto region well since it has
 2365 an additional contribution from χ_{c0} , which the fit does not account for. By integrating within
 2366 the selection window we find that we expect 44.97 ± 6.35 (13.25 ± 4.66) J/ψ -combinatorial events
 2367 in the combined 2015 and 2016 data, and 35.55 ± 5.85 (11.91 ± 4.51) in the 2016-only data
 2368 without (with) the HERSCHEL cut applied. Hence we conclude that HERSCHEL suppresses
 2369 this source of background by around 70%.

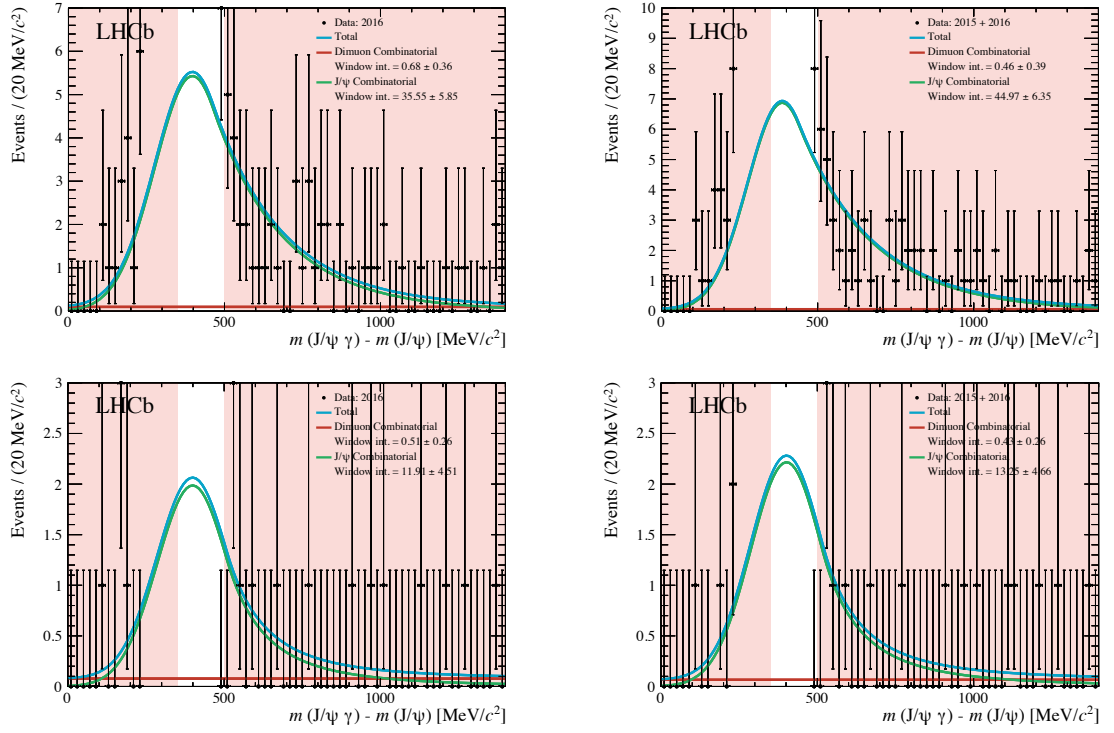


Figure 6.3. Fit of Δm_{χ_c} distribution from CEP χ_c selection before (top) and after (bottom) the HERSCHEL cut is applied, $\ln(\chi_{\text{HRC}}^2) < 5$, for the 2016-only (left), and combined 2015 and 2016 (right). The Δm_{χ_c} ranges vetoes in the main analysis are highlighted in red. The entries in the resonant region are not shown as they are signal dominated.

Table 6.2. Parameters of Δm_{χ_c} and p_{T}^2 fits of J/ψ -combinatorial background for the 2016-only, and combined 2015 and 2016 data with a HERSCHEL cut, $\ln(\chi_{\text{HRC}}^2) < 5$, applied.

Variable	Units	Without HERSCHEL		With HERSCHEL	
		2016	2015 + 2016	2016	2015 + 2016
Δm_{χ_c} combinatorial					
μ	MeV/c^2	397.27 ± 6.72	386.61 ± 6.04	399.20 ± 10.34	401.52 ± 9.68
σ	MeV/c^2	121.46 ± 4.47	111.77 ± 3.79	114.35 ± 7.87	115.123 ± 7.41
n_{Left}	-	50.00 ± 111.32	50.00 ± 111.32	50.00 ± 111.32	50 ± 111.32
n_{Right}	-	124.65 ± 2.58	108.49 ± 311.77	3.31 ± 1.06	2.96 ± 0.83
α_{Left}	-	52.06 ± 47.94	52.06 ± 122.44	55.08 ± 125.42	52.06 ± 122.44
α_{Right}	-	-0.55 ± 0.03	-0.48 ± 0.02	-0.97 ± 0.10	-0.99 ± 0.11
$p_{\text{T}}^2(J/\psi \gamma)$ combinatorial					
a	$[\text{MeV}/c]^{-2}$	-0.58 ± 0.04	-0.56 ± 0.04	-2.78 ± 0.68	-2.60 ± 1.01
b	$[\text{MeV}/c]^{-2}$	-	-	-0.64 ± 0.18	-0.77 ± 0.19
A	$[\text{MeV}/c]^{-2}$	0.44 ± 0.60	0.43 ± 0.42	0.92 ± 0.83	0.82 ± 0.59
B	$[\text{MeV}/c]^{-2}$	-	-	0.14 ± 0.76	0.33 ± 0.62

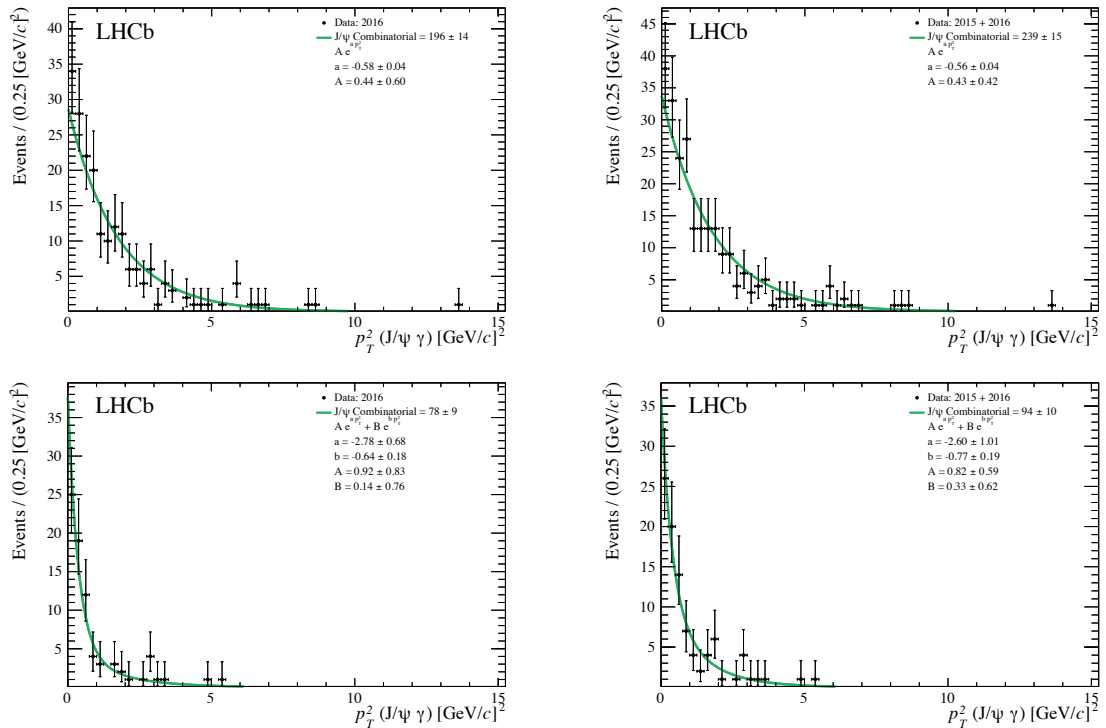


Figure 6.4. Fit of p_T^2 distribution of J/ψ -combinatorial background modelled by mismatched J/ψ mesons and converted photons from different events before (top) and after (bottom) the HERSCHEL cut is applied, $\ln(\chi_{\text{HRC}}^2) < 5$, for the 2016-only (left), and combined 2015 and 2016 (right) data with our CEP χ_c selection applied. We use one exponential to fit the p_T^2 distribution with all parameters left floating shown in green.

2370 We can also determine the p_T^2 distribution of the $J/\psi\gamma$ background system with this
 2371 method. Prior to the application of the HERSCHEL cut, the shape is well described by a single
 2372 exponential, $A \cdot \exp(a \cdot p_T^2)$, where A is a normalisation parameter and a is the slope of the
 2373 exponential. However, once the HERSCHEL cut is applied a single exponential is not sufficient
 2374 to successfully describe the p_T^2 distribution. Therefore, we use the sum of two exponentials to fit
 2375 the p_T^2 distribution such that, $A \cdot \exp(a \cdot p_T^2) + B \cdot \exp(b \cdot p_T^2)$, where A and B are normalisation
 2376 parameters and a and b are the slopes of the exponentials. All parameters are floated during
 2377 the unbinned-maximum-likelihood fit of both samples. The fit results are shown in Fig. 6.4 and
 2378 the fit parameter values are detailed in Table 6.2. We use these results to fix the fit parameters
 2379 and the yield of the Δm_{χ_c} , as well as p_T^2 in the CEP χ_c fit.

2380 6.2 $\psi(2S)$ feed-down background modelling

2381 In this section we discuss possible contributions from $\psi(2S)$ feed-down through decays that
 2382 include an intermediate J/ψ meson and a photon. These events are accompanied by one or
 2383 more particles other than the $J/\psi\gamma$ system and can therefore be rejected by the exclusivity
 2384 requirement of CEP. However, we expect feed-down contributions from $\psi(2S)$ decays that

2385 mimic our signal when one or more of the decay particles are not reconstructed by the main
 2386 spectrometer, or if we fail to veto them.

2387 6.2.1 $\psi(2S)$ feed-down reconstruction

2388 To calculate the contribution of $\psi(2S)$ feed-down background on our CEP χ_c selection, we
 2389 use the $\psi(2S) \rightarrow J/\psi X$ Monte Carlo described in Sec. 4.1.4. Here, X represents all possible
 2390 decay products in a $\psi(2S)$ decay containing a J/ψ meson. The same criteria used for the CEP
 2391 χ_c selection are applied to the $\psi(2S)$ Monte Carlo. Some of these decays have two or more
 2392 photons in the final state. This reduces the available phase space and, on average, results in low
 2393 transverse-momentum photons. As expected from the photon-conversion efficiency results, the
 2394 reconstruction rate of these events is low. As a result of this and the limited Monte Carlo sample
 2395 size (100,000 generated events) fully reconstructing the $J/\psi[\mu^+\mu^-]\gamma[e^+e^-]$ system results in
 2396 a sample with limited statistical precision. In addition, the Monte Carlo description of the
 2397 photon-conversion probability and reconstruction may not match the data efficiency well.

2398 To take advantage of the more precise and reliable photon-conversion efficiency measured from
 2399 data, detailed in Sec. 5.1, we reconstruct only the J/ψ meson while keeping the generator-level
 2400 information of the photons associated with the decay irrespective of whether the photons convert
 2401 in Monte Carlo. we later apply our knowledge of the photon-conversion and reconstruction
 2402 efficiency from data. These decay modes involve more than one photon and the reconstructed-
 2403 mass distributions vary according to which photon is paired with the J/ψ mesons. The vast
 2404 majority of the decays involve two photons, however, the $\psi(2S) \rightarrow J/\psi[\mu^+\mu^-]\pi^0[\gamma\gamma]\pi^0[\gamma\gamma]$
 2405 decay has four photons, two from each π^0 meson. We save up to four photons involved in the
 2406 main decay chain, $\gamma_1, \gamma_2, \gamma_3,$ and $\gamma_4,$ then reconstruct the $J/\psi\gamma$ system for all possible pairs.
 2407 All bremsstrahlung photons are omitted from this selection process.

2408 The reconstruction resolution of the photons will have an effect on the number of events
 2409 that fall within our CEP $\chi_c \Delta m_{\chi_c}$ selection window, and ultimately the Δm_{χ_c} shape we extract
 2410 for later use in our CEP χ_c signal fit. These photons are particularly sensitive to resolution
 2411 effects due to bremsstrahlung radiation and our ability to correct for it. Therefore, to account
 2412 for detector-resolution effects for the converted photons we use the combined 2015 and 2016
 2413 χ_{c2} Monte Carlo introduced in section Sec. 6.5.1. The CEP χ_c analysis selection is applied
 2414 and we use generator-level information to check that the reconstructed particles belong to our
 2415 decay. The resolution for each of the four-momentum components is given by subtracting the
 2416 true value from the reconstructed value. These resolution distributions are shown in Fig. 6.5
 2417 for 2015 run conditions. For any given event, the amount of smearing necessary to account for
 2418 the detector-resolution effects is given by the product of a randomly selected resolution value
 2419 from the corresponding normalised-momentum resolution distribution, and the absolute value
 2420 of the true-momentum component of the accompanying photon, which is saved alongside the
 2421 reconstructed J/ψ in the $\psi(2S) \rightarrow J/\psi X$ Monte Carlo.

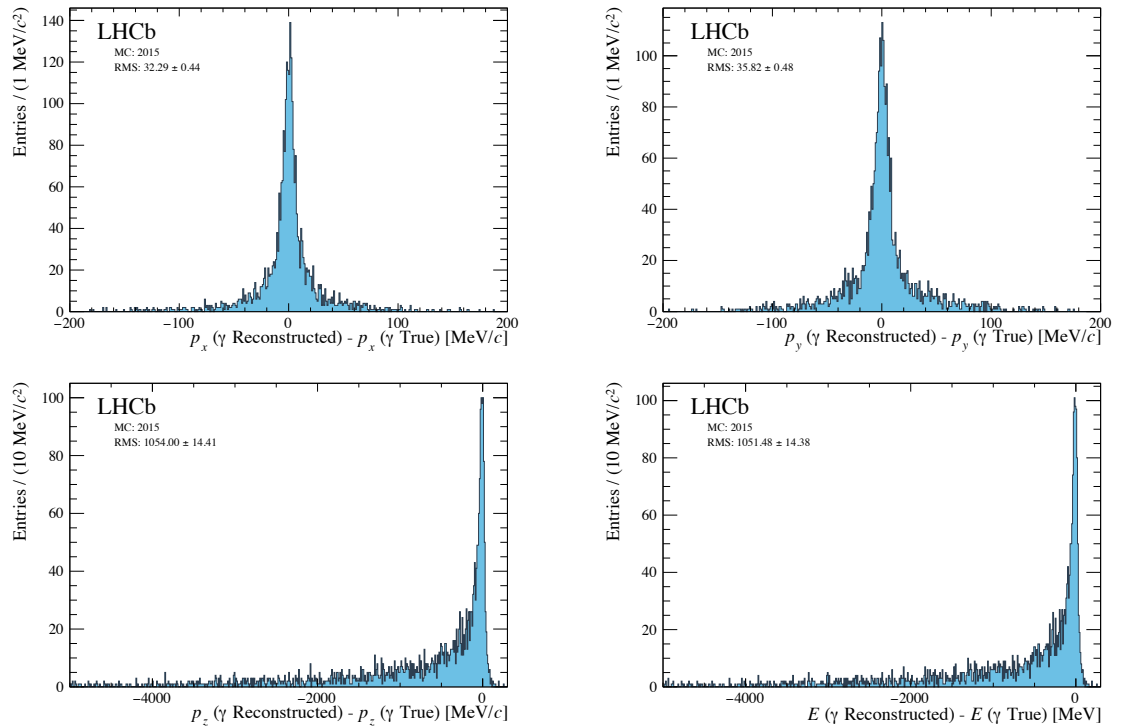


Figure 6.5. Photon-reconstruction-resolution distributions for p_x (top left), p_y (top right), p_z (bottom left), and E (bottom right) using reconstructed CEP χ_{c2} Monte Carlo from pp collisions at a centre-of-mass energy $\sqrt{s} = 13$ TeV for 2015 run conditions.

2422 The resolution of the three-momentum components are not significantly correlated and can
 2423 be used to smear the momentum of the accompanying photons independently. Similarly, no
 2424 strong correlations are observed between the energy resolution and the momentum resolution
 2425 along the x and y -axis. However, there is a strong correlation between the energy resolution
 2426 and the momentum resolution along the z -axis. As a result of this strong correlation, the energy and
 2427 momentum along the z -axis can not be randomly smeared simultaneously. Instead, the same
 2428 randomly selected smear factor is used for both p_z and E . The smeared photon four-vector can
 2429 now be used to calculate the Δm_{χ_c} together with their corresponding p_T^2 distributions, shown
 2430 in Fig. 6.6.

2431 The difference in the profile of the distributions is due to the nature of the algorithm designed
 2432 to search for the photons associated with the $\psi(2S)$ meson, namely γ_1 to γ_4 . For example, in
 2433 $\psi(2S) \rightarrow \chi_c \gamma$ decays the χ_c mesons tend to appear earlier in the decay list. Therefore, the
 2434 first photon the algorithm encounters is associated with the χ_c decay, $\chi_c \rightarrow J/\psi \gamma$. This is
 2435 reflected in the presence of the three resonant χ_{c0} , χ_{c1} , and χ_{c2} peaks in invariant-mass-difference
 2436 distributions in Fig. 6.6 (first row). The second photon encountered by the algorithm would
 2437 then be the one associated with $\psi(2S)$ decay, $\psi(2S) \rightarrow \chi_c \gamma$. This is also reflected as three peaks
 2438 in the invariant-mass distribution in Fig. 6.6 (second row). However, due to the higher invariant
 2439 mass of the χ_{c2} meson the phase space available for the photon is lower than that in decays

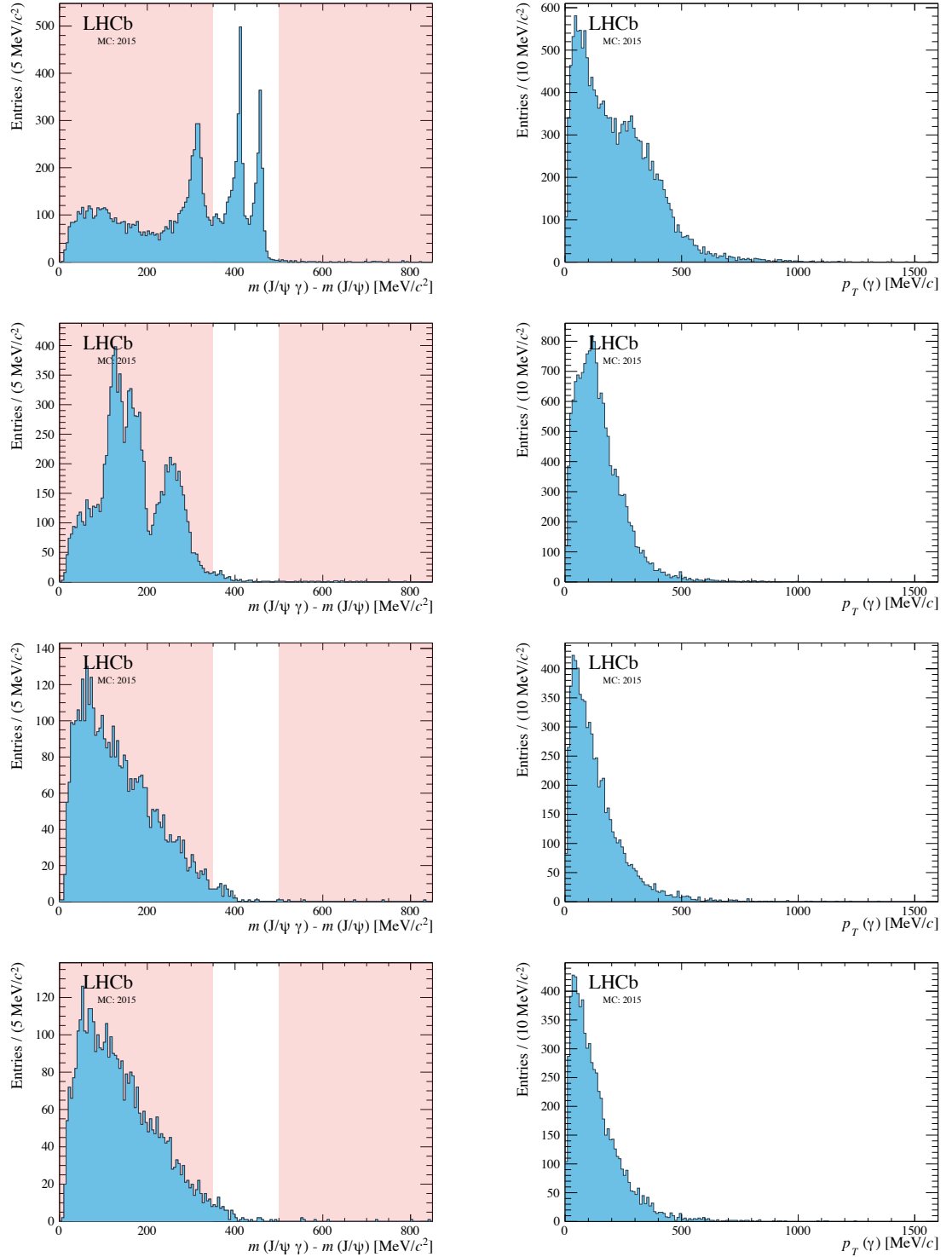


Figure 6.6. Delta-mass (left) and p_T^2 (right) distributions of reconstructed J/ψ mesons and generator-level photons prior to conversion and reconstruction, from $\psi(2S) \rightarrow J/\psi[\mu^+\mu^-]X$ Monte Carlo from pp collisions at $\sqrt{s} = 13$ TeV for 2015 run conditions. Since there are decay modes with more than one photon, we consider four possible combinations displayed separately: γ_1 , γ_2 , γ_3 , and γ_4 from top to bottom. The vetoed Δm_{χ_c} region in the CEP χ_c selection is highlighted in red.

2440 with a χ_{c0} . Therefore, when we reconstruct the $J/\psi\gamma$ system with the second photon the order
 2441 of the peaks is inverted. That is, the χ_{c2} decay is the one at lower Δm_{χ_c} values followed by χ_{c1}
 2442 and χ_{c0} . Finally, there are cases where more than one photon appears within the same decay
 2443 generation such as in $\psi(2S) \rightarrow J/\psi[\mu^+\mu^-]\pi^0[\gamma\gamma]\pi^0[\gamma\gamma]$. In this case, similar shapes are present
 2444 in all four Δm_{χ_c} distributions. The Δm_{χ_c} distributions in Fig. 6.6 (rows three and four) come
 2445 from these decay channels and are also present in the other two plots.

2446 6.2.2 Photon-conversion efficiency and production-mechanism weights

2447 Using the true transverse momentum of the photon, we weight each event by the photon-
 2448 conversion efficiency as determined in data according to Fig. 5.13 in Sec. 5.1. We multiply this
 2449 efficiency by a factor of two to account for the dependence of the photon-conversion efficiency on
 2450 the detector occupancy, so as to be appropriate for CEP-like events, as described in Sec. 5.1.6.

2451 The feed-down background receives contributions from both exclusive and inclusive (i.e.
 2452 inelastic) $\psi(2S)$ mesons. To model these two contributions, the Monte Carlo kinematics of
 2453 $\psi(2S)$ mesons are reweighted to match the characteristic kinematics of each production mode
 2454 according to the results of an earlier LHCb analysis [43], where two exponentials are used to fit
 2455 the p_T^2 ($\psi(2S)$) distribution: one for the inelastic background, B_I , and another for the exclusive
 2456 background, B_E . Each shape consists of two parameters: one for normalization, p_0 and p_2
 2457 respectively, and another for the slope of the exponential, p_1 and p_3 respectively, such that,

$$B_I(p_T^2) = e^{(p_0+p_1 \cdot p_T^2)} \quad \text{and} \quad B_E(p_T^2) = e^{(p_2+p_3 \cdot p_T^2)}. \quad (6.2)$$

2458 The experimental fit result of the $\psi(2S)$ study is reproduced in Fig. 6.7. The parameters from
 2459 these fits are: $p_0 = 3.536 \pm 0.340$, $p_1 = -0.7966 \pm 0.2490$ [MeV/c] $^{-2}$, $p_2 = 5.667 \pm 0.082$, and
 2460 $p_3 = -6.075 \pm 0.799$ [MeV/c] $^{-2}$.

2461 To perform the re-weighting, the generator-level kinematic information of the $\psi(2S)$ is saved
 2462 alongside the reconstructed $J/\psi \rightarrow \mu^+\mu^-$ mesons. The weights for each case, CEP and inelastic,
 2463 are calculated by taking the ratio of the $p_T^2(\psi(2S))$ extracted from the $\psi(2S)$ experimental
 2464 fit results, and the $p_T^2(\psi(2S))$ of the generator-level $\psi(2S)$ Monte Carlo. Furthermore, the
 2465 inelastic events are assigned an additional weight factor of 0.776, which is the ratio of exclusive-
 2466 to-inclusive processes measured in an LHCb study of $\psi(2S)$ CEP [43]. Meanwhile the CEP
 2467 events are assigned a complementary weight factor of $1 - 0.776$, assuring the two backgrounds
 2468 are produced in the correct proportions. The Δm_{χ_c} distribution of the CEP and inclusive $J/\psi\gamma$
 2469 system from $\psi(2S)$ decays, after the selection and weights are applied, is shown in Fig. 6.8 for
 2470 each of the four photons used to construct the $J/\psi\gamma$ pair.

2471 6.2.3 $\psi(2S)$ feed-down fit and number of expected events

2472 The Δm_{χ_c} distributions are fitted with a kernel estimation PDF (KE PDF), which is an
 2473 extremely flexible fit method capable of describing the intricate shapes of this background. Since
 2474 up to four photons are saved for each $\psi(2S)$ meson, the simulated data sets for each $J/\psi\gamma$ pair
 2475 are treated independently and their fit results are shown in Fig. 6.8. The PDFs are then merged

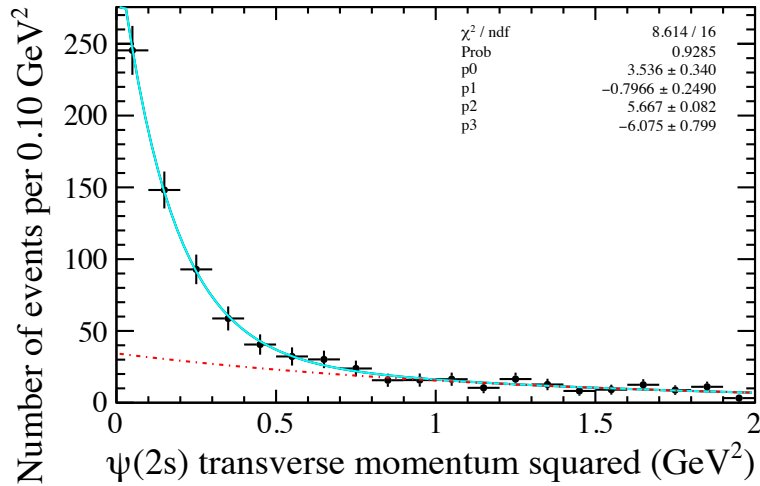


Figure 6.7. Transverse-momentum-squared distribution of $\psi(2S) \rightarrow \mu^+\mu^-$ CEP candidates from 2015 pp collisions at a centre-of-mass energy $\sqrt{s} = 13$ TeV. The distribution is fitted with two exponentials: one for CEP events in cyan and another for the inelastic background in dashed red. Reproduced from Ref. [43].

2476 for both the CEP and inelastic components in proportion to their calculated contribution, as
 2477 detailed below. The resulting distribution is used as an input for the fit of the CEP χ_c sample.

2478 From the weighted Monte Carlo we can determine an effective efficiency of the selection
 2479 process, ϵ_s , defined here as the number of events that pass the reconstruction and our selection
 2480 from the 100,000 generated events. This includes the effects of the weights associated with
 2481 the production mechanism, the reconstruction efficiency of the dimuons, the photon-conversion
 2482 efficiency, and the multiplicity-correction factor. In the case of CEP production, we have an
 2483 average-effective efficiency for up to four possible photon combinations of 8.87×10^{-6} within
 2484 our Δm_{χ_c} selection window, 350 to 500 MeV/ c^2 . In the case of inelastic production we have an
 2485 average-effective efficiency of 4.15×10^{-6} within the same range.

2486 The number of expected $\psi(2S)$ feed-down background events, $N(\psi(2S))_{\text{FD}}$, is calculated as
 2487 follows:

$$N(\psi(2S))_{\text{FD}} = \frac{\mathcal{L} \cdot \sigma(\psi(2S) \rightarrow \mu^+\mu^-) \cdot \mathcal{B}(J/\psi \rightarrow \mu^+\mu^-) \cdot \mathcal{B}(\psi(2S) \rightarrow J/\psi X) \cdot \epsilon_s}{\mathcal{B}(\psi(2S) \rightarrow \mu^+\mu^-)}, \quad (6.3)$$

2488 where \mathcal{L} is the integrated luminosity, $\sigma(\psi(2S) \rightarrow \mu^+\mu^-) = 11.1 \pm 1.1 \pm 0.3 \pm 0.4$ pb is the
 2489 cross-section for the CEP of $\psi(2S)$ reconstructed with two muons within the acceptance of
 2490 the LHCb experiment ($2 < \eta(\mu^+\mu^-) < 4.5$) [43]. $\mathcal{B}(J/\psi \rightarrow \mu^+\mu^-) = (5.961 \pm 0.033)$ %
 2491 and $\mathcal{B}(\psi(2S) \rightarrow \mu^+\mu^-) = (8.0 \pm 0.6) \times 10^{-3}$ are the branching fractions for J/ψ and $\psi(2S)$
 2492 decaying into a pair of muons, and $\mathcal{B}(\psi(2S) \rightarrow J/\psi X) = (61.4 \pm 0.6)$ % is the branching
 2493 fraction for $\psi(2S)$ mesons decaying into $J/\psi X$ according to the PDG [81]. The total number
 2494 of expected $\psi(2S)$ feed-down events is calculated for each $J/\psi\gamma$ pair independently and their

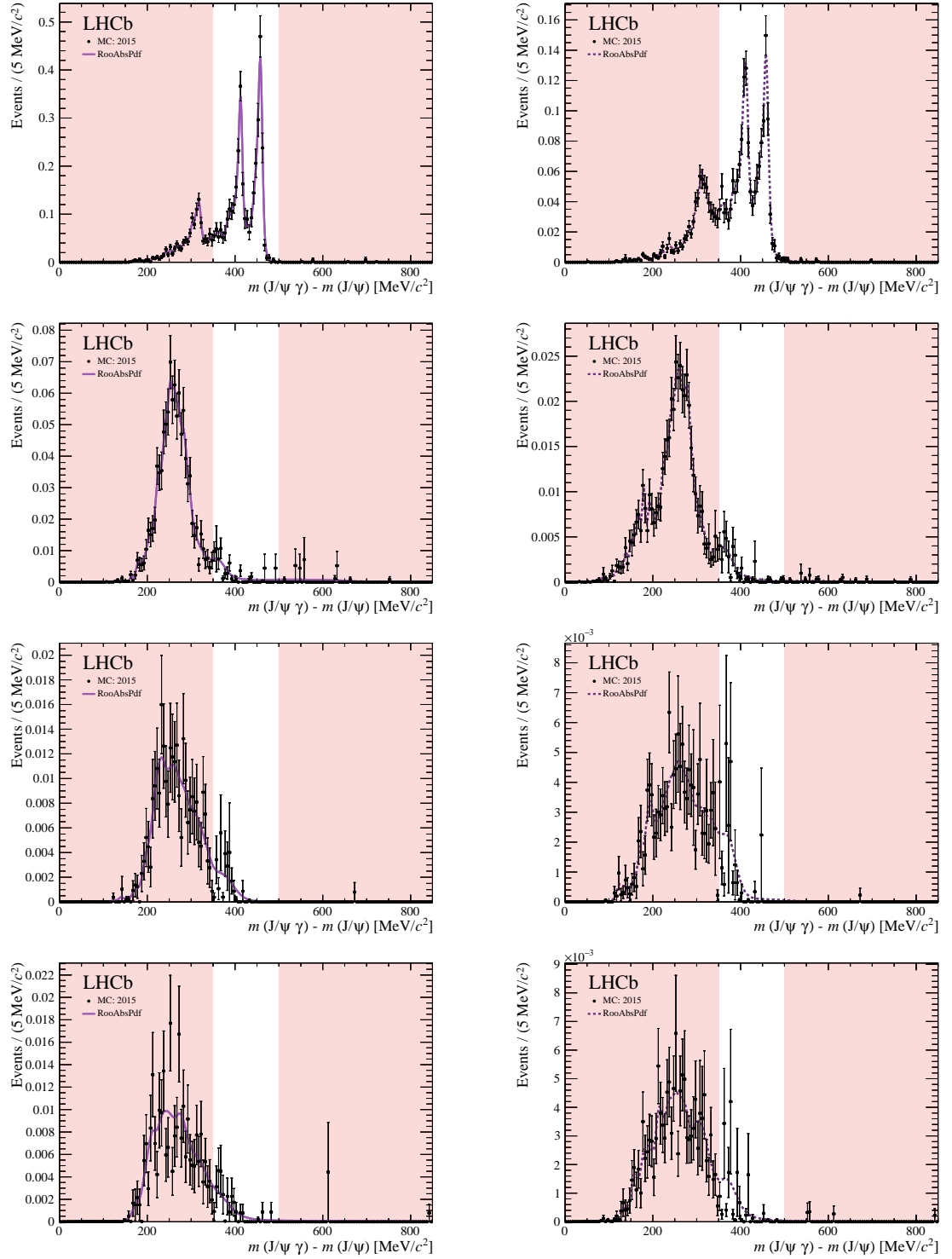


Figure 6.8. Delta-mass of $J/\psi\gamma$ system from $\psi(2S) \rightarrow J/\psi X$ feed-down using weighted Monte Carlo of pp collisions at a centre-of-mass energy $\sqrt{s} = 13$ TeV to match CEP (left column) and inelastic (right column) experimental $\psi(2S)$ kinematics. This is done for four potentially reconstructible photons, γ_1 , γ_2 , γ_3 , and γ_4 , from top to bottom.

Table 6.3. Summary of $\psi(2S)$ feed-down (FD) and combinatorial-background studies including the number of expected background events within the CEP χ_c Δm_{χ_c} selection, 350 to 500 MeV/ c^2 , for the 2015 (2016), and combined 2015 and 2016 CEP χ_c data, both with and without the HERSCHEL cut. The effective-efficiency value, ϵ_s , used in the calculation of the total number of events is also included for 2015 Monte Carlo. Also listed is the total number of events passing the signal selection.

Mechanism	$\ln(\chi_{\text{HRC}}^2)$	γ_n	ϵ_s $\times 10^{-5}$	Events 2015 (2016)	Total 2015 (2016)	Combined 2015 + 2016
Selected	-	-	-	-	88 (451)	539
	< 5	-	-	-	23 (127)	150
$\psi(2S)_{\text{FD}}^{\text{CEP}}$	-	γ_1	3.45	0.98 ± 0.24 (5.80 ± 1.4)	1.02 ± 0.61 (5.97 ± 3.58)	6.98 ± 5.93
	-	γ_2	0.069	0.0196 ± 0.0058 (0.11 ± 0.03)		
	-	γ_3	0.026	0.007 ± 0.003 (0.043 ± 0.015)		
	-	γ_4	0.027	0.008 ± 0.002 (0.045 ± 0.014)		
$\psi(2S)_{\text{FD}}^{\text{CEP}}$	< 5	γ_1	-	0.69 ± 0.17 (4.91 ± 1.19)	0.72 ± 0.43 (5.08 ± 3.05)	5.80 ± 4.92
	< 5	γ_2	-	0.0138 ± 0.0041 (0.1 ± 0.03)		
	< 5	γ_3	-	0.005 ± 0.002 (0.036 ± 0.013)		
	< 5	γ_4	-	0.005 ± 0.002 (0.039 ± 0.012)		
$\psi(2S)_{\text{FD}}^{\text{In.}}$	-	γ_1	1.58	0.45 ± 0.11 (2.6 ± 0.6)	0.47 ± 0.29 (2.76 ± 1.70)	3.23 ± 2.81
	-	γ_2	0.035	0.01 ± 0.003 (0.058 ± 0.017)		
	-	γ_3	0.024	0.007 ± 0.002 (0.04 ± 0.014)		
	-	γ_4	0.016	0.005 ± 0.002 (0.027 ± 0.009)		
$\psi(2S)_{\text{FD}}^{\text{In.}}$	< 5	γ_1	-	0.32 ± 0.08 (1.8 ± 0.4)	0.34 ± 0.21 (1.86 ± 1.15)	2.20 ± 1.92
	< 5	γ_2	-	0.007 ± 0.002 (0.039 ± 0.011)		
	< 5	γ_3	-	0.005 ± 0.002 (0.027 ± 0.009)		
	< 5	γ_4	-	0.003 ± 0.001 (0.018 ± 0.006)		
$\mu^+\mu^-$ comb.	-	-	-	-	(0.68 ± 0.36)	0.46 ± 0.39
	< 5	-	-	-	(0.51 ± 0.26)	0.43 ± 0.26
J/ψ comb.	-	-	-	-	(35.55 ± 5.85)	44.97 ± 6.35
	< 5	-	-	-	(11.91 ± 4.51)	13.25 ± 4.66

2495 results are summed together to account for the full range of decay modes that contribute to
2496 this background. We find a total of 5.97 ± 3.58 (6.98 ± 5.93) CEP $\psi(2S)$ feed-down background
2497 and 2.76 ± 1.70 (3.23 ± 2.81) inelastic $\psi(2S)$ feed-down background events within our Δm_{χ_c}
2498 selection window in the 2016-only (combined 2015 and 2016) data. Therefore, we expect to see
2499 a very small contribution of feed-down events. These results are summarised in Table 6.3.

2500 6.2.4 $\psi(2S)$ feed-down background with HERSCHEL

2501 To account for the effects of the HERSCHEL cut we use the efficiency for CEP, $\epsilon_{\text{HRC}}^{\text{CEP}}$, and
2502 inelastic, $\epsilon_{\text{HRC}}^{\text{In.}}$, events calculated in Sec. 5.6. With these efficiencies, we can scale down the
2503 calculated $\psi(2S)$ feed-down background prior to the implementation of the HERSCHEL cut, as
2504 calculated in Sec. 6.2. For a HERSCHEL cut of $\ln(\chi_{\text{HRC}}^2) < 5$, $\epsilon_{\text{HRC}}^{\text{CEP}} = 85.1 \pm 0.8$ (83.0 ± 0.8)
2505 and $\epsilon_{\text{HRC}}^{\text{In.}} = 67.6 \pm 0.8$ (68.2 ± 0.7) for 2016-only (combined 2015 and 2016), we expect to see

2506 5.08 ± 3.05 (5.80 ± 4.92) CEP and 1.86 ± 1.15 (2.20 ± 1.92) inelastic $\psi(2S)$ feed-down events in
 2507 2016-only (combined 2015 and 2016) χ_c data after the HERSCHEL cut is applied. The results
 2508 are summarised in Table 6.3.

2509 6.3 Inelastic χ_c background

2510 The background in the CEP χ_c selection is dominated by the inelastic production of χ_c mesons.
 2511 In this process the proton fragments, or debris from gluon radiation, may leave traces in the
 2512 main spectrometer. In the case that they do, we are able to suppress the background via our
 2513 CEP track selection, which requests two long tracks for the two muons associated with the
 2514 J/ψ , and two downstream tracks for the two electrons used to reconstruct the photon in an
 2515 otherwise empty detector. However, due to the high longitudinal momentum of the protons,
 2516 the proton fragments tend to continue their trajectory down the beam line and outside the
 2517 detector acceptance. We are able to reject some of these high-rapidity inelastic events by
 2518 looking for activity in the HERSCHEL modules. In addition, we can exploit the different
 2519 transverse-momentum signatures of CEP and inelastic events to determine the contribution of
 2520 inelastic events we fail to veto by simultaneously fitting the Δm_{χ_c} and p_T^2 distributions of the
 2521 χ_c candidates. In particular, this study allows us to determine the following information to
 2522 later constrain the global CEP χ_c fit necessary to determine the contributions from CEP and
 2523 inelastic processes:

- 2524 • The production ratio of inelastic χ_{c1} and χ_{c2} within our Δm_{χ_c} selection window.
- 2525 • Understand the Δm_{χ_c} fit model for inelastic χ_c candidates.
- 2526 • Extract the p_T^2 fit model for inelastic χ_c candidates.

2527 6.3.1 Inelastic data set and selection

2528 To study the inelastic χ_c contribution, we select a sample guaranteed to be inelastic by ensuring
 2529 events violate the rapidity-gap criteria through the presence of additional tracks, other than
 2530 those associated with the χ_c decay mode. We use the main analysis χ_c data samples but omit
 2531 the CEP track-selection criteria used to meet the rapidity-gap criteria and, in its place, we
 2532 select events that have two downstream tracks for the converted-photon reconstruction and
 2533 three or more long tracks, two of which are muons from the J/ψ meson reconstruction, and no
 2534 other tracks. This guarantees we are selecting inelastic χ_c events and associated backgrounds.
 2535 From this point forth, we will refer to this data set as the $\geq 3\text{Long}$ sample. A total of 3099 and
 2536 2096 events pass our selection for the 2015 and 2016 data respectively, of which 838 and 778
 2537 events fall within our Δm_{χ_c} selection window.

2538 In addition, we apply the HERSCHEL cut, $\ln(\chi_{\text{HRC}}^2) < 5$, to the $\geq 3\text{Long}$ sample to study
 2539 its effects on the inelastic background. From here on, we will refer to this sample as the
 2540 $\geq 3\text{Long} + \text{HRC}$ sample. A total of 187 and 191 events pass our $\geq 3\text{Long} + \text{HRC}$ selection for
 2541 2015 and 2016 data, adding up to a total of 378 for the combined 2015 and 2016 sample. As
 2542 expected, the HERSCHEL cut has reduced the size of this sample significantly compared to the

2543 ≥ 3 Long sample. Of these events, 55 and 60 fall within our Δm_{χ_c} selection window for each
 2544 year respectively, summing to 115 events for the combined data set.

2545 Recall that the CEP selection has a tight requirement for the maximum number of SPD hits
 2546 imposed at the hardware-trigger level, and so the multiplicity in these events is still low. The
 2547 2015 data set has a larger number of events due to looser requirements on the event multiplicity
 2548 at the hardware-trigger level, in spite of 2016 being the sample with higher integrated luminosity
 2549 since higher-multiplicity events are more common. The number of events in the ≥ 3 Long and
 2550 ≥ 3 Long + HRC samples are summarised in Table 6.4.

Table 6.4. Summary of ≥ 3 Long sample with and without the HERSCHEL cut, $\ln(\chi_{\text{HRC}}^2)$, including $\psi(2S)$ feed-down and combinatorial-background results for events within the CEP χ_c Δm_{χ_c} selection window, 350 to 500 MeV/ c^2 , for 2015 (2016), and the combined 2015 and 2016 luminosities. The effective-efficiency value, ϵ_s , used in the calculation of the total number of events is also included for Monte Carlo with 2015 run conditions. Also listed is the total number of events passing the signal selection

Mechanism	$\ln(\chi_{\text{HRC}}^2)$	γ_n	ϵ_s $\times 10^{-5}$	Events 2015 (2016)	Total 2015 (2016)	Combined 2015 + 2016
Selected	-	-	-	-	838 (778)	1616
	< 5	-	-	-	55 (60)	115
$\psi(2S)_{\text{FD}}^{\text{In}}$ ≥ 3 Long	-	γ_1	0.146	0.041 ± 0.011 (0.243 ± 0.063)		
	-	γ_2	0.017	0.005 ± 0.002 (0.028 ± 0.01)	0.05 ± 0.03	
	-	γ_3	0.003	0.0009 ± 0.0003 (0.005 ± 0.002)	(0.29 ± 0.2)	0.33 ± 0.33
	-	γ_4	0.005	0.0015 ± 0.0006 (0.009 ± 0.004)		
$\psi(2S)_{\text{FD}}^{\text{In}}$ ≥ 3 Long + HRC	< 5	γ_1	-	0.03 ± 0.008 (0.164 ± 0.042)		
	< 5	γ_2	-	0.003 ± 0.001 (0.019 ± 0.007)	0.04 ± 0.02	
	< 5	γ_3	-	0.0007 ± 0.0002 (0.004 ± 0.001)	(0.19 ± 0.14)	0.23 ± 0.23
	< 5	γ_4	-	0.0011 ± 0.0004 (0.006 ± 0.002)		
Comb.	-	-	-	-	(439.37 ± 14.56)	1177.77 ± 22.92
	< 5	-	-	-	(52.52 ± 5.58)	90.74 ± 6.54

2551 As well as genuine χ_c events, this samples will also contain combinatorial and feed-down
 2552 backgrounds. To determine these non- χ_c backgrounds, we repeat the procedures detailed in
 2553 the two previous sections, Sec. 6.1 and Sec. 6.2, used to model combinatorial and feed-down
 2554 backgrounds in order to access the pure inelastic χ_c component. Table 6.4 also summarises these
 2555 contributions to the inelastic sample, the determination of which is detailed in the following
 2556 sections. As will be seen, the combinatorial background is dominant in this sample.

2557 6.3.2 Combinatorial background in inelastic χ_c sample

2558 To study the combinatorial background in the ≥ 3 Long and ≥ 3 Long + HRC samples, we
 2559 apply the same data-driven approach described in Sec. 6.1.2 to model the J/ψ combinatorial
 2560 background for the CEP χ_c sample and fit the purely combinatorial Δm_{χ_c} range. Since this
 2561 method is also sensitive to the much smaller continuum-combinatorial background, we use a
 2562 single shape to account for both backgrounds. We mismatch J/ψ mesons with converted photons

2563 from different events using the $\geq 3\text{Long}$ sample, then fit the p_T^2 and the Δm_{χ_c} distributions of
 2564 the $J/\psi\gamma$ system. To model the $p_T^2(J/\psi\gamma)$ distribution of the $\geq 3\text{Long}$ sample we use the sum
 2565 of two exponentials, such that

$$A \cdot e^{-a \cdot p_T^2} + B \cdot e^{-b \cdot p_T^2}, \quad (6.4)$$

2566 where A and B are normalising factors while a and b are the slopes of the exponentials. In
 2567 the case of the $\geq 3\text{Long} + \text{HRC}$ sample, we use a single exponential, $A \cdot \exp(-a \cdot p_T^2)$. The fit
 2568 results are shown in Fig. 6.9 where we see small contributions from the second exponential in
 2569 the fit of the $\geq 3\text{Long}$ sample.

2570 We use a double-sided Crystal Ball in a maximum-unbinned-likelihood fit to model the
 2571 Δm_{χ_c} distribution. The fit results are shown in Fig. 6.10. The parameter values for the p_T^2
 2572 and Δm_{χ_c} fits are summarised in Table 6.5. These shapes are then fixed and used to fit the
 2573 Δm_{χ_c} and $p_T^2(J/\psi\gamma)$ in the $\geq 3\text{Long}$ and $\geq 3\text{Long} + \text{HRC}$ inelastic χ_c data set, as shown in
 2574 Fig. 6.11. The data in the resonant region are not shown as this is signal dominated and is
 2575 not accounted for in this fit model. The normalisation of the fit is based on the combinatoric
 2576 region above $500 \text{ MeV}/c^2$ and the PDF is extrapolated into our CEP χ_c selection window, 350
 2577 to $500 \text{ MeV}/c^2$. Although there is significantly more combinatorial background in this sample
 2578 compared to the CEP χ_c sample, the data-driven method does an excellent job at modelling
 2579 this contribution. We see a total of 1177.77 ± 22.92 (13.25 ± 4.66) events in the combined 2015
 2580 and 2016 data, and 439.37 ± 14.56 (11.91 ± 4.51) events in the 2016-only data without (with)
 2581 the HERSCHEL cut applied. These results are summarised in Table 6.4.

Table 6.5. Parameters of Δm_{χ_c} and p_T^2 fits of J/ψ -combinatorial background of the $\geq 3\text{Long}$ and $\geq 3\text{Long} + \text{HRC}$ sample for the 2016-only, and combined 2015 and 2016 data.

Variable	Units	Without HERSCHEL		With HERSCHEL	
		2016	2015 + 2016	2016	2015 + 2016
Δm_{χ_c} Combinatorial					
μ	MeV/c^2	384.27 ± 4.57	382.86 ± 3.10	439.08 ± 1.34	431.24 ± 11.94
σ	MeV/c^2	112.38 ± 2.80	114.30 ± 1.89	145.89 ± 1.53	143.62 ± 8.13
n_{Left}	-	50.00 ± 111.32	50.00 ± 111.32	50.00 ± 111.32	50.00 ± 111.32
n_{Right}	-	113.85 ± 0.29	107.08 ± 92.53	1.81 ± 0.60	119.16 ± 1.44
α_{Left}	-	62.84 ± 48.13	69.27 ± 126.77	52.06 ± 47.94	52.06 ± 47.94
α_{Right}	-	-0.28 ± 0.01	-0.26 ± 0.01	-0.82 ± 0.01	-0.40 ± 0.03
$p_T^2(J/\psi\gamma)$ Combinatorial					
a	$[\text{MeV}/c]^{-2}$	-0.19 ± 0.05	-0.17 ± 0.02	-0.52 ± 0.07	-0.39 ± 0.04
b	$[\text{MeV}/c]^{-2}$	-0.62 ± 0.12	-0.62 ± 0.09	-	-
A	$[\text{MeV}/c]^{-2}$	0.14 ± 0.55	0.17 ± 0.58	0.34 ± 0.24	0.36 ± 0.68
B	$[\text{MeV}/c]^{-2}$	0.99 ± 0.93	0.86 ± 0.57	-	-

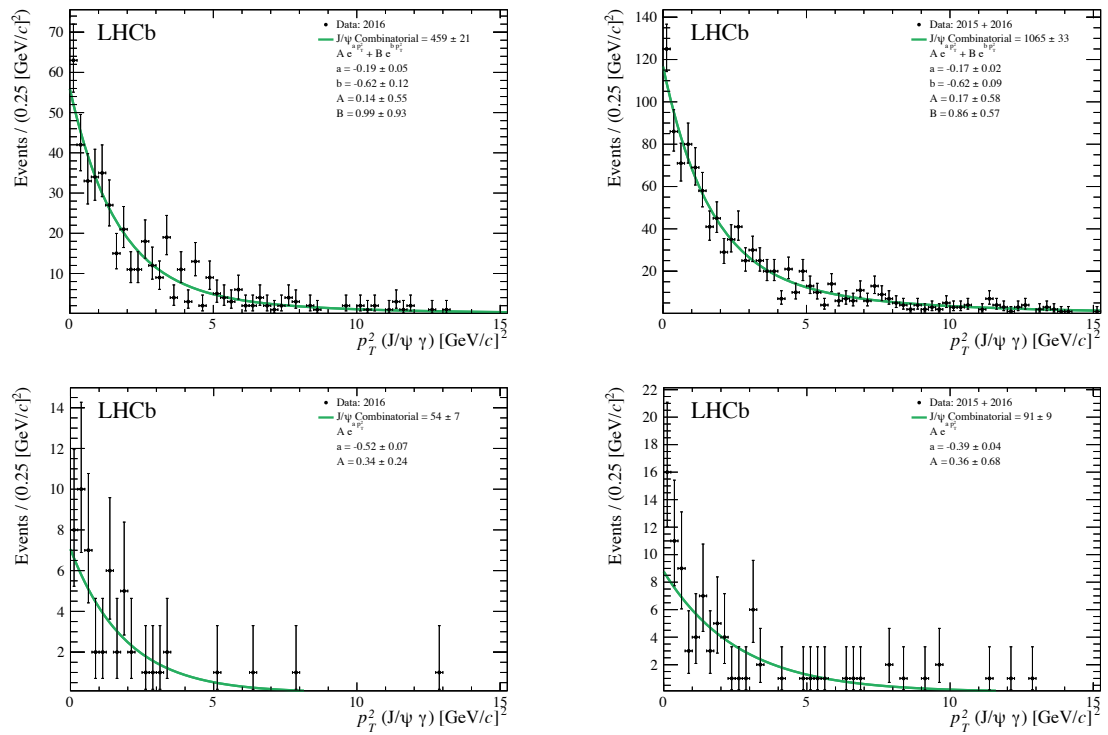


Figure 6.9. Fit of the p_T^2 distribution of the artificial-combinatorial background from the $\geq 3\text{Long}$ (top), fitted with the sum of two exponentials, and $\geq 3\text{Long} + \text{HRC}$ (bottom) samples, fitted with a single exponential, for 2016-only (left), and combined 2015 and 2016 (right) data.

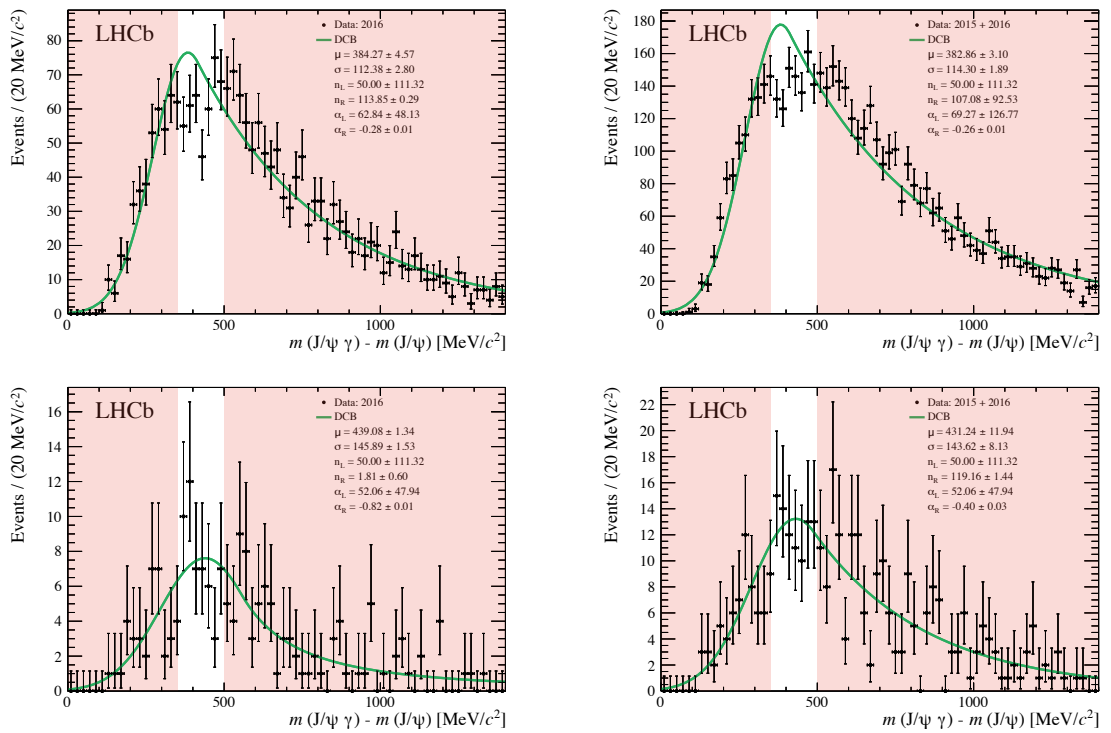


Figure 6.10. Fit of the Δm_{χ_c} distribution of the artificial-combinatorial background using the events from the ≥ 3 Long (top) and ≥ 3 Long + HRC (bottom) sample for the 2016-only (left), and combined 2015 and 2016 (right) data. The vetoed range of our CEP χ_c selection is highlighted in red.

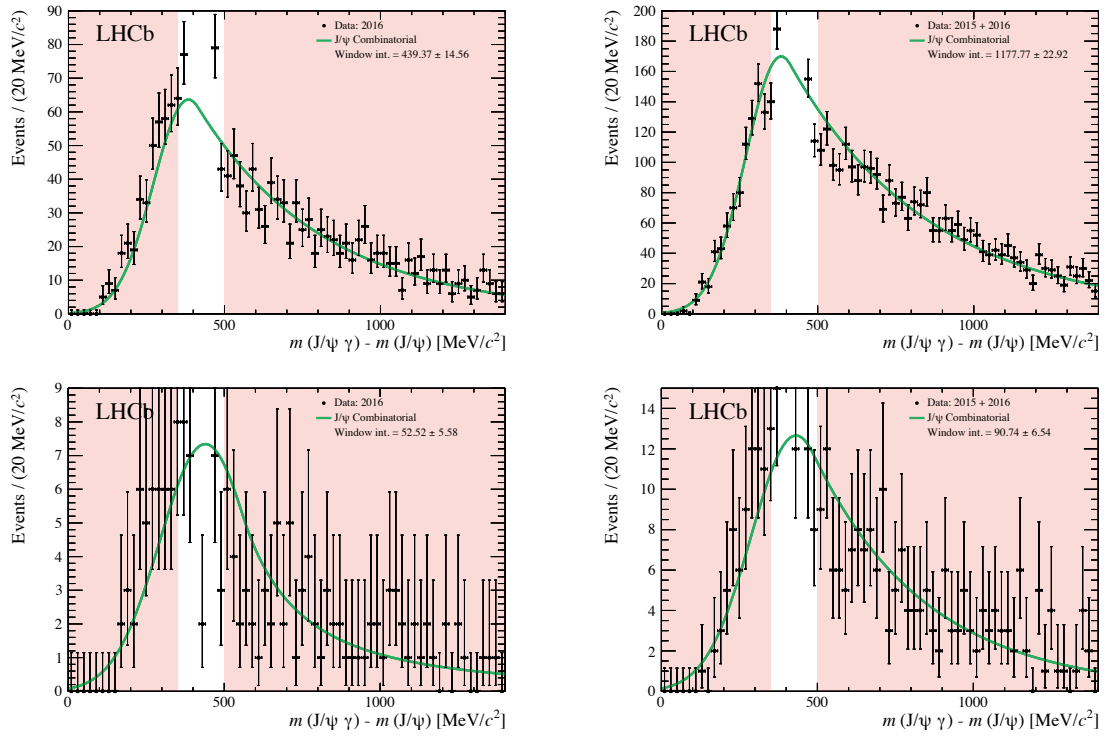


Figure 6.11. Fit of the Δm_{χ_c} distribution of inelastic $\chi_c \rightarrow J/\psi[\mu^+\mu^-]\gamma[e^+e^-]$ decays from the $\geq 3\text{Long}$ (top) and $\geq 3\text{Long} + \text{HRC}$ (bottom) sample, shown in truncated scale for the 2016-only (left), and combined 2015 and 2016 (right) data. The vetoed range of our CEP χ_c selection is highlighted in red.

2582 6.3.3 $\psi(2S)$ feed-down background in inelastic χ_c sample

2583 To calculate the number of expected inelastic $\psi(2S)$ feed-down background events in the
 2584 ≥ 3 Long sample, as well as extract an invariant-mass fit shape, we use the same procedure
 2585 detailed in Sec. 6.2 using the $\psi(2S) \rightarrow J/\psi X$ Monte Carlo. Our selection is identical with the
 2586 exception of the track selection where we replace the CEP track selection criteria with that of
 2587 the ≥ 3 Long sample, by requiring that an event has one or more long tracks on top of the two
 2588 long muon tracks and two downstream electron tracks. We apply the weights associated with
 2589 the photon-conversion efficiency as well as the weights necessary to match the experimental
 2590 p_T^2 ($\psi(2S)$) results of inelastic $\psi(2S)$ mesons. From this, we expect 0.33 ± 0.33 events in the
 2591 combined 2015 and 2016 data set, and 0.29 ± 0.20 in the 2016-only sample. We account for the
 2592 effects of the HERSCHEL cut by scaling the results in Sec. 6.3.3 by $\epsilon_{\text{HRC}}^{\text{In}}$. After performing this
 2593 procedure, we find that we expect a total of 0.23 ± 0.23 inelastic $\psi(2S)$ feed-down events in the
 2594 combined 2015 and 2016 data, and 0.19 ± 0.14 events in the 2016-only data. These results are
 2595 summarised in Table 6.4 for each of the $J/\psi\gamma$ combinations. To extract the PDFs, we apply the
 2596 resolution effects to the photon's kinematics before reconstructing the $J/\psi\gamma$ system. As before,
 2597 the p_T^2 shape is fixed according to the inelastic $\psi(2S)$ component presented in the results of the
 2598 J/ψ and $\psi(2S)$ CEP measurement [43].

2599 6.3.4 Inelastic χ_c background fit

2600 We model each of the inelastic χ_c resonant peaks with a double-sided Crystal Ball and use the
 2601 CEP χ_c Monte Carlo samples described in Sec. 4.1 to constrain the fit parameters. The CEP χ_c
 2602 selection criteria are applied to the reconstructed Monte Carlo and generator-level information
 2603 is used to verify each reconstructed particle in the event matches its type and position within
 2604 the $\chi_c \rightarrow J/\psi[\mu^+\mu^-]\gamma[e^+e^-]$ decay chain. To extract the resonant shapes, we use an unbinned
 2605 maximum-likelihood fit on the Δm_{χ_c} distribution while floating all shape parameters. The
 2606 flexibility of the double-sided Crystal Ball allows for an adequate description of the asymmetric
 2607 shape, which results from the energy loss of the electrons to bremsstrahlung radiation. The
 2608 fit results are shown in Fig. 6.12 and the final values of the fit parameters are summarised in
 2609 Table 6.6.

2610 In the fit of the ≥ 3 Long sample, the two double-sided Crystal Balls for the χ_{c1} and χ_{c2}
 2611 contributions are joined together into a single composite shape. This allows us to simplify the
 2612 model of the inelastic p_T^2 contribution to a single shape and a single yield parameter shared
 2613 between the mass and p_T^2 shapes, thereby improving the fit's stability. The Monte Carlo fit
 2614 results are used to constrain the ratio of the widths of the χ_c resonances in the data fit, providing
 2615 some flexibility for resolution differences between data and Monte Carlo. The mean value of the
 2616 χ_{c1} is fixed relative to the mean value of the χ_{c2} according to the mass difference between χ_{c1}
 2617 and χ_{c2} mesons. These mean values are expected to be slightly lower than the nominal values,
 2618 which are 3510.67 ± 0.05 MeV/ c^2 and 3556.17 ± 0.07 MeV/ c^2 [81]. This is due to bremsstrahlung
 2619 radiation. The tail parameters, on the other hand, are completely fixed according to the Monte

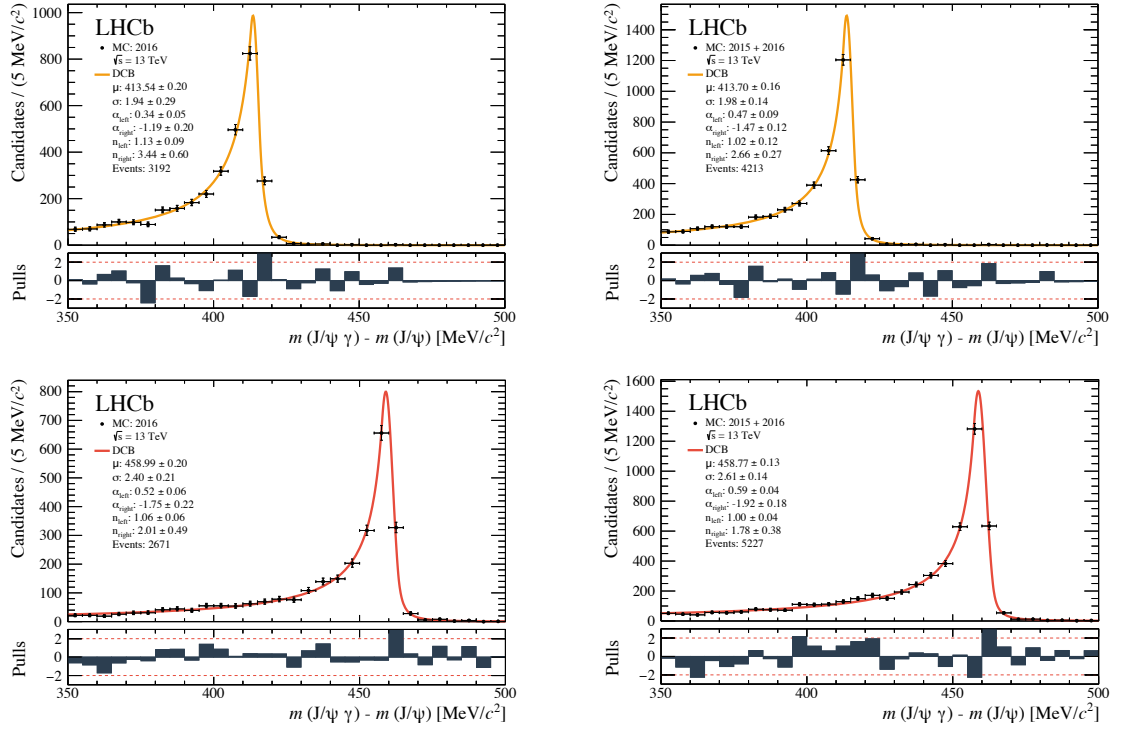


Figure 6.12. Fit of the Δm_{χ_c} distributions of CEP χ_{c1} (top) and χ_{c2} (bottom) Monte Carlo from pp collisions at a centre-of-mass energy of $\sqrt{s} = 13$ TeV generated with SuperChic v2 for the 2016-only (left), and combined 2015 and 2016 (right) run conditions. The Monte Carlo is reconstructed using converted photons and the CEP χ_c selection is applied before the distributions are fitted with a double-sided Crystal Ball with all parameters left floating.

Table 6.6. Summary of the parameter values pertaining to the fit parameters of the double-sided Crystal Balls used to fit the Δm_{χ_c} distributions of CEP χ_{c1} and χ_{c2} mesons from the 2016-only, and combined 2015 and 2016 Monte Carlo of pp collisions at centre-of-mass energy $\sqrt{s} = 13$ TeV.

Parameter	Units	χ_{c1}		χ_{c2}	
		2016	2015 + 2016	2016	2015 + 2016
μ	MeV/ c^2	413.54 ± 0.20	413.70 ± 0.16	458.99 ± 0.20	458.77 ± 0.13
σ	MeV/ c^2	1.94 ± 0.29	1.98 ± 0.14	2.40 ± 0.21	2.61 ± 0.14
α_{Left}	-	0.34 ± 0.05	0.47 ± 0.09	0.52 ± 0.06	0.59 ± 0.04
α_{Right}	-	-1.19 ± 0.20	-1.47 ± 0.12	-1.75 ± 0.22	-1.92 ± 0.18
n_{Left}	-	1.13 ± 0.09	1.02 ± 0.12	1.06 ± 0.06	1.00 ± 0.04
n_{Right}	-	3.44 ± 0.60	2.66 ± 0.27	2.01 ± 0.49	1.78 ± 0.38

2620 Carlo results. For the p_{T}^2 , we use the sum of two exponentials (Eq. 6.4) where all parameters are
 2621 left floating for the Monte Carlo unbinned-simultaneous-maximum-likelihood fit. The Δm_{χ_c} and
 2622 p_{T}^2 fit results are shown in Fig. 6.13 while the values of the floated parameters are summarised
 2623 in Table 6.7. From these fit results we are able to extract two important pieces of information.
 2624 The first is the yield ratio of the inelastic χ_{c1} to χ_{c2} mesons, $\chi_{c1}/\chi_{c2} = 0.91 \pm 0.16$ for 2016-only

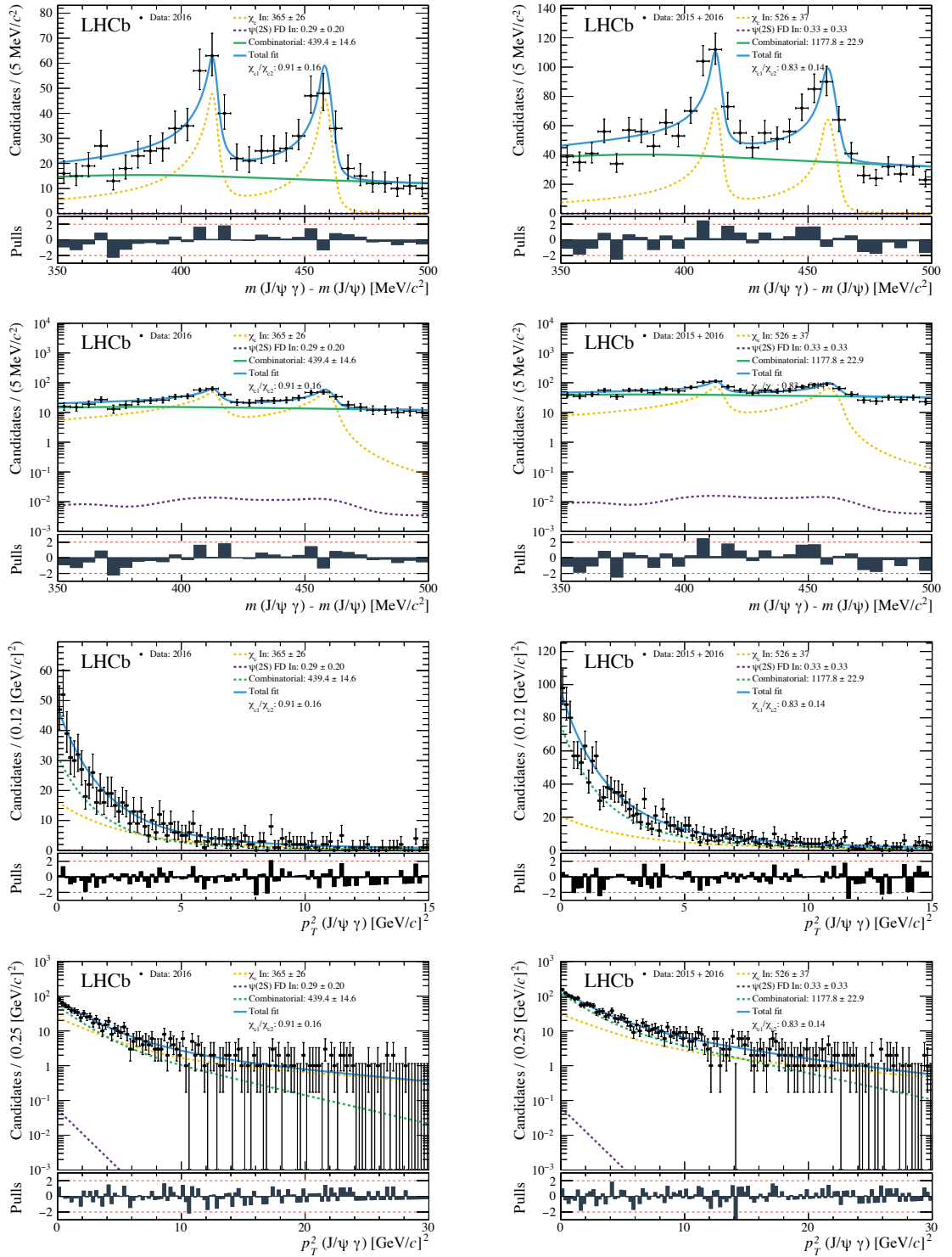


Figure 6.13. Fit of the Δm_{χ_c} (first and second row) and p_T^2 (third and fourth row) distribution of χ_c candidates from the ≥ 3 Long sample in linear (first and third row) and logarithmic scale (second and fourth row) for the 2016-only (left), and combined 2015 and 2016 (right) data. The p_T^2 distribution is modelled by a single shape composed two exponentials for the inelastic χ_{c1} and χ_{c2} mesons. Note that the x -axis scales are different for the linear and logarithmic versions for the p_T^2 distribution.

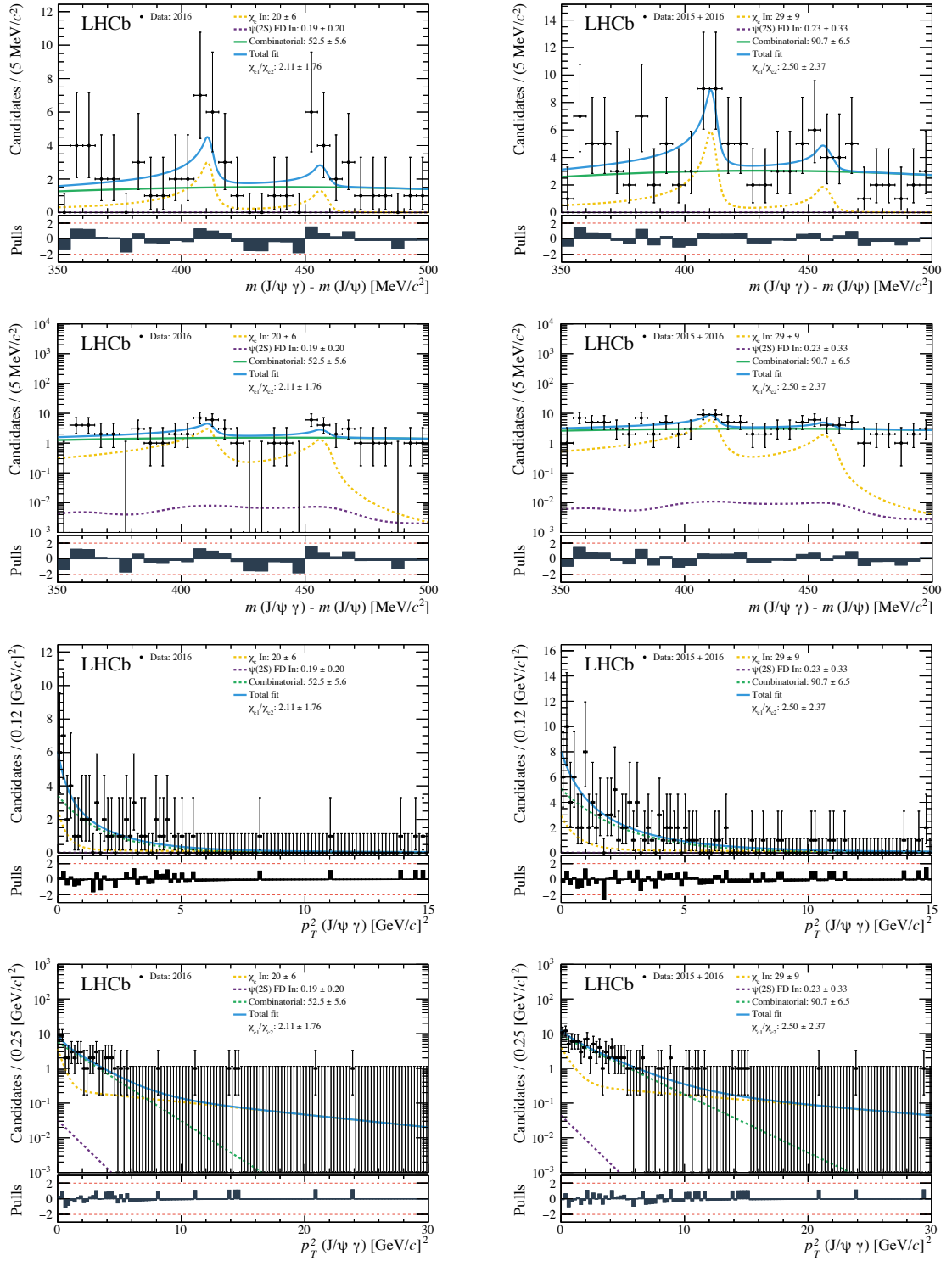


Figure 6.14. Fit of the Δm_{χ_c} (first and second row) and p_T^2 (third and fourth row) distribution of χ_c candidates from the ≥ 3 Long + HRC sample in linear (first and third row) and logarithmic scale (second and fourth row) for the 2016-only (left), and combined 2015 and 2016 (right) data. Note that the x -axis scales are different for the linear and logarithmic versions for the p_T^2 distribution.

2625 data, and $\chi_{c1}/\chi_{c2} = 0.83 \pm 0.14$ for the combined 2015 and 2016 data. In addition, we can
 2626 determine the p_T^2 shape parameter and fix them in our simultaneous fit of the CEP χ_c sample.

2627 Finally, we perform a simultaneous fit of the Δm_{χ_c} and the p_T^2 distributions of the inelastic
 2628 χ_{c1} and χ_{c2} candidates in the $\geq 3\text{Long} + \text{HRC}$ sample. Because this sample is much smaller, on
 2629 account of the HERSCHEL cut, we fix the width of the double-sided Crystal Ball to the fit results
 2630 of the $\geq 3\text{Long} + \text{HRC}$ sample, detailed in Table 6.7. The Δm_{χ_c} and p_T^2 fit results are shown in
 2631 Fig. 6.14. As before, we extract the χ_{c1} to χ_{c2} production ratio for later use in the CEP χ_c fit: for
 2632 the combined 2015 and 2016 data, $\chi_{c1}/\chi_{c2} = 2.50 \pm 2.37$ and $\chi_{c1}/\chi_{c2} = 2.11 \pm 1.76$ for 2016-only
 2633 data. The production ratios and the values of floated parameters are summarised in Table 6.7
 2634 for both $\geq 3\text{Long} + \text{HRC}$ and $\geq 3\text{Long}$ samples. We observe a total of 20 ± 6 (29 ± 9) inelastic
 2635 χ_c events in the 2016-only (combined 2015 and 2016) data. This compares to 366 ± 26 (526 ± 37)
 2636 events prior to the HERSCHEL cut, corresponding to a 5.46 ± 1.68 (5.51 ± 1.75) percent retention
 2637 of inelastic χ_c events for the 2016-only (combined 2015 and 2016) data. This suggests that
 2638 HERSCHEL is successfully eliminating inelastic events. Finally, we use the fit results of the p_T^2
 2639 distribution to fix the parameters in the CEP χ_c fit.

2640 As a systematic check we repeat the fit using a single exponential, Eq. 6.1, to model the
 2641 p_T^2 distribution from the combined contribution of inelastic χ_{c1} and χ_{c2} mesons. From the
 2642 fit of the Δm_{χ_c} we obtain the χ_c yield ratios consistent with the results presented above,

Table 6.7. Floated parameter values of Δm_{χ_c} and p_T^2 fits of $\geq 3\text{Long}$ and $\geq 3\text{Long} + \text{HRC}$ sample for the 2016-only, and combined 2015 and 2016 data. Results are shown for the case where the p_T^2 of inelastic χ_c candidates is modelled with one and with two exponentials.

Variable	Units	$\ln(\chi_{\text{HRC}}^2)$	1 Exp.		2 Exp.	
			2016	2015 + 2016	2016	2015 + 2016
Δm_{χ_c} Inelastic						
σ	MeV/ c^2	-	3.00 ± 0.51	3.41 ± 0.51	3.09 ± 0.53	3.49 ± 0.64
μ	MeV/ c^2	-	457.97 ± 0.60	458.13 ± 0.54	458.05 ± 0.62	457.98 ± 0.68
		< 5	456.58 ± 1.66	455.79 ± 1.84	455.94 ± 1.69	455.86 ± 2.08
χ_{c1}/χ_{c2}	-	-	0.88 ± 0.18	0.83 ± 0.14	0.91 ± 0.16	0.83 ± 0.14
		< 5	1.49 ± 1.15	1.78 ± 1.44	2.11 ± 1.76	2.50 ± 2.37
$p_T^2(J/\psi \gamma)$ Inelastic						
a	$[\text{MeV}/c]^{-2}$	-	-0.17 ± 0.01	-0.16 ± 0.01	-0.06 ± 0.03	-0.07 ± 0.03
		< 5	-0.11 ± 0.04	-0.11 ± 0.04	-0.08 ± 0.06	-0.07 ± 0.05
b	$[\text{MeV}/c]^{-2}$	-	-	-	-0.38 ± 0.08	-0.36 ± 0.09
		< 5	-	-	-2.54 ± 2.38	-1.45 ± 1.57
A	$[\text{MeV}/c]^{-2}$	-	0.7 ± 0.39	0.46 ± 0.65	0.04 ± 0.56	0.15 ± 0.52
		< 5	0.46 ± 0.23	0.57 ± 0.21	0.02 ± 0.76	0.02 ± 0.84
B	$[\text{MeV}/c]^{-2}$	-	-	-	0.37 ± 0.80	0.91 ± 0.51
		< 5	-	-	0.28 ± 0.59	0.23 ± 0.86

2643 $\chi_{c1}/\chi_{c2} = 0.88 \pm 0.18$ (1.49 ± 1.15) for 2016-only data, and $\chi_{c1}/\chi_{c2} = 0.83 \pm 0.14$ (1.78 ± 1.44)
 2644 for the combined 2015 and 2016 data without (with) the HERSCHEL cut applied. All floated
 2645 parameters are summarised in Table 6.7.

2646 Unlike the combinatorial and feed-down background, the amount of inelastic χ_c background
 2647 expected in the CEP χ_c sample is not presented in this section as it is determined together with
 2648 the amount of CEP χ_c signal in the simultaneous fit of the CEP χ_c sample. The results of the
 2649 CEP χ_c sample fit are presented in detail in Chapter 7.

2650 6.4 Background summary

2651 In this section, we summarise the results of the background studies necessary to model our CEP
 2652 χ_c selection data with and without the HERSCHEL cut applied. Table 6.8 lists the expected
 2653 contributions of the combinatorial and feed-down components in our CEP χ_c selection.

2654 Using the CEP χ_c data set we were able to model the J/ψ -combinatorial by mismatching J/ψ
 2655 mesons with converted photons from different events. We combined this with a flat distribution
 2656 for the continuum combinatorial such that it matches the measured background under our
 2657 selected J/ψ mesons. We used this model to fit the Δm_{χ_c} distribution based on the purely
 2658 combinatorial side-band and extrapolate into our signal range. The Δm_{χ_c} and p_T^2 PDFs for the
 2659 combinatorial background are shown in Fig. 6.2 and Fig. 6.4 with and without the HERSCHEL
 2660 cut, respectively. The fit parameters are detailed in Table 6.2.

2661 We modeled $\psi(2S)$ feed-down by applying weights to CEP $\psi(2S)$ Monte Carlo to match
 2662 the $\psi(2S)$ kinematics of CEP and the inelastic production mechanism, and to account for
 2663 photon-conversion efficiency. The transverse-momentum of these photons tends to be softer and
 2664 as a result have a lower effective-reconstruction efficiency, making this our smallest background.
 2665 The final Δm_{χ_c} PDFs for the $\psi(2S)$ feed-down background are shown in Fig. 6.8 and p_T^2 shapes
 2666 are extracted from the CEP J/ψ and $\psi(2S)$ LHCb paper [43]. We observe that ninety-six
 2667 percent of these background events originate from $\psi(2S) \rightarrow \chi_c \gamma$ decays.

2668 The inelastic χ_c background is not included in this table as its yield and exact shape are
 2669 determined concurrently with the CEP χ_c signal in a two-dimensional fit of the Δm_{χ_c} and p_T^2 .
 2670 By selecting events with three or more long tracks we were able to select a χ_c sample guaranteed
 2671 to be inelastic. We were able to isolate the inelastic signal and extract crucial information
 2672 from the fit including the yield ratio between χ_{c1} and χ_{c2} , as well as the $p_T^2(\chi_c)$ shape for these
 2673 events. Since the Δm_{χ_c} shapes of the inelastic and CEP χ_c signal are assumed to be identical,
 2674 it is crucial to have a good model for the inelastic p_T^2 necessary to determine the contribution of
 2675 the CEP signal and the inelastic background. The final Δm_{χ_c} and p_T^2 PDFs for the χ_c inelastic
 2676 background are shown in Fig. 6.13 and Fig. 6.14. The values of the floated parameters are
 2677 summarised in Table 6.7.

Table 6.8. Summary of the number of expected background events in our CEP $\chi_c \rightarrow J/\psi[\mu^+\mu^-]\gamma[e^+e^-]$ selection sample between our Δm_{χ_c} selection window, 350 to 500 MeV/ c^2 , with and without the HERSCHEL cut applied, $\ln(\chi_{\text{HRC}}^2) < 5$. The values are presented for the 2016-only, and combined 2015 and 2016 data. This table does not include the important contribution from inelastic χ_c events, which is determined in the final fit to the signal sample.

Component	No $\ln(\chi_{\text{HRC}}^2)$ Cut		With $\ln(\chi_{\text{HRC}}^2) < 5$ Cut	
	2016	2015 + 2016	2016	2015 + 2016
$\mu^+\mu^-$ combinatorial	0.68 ± 0.36	0.46 ± 0.39	0.51 ± 0.26	0.43 ± 0.26
J/ψ combinatorial	35.55 ± 5.85	44.97 ± 6.35	11.91 ± 4.51	13.25 ± 4.66
$\psi(2S)_{\text{FD}}^{\text{CEP}}$	5.97 ± 3.58	6.98 ± 5.93	5.08 ± 3.05	5.80 ± 4.92
$\psi(2S)_{\text{FD}}^{\text{In.}}$	2.76 ± 1.70	3.23 ± 2.81	1.86 ± 1.15	2.20 ± 1.92

2678 6.5 CEP χ_c fit model

2679 A simultaneous unbinned maximum-likelihood fit is performed on the Δm_{χ_c} and p_{T}^2 spectrum
 2680 of CEP $\chi_c \rightarrow J/\psi[\mu^+\mu^-]\gamma[e^+e^-]$ candidates on the $350 < \Delta m_{\chi_c} < 500 \text{ MeV}/c^2$ and $p_{\text{T}}^2(\chi_c) <$
 2681 $30 [\text{MeV}/c]^2$ range, for 2016-only, and combined 2015 and 2016 data. This fitting method allows
 2682 us to determine the contribution of inelastic χ_c background events from our CEP signal. We
 2683 fit the Δm_{χ_c} distribution with a model composed of seven components: the CEP χ_{c1} and χ_{c2}
 2684 signal, a single inelastic χ_c shape accounting for both inelastic χ_{c1} and χ_{c2} background, J/ψ -
 2685 combinatorial background, continuum-combinatorial background, as well as CEP and inelastic
 2686 $\psi(2S)$ feed-down background. Of these shapes, only the CEP χ_c signal and the inelastic χ_c
 2687 background have free parameters and yields in the fit. All other background shapes and yields
 2688 are fixed according to results detailed in previous sections of this chapter. Each of these Δm_{χ_c}
 2689 shapes is accompanied by a p_{T}^2 distribution that shares the same yield parameter. All p_{T}^2
 2690 shapes are fixed according to data, Monte Carlo, or previous studies from the LHCb experiment.
 2691 Table 6.9 provides a summary of all the fit components, their shapes, the parameters that are
 2692 floated, and a brief description of how each shape is calculated and constrained. The fit is
 2693 performed with and without a HERSCHEL cut applied.

2694 6.5.1 Invariant-mass-difference parameterisation

2695 CEP χ_c fit model

2696 The CEP χ_{c1} and χ_{c2} resonances are each fitted with a double-sided Crystal Ball [132]. To
 2697 help constrain the fits to the CEP χ_c data, the values of the tail parameters are fixed (α_{Left} ,
 2698 α_{Right} , n_{Left} , and n_{Right}) to the values obtained from the CEP χ_c Monte Carlo fit results,
 2699 shown in Fig. 6.12 and Table 6.6 where they were first presented as part of the inelastic χ_c
 2700 background study in Sec. 6.3.4. In addition, the width of χ_{c1} and χ_{c2} are described by a single
 2701 free parameter, $\sigma(\chi_{c2})$, whereby the width of χ_{c1} is fitted by taking $\sigma(\chi_{c2})$ times the ratio of
 2702 the χ_{c1} to χ_{c2} width extracted from the Monte Carlo fit results. Similarly, the mean value of
 2703 χ_{c1} is constrained relative to the mean of χ_{c2} by the difference of the nominal-mass value of χ_{c1}

Table 6.9. Summary of the simultaneous-fit strategy of the CEP χ_c sample. Yield values (Y) between corresponding Δm_{χ_c} and p_T^2 shapes are shared.

Fit Component	Dist.	Fitted Shape	Floated Values	Model Description
CEP χ_{c1}	Δm_{χ_c} p_T^2	DCB Eq. 6.5	μ^*, σ^*, Y Y	- Fixed tails and constraint σ to CEP χ_{c1} MC fit results. - Fixed shape to CEP χ_{c1} MC fit results.
CEP χ_{c2}	Δm_{χ_c} p_T^2	DCB Eq. 6.5	μ, σ, Y Y	- Fixed tails and constraint σ to CEP χ_{c2} MC fit results. - Fixed shape to CEP χ_{c2} MC fit results.
In. χ_c	Δm_{χ_c} p_T^2	DCB Eq. 6.4	μ, σ, Y Y	- Shares shape parameters with CEP χ_c counterparts. χ_{c1}/χ_{c2} Y ratio fixed to ≥ 3 Long Δm_{χ_c} fit results. - Shape fixed to ≥ 3 Long p_T^2 fit results
$\psi(2S)_{FD}^{CEP}$	Δm_{χ_c} p_T^2	KE Eq. 6.2	- -	- Modelled from $\psi(2S) \rightarrow J/\psi X$ MC. Yield calculated with Eq. 6.3. - Parameters fixed from LHCb CEP J/ψ and $\psi(2S)$ paper [43].
$\psi(2S)_{FD}^{In.}$	Δm_{χ_c} p_T^2	KE Eq. 6.2	- -	- Modelled from $\psi(2S) \rightarrow J/\psi X$ MC. Yield calculated with Eq. 6.3. - Parameters fixed from LHCb CEP J/ψ and $\psi(2S)$ paper [43].
$\mu^+ \mu^-$ Com.	Δm_{χ_c} p_T^2	Horizontal line Eq. 6.1, 6.4	- -	- Yield calculated from fit to $m(J/\psi)$ in CEP χ_c sample. - Same p_T^2 shape used as in J/ψ combinatorial.
J/ψ Com.	Δm_{χ_c} p_T^2	DCB Eq. 6.1, 6.4	- -	- Shape for Δm_{χ_c} and p_T^2 are fixed to fit result of mismatched J/ψ and γ from CEP χ_c sample. - Yield extrapolated from fit to χ_c $\Delta m_{\chi_c} > 500$ MeV/ c^2 tail.

* Parameters floated relative to their corresponding parameter in the CEP χ_{c2} shape.

2704 and χ_{c2} according to the PDG [81]. Finally, all yield values are floated and shared with the
2705 corresponding $p_T^2(J/\psi\gamma)$ shape.

2706 Inelastic χ_c fit model

2707 The Δm_{χ_c} shapes for the CEP χ_{c1} signal and the inelastic χ_{c1} background are assumed to
2708 be identical. The same applies to χ_{c2} . That is, the tails are fixed to CEP χ_c Monte Carlo
2709 results and the resonances share the same floated width and mean parameters as their CEP
2710 counterparts. However, in the case of the inelastic χ_{c1} and χ_{c2} background, the two double-sided
2711 Crystal Balls are joined together into a single composite shape. This allows us to simplify the
2712 model of the inelastic p_T^2 contribution to a single shape and a single yield parameter shared
2713 between the mass and p_T^2 shapes, thereby improving the fit's stability.

2714 These assumptions were studied and validated using our inelastic-control sample, ≥ 3 Long
2715 and ≥ 3 Long + HRC, as described in Sec. 6.3. The fit results of the control sample are shown
2716 in Fig. 6.13 (Fig. 6.14) before (after) the HERSCHEL cut is applied. From these results, we

2717 see that the shapes extracted from the CEP χ_c Monte Carlo sample describe the distribution
 2718 successfully. In addition, we extract the yield ratio of the two resonances, χ_{c1}/χ_{c2} , to constrain
 2719 the χ_c yield ratio of our CEP χ_c fit. The yield ratios are summarised in Table 6.8.

2720 $\psi(2S)$ feed-down fit model

2721 Two fixed shapes are used to model the CEP and inelastic $\psi(2S)$ feed-down. Each PDF is
 2722 composed of four contributions, one for each of the possible $J/\psi\gamma$ combinations from $\psi(2S) \rightarrow$
 2723 $J/\psi[\mu^+\mu^-]X$ decays, where X stands for all possible particles in $\psi(2S)$ decays accompanied by
 2724 an intermediate J/ψ meson. The shapes and their contributions, within our delta-mass window,
 2725 are calculated in Sec. 6.2.3 using 2015 $\psi(2S) \rightarrow J/\psi[\mu^+\mu^-]X$ Monte Carlo together with results
 2726 from the LHCb CEP $\psi(2S)$ paper [43] and the photon-conversion efficiency, described in Sec. 5.1.
 2727 The shapes are extracted with KE fits, shown in Fig. 6.8. The contributions of this background
 2728 are summarised in Table 6.3 and are fixed according to these results for the CEP χ_c fit.

2729 Continuum-combinatorial fit model

2730 The contribution from non-resonant continuum combinatorial is measured in Sec. 6.1.1 by fitting
 2731 the invariant-mass distribution of the J/ψ mesons in our CEP χ_c selection within a 100 MeV/ c^2
 2732 mass window centred about the nominal J/ψ mass value. The yields within our Δm_{χ_c} window,
 2733 350 to 500 MeV/ c^2 , are found to be very small. They are summarised in Table 6.3, and used
 2734 to fix their contributions in the CEP χ_c fit. We assume the Δm_{χ_c} distribution of this small
 2735 background to be uniformly distributed and model it with a horizontal line.

2736 J/ψ -combinatorial fit model

2737 The second class of combinatorial background is composed of true J/ψ mesons wrongly matched
 2738 with a converted photon. This background is modelled with a data-driven method where J/ψ
 2739 mesons from one event are matched with converted photons from another event and fitted with
 2740 a double-sided Crystal Ball. The shape is then completely fixed according to the fit results of
 2741 this artificial background, shown in Fig. 6.2. The parameters are summarised in Table 6.2.

2742 The yield within our Δm_{χ_c} selection window is calculated by fitting the Δm_{χ_c} range of our
 2743 CEP χ_c candidates above 500 MeV/ c^2 , a region dominated by combinatorial background, and
 2744 extrapolating into our Δm_{χ_c} selection window. When performing the fit, we account for the
 2745 small contribution from dimuon continuum. This process is detailed in Sec. 6.1.2. The yields
 2746 for each data sample are summarised in Table 6.3.

2747 6.5.2 $p_{\text{T}}^2(\chi_c)$ parameterisation

2748 CEP χ_c fit model

2749 In a similar way to the Δm_{χ_c} model, the parameters of the CEP χ_c p_{T}^2 distribution are all
 2750 fixed according to the results of a maximum-likelihood fit on fully reconstructed CEP χ_c Monte
 2751 Carlo. The $p_{\text{T}}^2(\chi_c)$ distribution for each of the χ_c mesons is different and deviates from a single
 2752 exponential due to reconstruction efficiencies, differences in spin-structure of each $gg \rightarrow \chi_{c1,2}$
 2753 vertex, as well as effects of spin-survival factor: a measurement of how likely the proton is to

2754 survive the interaction. As a result, a flexible parametrization is needed to model the CEP
 2755 $p_T^2(\chi_c)$ component where all the parameters are floated:

$$\exp(a \cdot p_T^2) (b + c \cdot p_T^2 + d \cdot (p_T^2)^2 + e \cdot (p_T^2)^3). \quad (6.5)$$

2756 The results of the fit are shown in Fig. 6.15 and the final value of the fit parameters are
 2757 summarised in Table 6.10.

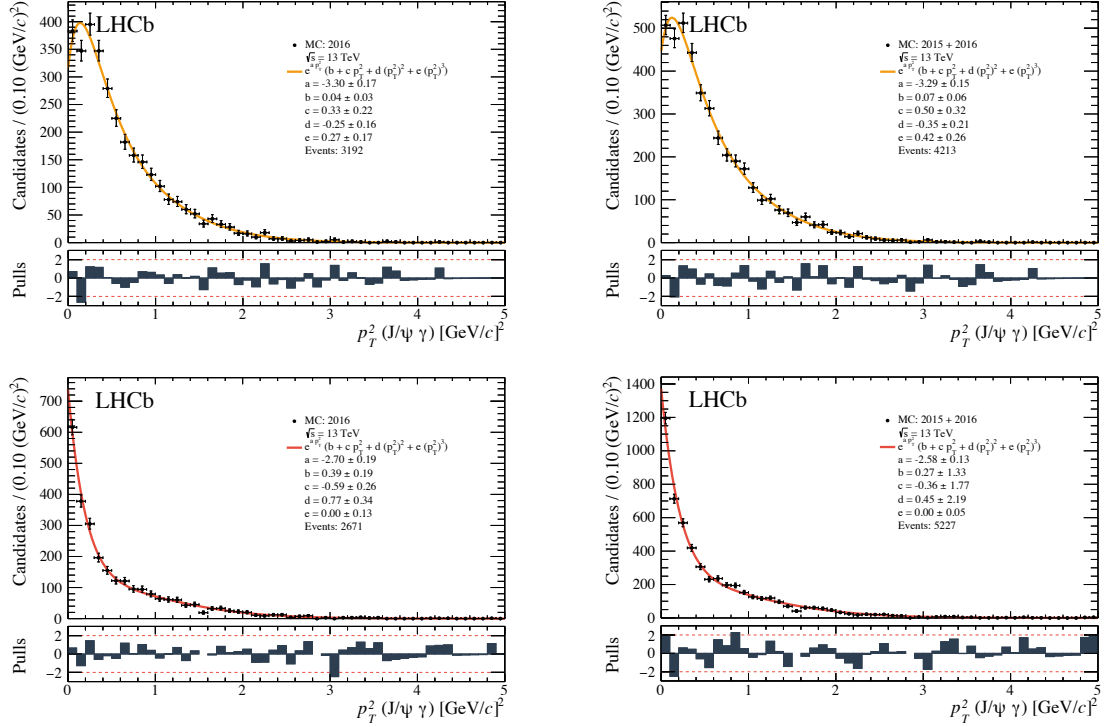


Figure 6.15. Fit of the p_T^2 distributions of CEP χ_{c1} (top) and χ_{c2} (bottom) Monte Carlo reconstructed with converted photons for the 2016-only (left), and combined 2015 and 2016 (right) run conditions for pp collisions at a centre-of-mass energy $\sqrt{s} = 13$ TeV generated with SuperChic v2. The distributions are shown within the Δm_{χ_c} selection widow, 350 to 500 MeV/ c^2 . The distributions are fitted with Eq. 6.5.

Table 6.10. Summary of the final parameter values pertaining to the fit parameters of the p_T^2 distributions of CEP χ_{c1} and χ_{c2} Monte Carlo reconstructed with converted photons for the 2016-only, and combined 2015 and 2016 data from pp collisions at a centre-of-mass energy $\sqrt{s} = 13$ TeV.

Parameter	Units	χ_{c1}		χ_{c2}	
		2016	2015 + 2016	2016	2015 + 2016
a	[MeV/ c] $^{-2}$	-3.30 ± 0.17	-3.29 ± 0.15	-2.70 ± 0.19	-2.58 ± 0.13
b	[MeV/ c] $^{-2}$	0.04 ± 0.03	0.07 ± 0.06	0.39 ± 0.19	0.27 ± 1.33
c	[MeV/ c] $^{-4}$	0.33 ± 0.22	0.50 ± 0.32	0.59 ± 0.26	-0.36 ± 1.77
d	[MeV/ c] $^{-6}$	-0.25 ± 0.16	-0.35 ± 0.21	0.77 ± 0.34	0.45 ± 2.19
e	[MeV/ c] $^{-8}$	0.27 ± 0.17	0.42 ± 0.26	0.0 ± 0.13	-0.00 ± 0.05

2758 **Inelastic χ_c fit model**

2759 As with the Δm_{χ_c} fit model, the $\geq 3\text{Long}$ and $\geq 3\text{Long}+\text{HRC}$ samples are used to determine
 2760 the p_{T}^2 distribution for the inelastic χ_c mesons. The fit of the inelastic-control samples is detailed
 2761 in Sec. 6.3. The combined $p_{\text{T}}^2(J/\psi\gamma)$ for χ_{c1} and χ_{c2} contributions are fitted with a single shape
 2762 composed of the sum of two exponentials, Eq. 6.4. The fit results are shown in Sec. 6.3.4 and the
 2763 fit parameters are detailed in Table 6.7. The results are used to fix the shapes of the inelastic
 2764 χ_c component in the CEP χ_c simultaneous fit while floating the yield shared with its Δm_{χ_c}
 2765 counterpart.

2766 **$\psi(2S)$ feed-down-background fit model**

2767 The shapes associated with the $\psi(2S)$ feed-down are taken from observations detailed in a CEP
 2768 study of J/ψ and $\psi(2S)$ mesons in pp collisions at $\sqrt{s} = 13\text{ TeV}$ in the LHCb experiment [43]
 2769 where inelastic and CEP $p_{\text{T}}^2(\psi(2S))$ is modelled with an exponential, Eq. 6.2. Their fit results
 2770 for this study are reproduced in Fig. 6.7. The same shapes are used for all data samples, before
 2771 and after the HERSCHEL selection is applied. The yields are shared and fixed to the values
 2772 described for the invariant-mass-difference counterpart.

2773 **Combinatorial-background fit model**

2774 As with the Δm_{χ_c} model, the p_{T}^2 combinatorial background has two contributions: continuum
 2775 combinatorial and J/ψ combinatorial. As the minor continuum-combinatorial contribution is
 2776 very small, we model all combinatorial background with the same p_{T}^2 distribution of the J/ψ
 2777 combinatorial background described below, but keep their contributions separate.

2778 The p_{T}^2 shape associated with combinatorial background is determined using the same
 2779 data-driven study used to ascertain the Δm_{χ_c} distribution of this background, described in
 2780 Sec. 6.1. The selection for the p_{T}^2 model is restricted to events that fall within the Δm_{χ_c} selection
 2781 window, 350 to 500 MeV/c^2 . In this case, the p_{T}^2 shape prior to the HERSCHEL cut is well
 2782 modelled by a single exponential, Eq. 6.1, with fit results shown in Fig. 6.4. However, once the
 2783 HERSCHEL cut is applied, a small contribution from a second exponential is required, Eq. 6.4.
 2784 These fit results are shown in Fig. 6.4. Both fits are performed with all parameters floated.
 2785 These parameters are then fixed and fitted to the CEP χ_c data where the yields are shared and
 2786 fixed to the same value as the Δm_{χ_c} counterpart. The parameter values are summarised in
 2787 Table 6.2.

CHAPTER 7

2788

2789

2790

2791

Results and assignment of systematic uncertainties

2792 In this chapter we present the simultaneous fit results of the Δm_{χ_c} and p_T^2 distributions of our
 2793 CEP χ_c selection, with and without the HERSCHEL cut applied in Sec. 7.1. We then perform
 2794 a validation study of the fit model in Sec. 7.2 to assess its stability. In addition, we present a
 2795 series of studies that rely on these fit results. These studies include the calculation of a global
 2796 photon-conversion efficiency for our selected CEP χ_{c1} and χ_{c2} candidates, as well as their yields
 2797 corrected for this efficiency, described in Sec. 7.3. We also perform a stability study of the
 2798 HERSCHEL cut in Sec. 7.4. A description of the luminosity determination for single-interaction
 2799 crossings is presented in Sec. 7.5. We finish with the cross-section calculation of CEP χ_{c1} and
 2800 χ_{c2} in Sec. 7.6 and the assignment of systematic uncertainties in Sec. 7.7.

2801 7.1 CEP χ_c fit results

2802 To fit the CEP χ_c sample, we combine the signal and background components described in
 2803 Chapter 6 into a single composite probability-density function, with which we perform an
 2804 unbinned simultaneous maximum-likelihood fit of the Δm_{χ_c} and p_T^2 distributions of the selected
 2805 χ_c candidates. The fit results are shown in Fig. 7.1 and Fig. 7.2, respectively, before and after
 2806 the HERSCHEL cut is applied, $\ln(\chi_{\text{HRC}}^2) < 5$, for the 2016-only, and combined 2015 and 2016
 2807 data. The final values for the floated fit parameters and yields are shown in Table 7.1. We
 2808 observe 0.00 ± 18.6 (0.00 ± 26.5) CEP χ_{c1} events, 176.69 ± 17.96 (229.71 ± 19.85) CEP χ_{c2}
 2809 events, and 227.03 ± 19.22 (249.74 ± 20.23) inelastic χ_c events in the 2016-only (combined 2015
 2810 and 2016) data prior to the HERSCHEL cut. When the HERSCHEL cut is applied we observe
 2811 13.27 ± 6.84 (9.41 ± 7.24) CEP χ_{c1} events, 75.34 ± 10.84 (96.30 ± 12.32) CEP χ_{c2} events, and
 2812 19.71 ± 6.68 (924.47 ± 7.50) inelastic χ_c events.

2813 The measured width of the χ_c mesons prior to the HERSCHEL cut is slightly larger than
 2814 expected compared to the χ_c Monte Carlo fit, while the measured value with the HERSCHEL cut
 2815 applied is in good agreement with the Monte Carlo fit. We repeat the fit while fixing the χ_{c1} and
 2816 χ_{c2} width to the value predicted by Monte Carlo, 1.94 ± 0.29 (1.98 ± 0.14) and 2.40 ± 0.21 ($2.61 \pm$
 2817 0.14) MeV/c respectively for the 2016-only (combined 2015 and 2016) data, and check that this
 2818 does not lead to significantly different results. We measure 1.44 ± 19.03 (2.89 ± 11.07) CEP χ_{c1}

2819 events, 169.34 ± 18.08 (220.75 ± 20.04) CEP χ_{c2} events, and 226.20 ± 19.89 (248.15 ± 20.85)
 2820 inelastic χ_c events in the 2016-only (combined 2015 and 2016) data. Although fixing the widths
 2821 of the resonant peaks leads to slightly different yields, they are consistent with the results
 2822 presented above. This highlights the benefits of performing the study with the HERSCHEL
 2823 sample which has a much smaller inelastic χ_c background.

Table 7.1. Summary of fit parameter results for the simultaneous fit of the Δm_{χ_c} and p_T^2 of χ_c candidates in the 2016-only, and combined 2015 and 2016 data before and after the HERSCHEL cut, $\ln(\chi_{\text{HRC}}^2) < 5$, is applied.

Parameter	Units	$\ln(\chi_{\text{HRC}}^2)$	χ_{c1}		χ_{c2}	
			2016	2015 + 2016	2016	2015 + 2016
Gaussian mean	MeV/ c^2	- < 5	- -	- -	458.26 ± 0.66 458.19 ± 0.80	457.59 ± 0.59 457.70 ± 0.95
Gaussian width	MeV/ c^2	- < 5	- -	- -	4.40 ± 0.59 2.74 ± 0.31	4.76 ± 0.58 3.66 ± 0.80
$N_{\text{CEP}}(\chi_c)$	-	- < 5	0.00 ± 18.6 13.27 ± 6.84	0.00 ± 26.5 9.41 ± 7.24	176.69 ± 17.96 75.34 ± 10.84	229.71 ± 19.85 96.30 ± 12.32
Parameter	Units	$\ln(\chi_{\text{HRC}}^2)$	2016		2015 + 2016	
$N_{\text{In.}}(\chi_c)$	-	- < 5	227.03 ± 19.22 19.71 ± 6.68		249.74 ± 20.23 19.71 ± 6.68	

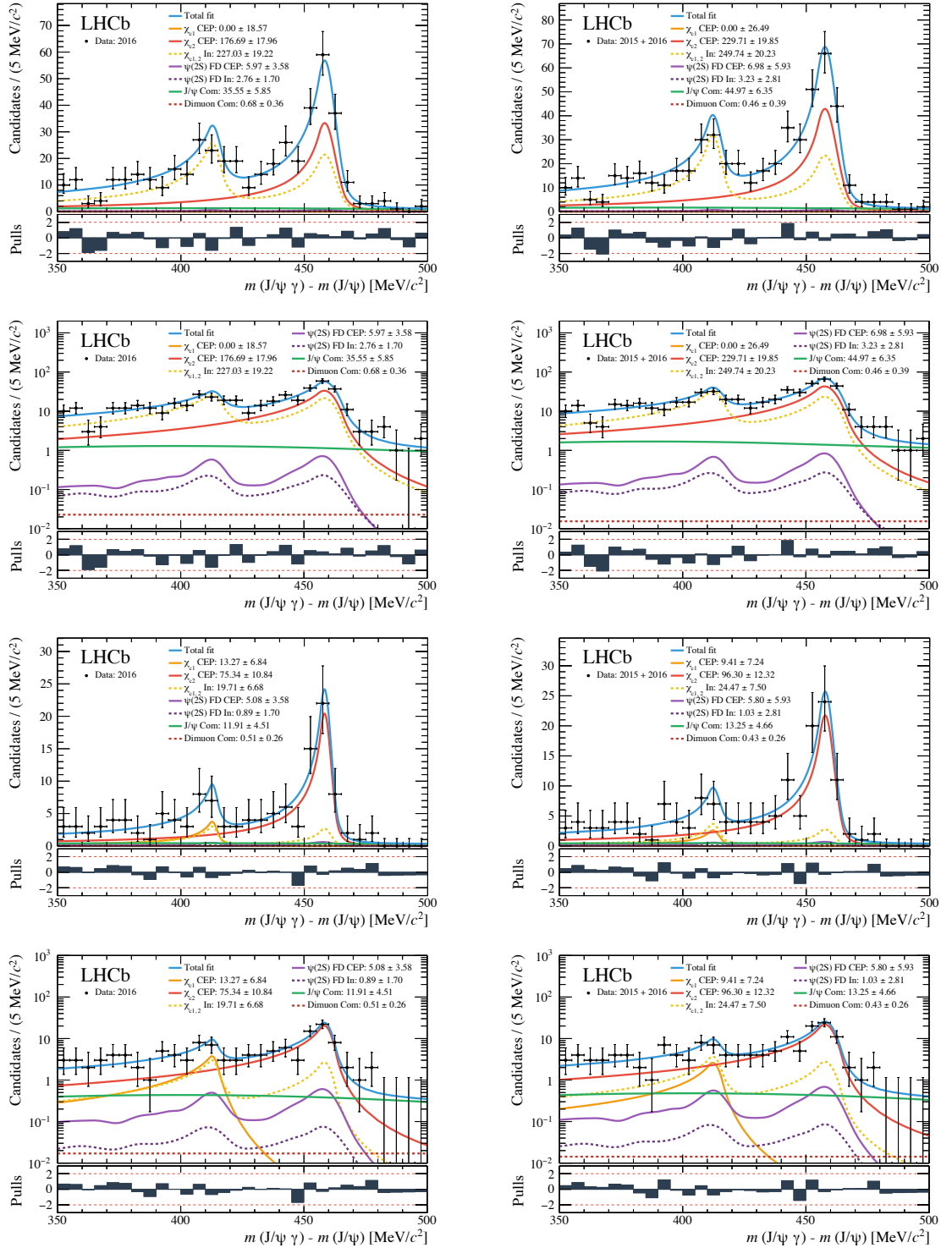


Figure 7.1. Delta-mass component of two-dimensional fit of the invariant mass of χ_{c1} and χ_{c2} candidates for the 2016-only (left), and combined 2015 and 2016 (right) data before (first and second row) and after (third and fourth row) the HERSCHEL cut, $\ln(\chi_{\text{HRC}}^2) < 5$, is applied. The overall fit is shown in solid blue, the CEP χ_{c1} component in solid orange, the CEP χ_{c2} component in solid red, the inelastic χ_c sample in dashed yellow, the continuum-combinatorial background in dashed-dark red, the J/ψ combinatorial background in green, the CEP $\psi(2S)$ feed-down in solid purple, and the inelastic $\psi(2S)$ feed-down in dashed purple.

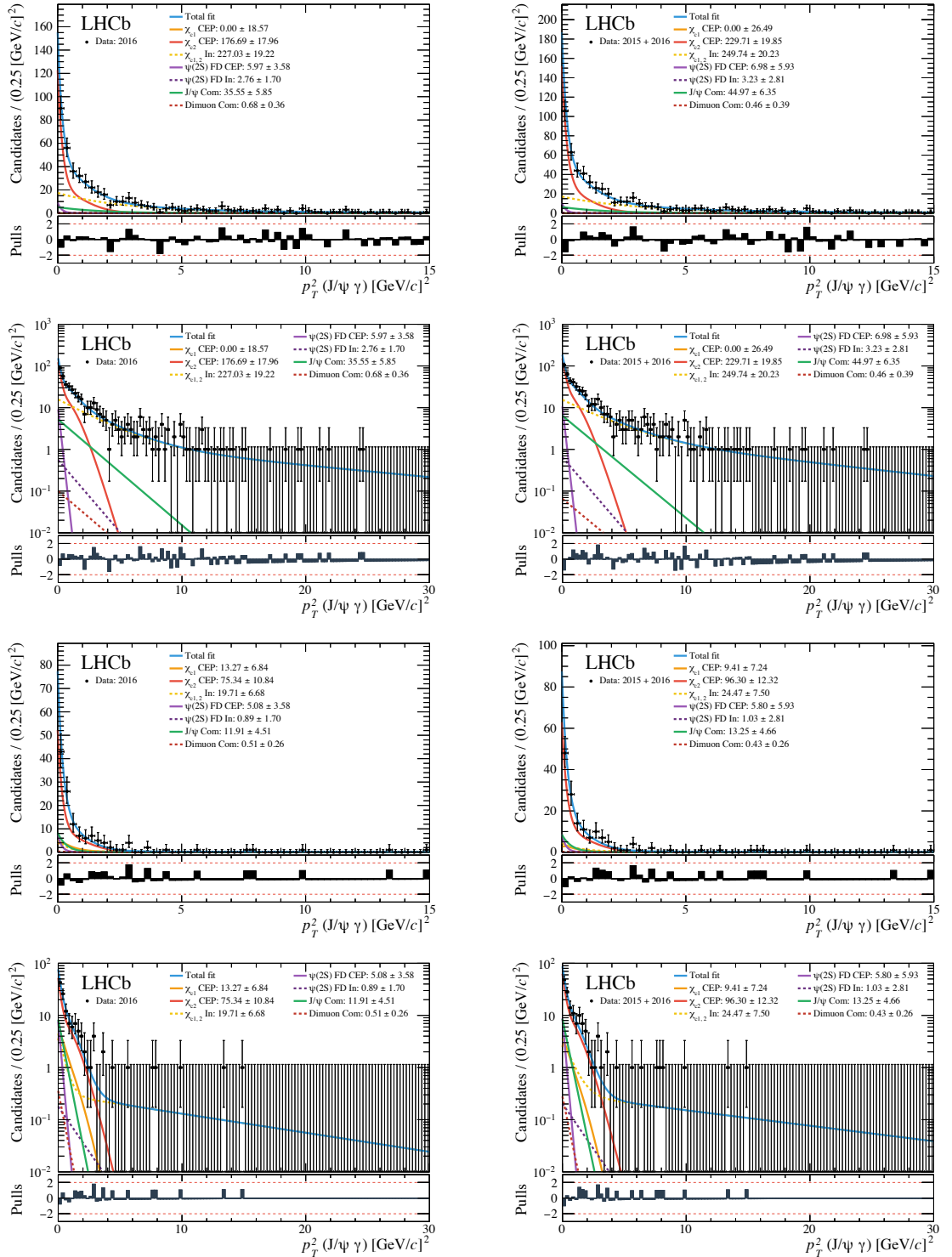


Figure 7.2. Transverse-momentum-squared component of two-dimensional fit of the invariant mass of χ_{c1} and χ_{c2} candidates for the 2016-only (left), and combined 2015 and 2016 (right) data before (first and second row) and after (third and fourth row) the HERSCHEL cut, $\ln(\chi_{\text{HRC}}^2) < 5$, is applied. The overall fit is shown in solid blue, the CEP χ_{c1} component in solid orange, the CEP χ_{c2} component in solid red, the inelastic χ_c sample in dashed yellow, the continuum-combinatorial background in dashed-dark red, the J/ψ combinatorial background in green, the CEP $\psi(2S)$ feed-down in solid purple, and the inelastic $\psi(2S)$ feed-down in dashed purple. Note that the range is different between the linear and logarithmic plots.

2824 7.2 CEP χ_c fit-validation study

2825 The fit is validated to make sure it is well-behaved and returns unbiased results. This is done by
 2826 taking the fit results obtained from the data, and generating pseudo-experiments with the fitted
 2827 PDF to match the data-set sizes of the CEP χ_c selection. We generate ten thousand *toy-data*
 2828 sets for each of the four samples: the 2016-only, and combined 2015 and 2016 samples with and
 2829 without the HERSCHEL cut applied. The toy-data sets are then fitted with the same model
 2830 originally used for the CEP χ_c sample. However, because the mean value of the χ_{c1} yield is
 2831 close to zero the χ_{c1} yield is allowed to take negative values in order to prevent the fit from
 2832 reaching the limit of the floating range. In all cases, the fits complete successfully with a small
 2833 percentage of cases ($\sim 1\%$) where the covariant matrix is forced to be positive definite.

2834 The pull distributions for the toy studies are shown in Fig. 7.3 (Fig. 7.4) before (after)
 2835 the HERSCHEL cut is applied and the pulls' mean and width values are summarised in
 2836 Table 7.2. For the most important parameters, which are the yields of the CEP χ_{c1} and χ_{c2}
 2837 contributions, we see satisfactory results with indications of small biases at the $\sim 5\%$ level and
 2838 error underestimation. We assign this as a systematic uncertainty to the CEP χ_{c1} and χ_{c2} yield.
 2839 We also see that the pulls for the χ_{c2} mean and width parameters have widths $\sim 20\%$ bigger than
 2840 one both with and without the HERSCHEL cut. After the HERSCHEL is applied the width
 2841 and inelastic χ_c yield develops a bias of 0.24 ± 0.01 (0.19 ± 0.01) and 0.18 ± 0.01 (0.18 ± 0.01)
 2842 respectively. Other parameters have a bias of up to nine percent.

Table 7.2. Summary of pull results from toy studies used to validate the fit to the CEP χ_c sample.

Parameter	Units	$\ln(\chi^2_{\text{HRC}})$	Mean		Width	
			2016	2015 + 2016	2016	2015 + 2016
$\mu (\chi_{c2})$	MeV/ c^2	-	0.03 ± 0.01	-0.01 ± 0.01	1.21 ± 0.01	1.16 ± 0.01
		< 5	-0.05 ± 0.01	-0.05 ± 0.01	1.21 ± 0.01	1.22 ± 0.01
$\sigma (\chi_{c2})$	MeV/ c^2	-	0.05 ± 0.01	0.07 ± 0.01	1.16 ± 0.01	1.17 ± 0.01
		< 5	0.24 ± 0.01	0.19 ± 0.01	1.24 ± 0.01	1.25 ± 0.01
$N_{\text{CEP}}(\chi_{c1})$	-	-	0.07 ± 0.01	0.06 ± 0.01	1.07 ± 0.01	1.04 ± 0.01
		< 5	0.07 ± 0.01	0.08 ± 0.01	1.05 ± 0.01	1.05 ± 0.01
$N_{\text{CEP}}(\chi_{c2})$	-	-	-0.03 ± 0.01	-0.06 ± 0.01	1.05 ± 0.01	1.05 ± 0.01
		< 5	0.06 ± 0.01	0.12 ± 0.01	1.05 ± 0.01	1.06 ± 0.01
$N_{\text{In.}}(\chi_c)$	-	-	-0.02 ± 0.01	-0.08 ± 0.01	1.05 ± 0.01	1.05 ± 0.01
		< 5	0.18 ± 0.01	0.18 ± 0.01	1.14 ± 0.01	1.12 ± 0.01

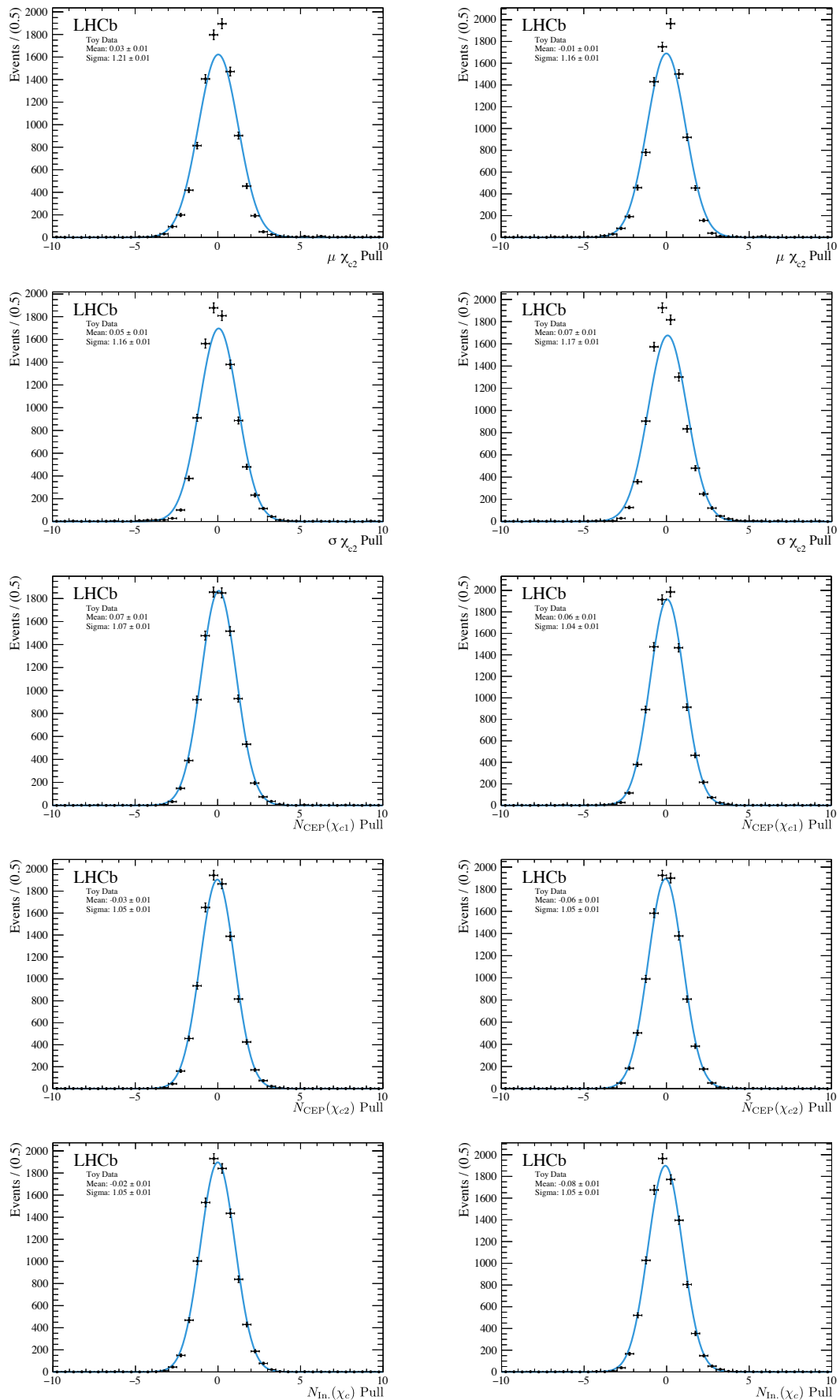


Figure 7.3. Pulls from toy studies for the 2016-only (left), and combined 2015 and 2016 (right) data before the HERSCHEL cut is applied.

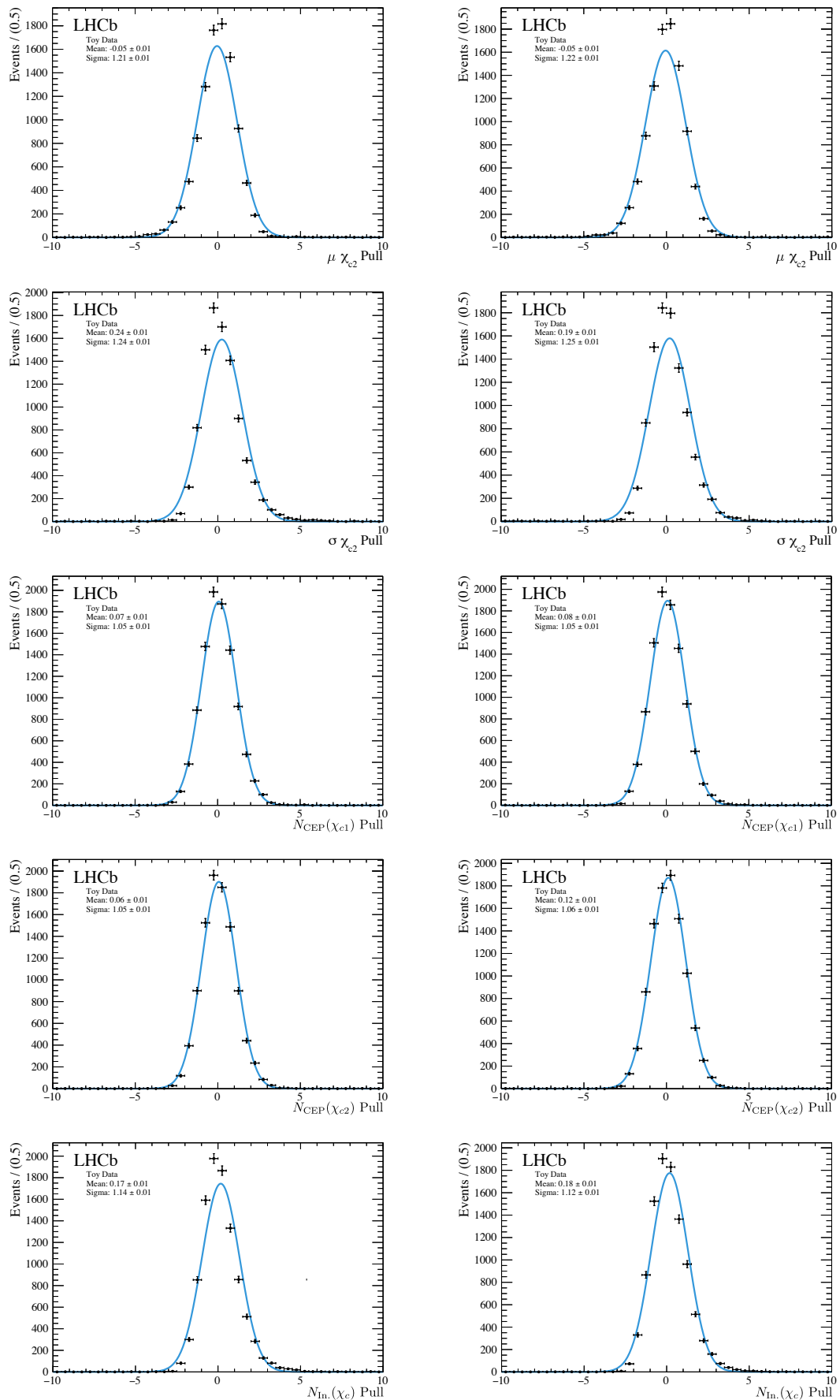


Figure 7.4. Pulls from toy studies for the 2016-only(left), and combined 2015 and 2016 (right) data after the HERSCHEL cut is applied.

2843 7.3 Applying the photon-conversion-efficiency correction to the fit results

2844 To apply the photon-conversion-efficiency correction to the χ_c data-fit results we calculate a
 2845 global photon-conversion efficiency for χ_{c1} , $\varepsilon_{\gamma \rightarrow e^+e^-}^{\text{Global}(\chi_{c1})}$, and χ_{c2} , $\varepsilon_{\gamma \rightarrow e^+e^-}^{\text{Global}(\chi_{c2})}$, that also accounts
 2846 for the multiplicity correction factor described in Sec. 5.1.6. The correction that is applied
 2847 must be appropriate for the photon transverse-momentum distribution of the signal in our
 2848 sample. We do this by studying the impact of the efficiency function determined from data
 2849 on the CEP χ_c Monte Carlo described in Sec. 4.1. We apply the selection criteria previously
 2850 referred to as the reconstructed J/ψ selection, where we reconstruct all the J/ψ mesons while
 2851 saving the generator-level information of the accompanying photon from the $\chi_c \rightarrow J/\psi \gamma$ decay.
 2852 The sample is truth matched and the selection criteria related to the J/ψ meson used in the
 2853 CEP χ_c analysis are applied, while omitting the selection criteria related to the photon. The
 2854 reader is reminded that the p_T^2 function used to fit the data derives from a fit to this same χ_c
 2855 Monte Carlo sample (see Table 6.5.2).

2856 We apply resolution effects to the generator-level kinematics of the photon using the
 2857 method described in Sec. 6.2.1. With the resolution effects applied, we are able to calculate
 2858 the Δm_{χ_c} distribution of the $J/\psi \gamma$ system and apply our selection window. The events
 2859 that pass this selection are the denominator for our global-efficiency calculation. A total of
 2860 702451 ± 838 (1390068 ± 1179) χ_{c1} and 678856 ± 823 (1390717 ± 1179) χ_{c2} events pass our
 2861 selection criteria for the 2016-only (combined 2015 and 2016) Monte Carlo.

2862 To calculate the numerator we apply the weights for the photon-conversion efficiency as
 2863 given by the data-driven study, shown in Fig. 5.13, according to the generator-level transverse
 2864 momentum of the photon. We finally apply an additional factor of two to account for the
 2865 low-multiplicity improvement in the reconstruction efficiency, as shown in the Sec. 5.1.6 study.
 2866 After the weights are applied we find 1581 (3129) χ_{c1} and 2100 (4305) χ_{c2} events for 2016-
 2867 only (combined 2015 and 2016) Monte Carlo. This corresponds to a global-photon-conversion
 2868 efficiency of 0.2250% (0.2251%) for χ_{c1} mesons, and 0.3094% (0.3096%) for χ_{c2} mesons for
 2869 2016-only (combined 2015 and 2016) data. The statistical uncertainties on these values are
 2870 negligible. Due to its larger mass, the photons from χ_{c2} decays have a larger phase space.
 2871 On average, this results in photons with a larger transverse momentum and therefore a larger
 2872 global-photon-conversion efficiency.

2873 7.4 HERSCHEL stability check

2874 We measure 13.27 ± 6.84 (9.41 ± 7.24) χ_{c1} mesons and 75.34 ± 10.84 (96.3 ± 12.32) χ_{c2} mesons
 2875 using our simultaneous-fit method with a HERSCHEL cut of $\ln(\chi_{\text{HRC}}^2) < 5$ applied to 2016-
 2876 only (combined 2015 and 2016) data. When corrected for the HERSCHEL efficiency, using
 2877 the results from the study presented in Sec. 5.6, this corresponds to 15.59 ± 8.04 ($11.34 \pm$
 2878 8.72) χ_{c1} mesons and 88.53 ± 12.77 (116.04 ± 14.88) χ_{c2} mesons, or a combined signal of
 2879 104.12 ± 15.10 (127.38 ± 17.25) CEP χ_c mesons. These numbers may be compared to the
 2880 results obtained with no HERSCHEL cut, which are 0 ± 18.57 (0 ± 26.49) χ_{c1} mesons and
 2881 176.69 ± 17.96 (229.71 ± 19.85) χ_{c2} mesons, or 176.7 ± 25.8 (229.7 ± 33.1) CEP χ_c mesons in

2882 total. There is a difference of 72.6 ± 29.9 (102.3 ± 37.3) in the determined number of χ_c decays
 2883 between the two measurements, which are different from zero with a significance of 2.4 (2.7)
 2884 standard deviations.

2885 The instability in results suggests some systematic bias in one or both of the measurements.
 2886 A priori we expect the results obtained with the HERSCHEL cut to be more reliable because of
 2887 the lower level of inelastic background. A plausible hypothesis is that the understanding of the
 2888 inelastic background behaviour is imperfect, and this leads to biases in the separation between
 2889 background and signal estimations in the simultaneous fit. This effect would be most marked
 2890 in the measurement without the HERSCHEL cut, where the estimated proportion of inelastic
 2891 background is $(51 \pm 6)\%$ ($(47 \pm 5)\%$), in contrast with $(16 \pm 5)\%$ ($(16 \pm 5)\%$) in the measurement
 2892 that benefits from the HERSCHEL cut. The observed difference between the two results can
 2893 be explained if $(32 \pm 13)\%$ ($(41 \pm 15)\%$) of inelastic background in the no-HERSCHEL case
 2894 is wrongly attributed as signal by the fit. Such a misassignment would have a much smaller
 2895 effect in the sample after the HERSCHEL cut, resulting in a migration of 6.3 ± 4.5 (10.0 ± 4.8)
 2896 background candidates from the background to the signal sample for the 2016-only (combined
 2897 2015 and 2016) data.

2898 To test this hypothesis, we repeat the measurement with a HERSCHEL cut applied at different
 2899 working points and monitor the consistency of the results. We place tighter requirements on
 2900 HERSCHEL to increase signal purity of $\ln(\chi_{\text{HRC}}^2) < 4$ and $\ln(\chi_{\text{HRC}}^2) < 3$. With the background
 2901 recalculated, we repeat the simultaneous fits of the Δm_{χ_c} and p_{T}^2 , the results of which are shown
 2902 in Fig. 7.5 and Fig. 7.6, for $\ln(\chi_{\text{HRC}}^2) < 4$ and $\ln(\chi_{\text{HRC}}^2) < 3$, respectively. The combined yield
 2903 of CEP χ_{c1} and χ_{c2} mesons is summarised in Table 7.3 for $\ln(\chi_{\text{HRC}}^2) < 5, 4$, and 3, before and
 2904 after being corrected for the HERSCHEL efficiency, as well as fit results with no HERSCHEL cut.
 2905 The corrected yields are consistent among the different HERSCHEL working points, suggesting
 2906 that the understanding of the signal efficiency is reliable, and that any imperfections in the
 2907 understanding of the residual inelastic background has a small impact once HERSCHEL is
 2908 applied. Noting this, and the initial change in results when moving from the no-HERSCHEL
 2909 case, we assign a systematic uncertainty of $\pm 40\%$ to the measurement of the inelastic χ_c mesons
 2910 for both the 2016-only data, and the combined 2015 and 2016 data. In the case of the χ_c
 2911 sample with the $\ln(\chi_{\text{HRC}}^2) < 5$ this corresponds to a systematic uncertainty of 40% (74%) for χ_{c1}
 2912 yields in the 2016-only (combined 2015 and 2016) data. The effect of this systematic is reduced
 2913 significantly for the calculation of the χ_{c2} yields due to the greater CEP purity in this region,
 2914 as explained above, which has a systematic uncertainty of 3.4% (2.9%) for 2016-only (combined
 2915 2015 and 2016) data. In addition, we take the largest differences between the corrected χ_c yields
 2916 as the systematic uncertainty associated with our HERSCHEL cut, which corresponds to a
 2917 5% (6%) uncertainty for 2016-only (combined 2015 and 2016) data.

Table 7.3. Combined CEP χ_{c1} and χ_{c2} yields before and after HERSCHEL cut correction.

Year	$\ln(\chi_{\text{HRC}}^2)$	Eff. [%]	$N_{\text{CEP}}(\chi_c)$	Corrected $N_{\text{CEP}}(\chi_c)$
2016	No Cut	100	176.69 ± 25.83	176.69 ± 25.83
	< 5	85.1 ± 0.8	88.6 ± 13	104.1 ± 15.1
	< 4	70.3 ± 0.7	69.5 ± 13	98.9 ± 15.2
	< 3	40.8 ± 0.5	40.9 ± 13	100.2 ± 21.1
2015 + 2016	No Cut	100	229.7 ± 33.1	229.7 ± 33.1
	< 5	83.0 ± 0.8	105.7 ± 13	127.4 ± 17.3
	< 4	67.9 ± 0.7	87.7 ± 13	129.2 ± 17.7
	< 3	39.6 ± 0.5	53.3 ± 13	134.5 ± 23.9

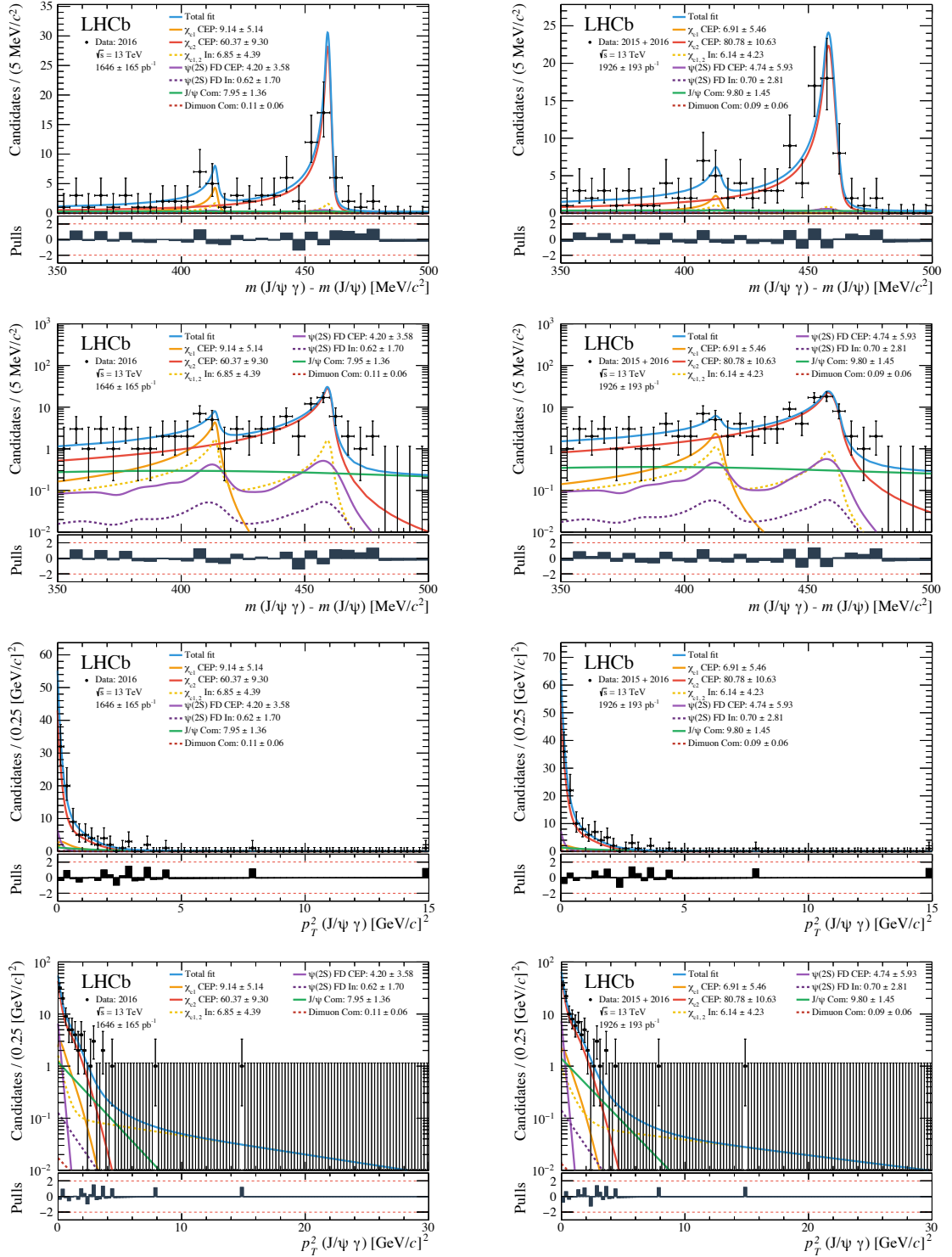


Figure 7.5. Two-dimensional fit of the Δm_{χ_c} (first and second row) and p_T^2 (squared) distribution of CEP χ_{c1} and χ_{c2} candidates for the 2016-only (left), and combined 2015 and 2016 (right) data, after the HERSCHEL cut, $\ln(\chi_{\text{HRC}}^2) < 4$, is applied. The overall fit is shown in solid blue, the CEP χ_{c1} component in solid orange, the CEP χ_{c2} component in solid red, the inelastic χ_c sample in yellow, the continuum-combinatorial background in broken-dark red, the J/ψ combinatorial background in green, the CEP $\psi(2S)$ in solid purple, and the inelastic $\psi(2S)$ in broken purple.

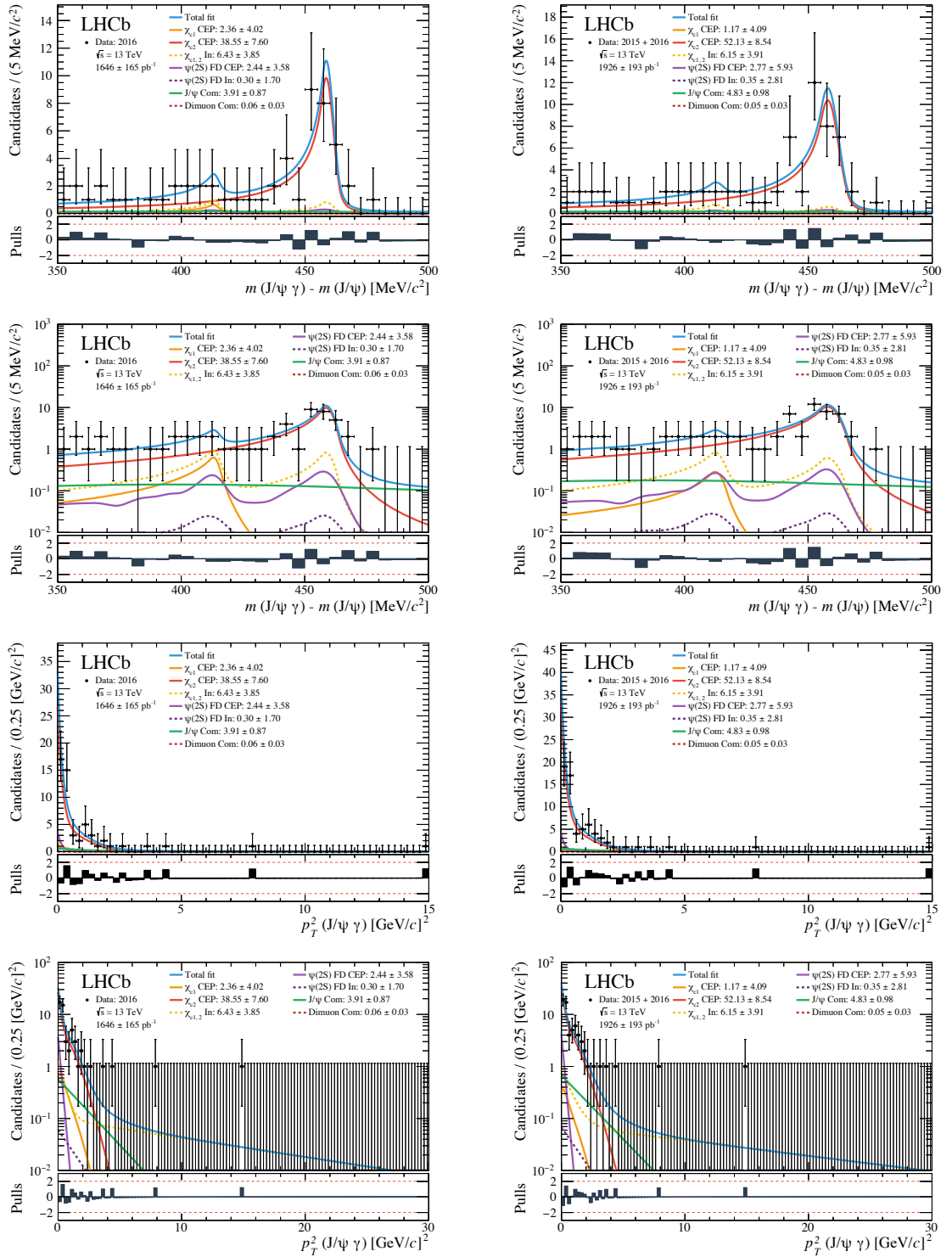


Figure 7.6. Two-dimensional fit of the Δm_{χ_c} (first and second row) and p_T^2 (squared) distribution of CEP χ_{c1} and χ_{c2} candidates for the 2016-only (left), and combined 2015 and 2016 (right) data, after the HERSCHEL cut, $\ln(\chi_{\text{HRC}}^2) < 3$, is applied. The overall fit is shown in solid blue, the CEP χ_{c1} component in solid orange, the CEP χ_{c2} component in solid red, the inelastic χ_c sample in yellow, the continuum-combinatorial background in broken-dark red, the J/ψ combinatorial background in green, the CEP $\psi(2S)$ in solid purple, and the inelastic $\psi(2S)$ in broken purple.

2918 7.5 Luminosity determination

2919 To calculate the total integrated luminosity, $\mathcal{L}_{\text{Total}}$, for each sample we sum over the integrated
2920 luminosity of all processed runs such that,

$$\mathcal{L}_{\text{Total}} = \sum_{\text{run}} \mathcal{L}^{\text{run}}. \quad (7.1)$$

2921 The integrated luminosity is taken from the latest calibration which has an uncertainty of
2922 2% [136]. For a small number of runs, less than one percent of the total, the new calibration
2923 is not available and we use an older calculation of the integrated luminosity. We validate
2924 the assigned integrated luminosity for these additional runs by checking that the number of
2925 CEP-like J/ψ events is as expected when compared to the well calibrated bulk of the data. The
2926 total-integrated luminosity for 2015 is $284 \pm 6 \text{ pb}^{-1}$ and $1637 \pm 33 \text{ pb}^{-1}$ for 2016. This results
2927 in a total-integrated luminosity of $1921 \pm 38 \text{ pb}^{-1}$ for the combined 2015 and 2016 data.

2928 However, since we are interested in CEP events that appear in isolation, we have to calculate
2929 the fraction of events that have a single interaction per beam-crossing, ϵ_{Single} . The average
2930 number of interactions per beam-crossing, μ , is calculated on a run-by-run basis and stored in
2931 the run database. Assuming proton-proton interactions during beam crossings follow Poisson
2932 statistics, we can calculate ϵ_{Single} per run such that,

$$\epsilon_{\text{Single}} = \mu e^{-\mu}. \quad (7.2)$$

2933 As a result, the single interaction total integrated luminosity is given by,

$$\mathcal{L}_{\text{Single}}^{\text{Total}} = \sum_{\text{run}} \epsilon_{\text{Single}}^{\text{run}} \mathcal{L}^{\text{run}}. \quad (7.3)$$

2934 The total-integrated luminosity for single-interaction events is $105 \pm 2 \text{ pb}^{-1}$ and $606 \pm 12 \text{ pb}^{-1}$ for
2935 the 2015 and 2016 runs, respectively. Summing up to $711 \pm 14 \text{ pb}^{-1}$ for the combined 2015 and
2936 2016 data. This implies an average value of $\langle \mu \rangle = 1.099$ (1.1007) and $\langle \epsilon_{\text{Single}} \rangle = 0.3662$ (0.3661)
2937 for 2015 (2016).

2938 7.6 Cross-section calculation

2939 The product of the integrated cross-section and the branching fraction for CEP $\chi_{cn} \rightarrow$
2940 $J/\psi [\mu^+ \mu^-] \gamma$ production with muons in the pseudorapidity region $2 < \eta_{\mu^+ \mu^-} < 4.5$ is given by

$$\sigma_{\chi_{cn} \rightarrow J/\psi [\mu^+ \mu^-] \gamma}^{(2 < \eta_{\mu^+ \mu^-} < 4.5)} = \frac{N_{\text{CEP}}(\chi_{cn})}{\mathcal{L}_{\text{Single}}^{\text{Total}} \cdot \epsilon_{\text{HRC}} \cdot \epsilon_{\gamma \rightarrow e^+ e^-}^{\text{Global}(\chi_{cn})} \cdot \epsilon_{\mu\mu}^{\text{Global}} \cdot \epsilon_{m(J/\psi)} \cdot \epsilon_{\Delta m(\chi_{cn})} \cdot \epsilon_{\text{SPD}}}, \quad (7.4)$$

2941 where $n = 1, 2$ corresponding to χ_{c1} and χ_{c2} mesons respectively. The CEP χ_c yields, $N_{\text{CEP}}(\chi_{cn})$,
2942 are calculated in Sec. 7.1 and the determination of the integrated luminosity for single-interaction
2943 crossings, $\mathcal{L}_{\text{Single}}^{\text{Total}}$, is detailed above in Sec. 7.5. The efficiency associated with the HERSCHEL
2944 figure-of-merit cut, ϵ_{HRC} , is described in Sec. 5.6.3 and Sec. 7.4; the photon-conversion efficiencies,

2945 $\varepsilon_{\gamma \rightarrow e^+e^-}^{\text{Global}(\chi_{c1})}$ and $\varepsilon_{\gamma \rightarrow e^+e^-}^{\text{Global}(\chi_{c2})}$, are presented in Sec. 5.1 and Sec. 7.3. The efficiency associated
 2946 with the J/ψ mass window, $\varepsilon_{m(J/\psi)}$, is discussed in Sec. 5.3; the efficiency associated with the
 2947 χ_c delta-mass cut, $\varepsilon_{\Delta m(\chi_{cn})}$, is described in Sec. 5.4, and the efficiency associated with the
 2948 SPD requirements at hardware-trigger level, ε_{SPD} , is discussed in Sec. 5.5. The total efficiency,
 2949 $\varepsilon_{\text{Total}}(\chi_{cn})$, is given by the product of all efficiencies such that,

$$\varepsilon_{\text{Total}}(\chi_{cn}) = \varepsilon_{\text{HRC}} \cdot \varepsilon_{\gamma \rightarrow e^+e^-}^{\text{Global}(\chi_{cn})} \cdot \varepsilon_{\mu\mu}^{\text{Global}} \cdot \varepsilon_{m(J/\psi)} \cdot \varepsilon_{\Delta m(\chi_{cn})} \cdot \varepsilon_{\text{SPD}}. \quad (7.5)$$

2950 The values of these parameters are summarised in Table 7.4 for both 2016 data, and the
 2951 combined 2015 and 2016 data. This leads to the product of the integrated cross-section and the
 2952 branching fraction results of

$$\sigma_{\chi_{c1} \rightarrow J/\psi [\mu^+\mu^-]\gamma}^{(2 < \eta_{\mu^+\mu^-} < 4.5)} = 21.5 \pm 11.1 \pm 10.2 \text{ pb} \quad (7.6)$$

2953

$$\sigma_{\chi_{c2} \rightarrow J/\psi [\mu^+\mu^-]\gamma}^{(2 < \eta_{\mu^+\mu^-} < 4.5)} = 83.1 \pm 12.0 \pm 20.8 \text{ pb} \quad (7.7)$$

2954 for 2016-only data, and

$$\sigma_{\chi_{c1} \rightarrow J/\psi [\mu^+\mu^-]\gamma}^{(2 < \eta_{\mu^+\mu^-} < 4.5)} = 13.9 \pm 10.7 \pm 10.9 \text{ pb} \quad (7.8)$$

2955

$$\sigma_{\chi_{c2} \rightarrow J/\psi [\mu^+\mu^-]\gamma}^{(2 < \eta_{\mu^+\mu^-} < 4.5)} = 99.6 \pm 12.7 \pm 24.5 \text{ pb} \quad (7.9)$$

2956 for the combined 2015 and 2016 data where the first uncertainty is statistical and the second
 2957 systematic, with sources discussed in Sec. 7.7. The results from the 2016-only and combined
 2958 2015 and 2016 data are compatible with one another. We will use the results from the full data
 2959 set to determine our nominal values.

2960 As we do not observe a significant number of χ_{c1} mesons, we calculate an upper limit of
 2961 the product of the cross-section and the branching fraction at a ninety-percent confidence
 2962 level. To do this, we perform a similar procedure as the one used to check the stability of the
 2963 simultaneous Δm_{χ_c} and p_{T}^2 fit model, presented in Sec. 7.2. As before, we generate a series
 2964 of ten-thousand toy studies using the fit results to the data. However, this time we manually
 2965 set the yield of χ_{c1} mesons to zero. We fit the generated distributions with the same model
 2966 used to fit the CEP χ_c sample and use the result to determine the χ_{c1} yield value for which
 2967 ninety-percent of the toys return. In doing so, we account for the the systematic uncertainties
 2968 presented throughout the thesis and summarised in Sec. 7.7. We determine this value to be
 2969 13.2 ± 10.2 events, which compares to a nominal value of 9.41 ± 7.24 events as calculated with the
 2970 HERSCHEL cut applied. Therefore, the product of the cross-section and the branching fraction
 2971 of CEP $\chi_c \rightarrow J/\psi [\mu^+\mu^-]\gamma$ within a ninety-percent confidence interval is $19.5 \pm 15.0 \pm 15.2$ pb,
 2972 which compares to $13.9 \pm 10.7 \pm 10.9$ pb, respectively.

Table 7.4. Summary of the fitted-signal yields, integrated luminosity for single-crossing interactions, and efficiencies necessary for the calculation of the product of the cross-section and the branching fraction of CEP $\chi_c \rightarrow J/\psi[\mu^+\mu^-]\gamma$ production in proton-proton collisions at centre-of-mass energies of $\sqrt{s} = 13$ TeV at the LHCb experiment with muons in the $2 < \eta_{\mu^+\mu^-} < 4.5$ pseudorapidity region.

Variable	2016	2015 + 2016
Yield(χ_{c1}) _{CEP}	13.3	9.4
Yield(χ_{c2}) _{CEP}	75.3	96.3
$\mathcal{L}_{\text{Single}}^{\text{Total}}$	606 pb ⁻¹	711 pb ⁻¹
$\varepsilon_{\mu\mu}^{\text{Global}}$	0.635	0.631
$\varepsilon_m(J/\psi)$	0.954	0.955
$\varepsilon_{\Delta m(\chi_{c1})}$	0.885	0.892
$\varepsilon_{\Delta m(\chi_{c2})}$	0.944	0.926
$\varepsilon_{\gamma \rightarrow e^+e^-}^{\text{Global}(\chi_{c1})} (\times 10^{-2})$	0.225	0.225
$\varepsilon_{\gamma \rightarrow e^+e^-}^{\text{Global}(\chi_{c2})} (\times 10^{-2})$	0.309	0.310
ε_{SPD}	0.994	0.950
ε_{HRC}	0.851	0.830
$\varepsilon_{\text{Total}}(\chi_{c1}) (\times 10^{-2})$	0.0988	0.0928
$\varepsilon_{\text{Total}}(\chi_{c2}) (\times 10^{-2})$	0.148	0.136

2973 We compare our results with theoretical predictions of the Durham model as implemented
2974 in SuperChic v4 [80]. SuperChic calculates the $gg \rightarrow \chi_c$ vertex to leading order. Therefore, we
2975 select three leading-order parton distribution functions for the calculation: **CT14** ($\alpha_S(M_Z^2) =$
2976 $0.118)$ [137], **MSHT20** ($\alpha_S(M_Z^2) = 0.13)$ [138], and **NNPDF 3.1** ($\alpha_S(M_Z^2) = 0.13)$ [139]. The
2977 theoretical predictions are shown in Table 7.5, where the uncertainties are statistical from the
2978 simulation calculation. **CT14** and **MSHT20** PDFs are calculated from global fits to data from
2979 multiple experiments, including fixed target experiments, HERA, Tevatron, and Run 1 LHC
2980 data collected at 7 TeV and 8 TeV. **NNPDF 3.1**, on the other hand, uses a neural network trained
2981 with genetic algorithms to calculate PDFs. The measured results are compatible with the
2982 theoretical predictions given the large uncertainties in the PDF distribution. This measurement
2983 is particularly susceptible to the gluon PDF at low Bjorken- x and Q^2 where the PDF is not
2984 well determined. For example, the uncertainty of the gluon PDF of NNPDF at low Bjorken- x is
2985 approximately fifty percent. As is evident, the nominal value of the theoretical predictions can
2986 vary significantly depending on the choice of PDF. At such low scales, the uncertainty of the
2987 perturbative predictions can be off by a factor of four or five. We expect improvement in the
2988 PDFs as new studies are incorporated into the global studies, such as those conducted with
2989 data from the LHC at a centre-of-mass energy $\sqrt{s} = 13$ TeV.

2990 However, several of the uncertainties associated with the calculation of the PDFs as well as
2991 some of the systematic uncertainties in our measurement will cancel when we take the ratio of
2992 the cross-sections. The ratio of the theoretical calculations of the product of the cross-section
2993 and the branching fraction of χ_{c2} and χ_{c1} also exhibit small PDF dependence, as shown in

Table 7.5. Measurements of the product of the cross-section times the branching fraction for the full data set (combined 2015 and 2016 data) together with predictions in pb for CEP $\chi_c \rightarrow J/\psi [\mu^+ \mu^-] \gamma$ production in the rapidity region $2 < \eta_{\mu^+ \mu^-} < 4.5$ for pp collisions at a centre-of-mass energy $\sqrt{s} = 13$ TeV, using SuperChic v4 [80] for three LO PDFs: CT14 ($\alpha_S(M_Z^2) = 0.118$) [137], MSHT20 ($\alpha_S(M_Z^2) = 0.13$) [138], and NNPDF 3.1 ($\alpha_S(M_Z^2) = 0.13$) [139].

Source	Order	$\alpha_S(M_Z^2)$	$\sigma_{\chi_{c1} \rightarrow J/\psi [\mu^+ \mu^-] \gamma}^{(2 < \eta_{\mu^+ \mu^-} < 4.5)}$	$\sigma_{\chi_{c2} \rightarrow J/\psi [\mu^+ \mu^-] \gamma}^{(2 < \eta_{\mu^+ \mu^-} < 4.5)}$	$\sigma_{\chi_{c2}} / \sigma_{\chi_{c1}}$
CT14	L0	0.118	26.03 ± 0.12 [pb]	71.98 ± 0.34 [pb]	2.77 ± 0.02
MSHT20	L0	0.130	48.48 ± 0.20 [pb]	138.24 ± 0.51 [pb]	2.85 ± 0.02
NNPDF 3.1	L0	0.130	6.42 ± 0.27 [pb]	16.16 ± 0.08 [pb]	2.52 ± 0.11
Measurement	-	-	$13.9 \pm 10.7 \pm 10.9$ [pb]	$99.6 \pm 12.7 \pm 24.5$ [pb]	$5.11 \pm 3.98 \pm_{-2.09}^{+14.19}$
90% C.L.	-	-	$19.5 \pm 15.0 \pm 15.2$ [pb]	-	-

2994 Table 7.5. We measure a ratio of $\sigma_{\chi_{c2}} / \sigma_{\chi_{c1}} = 5.11 \pm 3.98 \pm_{-2.09}^{+14.19}$, which hints at a higher result
2995 than theoretical predictions by approximately a factor of 2.6. However, our measured value and
2996 theoretical predictions are in agreement within one standard deviation. As a reminder, the large
2997 statistical uncertainty in this observable is due to the low number of observed χ_{c1} mesons while
2998 the large systematic uncertainty is dominated by the misassignment of inelastic χ_{c1} background.

2999 7.7 Assignment of systematic uncertainties

3000 The systematic uncertainties associated with the cross-section calculation are summarised in
3001 Table 7.6 and briefly discussed below in order of significance. The origin of most of these sources
3002 of potential bias, and the assigned uncertainty has already been discussed in earlier chapters.

Table 7.6. Summary of systematic uncertainties for the cross-section calculation of CEP $\chi_c \rightarrow J/\psi [\mu^+ \mu^-] \gamma [e^+ e^-]$ production.

Source	2016		2015 + 2016	
	χ_{c1}	χ_{c2}	χ_{c1}	χ_{c2}
$\varepsilon_{\gamma \rightarrow e^+ e^-}^{\text{Global}(\chi_{cn})}$	22%	22%	22%	22%
Inelastic background	40%	3%	74%	3%
$\varepsilon_{\mu\mu}^{\text{Global}}$	7%	7%	5%	5%
ε_{HRC}	6%	6%	5%	5%
ε_{SPD}	4%	4%	5%	5%
Fit bias	5%	5%	5%	5%
$\varepsilon_{\Delta m(\chi_{cn})}$	4%	2%	4%	3%
$\mathcal{L}_{\text{SingleTotal}}$	2%	2%	2%	2%
$\varepsilon_{m(J/\psi)}$	< 1%	< 1%	< 1%	< 1%
$\varepsilon_{\text{Total}}$	47%	25%	78%	25%

3003 The most significant systematic uncertainty for the cross-section calculation of CEP χ_c
 3004 production is related to the photon-conversion efficiency, described in Sec. 5.1, where we calculate
 3005 the efficiency using a high-multiplicity sample and extrapolate in to a CEP-like, low-multiplicity,
 3006 environment. As a systematic check, we vary the binning and fit model used in the extrapolation
 3007 and assign a 20% systematic uncertainty for both the 2016-only, and combined 2015 and 2016
 3008 data. The dominant systematic uncertainty in the normalisation of the efficiency is a relative
 3009 $\pm 8\%$ associated with the knowledge of the number of D^{*0} mesons produced in the sample.
 3010 Summing the systematic uncertainty components in quadrature, we obtain a total systematic
 3011 uncertainty associated with the photon-conversion and reconstruction efficiency of 21.5%.

3012 The next most prominent systematic uncertainty is associated with the fit model and
 3013 the difficulties inherent with determining the contribution of inelastic χ_c background. When
 3014 comparing the yields with and without the HERSCHEL cut applied we observe a shift in results
 3015 that we attribute to a 40% misassignment of inelastic χ_c events as CEP χ_c events, a procedure
 3016 described in Sec. 7.4. This translates into a systematic uncertainty of 40.0% (74.3%) for χ_{c1}
 3017 yields and 3.4% (2.9%) for χ_{c2} yields in 2016-only (combined 2015 and 2016) data. The effect
 3018 of this systematic is reduced significantly for the calculation of the χ_{c2} yields due to the greater
 3019 CEP purity in this region.

3020 The largest source of systematic uncertainty in the muon reconstruction efficiency, described
 3021 in Sec. 5.2, comes from the extrapolation of the muon-reconstruction efficiency from 2015 to
 3022 2016 data. Although reasonable, the assumption that there is no significant difference in the
 3023 detector's muon-reconstruction performance is not perfect. As a result, we allocate the full
 3024 correction required to match 2016 results as a systematic uncertainty to the reconstruction
 3025 efficiency. This corresponds to 7% (5%) for the 2016-only (combined 2015 and 2016) data.

3026 The largest systematic uncertainty with the HERSCHEL efficiency calculation, presented
 3027 in Sec. 5.6.3, is associated with the dimuon fit used to separate the CEP from the non-CEP
 3028 contributions. To test this, we vary the signal model and background independently then
 3029 recalculate the efficiency for our working point, $\ln(\chi_{\text{HRC}}^2) < 5$. We find the biggest contribution
 3030 to the systematic originating from the signal model, and assign this difference as the full
 3031 systematic for an uncertainty of 6% (5%) for 2016-only (combined 2015 and 2016) data. In
 3032 addition, stability checks are reported in Sec. 7.4, which showed no significant changes when
 3033 varying the cut on $\ln(\chi_{\text{HRC}}^2)$.

3034 To assign a systematic to the efficiency associated with the SPD hardware trigger requirement,
 3035 detailed in Sec. 5.5, we vary the mean number of hits expected in the SPD from each muon and
 3036 electron in our model and recalculate the efficiency. We take the largest difference from our
 3037 nominal efficiency as the systematic uncertainty, and assign a 4% (5%) uncertainty to the SPD
 3038 efficiency of 2016-only (combined 2015 and 2016) data.

3039 We validate the Δm_{χ_c} and p_{T}^2 simultaneous fit of our CEP χ_c candidates by performing a
 3040 series of toy studies, as presented in Sec. 7.2. From the pull distributions we see that there is

3041 a small bias in the order of $\sim 5\%$ in the CEP χ_{c1} and χ_{c2} yields. We assign this fit bias as a
3042 systematic uncertainty.

3043 We calculate the efficiency associated with the Δm_{χ_c} cut, described in Sec. 5.4. In this case,
3044 the biggest limitation does not come from the fit model, but instead from the photon-conversion-
3045 efficiency corrections. As a result, we calculate the cut's efficiency using both Monte Carlo and
3046 data driven photon-conversion efficiencies and compare the difference in results. We assign an
3047 uncertainty of 3.8% (4.0%) for χ_{c1} and 1.7% (2.7%) for χ_{c2} for the 2016-only (combined 2015
3048 and 2016) data.

3049 For the determination of the single-interaction integrated luminosity we use the latest
3050 calibration sample which has an uncertainty of 2%. We validate the small number of runs,
3051 where the calibration is not available, less than one percent of said runs, by making sure the
3052 number of CEP-like J/ψ mesons matches the assigned integrated luminosity.

3053 To calculate a systematic uncertainty for the efficiency of the J/ψ mass-window cut, described
3054 in Sec. 5.3, we vary the signal model and repeat the fit used to calculate the efficiency. We
3055 take the difference as the systematic uncertainty and assign a 0.4% (0.3%) uncertainty to the
3056 2016-only (combined 2015 and 2016) data.

3057 The total systematic uncertainty is the quadrature sum of all the sources of uncertainty
3058 detailed above and leads to a relative systematic uncertainty of 47% (78%) for the χ_{c1}
3059 and 25% (25%) for the χ_{c2} cross-section-times-branching-fraction calculation for the 2016-
3060 only (combined 2015 and 2016) data. This corresponds to an absolute systematic uncertainty
3061 of 10.1 pb (10.8 pb) for the χ_{c1} and 20.8 pb (24.9 pb) for the χ_{c2} cross-section-times-branching-
3062 fraction calculation.

CHAPTER 8

Summary and outlook

We presented a study of the CEP of χ_{c1} and χ_{c2} mesons using proton-proton collisions at a centre-of-mass energy of $\sqrt{s} = 13$ TeV, using data collected with the LHCb experiment during the 2015 and 2016 runs corresponding to single-interaction integrated luminosities of 711 pb^{-1} . The study was performed through the χ_c meson's radiative decay into $J/\psi[\mu^+\mu^-]\gamma[e^+e^-]$ where the muons from the J/ψ decay are measured within the pseudorapidity region $2 < \eta_{\mu^+\mu^-} < 4.5$.

To obtain the best possible χ_c mass resolution we used converted photons, taking advantage of the improved momentum resolution from the tracking information of the electrons. As a result, we have been able to clearly separate contributions from χ_{c1} and χ_{c2} mesons. However, this came at the cost of a smaller event yield when compared to a sample reconstructed with photons detected by the electromagnetic calorimeter. Using converted photons also meant that having a clear understanding of the photon-conversion and reconstruction efficiency was crucial to the success of this analysis. Consequently, we developed a unique data-driven method using $D^{*0} \rightarrow D^0[K^\pm\pi^\mp]\gamma$ decays through which we measured the photon-conversion and reconstruction efficiency of photons with transverse-momentum as low as $200 \text{ MeV}/c$. These events are normally accompanied by a large number of particles, resulting in a high detector occupancy. Therefore, the procedure required the extrapolation of the results into a low multiplicity environment typical of CEP, giving rise to our primary systematic uncertainty.

We enforced the characteristic double rapidity-gap criteria of CEP by selecting low-multiplicity events at the trigger level and requiring that there are no additional tracks in the forward and backward direction within the main spectrometer's acceptance. In addition, we used HERSCHEL to reject events accompanied by proton dissociation, gluon radiation, multiple scattering, or pile-up. HERSCHEL has proven to be a powerful tool for the study of CEP that allows us to significantly reduce inelastic background while retaining CEP signal. To determine the performance of the HERSCHEL figure of merit, we used a sample of CEP dimuons; a well understood CEP process. The observed signal retention and background rejection in the CEP χ_c sample were in good agreement with the calibration sample, even though our signal had two additional final-state particles. In addition, we observed stable and consistent results across different HERSCHEL figure of merit working points.

3094 To separate the CEP χ_c signal from inelastic χ_c background contributions we failed to
 3095 veto through our low-multiplicity selection, exclusivity-track requirements, or HERSCHEL
 3096 cut, we performed a simultaneous fit of the χ_c meson's delta-mass and transverse-momentum-
 3097 squared distribution to take advantage of the characteristically low p_T^2 of CEP relative to its
 3098 inelastic counterpart. The signal component shapes are taken from SuperChic simulation while
 3099 background shapes are taken from simulation, data-driven studies, and previous experimental
 3100 results, which makes this a model-dependent study. The fit benefits from lower inelastic χ_c
 3101 background achieved through the implementation of the HERSCHEL cut. However, given the
 3102 low reconstruction efficiency of events with soft photons we only observe a few χ_{c1} candidates
 3103 and, as a result, are able to present a ninety percent confidence limit for the product of the
 3104 cross-section and the branching fraction of χ_{c1} mesons. The product of the cross-section and
 3105 branching fraction are measured to be

$$\sigma_{\chi_{c1} \rightarrow J/\psi [\mu^+ \mu^-] \gamma}^{(2 < \eta_{\mu^+ \mu^-} < 4.5)} = 19.5 \pm 15.0 \pm 15.2 \text{ pb} \quad (8.1)$$

3106

$$\sigma_{\chi_{c2} \rightarrow J/\psi [\mu^+ \mu^-] \gamma}^{(2 < \eta_{\mu^+ \mu^-} < 4.5)} = 99.6 \pm 12.7 \pm 24.5 \text{ pb}, \quad (8.2)$$

3107 where the first uncertainty is statistical and the second is systematic. These results are compatible
 3108 with theoretical predictions given the large uncertainties.

3109 There are two additional low-multiplicity dimuon samples of comparable size to the 2016
 3110 sample collected during the 2017 and 2018 runs that included the HERSCHEL detector. However,
 3111 crucial information is missing from the D^{*0} sample collected during these run periods, which
 3112 is necessary for the photon-conversion calibration. Consequently, a new method needs to be
 3113 developed before we can incorporate the full Run 2 data set into the analysis. The study would
 3114 greatly benefit from a larger data set. This would allow us to significantly improve the stability
 3115 of the fit model and increase our sensitivity to the cross-section measurement of χ_c , especially
 3116 that of χ_{c1} . The larger sample and improved fit stability might in turn allow us to reincorporate
 3117 the χ_{c0} mass region into our analysis and give us sensitivity to its CEP contribution. In addition,
 3118 a larger sample would make the cross-sectional measurement as a function of rapidity possible
 3119 and allow us to shed light on low Bjorken- x physics.

3120 LHCb is undergoing an upgrade period known as the second long-shutdown, which started
 3121 in 2019 and is expected to end in 2021. This is in preparation for the high-luminosity stage
 3122 of the LHC (HL-LHC). The LHC was calibrated to deliver approximately 1.5 and 1.1 visible
 3123 interactions per bunch crossing during Run 1 and Run 2, respectively. This allowed for the
 3124 collection of approximately 10 fb^{-1} of data. During Run 3 and Run 4 the LHC will deliver
 3125 approximately five interactions per bunch crossing at the LHCb interaction point, which is
 3126 expected to deliver an integrated luminosity of 50 fb^{-1} by the end of Run 3 and Run 4. However,
 3127 the higher interaction rate means that only three percent of the bunch crossing will correspond
 3128 to a single interaction compared to the thirty-seven percent for Run 2. As a result, LHCb will

3129 only collect a fraction of the single-interaction events during Run 3 and Run 4 compared to
 3130 the currently available data set. Therefore, the useful sample size is not competitive and the
 3131 harsher environment would quickly degrade the HERSCHEL modules. This in turn means that
 3132 HERSCHEL will not be available for proton-proton runs during this period.

3133 In order to cope with the higher occupancy while maintaining detector performance, key
 3134 LHCb sub-detectors are being replaced, including the tracking detectors, the RICH detectors,
 3135 and the VELO. In addition, all trigger lines will be entirely software based and all detectors
 3136 will be read at 40 MHz. This will allow us to apply more sophisticated selection criteria at
 3137 trigger level. With the full software trigger it is possible to identify isolated low-multiplicity
 3138 vertices from CEP even in a bunch crossing with multiple interactions and many other vertices.
 3139 However, Herschel information cannot be used in this case because we cannot associate the
 3140 signals in Herschel with the individual vertices.

3141 However, through an alternative method known as proton tagging, we could guarantee
 3142 the exclusivity requirement of the event in spite of the presence of pile-up. In this process
 3143 the two interacting protons scatter at small angles, are detected by instrumentation near the
 3144 beam line and their kinematics are reconstructed. We could then use the information of the
 3145 proton's momentum loss to calculate the mass of the central system independent of its decay
 3146 mode. For CEP events, we would expect agreement between this measurement and the mass
 3147 calculated using information from decay products detected in the main spectrometer, and
 3148 expect disagreement between the two measurements for background events. In addition, by
 3149 reconstructing the full kinematics of the event we would be able to constrain the mass calculation
 3150 of the central system and improve its resolution as well as detect events with missing energy.
 3151 Currently, however, there are no plans to install proton taggers at LHCb.

3152 The χ_c measurements could be significantly improved by incorporating hadronic decays
 3153 where candidates can be reconstructed in the K^+K^- , $\pi^+\pi^-$, and p^+p^- final state, as well
 3154 as decays with a larger number of hadrons in the final state such as $2(\pi^+\pi^-)$, $3(\pi^+\pi^-)$, and
 3155 $\pi^+\pi^-K^+K^-$. Data were collected in Run 2 with trigger lines sensitive to these decays. This
 3156 would significantly increase our sensitivity to χ_{c0} production. LHCb is well suited for this study
 3157 thanks to its strong particle-identification capabilities. The study presented in this thesis has
 3158 also shown that the multiplicity trigger requirements are sufficiently loose to cope with a four
 3159 and six particle final state necessary for some of the hadronic studies.

3160 The next test of our theoretical understanding of the DPE mechanism of CEP is the study
 3161 of the bottomonium counterpart of the χ_c mesons, the χ_b states. Similar to χ_c , there are three
 3162 states of χ_b with $J^{CP} = 0^{++}$, 1^{++} , and 2^{++} that follow a similar hierarchy. Although it has a
 3163 smaller cross-section, the χ_b state's higher mass scale places it safely within the perturbative
 3164 regime. We can apply the knowledge learned in this study to investigate the CEP of χ_b mesons
 3165 through a similar radiative decay, $\chi_b \rightarrow \Upsilon[\mu^+\mu^-]\gamma$. The invariant mass of χ_{b0} and χ_{b1} mesons
 3166 are within $33 \text{ MeV}/c^2$ of one another, and that of χ_{b1} and χ_{b2} is within $20 \text{ MeV}/c^2$ of one

3167 another. As a result, this analysis would also greatly benefit from the use of converted photons
3168 to increase the invariant-mass resolution of the χ_b states.

3169 We can also apply the lessons learned to the study of exotic particles, such as the $X(3872)$
3170 state [140–144], which can be studied through the radiative decay into $J/\psi[\mu^+\mu^-]\gamma$ or with a
3171 more favourable branching fraction into $\psi(2S)[\mu^+\mu^-]\gamma$. This state has an unusually narrow
3172 width, with an upper limit of $1.2\text{ MeV}/c^2$ set at a ninety percent confidence level. Although the
3173 quantum numbers have been determined to be $J^{CP} = 1^{++}$ the nature of this particle has yet to
3174 be understood.

3175 In summary, we have demonstrated that the LHCb is well equipped for the study of CEP
3176 and shown that HERSCHEL plays an important role in background reduction by expanding
3177 the sensitivity of LHCb to higher rapidity regions. We have demonstrated the benefits of
3178 using converted photons as a mechanism to improve mass resolution at the LHCb. We also
3179 conducted an important measurement necessary to test our theoretical understanding of CEP.
3180 More importantly, by studying the CEP of χ_c mesons (considered the standard candle of CEP
3181 via DPE) we have opened a new frontier for LHCb through which to probe the Standard Model.

Bibliography

- 3183 [1] R. Devenish, E. P. P. R. Devenish, A. Cooper-Sarkar, and O. U. Press, *Deep Inelastic*
3184 *Scattering*, Oxford University Press, 2004.
- 3185 [2] M. Thomson, *Modern particle physics*, Cambridge University Press, New York, 2013.
- 3186 [3] I. J. R. Aitchison and A. J. G. Hey, *Gauge Theories in Particle Physics: A Practical*
3187 *Introduction, Volume 1: From Relativistic Quantum Mechanics to QED, Fourth Edition*,
3188 no. v. 1, CRC Press, 2012.
- 3189 [4] M. Gell-Mann, *A schematic model of baryons and mesons*, Physics Letters **8** (1964), no. 3
3190 214.
- 3191 [5] J. Matthew Durham, on behalf of the LHCb collaboration, *LHCb measurements of the*
3192 *exotic tetraquark candidate $\chi_{c1}(3872)$ in high-multiplicity pp and pPb collisions*, Nucl.
3193 Phys. A **1005** (2021) 121918, arXiv:2002.01551.
- 3194 [6] LHCb collaboration, *Observation of structure in the J/ψ -pair mass spectrum*, Sci. Bull.
3195 **65** (2020), no. 23 1983, arXiv:2006.16957.
- 3196 [7] LHCb collaboration, *Observation of new resonances decaying to $J/\psi K^+$ and $J/\psi \phi$* ,
3197 arXiv:2103.01803.
- 3198 [8] S.-Y. Li *et al.*, *Pentaquark states with the $QQQq\bar{q}$ configuration in a simple model*, Eur.
3199 Phys. J. C **79** (2019), no. 1 87, arXiv:1809.08072.
- 3200 [9] LHCb collaboration, *Observation of the doubly charmed baryon Ξ_{cc}^{++}* , Phys. Rev. Lett.
3201 **119** (2017), no. 11 112001, arXiv:1707.01621.
- 3202 [10] LHCb collaboration, *Observation of $J/\psi p$ Resonances Consistent with Pentaquark States*
3203 *in $\Lambda_b^0 \rightarrow J/\psi K^- p$ Decays*, Phys. Rev. Lett. **115** (2015) 072001, arXiv:1507.03414.
- 3204 [11] LHCb collaboration, *Observation of a narrow pentaquark state, $P_c(4312)^+$, and of two-peak*
3205 *structure of the $P_c(4450)^+$* , Phys. Rev. Lett. **122** (2019), no. 22 222001, arXiv:1904.03947.
- 3206 [12] J. C. Ward, *An Identity in Quantum Electrodynamics*, Phys. Rev. **78** (1950) 182.
- 3207 [13] P. D. Group, *Review of Particle Physics*, Progress of Theoretical and Experimental Physics
3208 **2020** (2020) , arXiv:https://pdglive.lbl.gov, 083C01.

- 3209 [14] F. E. Low, *A Model of the Bare Pomeron*, Phys. Rev. D **12** (1975) 163.
- 3210 [15] I. Y. Pomeranchuk, V. V. Sudakov, and K. A. Ter-Martirosyan, *Vanishing of Renormalized*
3211 *Charges in Field Theories with Point Interaction*, Phys. Rev. **103** (1956) 784.
- 3212 [16] G. F. Chew and S. C. Frautschi, *Dynamical Theory for Strong Interactions at Low*
3213 *Momentum Transfers but Arbitrary Energies*, Phys. Rev. **123** (1961), no. 4 1478.
- 3214 [17] P. D. B. Collins, *An Introduction to Regge Theory and High-Energy Physics*, Cambridge
3215 Monographs on Mathematical Physics, Cambridge Univ. Press, Cambridge, UK, 5, 2009.
3216 doi: 10.1017/CBO9780511897603.
- 3217 [18] V. Barone and E. Predazzi, *High-Energy Particle Diffraction*, vol. v.565 of *Texts and*
3218 *Monographs in Physics*, Springer-Verlag, Berlin Heidelberg, 2002.
- 3219 [19] M. Albrow, *Central exclusive production issue: Introduction*, Int. J. Mod. Phys. **A29**
3220 (2014) 1402006.
- 3221 [20] M. G. Albrow, T. D. Coughlin, and J. R. Forshaw, *Central Exclusive Particle Production*
3222 *at High Energy Hadron Colliders*, Prog. Part. Nucl. Phys. **65** (2010) 149, arXiv:1006.1289.
- 3223 [21] A. D. Martin, M. G. Ryskin, and V. A. Khoze, *Forward Physics at the LHC*, Acta Phys.
3224 Polon. B **40** (2009) 1841, arXiv:0903.2980.
- 3225 [22] A. B. Kaidalov, V. A. Khoze, A. D. Martin, and M. G. Ryskin, *Central exclusive diffractive*
3226 *production as a spin-parity analyser: From Hadrons to Higgs*, Eur. Phys. J. C **31** (2003)
3227 387, arXiv:hep-ph/0307064.
- 3228 [23] W. Ochs, *The Status of Glueballs*, J. Phys. G **40** (2013) 043001, arXiv:1301.5183.
- 3229 [24] J. R. Forshaw, *Central Exclusive Production at the LHC*, Nucl. Phys. Proc. Suppl. **191**
3230 (2009) 247, arXiv:0901.3040.
- 3231 [25] D. d'Enterria, *Forward Physics at the LHC: within and beyond the Standard Model*, AIP
3232 Conf. Proc. **1038** (2008), no. 1 95, arXiv:0806.0883.
- 3233 [26] ATLAS collaboration, *Observation of light-by-light scattering in ultraperipheral Pb +*
3234 *Pb collisions with the ATLAS detector*, Phys. Rev. Lett. **123** (2019), no. 5 052001,
3235 arXiv:1904.03536.
- 3236 [27] CDF collaboration, *Observation of Exclusive Electron-Positron Production in Hadron-*
3237 *Hadron Collisions*, Phys. Rev. Lett. **98** (2007) 112001, arXiv:hep-ex/0611040.
- 3238 [28] CDF collaboration, *Search for exclusive Z boson production and observation of high mass*
3239 *$p\bar{p} \rightarrow \gamma\gamma \rightarrow p + \ell\ell + \bar{p}$ events in $p\bar{p}$ collisions at $\sqrt{s} = 1.96$ TeV*, Phys. Rev. Lett. **102**
3240 (2009) 222002, arXiv:0902.2816.
- 3241 [29] CDF collaboration, *Observation of Exclusive Dijet Production at the Fermilab Tevatron*

- 3242 $p^- \bar{p}$ Collider, Phys. Rev. D **77** (2008) 052004, arXiv:0712.0604.
- 3243 [30] CMS collaboration, *Exclusive photon-photon production of muon pairs in proton-proton*
3244 *collisions at $\sqrt{s} = 7$ TeV*, JHEP **01** (2012) 052, arXiv:1111.5536.
- 3245 [31] K. Piotrkowski, *Study of exclusive two-photon production of W^+W^- pairs in pp collisions*
3246 *at 7 TeV, and constraints on anomalous quartic couplings in CMS*, PoS **Photon2013**
3247 (2013) 026.
- 3248 [32] S. R. Klein, *Comment on “ η_c production in photon-induced interactions at the LHC”*, Phys.
3249 Rev. D **98** (2018), no. 11 118501, arXiv:1808.08253.
- 3250 [33] B. R. Gruberg Cazon, *Studies of the Photoproduction of Charm-Anticharm Resonances in*
3251 *Ultra-Peripheral Collisions of Lead Ions in ALICE at the LHC*, PhD thesis, Creighton
3252 University, 2015.
- 3253 [34] B. Pire, F. Schwennsen, L. Szymanowski, and S. Wallon, *Hard Pomeron-Odderon interfer-*
3254 *ence effects in the production of $\pi^+\pi^-$ pairs in high energy gamma-gamma collisions at*
3255 *the LHC*, Phys. Rev. D **78** (2008) 094009, arXiv:0810.3817.
- 3256 [35] U. Gastaldi and M. Berretti, *Decays into $\pi^+\pi^-$ of the $f_0(1370)$ scalar glueball candidate*
3257 *in pp central exclusive production experiments*, arXiv:1804.09121.
- 3258 [36] STAR collaboration, *Coherent ρ^0 production in ultraperipheral heavy ion collisions*, Phys.
3259 Rev. Lett. **89** (2002) 272302, arXiv:nucl-ex/0206004.
- 3260 [37] CMS Collaboration, *Measurement of exclusive $\rho(770)^0$ photoproduction in ultraperipheral*
3261 *pPb collisions at $\sqrt{s_{NN}} = 5.02$ TeV*, Eur. Phys. J. C **79** (2019) 702. 39 p, arXiv:1902.01339.
- 3262 [38] ALICE collaboration, *Production of the $\rho(770)^0$ meson in pp and Pb-Pb collisions at*
3263 *$\sqrt{s_{NN}} = 2.76$ TeV*, Phys. Rev. C **99** (2019), no. 6 064901, arXiv:1805.04365.
- 3264 [39] STAR collaboration, *ρ^0 photoproduction in ultraperipheral relativistic heavy ion collisions*
3265 *at $\sqrt{s_{NN}} = 200$ GeV*, Phys. Rev. C **77** (2008) 034910, arXiv:0712.3320.
- 3266 [40] PHENIX collaboration, *Photoproduction of J/ψ and of high mass e^+e^- in ultra-peripheral*
3267 *Au + Au collisions at $\sqrt{s_{NN}} = 200$ GeV*, Phys. Lett. B **679** (2009) 321, arXiv:0903.2041.
- 3268 [41] CDF collaboration, *Observation of exclusive charmonium production and $\gamma + \gamma$ to $\mu^+\mu^-$*
3269 *in $p\bar{p}$ collisions at $\sqrt{s} = 1.96$ TeV*, Phys. Rev. Lett. **102** (2009) 242001, arXiv:0902.1271.
- 3270 [42] LHCb collaboration, *Measurement of J/ψ production in pp collisions at $\sqrt{s} = 7$ TeV*, Eur.
3271 Phys. J. C **71** (2011) 1645, arXiv:1103.0423.
- 3272 [43] LHCb collaboration, *Central exclusive production of J/ψ and $\psi(2S)$ mesons in pp collisions*
3273 *at $\sqrt{s} = 13$ TeV*, Submitted to: JHEP (2018) arXiv:1806.04079.
- 3274 [44] CMS collaboration, *Coherent J/ψ photoproduction in ultra-peripheral PbPb collisions*

- 3275 *at $\sqrt{s_{\text{NN}}} = 2.76 \text{ TeV}$ with the CMS experiment*, Phys. Lett. B **772** (2017) 489,
3276 arXiv:1605.06966.
- 3277 [45] ALICE collaboration, *Coherent J/ψ photoproduction in ultra-peripheral Pb-Pb collisions*
3278 *at $\sqrt{s_{\text{NN}}} = 2.76 \text{ TeV}$* , Phys. Lett. B **718** (2013) 1273, arXiv:1209.3715.
- 3279 [46] ALICE collaboration, *Charmonium and e^+e^- pair photoproduction at mid-rapidity in*
3280 *ultra-peripheral Pb-Pb collisions at $\sqrt{s_{\text{NN}}} = 2.76 \text{ TeV}$* , Eur. Phys. J. C **73** (2013), no. 11
3281 2617, arXiv:1305.1467.
- 3282 [47] K. Naskar, on behalf of the CMS collaboration, *Measurement of exclusive Upsilon photo-*
3283 *production in pPb collisions at $\sqrt{s_{\text{NN}}} = 5.02 \text{ TeV}$ with the CMS*, PoS **HardProbes2018**
3284 (2019) 180, arXiv:1903.10811.
- 3285 [48] CMS collaboration, *Measurement of exclusive Υ photoproduction from protons in pPb*
3286 *collisions at $\sqrt{s_{\text{NN}}} = 5.02 \text{ TeV}$* , Eur. Phys. J. C **79** (2019), no. 3 277, arXiv:1809.11080.
- 3287 [49] LHCb collaboration, *Measurement of the exclusive Υ production cross-section in pp*
3288 *collisions at $\sqrt{s} = 7 \text{ TeV}$ and 8 TeV* , JHEP **09** (2015) 084, arXiv:1505.08139.
- 3289 [50] Y. Chen *et al.*, *Glueball spectrum and matrix elements on anisotropic lattices*, Phys. Rev.
3290 D **73** (2006) 014516, arXiv:hep-lat/0510074.
- 3291 [51] C. J. Morningstar and M. J. Peardon, *The Glueball spectrum from an anisotropic lattice*
3292 *study*, Phys. Rev. D **60** (1999) 034509, arXiv:hep-lat/9901004.
- 3293 [52] V. A. Khoze, A. D. Martin, and M. G. Ryskin, *Can the Higgs be seen in rapidity gap events*
3294 *at the Tevatron or the LHC?*, Eur. Phys. J. C **14** (2000) 525, arXiv:hep-ph/0002072.
- 3295 [53] M. G. Albrow and A. Rostovtsev, *Searching for the Higgs at hadron colliders using the*
3296 *missing mass method*, arXiv:hep-ph/0009336.
- 3297 [54] V. A. Khoze, A. D. Martin, and M. G. Ryskin, *Prospects for new physics observa-*
3298 *tions in diffractive processes at the LHC and Tevatron*, Eur. Phys. J. C **23** (2002) 311,
3299 arXiv:hep-ph/0111078.
- 3300 [55] CDF collaboration, *Search for exclusive $\gamma\gamma$ production in hadron-hadron collisions*, Phys.
3301 Rev. Lett. **99** (2007) 242002, arXiv:0707.2374.
- 3302 [56] CMS collaboration, *Observation of a New Boson at a Mass of 125 GeV with the CMS*
3303 *Experiment at the LHC*, Phys. Lett. B **716** (2012) 30, arXiv:1207.7235.
- 3304 [57] M. Breidenbach *et al.*, *Observed behavior of highly inelastic electron-proton scattering*,
3305 Phys. Rev. Lett. **23** (1969) 935.
- 3306 [58] J. D. Bjorken, *Asymptotic sum rules at infinite momentum*, Phys. Rev. **179** (1969) 1547.
- 3307 [59] L. D. Broglie, *Xxxv. a tentative theory of light quanta*, Philosophical Magazine Letters **86**

- 3308 (2006), no. 7 411, arXiv:<https://doi.org/10.1080/09500830600914721>.
- 3309 [60] J. R. Forshaw and D. A. Ross, *Quantum chromodynamics and the pomeron*, vol. 9,
3310 Cambridge University Press, 1, 2011.
- 3311 [61] S. Donnachie, H. G. Dosch, O. Nachtmann, and P. Landshoff, *Pomeron physics and QCD*,
3312 vol. 19, Cambridge University Press, 12, 2004.
- 3313 [62] L. Sestini, on behalf of the LHCb collaboration, *Electroweak boson production at LHCb*,
3314 PoS **EPS-HEP2017** (2017) 402.
- 3315 [63] L. A. Harland-Lang, V. A. Khoze, M. G. Ryskin, and W. J. Stirling, *Central exclusive*
3316 *production within the Durham model: a review*, Int. J. Mod. Phys. A **29** (2014) 1430031,
3317 arXiv:1405.0018.
- 3318 [64] L. A. Harland-Lang, V. A. Khoze, M. G. Ryskin, and W. J. Stirling, *The Phenomenology*
3319 *of Central Exclusive Production at Hadron Colliders*, Eur. Phys. J. C **72** (2012) 2110,
3320 arXiv:1204.4803.
- 3321 [65] L. A. Harland-Lang, V. A. Khoze, and M. G. Ryskin, *Central exclusive production and*
3322 *the Durham model*, Int. J. Mod. Phys. A **29** (2014) 1446004.
- 3323 [66] L. A. Harland-Lang, *Simple form for the low- x generalized parton distributions in the*
3324 *skewed regime*, Phys. Rev. D **88** (2013), no. 3 034029, arXiv:1306.6661.
- 3325 [67] L. A. Harland-Lang, V. A. Khoze, M. G. Ryskin, and W. J. Stirling, *Central exclu-*
3326 *sive χ_c meson production at the Tevatron revisited*, Eur. Phys. J. C **65** (2010) 433,
3327 arXiv:0909.4748.
- 3328 [68] LHC Forward Physics Working Group, *LHC Forward Physics*, J. Phys. G **43** (2016)
3329 110201, arXiv:1611.05079.
- 3330 [69] V. A. Khoze, A. D. Martin, M. G. Ryskin, and W. J. Stirling, *Double diffractive χ meson*
3331 *production at the hadron colliders*, Eur. Phys. J. C **35** (2004) 211, arXiv:hep-ph/0403218.
- 3332 [70] V. V. Sudakov, *Vertex parts at very high energies in quantum electrodynamics*, Zh. Eksp.
3333 Teor. Fiz. **30** (1956) 87.
- 3334 [71] J. C. Collins, *Sudakov form-factors*, Adv. Ser. Direct. High Energy Phys. **5** (1989) 573,
3335 arXiv:hep-ph/0312336.
- 3336 [72] M. R. Pelicer, E. G. de Oliveira, A. D. Martin, and M. G. Ryskin, *Absorptive effects*
3337 *and power corrections in low x DGLAP evolution*, Eur. Phys. J. C **79** (2019), no. 1 9,
3338 arXiv:1810.05573.
- 3339 [73] H1 collaboration, *Elastic and inelastic photoproduction of J/ψ mesons at HERA*, Nucl.
3340 Phys. B **472** (1996) 3, arXiv:hep-ex/9603005.

- 3341 [74] V. A. Khoze, A. D. Martin, and M. G. Ryskin, *Soft diffraction and the elastic slope at*
3342 *Tevatron and LHC energies: A MultiPomeron approach*, Eur. Phys. J. C **18** (2000) 167,
3343 arXiv:hep-ph/0007359.
- 3344 [75] V. A. Khoze, A. D. Martin, and M. G. Ryskin, *Diffraction at the LHC*, Eur. Phys. J. C
3345 **73** (2013) 2503, arXiv:1306.2149.
- 3346 [76] L. A. Harland-Lang, V. A. Khoze, M. G. Ryskin, and W. J. Stirling, *Standard candle*
3347 *central exclusive processes at the Tevatron and LHC*, Eur. Phys. J. **C69** (2010) 179,
3348 arXiv:1005.0695.
- 3349 [77] R. S. Pasechnik, A. Szczurek, and O. V. Teryaev, *Elastic double diffractive production of*
3350 *axial-vector χ_c (1^{++}) mesons and the Landau-Yang theorem*, Phys. Lett. B **680** (2009)
3351 62, arXiv:0901.4187.
- 3352 [78] L. A. Harland-Lang, V. A. Khoze, and M. G. Ryskin, *Exclusive physics at the LHC with*
3353 *SuperChic 2*, Eur. Phys. J. **C76** (2016), no. 1 9, arXiv:1508.02718.
- 3354 [79] L. A. Harland-Lang, V. A. Khoze, and M. G. Ryskin, *Exclusive LHC physics with heavy*
3355 *ions: SuperChic 3*, Eur. Phys. J. C **79** (2019), no. 1 39, arXiv:1810.06567.
- 3356 [80] L. A. Harland-Lang, M. Tasevsky, V. A. Khoze, and M. G. Ryskin, *A new approach to*
3357 *modelling elastic and inelastic photon-initiated production at the LHC: SuperChic 4*, Eur.
3358 Phys. J. C **80** (2020), no. 10 925, arXiv:2007.12704.
- 3359 [81] Particle Data Group, P. A. Zyla *et al.*, *Review of Particle Physics*, PTEP **2020** (2020),
3360 no. 8 083C01.
- 3361 [82] Particle Data Group, M. Tanabashi *et al.*, *Review of particle physics*, Phys. Rev. D **98**
3362 (2018) 030001.
- 3363 [83] CDF collaboration, *The CDF-II detector: Technical design report*, .
- 3364 [84] V. A. Khoze, A. D. Martin, and M. G. Ryskin, *Double diffractive processes in high*
3365 *resolution missing mass experiments at the Tevatron*, Eur. Phys. J. C **19** (2001) 477,
3366 arXiv:hep-ph/0011393, [Erratum: Eur.Phys.J.C 20, 599 (2001)].
- 3367 [85] LHCb Collaboration, *Central Exclusive Dimuon Production at $\sqrt{s} = 7$ TeV*, , LHCb-
3368 CONF-2011-022, CERN-LHCb-CONF-2011-022.
- 3369 [86] S. R. Klein *et al.*, *STARlight: A Monte Carlo simulation program for ultra-peripheral*
3370 *collisions of relativistic ions*, Comput. Phys. Commun. **212** (2017) 258, arXiv:1607.03838.
- 3371 [87] S. R. Klein and J. Nystrand, *Photoproduction of quarkonium in proton proton and nucleus*
3372 *nucleus collisions*, Phys. Rev. Lett. **92** (2004) 142003, arXiv:hep-ph/0311164.
- 3373 [88] P. M. Bjornstad, *Central Exclusive Production of χ Mesons at LHCb*, PhD thesis, Manch-

- 3374 ester U., 11, 2013.
- 3375 [89] L. Evans and P. Bryant, *LHC machine*, Journal of Instrumentation **3** (2008) S08001.
- 3376 [90] J. Haffner, *The CERN accelerator complex. Complexe des accélérateurs du CERN*, <https://cds.cern.ch/record/1621894>, Oct, 2013.
- 3377
- 3378 [91] LHCb collaboration, *The LHCb detector at the LHC*, JINST **3** (2008) S08005.
- 3379 [92] LHCb collaboration, *LHCb reoptimized detector design and performance: Technical Design Report*, CERN-LHCC-2003-030. LHCb-TDR-009.
- 3380
- 3381 [93] C. Elsasser, *$b\bar{b}$ production at the LHCb experiment*, provided by the LHCb Speakers' Bureau: https://lhcb.web.cern.ch/lhcb/speakersbureau/html/bb_ProductionAngles.html,
- 3382
- 3383 June, 2021.
- 3384 [94] LHCb Operations Plots, *LHCb Integrated Recorded Luminosity in pp. 2010-2018*, <https://lbggroups.cern.ch/online/OperationsPlots/index.htm>, June, 2018.
- 3385
- 3386 [95] LHCb collaboration, *LHCb Detector Performance*, Int. J. Mod. Phys. **A30** (2015), no. 07
- 3387 1530022, arXiv:1412.6352.
- 3388 [96] LHCb collaboration, *LHCb VELO (Vertex LOcator): Technical Design Report*, CERN-
- 3389 LHCC-2001-011. LHCb-TDR-005.
- 3390 [97] LHCb collaboration, *LHCb VELO Upgrade Technical Design Report*, CERN-LHCC-2013-
- 3391 021. LHCb-TDR-013.
- 3392 [98] LHCb collaboration, *LHCb magnet: Technical Design Report*, CERN-LHCC-2000-007.
- 3393 LHCb-TDR-001.
- 3394 [99] LHCb collaboration, *Silicon strip detectors for the LHCb experiment*, Nucl. Instrum. Meth.
- 3395 **A541** (2005) 83.
- 3396 [100] LHCb collaboration, *LHCb RICH: Technical Design Report*, CERN-LHCC-2000-037.
- 3397 LHCb-TDR-003.
- 3398 [101] LHCb collaboration, *LHCb calorimeters: Technical Design Report*, CERN-LHCC-2000-
- 3399 036. LHCb-TDR-002.
- 3400 [102] K. C. Akiba *et al.*, *The HeRSChel detector: high-rapidity shower counters for LHCb*,
- 3401 JINST **13** (2018), no. 04 P04017, arXiv:1801.04281.
- 3402 [103] E. Technology, *EJ-200 plastic scintillator*, https://www.eljentechnology.com/images/stories/Data_Sheets/Plastic_Scintillators/EJ200%20data%20sheet.pdf, 2021.
- 3403
- 3404 [104] H. P. K. K. *Photomultiplier tube R1828-01*, <https://www.hamamatsu.com/eu/en/product/type/R1828-01/index.html>, 2021.
- 3405

- 3406 [105] LHCb collaboration, *LHCb trigger system: Technical Design Report*, CERN-LHCC-2003-
3407 031. LHCb-TDR-010.
- 3408 [106] G. Barrand *et al.*, *GAUDI - A software architecture and framework for building HEP data*
3409 *processing applications*, Comput. Phys. Commun. **140** (2001) 45.
- 3410 [107] M. Clemencic *et al.*, *Recent developments in the LHCb software framework Gaudi*, J. Phys.
3411 Conf. Ser. **219** (2010) 042006.
- 3412 [108] BRUNEL, The LHCb Event Reconstruction program
3413 <http://lhcb-release-area.web.cern.ch/LHCb-release-area/DOC/brunel>.
- 3414 [109] A. Hoecker *et al.*, *TMVA: Toolkit for multivariate data analysis*, PoS **ACAT** (2007) 040,
3415 [arXiv:physics/0703039](https://arxiv.org/abs/physics/0703039).
- 3416 [110] S. Benson, V. V. Gligorov, M. A. Vesterinen, and J. M. Williams, *The LHCb Turbo Stream*,
3417 J. Phys. Conf. Ser. **664** (2015), no. 8 082004.
- 3418 [111] DAVINCI, The physics analysis software for the LHCb experiment
3419 <http://lhcb-release-area.web.cern.ch/LHCb-release-area/DOC/davinci>.
- 3420 [112] R. Brun and F. Rademakers, *ROOT: An object oriented data analysis framework*, Nucl.
3421 Instrum. Meth. **A389** (1997) 81.
- 3422 [113] LHCb collaboration, *Triger Schemes*, [https://lhcb.web.cern.ch/speakersbureau/html/](https://lhcb.web.cern.ch/speakersbureau/html/TriggerScheme.html)
3423 [TriggerScheme.html](https://lhcb.web.cern.ch/speakersbureau/html/TriggerScheme.html), 2021.
- 3424 [114] M. Clemencic *et al.*, on behalf of the LHCb collaboration, *The LHCb simulation application,*
3425 *Gauss: Design, evolution and experience*, J. Phys. Conf. Ser. **331** (2011) 032023.
- 3426 [115] I. Belyaev *et al.*, on behalf of the LHCb collaboration, *Handling of the generation of*
3427 *primary events in GAUSS, the LHCb simulation framework*, Nuclear Science Symposium
3428 Conference Record (NSS/MIC) **IEEE** (2010) 1155.
- 3429 [116] LHCb collaboration, *The Gauss project*, <http://lhcbdoc.web.cern.ch/lhcbdoc/gauss>,
3430 2021.
- 3431 [117] D. J. Lange, *The EvtGen particle decay simulation package*, Nucl. Instrum. Meth. **A462**
3432 (2001) 152.
- 3433 [118] P. Golonka and Z. Was, *PHOTOS Monte Carlo: a precision tool for QED corrections in*
3434 *Z and W decays*, Eur. Phys. J. **C45** (2006) 97, [arXiv:hep-ph/0506026](https://arxiv.org/abs/hep-ph/0506026).
- 3435 [119] GEANT4, S. Agostinelli *et al.*, *GEANT4—a simulation toolkit*, Nucl. Instrum. Meth. A
3436 **506** (2003) 250.
- 3437 [120] T. Sjöstrand, S. Mrenna, and P. Skands, *PYTHIA 6.4 physics and manual*, JHEP **05**
3438 (2006) 026, [arXiv:hep-ph/0603175](https://arxiv.org/abs/hep-ph/0603175).

- 3439 [121] T. Sjöstrand, S. Mrenna, and P. Skands, *A brief introduction to PYTHIA 8.1*, Comput.
3440 Phys. Commun. **178** (2008) 852, arXiv:0710.3820.
- 3441 [122] LHCb collaboration, *The Boole project*, [http://lhcb-release-area.web.cern.ch/
3442 LHCb-release-area/DOC/boole/](http://lhcb-release-area.web.cern.ch/LHCb-release-area/DOC/boole/).
- 3443 [123] LHCb collaboration, *The Moore project*, <http://lhcbdoc.web.cern.ch/lhcbdoc/moore/>,
3444 2021.
- 3445 [124] G. Zunica, on behalf of the LHCb collaboration, *Design and performance of the LHCb
3446 detector and full real-time reconstruction in Run 2 of the LHC*, in *2019 IEEE Nu-
3447 clear Science Symposium (NSS) and Medical Imaging Conference (MIC)*, 10, 2019.
3448 doi: 10.1109/NSS/MIC42101.2019.9059669.
- 3449 [125] M. De Cian, S. Farry, P. Seyfert, and S. Stahl, *Fast neural-net based fake track rejection
3450 in the LHCb reconstruction*, tech. rep., CERN, Geneva, Mar, 2017.
- 3451 [126] R. Frühwirth, *Application of kalman filtering to track and vertex fitting*, Nuclear Instru-
3452 ments and Methods in Physics Research Section A: Accelerators, Spectrometers, Detectors
3453 and Associated Equipment **262** (1987), no. 2 444.
- 3454 [127] L. Harland-Lang, *Superchic 2 - a monte carlo for central exclusive production*,
3455 <https://superchic.hepforge.org>.
- 3456 [128] L. A. Harland-Lang, A. D. Martin, P. Motylinski, and R. S. Thorne, *Parton distributions in
3457 the LHC era: MMHT 2014 PDFs*, Eur. Phys. J. C **75** (2015), no. 5 204, arXiv:1412.3989.
- 3458 [129] LHCb collaboration, *Measurement of the relative rate of prompt χ_{c0} , χ_{c1} and χ_{c2} production
3459 at $\sqrt{s} = 7$ TeV*, JHEP **10** (2013) 115, arXiv:1307.4285.
- 3460 [130] LHCb collaboration, *Measurement of the $\chi_b(3P)$ mass and of the relative rate of $\chi_{b1}(1P)$
3461 and $\chi_{b2}(1P)$ production*, JHEP **10** (2014) 088, arXiv:1409.1408.
- 3462 [131] LHCb collaboration, *Measurements of prompt charm production cross-sections in
3463 pp collisions at $\sqrt{s} = 13$ TeV*, JHEP **03** (2016) 159, arXiv:1510.01707, [Erratum:
3464 JHEP05,074(2017)].
- 3465 [132] T. Skwarnicki, *A study of the radiative cascade transitions between the Upsilon-prime and
3466 Upsilon resonances*, PhD thesis, Institute of Nuclear Physics, Krakow, 1986, DESY-F31-
3467 86-02.
- 3468 [133] K. Cranmer, *Kernel estimation in high-energy physics*, Comput. Phys. Commun. **136**
3469 (2001) 198, arXiv:hep-ex/0011057.
- 3470 [134] S. P. Baranov, O. Duenger, H. Shooshtari, and J. A. M. Vermaseren, *LPAIR: A generator
3471 for lepton pair production*, in *Workshop on Physics at HERA*, 1991.

- 3472 [135] H1 collaboration, *Elastic and Proton-Dissociative Photoproduction of J/ψ Mesons at*
3473 *HERA*, Eur. Phys. J. C **73** (2013), no. 6 2466, arXiv:1304.5162.
- 3474 [136] LHCb collaboration, *LHCb Luminosity project*, [https://twiki.cern.ch/twiki/bin/view/](https://twiki.cern.ch/twiki/bin/view/LHCbPhysics/LHCbLuminosity#LumiRun2Instructions)
3475 [LHCbPhysics/LHCbLuminosity#LumiRun2Instructions](https://twiki.cern.ch/twiki/bin/view/LHCbPhysics/LHCbLuminosity#LumiRun2Instructions).
- 3476 [137] S. Dulat *et al.*, *New parton distribution functions from a global analysis of quantum*
3477 *chromodynamics*, Phys. Rev. D **93** (2016), no. 3 033006, arXiv:1506.07443.
- 3478 [138] S. Bailey *et al.*, *Parton distributions from LHC, HERA, Tevatron and fixed target data:*
3479 *MSHT20 PDFs*, arXiv:2012.04684.
- 3480 [139] NNPDF collaboration, *Parton distributions from high-precision collider data*, Eur. Phys.
3481 J. C **77** (2017), no. 10 663, arXiv:1706.00428.
- 3482 [140] Belle collaboration, *Observation of a narrow charmonium - like state in exclusive $B^\pm \rightarrow$*
3483 *$K^\pm \pi^+ \pi^- J/\psi$ decays*, Phys. Rev. Lett. **91** (2003) 262001, arXiv:hep-ex/0309032.
- 3484 [141] CDF collaboration, *Analysis of the quantum numbers J^{PC} of the $X(3872)$* , Phys. Rev.
3485 Lett. **98** (2007) 132002, arXiv:hep-ex/0612053.
- 3486 [142] LHCb collaboration, *Determination of the $X(3872)$ meson quantum numbers*, Phys. Rev.
3487 Lett. **110** (2013) 222001, arXiv:1302.6269.
- 3488 [143] LHCb collaboration, *Study of the lineshape of the $\chi_{c1}(3872)$ state*, Phys. Rev. D **102**
3489 (2020), no. 9 092005, arXiv:2005.13419.
- 3490 [144] LHCb collaboration, *Study of the $\psi_2(3823)$ and $\chi_{c1}(3872)$ states in $B^+ \rightarrow (J\psi\pi^+\pi^-)K^+$*
3491 *decays*, JHEP **08** (2020) 123, arXiv:2005.13422.